

# Torsional and lateral vibrations in flexible rotor systems with friction

**Citation for published version (APA):**

Mihajlovic, N. (2005). *Torsional and lateral vibrations in flexible rotor systems with friction*. [Phd Thesis 1 (Research TU/e / Graduation TU/e), Mechanical Engineering]. Technische Universiteit Eindhoven.  
<https://doi.org/10.6100/IR591879>

**DOI:**

[10.6100/IR591879](https://doi.org/10.6100/IR591879)

**Document status and date:**

Published: 01/01/2005

**Document Version:**

Publisher's PDF, also known as Version of Record (includes final page, issue and volume numbers)

**Please check the document version of this publication:**

- A submitted manuscript is the version of the article upon submission and before peer-review. There can be important differences between the submitted version and the official published version of record. People interested in the research are advised to contact the author for the final version of the publication, or visit the DOI to the publisher's website.
- The final author version and the galley proof are versions of the publication after peer review.
- The final published version features the final layout of the paper including the volume, issue and page numbers.

[Link to publication](#)

**General rights**

Copyright and moral rights for the publications made accessible in the public portal are retained by the authors and/or other copyright owners and it is a condition of accessing publications that users recognise and abide by the legal requirements associated with these rights.

- Users may download and print one copy of any publication from the public portal for the purpose of private study or research.
- You may not further distribute the material or use it for any profit-making activity or commercial gain
- You may freely distribute the URL identifying the publication in the public portal.

If the publication is distributed under the terms of Article 25fa of the Dutch Copyright Act, indicated by the "Taverne" license above, please follow below link for the End User Agreement:

[www.tue.nl/taverne](http://www.tue.nl/taverne)

**Take down policy**

If you believe that this document breaches copyright please contact us at:

[openaccess@tue.nl](mailto:openaccess@tue.nl)

providing details and we will investigate your claim.

Torsional and Lateral  
Vibrations in Flexible Rotor  
Systems with Friction

CIP-DATA LIBRARY TECHNISCHE UNIVERSITEIT EINDHOVEN

Mihajlović, Nenad

Torsional and Lateral Vibrations in Flexible Rotor Systems with Friction / by Nenad Mihajlović. -

Eindhoven: Technische Universiteit Eindhoven, 2005.

Proefschrift. - ISBN 90-386-2617-7

NUR 978

Subject headings: flexible rotor systems / drill-string system / discontinuous bifurcations / experimental non-smooth dynamics / parameter estimation / system stability; Lyapunov methods / interaction between torsional and lateral vibrations

Trefwoorden: flexibele rotor systemen / boorstang systeem / discontinue bifurcaties / experimentele niet-gladde dynamica / parameter schatting / stabiliteit; Lyapunov methode / interactie tussen torsionele en laterale vibratie

Printed by University Press Facilities, Eindhoven, The Netherlands

Cover design: JWL Producties

Copyright © 2005, by Nenad Mihajlović

This dissertation has been completed in partial fulfillment of the requirements of the Dutch Institute of Systems and Control (DISC) for graduate study.

This project has been supported by the Eindhoven University of Technology (Technische Universiteit Eindhoven).

# Torsional and Lateral Vibrations in Flexible Rotor Systems with Friction

PROEFSCHRIFT

ter verkrijging van de graad van doctor aan de  
Technische Universiteit Eindhoven,  
op gezag van de Rector Magnificus, prof.dr.ir. C.J. van Duijn,  
voor een commissie aangewezen door het College voor Promoties  
in het openbaar te verdedigen op  
donderdag 30 juni 2005 om 16.00 uur

door

Nenad Mihajlović

geboren te Zaječar, Servië en Montenegro

Dit proefschrift is goedgekeurd door de promotoren:

prof.dr. H. Nijmeijer  
en  
prof.dr.ir. D. H. van Campen

Copromotor:  
dr.ir. N. van de Wouw

# Preface

Almost five years ago I decided to come to The Netherlands for my Ph.D. Everything started with the following e-mail:

*Dear Mr. Mihajlovic,*

*We have carefully reviewed your cv and further information that you have provided for your application as a PhD student in my group. We consider you as a possible strong candidate for a PhD position, and we would be interested in pursuing this further...*

...

*Sincerely yours,*

*H.Nijmeijer*

Then, with a control and electrical engineering background, I started a research project in the field of dynamics of nonlinear mechanical systems at the Department of Mechanical Engineering at the Eindhoven University of Technology. At that time, I could not have dreamt that except successfully finishing my research in 2005, I would also succeed to learn a new language - Dutch (which according to some people represents a forerunner of German language), and I would start working in a research department of Philips Electronics - one of the biggest electronics company in the world. Moreover, I could not predict that I would continue playing handball, even be an assistant trainer in a Dutch handball team and meet so many cultures. What is most wonderful is that I have become husband of a wonderful wife and a father of a charming girl. At that time all this would be too much even for a wonderful dream.

Although the results presented in this thesis represent an overview on what I have been doing scientifically in the last four-and-a-half years, in this preface I would like to use this opportunity to show my gratitude to the people that helped me to finish this thesis and that were with me through this enjoyable, exciting and challenging journey.

I am particularly grateful to my promoters Henk Nijmeijer and Dick van Campen as well as to Bram de Kraker for being courageous enough to offer me the opportunity to do research in the field of nonlinear mechanical systems although my background was in the field of electric engineering and in control of linear dynamical systems. I hope that you never had doubts about such decision. Goran and Nataša Golo (kum Golson and kuma Nataša) and Dragan Kostić (Maher) deserve special acknowledgements. Five years ago, they encouraged and supported me very much when I was applying for this Ph.D. project.

Special thanks goes to my first promotor Henk Nijmeijer and my co-promotor Nathan van de Wouw, since they have steered, supported and helped me together, both in their own way, to successfully finish my research. The quality and readability of this thesis is thanks to their support. Henk, thank you for your constructive criticism, high demands and encouraging words. Thank you also for being determined

enough to help me to learn and to improve my Dutch. A few months ago I was told that I pronounced your name as Genk instead of Henk. Sorry for that. Nathan, thanks for being not only a co-promotor but also a friend. This helped me a lot to go more smoothly through many of challenges which were present during my Ph.D. work. It has been a real extraordinary and enjoyable experience to work with both of you.

At the beginning of my Ph.D. research I had a lot of help from Remco Leine in understanding discontinuous systems, discontinuous bifurcations, drill-string systems and I am very thankful for that. Remco, I really enjoyed very much discussing with you both about scientific and non-scientific matters. I would also like to thank Nick Rosielle. Without his help it would be very difficult to construct the experimental set-up. Furthermore, I also thank Harry van Leeuwen and Kees Meesters, who gave me hints in the field of tribology, that helped me to introduce torsional vibrations in the set-up. The set-up would never been finished in time without the assistance of Daniëlle Steman, Toon van Gils, Rob van de Berg and Sjef Garenfeld who helped me with the mechanics of the set-up, and Rens Kodde, Harrie van de Loo and Peter Hamels who helped me with the electrical part of the set-up. The collaboration with the master students Angelique Kessels, Marion Meijboom, Mariëlle van Veggel and Maarten Hendriks was really valuable for my Ph.D. research. Many thanks goes also to all former and current members of the Dynamics and Control Technology Group for the wonderful atmosphere and enjoyable time. They have always been ready to help.

Special greetings and thanks are devoted to my colleagues and nice friends Wilbert, Apostolos, Ronald, Rob, Ana, Alejandro, Niels, Alexey, Sasha, Ines and Devi. I will always remember the nice and pleasant discussion with you. I also like to thank Maarten Steinbuch, Pieter Nuij, Ron Hensen and Paul Lambrechts, who together with Henk and Nathan helped me a lot with their comments, constructive criticism in making decisions about my future employer. Lia, thanks for helping me with administrative matters during my time at the university in Eindhoven.

Being a member of the Oktopus handball team was really a wonderful experience. Thanks to Oktopus I met Bas, Kristel, Jan, Eric, Bianca, Hendri, Maartje, Michael, Dave, Johan, Femke, Erik, Wendy and Corrine; wonderful people and great friends. At this time I really miss handball trainings and competitions. Special thanks to Bas and Jan who succeeded to infect me with trainer activities.

Greetings to my Serbian friends here in The Netherlands: Tasa, bata Marko, Vesna, Milena, Mirjana, Vojkan, Maja, Dule, Aleksandra, Milan, Marija, Darko, Mirjana, Igor, Jelena, Ana, Aleksandar and Jelena. In particular, I would like to greet my Serbian friends who, despite the fact that they live around Europe and far from here, are still very close to me: "Zlatibor-team" Kum, Šone, Korunko and also kuma Sonja, kum Neša, Pepi, Kaća, Bulle, kum Željko, Zoka and many others.

I am very grateful to my whole family and in particular to my mother Živka, father Dragoslav and brother Predrag since I have been very lucky to grow up surrounded by them, their love and support.

Finally, I thank my wife Dragana knowing that I will never be able to express how much I am happy to be surrounded by her love and support. What is most wonderful is that, thanks to her, I became the father of wonderful daughter Teodora which is really a gift of God. Both of them represent for me an inexhaustible source of energy and love. For this reason I entirely dedicate this work to them.

*To Dragana and Teodora*





# Contents

<b>Preface</b>	<b>v</b>
<b>1 Introduction</b>	<b>3</b>
1.1 Friction-Induced Vibrations in Flexible Mechanical Systems . . . . .	4
1.1.1 Friction in Mechanical Systems . . . . .	4
1.1.2 Friction-Induced Vibrations in Various Flexible Mechanical Systems . . . . .	5
1.1.3 Friction-Induced Torsional Vibrations in Drill-String Systems . . . . .	6
1.2 Vibrations in Rotor Systems . . . . .	8
1.2.1 Vibrations in Various Rotor Systems . . . . .	8
1.2.2 Vibrations in Drill-String Systems . . . . .	8
1.3 Goals and Main Contribution of the Thesis . . . . .	9
1.4 Outline of the Thesis . . . . .	10
<b>2 Preliminaries</b>	<b>13</b>
2.1 Steady-State Behaviour of Nonlinear Mechanical Systems . . . . .	13
2.2 Tools for Prediction and Estimation of Steady-State Behaviour . . . . .	16
2.2.1 Equilibrium Points and Tools for Related Stability Analysis . . . . .	16
2.2.2 Periodic Solutions and Tools for Related Stability Analysis . . . . .	19
2.2.3 Switch Model . . . . .	23
2.3 Bifurcation Diagrams . . . . .	25
<b>3 The Experimental Drill-String Set-Up</b>	<b>29</b>
3.1 Description of the Set-Up . . . . .	29
3.2 Model of the Set-Up . . . . .	34
3.2.1 Friction Modelling . . . . .	34
3.2.2 Negative Damping in the Friction Force . . . . .	37
3.2.3 Model of the DC Motor . . . . .	38
3.2.4 The Full Model of the Set-Up . . . . .	39
3.3 Parameter Estimation . . . . .	43
3.3.1 Nonlinear Least-Squares Technique . . . . .	43
3.3.2 Parameter Estimation of the Set-Up . . . . .	44
<b>4 Torsional Vibrations in Drill-String Systems</b>	<b>55</b>
4.1 Parameter Estimation of the Friction Model . . . . .	55
4.2 Analysis of the Nonlinear Dynamic Behaviour . . . . .	56
4.2.1 Equilibria and Related Stability Analysis . . . . .	57

4.2.2	Bifurcation Diagram of the Set-Up . . . . .	66
4.2.3	The Influence of Friction Characteristics on the Steady-State Behaviour . . . . .	68
4.3	Experimental Results . . . . .	76
4.3.1	Validation of Steady-State Behaviour of the Set-Up . . . . .	76
4.3.2	Various Friction Situations . . . . .	83
4.4	Summary . . . . .	89
<b>5</b>	<b>Interaction Between Torsional and Lateral Vibrations in Drill-String Systems</b>	<b>91</b>
5.1	Model Validation . . . . .	91
5.2	Analysis of Nonlinear Dynamics Behaviour . . . . .	93
5.2.1	Equilibria and Related Stability Analysis . . . . .	94
5.2.2	Bifurcation Diagram of the System . . . . .	102
5.2.3	Friction-Induced Vibrations . . . . .	108
5.2.4	Vibrations due to Coupling Between Torsional and Lateral Dynamics . . . . .	111
5.3	Experimental Results . . . . .	118
5.3.1	Validation of Steady-State Behaviour of the Set-Up . . . . .	118
5.3.2	Various Levels of Mass-Unbalance . . . . .	122
5.4	Summary . . . . .	124
<b>6</b>	<b>Conclusions and Recommendations</b>	<b>127</b>
6.1	Concluding Remarks . . . . .	127
6.1.1	Friction-Induced Torsional Vibrations in Flexible Rotor Systems	128
6.1.2	Interaction Between Torsional and Lateral Vibrations in Flexible Rotor Systems . . . . .	129
6.2	Recommendations . . . . .	130
<b>A</b>	<b>Derivation of Equations of Motion of the Set-Up</b>	<b>133</b>
<b>B</b>	<b>Local and Global Asymptotic Stability Conditions</b>	<b>137</b>
<b>C</b>	<b>Derivation of <math>\dot{V}_i(\mathbf{x}_{i1}, \mathbf{x}_{i2}, \mathbf{x}_{i1eq}, \mathbf{x}_{i1eq})</math></b>	<b>143</b>
	Bibliography	145
	Summary	153
	Samenvatting	155
	Резиме	157
	Curriculum vitae	159

# Chapter 1

## Introduction

Self-sustained vibrations appear in a wide variety of systems and structures. In some systems, such vibrations are desired as, for example, the sound of a violin string is a result of a self-sustained oscillation of the strings. Furthermore, oscillations in electrical oscillators and ringing tones in electrical bells exist due to such a phenomenon. However, self-sustained oscillations often limit the performance and can also endanger the safety of operation of dynamical systems. In this respect, one can think of vibrations which appear in a CD-player due to mass-unbalance of the CD, the curving noise of tram wheels induced by nonlinear slipping forces, vibrations in suspension bridges excited by wind and/or traffic, vibrations in oil-drilling systems during a drilling process and many others.

Vibrations in dynamical systems can be caused by nonlinearities which induce forces locally in the system under consideration. However, their presence, in general, has important consequences for the overall dynamic behaviour. Some examples of nonlinearities in mechanical systems are: friction forces and backlash phenomena in certain connections of mechanical systems, mass-unbalance and fluid-film bearings in rotating machinery, nonlinear spring and damper supports in vehicle systems, etc.

Very often, more than one type of vibration appears in dynamical systems. For example, in brake mechanisms (e.g. in cars and bicycles) vibrations can be due to the Stribeck characteristic in the friction force, due to fluctuating normal forces or due to nonconservative restoring forces [Popp et al., 2002]. In a metal cutting processes, self-excited vibrations are mainly due to the nonlinearity in the friction force and intermittent contact between the cutting tool and the workpiece [Faasen et al., 2003; Wiercigroch and Budak, 2001; Wiercigroch and Krivtsov, 2001]. Therefore, in order to gain understanding and to predict different types of vibration it is not only important to understand the causes for such vibrations but also to understand the interaction between those vibrations.

In this thesis, we focus on the following issues:

- We analyze separately friction-induced vibrations in flexible mechanical systems and lateral vibrations in rotor systems caused by a mass-unbalance.
- A particular contribution of the thesis is on the interaction between those two types of vibrations.
- When analyzing the friction-induced vibrations a discontinuous static model for the friction is used. We choose such a model and not a more complicated dynamical model.

ical friction model since it accounts for several essential friction characteristics but avoids the inclusion of unnecessary complexity. A discontinuous friction model leads to a discontinuous model of the system dynamics which exhibits both friction-induced vibrations and the interaction between friction-induced vibrations and vibrations due to mass-unbalance. The discontinuity will have significant consequences for the analysis of the steady-state behaviour of the system. The occurrence, prediction and analysis of limit-cycling behaviour (vibrations) in systems with discontinuities is currently receiving a wide attention [Brogliato, 1999; Dankowitz and Nordmark, 2000; Di Bernardo et al., 1999; Galvanetto et al., 1997; Kunze and Küpper, 1997; Leine, 2000; Leine and Nijmeijer, 2004; Leine and Van Campen, 2003; Leine et al., 1998, 2003; Popp and Stelzer, 1990]. However, most of authors are studying such systems from a theoretical point of view.

- Therefore, the focus of this thesis is on the experimental study of these systems. For such purposes we constructed an experimental drill-string set-up. This set-up was inspired by a real drilling system which is used for the exploration of oil and gas and which undergoes several types of vibrations during drilling. In the considered experimental set-up, it is possible to obtain torsional vibrations, lateral vibrations and combination of those two types of vibrations. Moreover, the sticking phenomenon is observed in the friction forces of the set-up and, therefore, a discontinuous nonlinearity (in the friction) plays a crucial role in the dynamical behaviour of the system. Using this set-up, the obtained analytical results (on the nonlinear dynamics and (nonsmooth) bifurcations) can be validated experimentally.

Clearly, the results presented here, range from the adopted model, estimation procedure, the analysis techniques used and experimental results obtained, can be extended to rotor systems and more general mechanical systems with friction and flexibility. In Section 1.1, we give the literature overview on friction-induced vibrations in flexible mechanical systems. In that section, first we present a literature overview which considers various friction models, then an overview of friction-induced vibrations in various flexible mechanical systems is given and finally an overview which addresses torsional vibrations in drill-string system is given. In Section 1.2, first we give a literature overview on vibrations in general rotor systems and second, vibrations in drill-string systems are discussed in more details. Then, in Section 1.3, the contribution of this thesis is stated and finally, in Section 1.4, the outline of the thesis is provided.

## 1.1 Friction-Induced Vibrations in Flexible Mechanical Systems

### 1.1.1 Friction in Mechanical Systems

Friction is a common phenomenon and it arises between sliding surfaces due to various complex mechanisms. For some systems, friction is a desired characteristic as it enables, for example, the fixation of parts by screws, driving of vehicles by wheels and braking mechanisms. Usually, friction is an unwanted phenomenon since it is responsible for the dissipation of kinetic energy into heat and noise and also for the

wear of parts during relative motion. Moreover, the presence of friction can induce self-sustained vibrations, chatter and squeal which are unwanted in many engineering applications, since the phenomena generally limit the system performance.

The characteristics of friction in mechanical systems have been studied in the fields of tribology and dynamics. In tribology, researchers deal with microscopic and macroscopic details of friction and they explain the observed frictional phenomena in relation to surface materials, geometry and lubrication conditions. Engineers and applied mathematicians, on the other hand, are interested in the overall dynamic behaviour and stability characteristics of systems with friction. In general, friction can be defined as a force that resists the relative motion between two contacting surfaces.

An overview which considers friction mechanisms and friction models can be found in [Al-Bender et al., 2004; Armstrong-Hélouvry et al., 1994a; Ibrahim, 1994a,b; Olsson, 1996]. Olsson [1996] divides all friction models into three categories: static, dynamic, and special purpose models. Static friction models describe the friction force as a function of the relative velocity between two contacting surfaces. Those models give, to a varying extent, a qualitative understanding of friction. Dynamic models more accurately describe friction for low relative velocities by differential equations and these models are obtained through modification of static friction models. A well-known dynamic friction model is the LuGre friction model [Canudas de Wit et al., 1995; Hensen, 2002; Olsson, 1996]. A third category of friction models includes models that provides understanding of the physical mechanisms behind friction. On the other hand, Al-Bender et al. [2004] divide all friction models into the following two groups, depending on the approaches used to model friction: models based on the physics behind the friction phenomena and empirically motivated heuristic friction models, which are based on heuristic considerations of experimental data. In general, the reason for using a specific type of friction model depends on the purpose of such model. In this thesis, we are not interested in a detailed dynamic modelling of the friction for very small velocities nor to accurately describe the physical phenomenon which causes friction. We are interested in the steady-state behaviour of a dynamic system (equilibria, limit-cycles, bifurcations) caused by the friction. Therefore, we use a discontinuous static friction model which allows to properly describe stiction and can describe most of the important friction phenomena.

The use of such a discontinuous model for friction results in a differential equations of Filippov type. Filippov systems form a class of non-smooth systems described by differential equations with discontinuous right-hand side [Filippov, 1988; Leine, 2000; Leine and Nijmeijer, 2004]. Filippov extends discontinuous differential equations to differential inclusions [Filippov, 1988; Leine, 2000; Leine and Nijmeijer, 2004; Sastry, 1999]. Dynamic systems with friction are commonly modelled by differential inclusions, see [Deimling and Szilagyi, 1994; Fečkan, 1998; Kunze and Küpper, 1997; Leine, 2000; Leine and Van Campen, 2003; Leine et al., 2003, 2002; Mihajlović et al., 2005a,b, 2004a,b; Van de Wouw and Leine, 2004; Van de Wouw et al., 2005a,b].

### 1.1.2 Friction-Induced Vibrations in Various Flexible Mechanical Systems

Undesired friction-induced vibrations can cause excessive wear of machine components, surface damage and noise. Moreover, in controlled motion systems, such vibra-

tions can limit the positioning performance. Therefore, many researchers study how friction influences the overall dynamic behaviour of systems. Some of them deal with microscopic and macroscopic details of friction when describing stick-slip vibrations [Al-Bender et al., 2004; Batista and Carlson, 1998]. Other researchers are more interested in the overall friction-induced dynamic behaviour, than in the detailed friction modelling itself. In this field of research, one can distinguish between friction-induced vibrations in controlled and non-controlled systems. An overview of friction-induced oscillations in controlled mechanical systems is given in [Armstrong-Hélouvy et al., 1994a]. Mechanisms which cause oscillations in such systems are studied both analytically and experimentally in [Hensen, 2002; Hensen et al., 2002; Juloski et al., 2005; Mallon, 2003; Mallon et al., 2005; Olsson, 1996; Olsson and Åström, 1996, 2001; Putra, 2004; Putra et al., 2004; Putra and Nijmeijer, 2003, 2004; Van de Wouw et al., 2004]. On the other hand, an overview of self-excited vibrations in non-controlled systems with friction is given by Ibrahim [1994b]. According to [Ibrahim, 1994b], several mechanisms can lead to such oscillations.

In multi-degree-of-freedom systems, the phase difference between the coupled modes can supply energy to induce vibrations in systems with friction. The importance of the coupling between the system's degrees of freedom is recognized by Eerles and Lee [1976] and such vibrations are also analyzed in [Popp et al., 2002; Popp and Stelzer, 1989]. The experimental observations of Aronov et al. [1983] support the importance of such coupling for friction-induced vibrations. However, it is widely accepted that when the systems exhibit a combination of flexibility and negative damping in the friction force-velocity curve, stick-slip motion can appear [Brockley et al., 1967; Brockley and Ko, 1970; Ibrahim, 1994b; Krauter, 1981; Kunze and Küpper, 1997; Leine, 2000; Leine et al., 1998; Olsson, 1996; Popp and Stelzer, 1990]. With the term "negative damping" we refer to the effect of the friction decrease with velocity increase which results in a negative damping for a small perturbations around a steady sliding point in a certain velocity region of the friction. The following terms are also used for the same effect: "negative viscosity", "Stribeck effect" and "velocity weakening".

### 1.1.3 Friction-Induced Torsional Vibrations in Drill-String Systems

Deep wells for the exploration and production of oil and gas are drilled with a rotary drilling system. A rotary drilling system creates a borehole by means of a rock-cutting tool, called a bit. The torque driving the bit is generated at the surface by a motor with a mechanical transmission box. Via the transmission, the motor drives the rotary table: a large disc that acts as a kinetic energy storage unit. The medium to transport the energy from the surface to the bit is a drill-string, mainly consisting of drill pipes. The drill-string can be up to 8 km long. The lowest part of the drill-string is the Bottom-Hole-Assembly (BHA in figure 1.1 [Leine, 2000]) consisting of drill collars and the bit. The Bottom-Hole-Assembly can be several hundreds meters long.

The drill-string undergoes various types of vibrations during drilling [Jansen, 1991, 1993; Leine, 2000; Leine et al., 2002; Van den Steen, 1997]: torsional (rotational) vibrations, caused by nonlinear interaction between the bit and the rock or the drill-string and the borehole wall; bending (lateral) vibrations, often caused by pipe eccentricity,

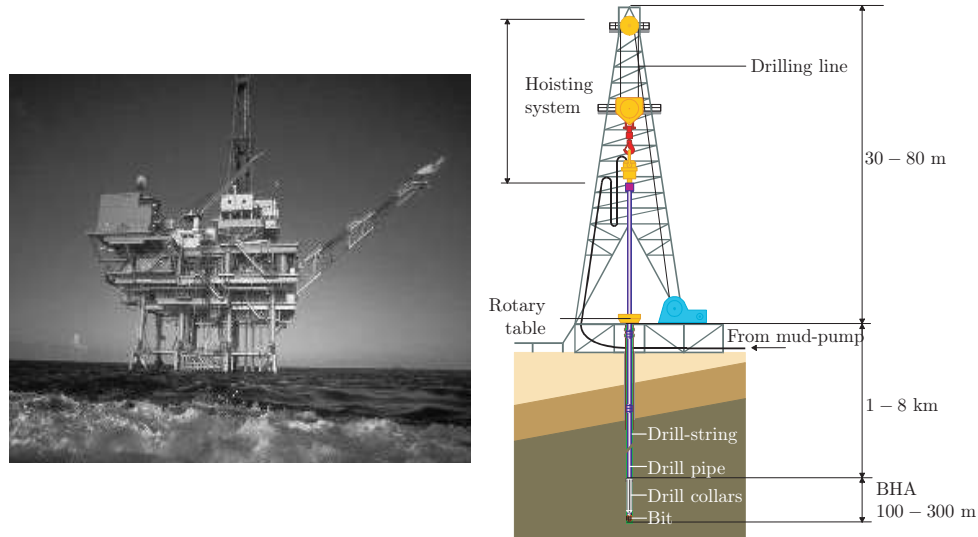


Figure 1.1: Photo and schematic view of a real drilling system.

leading to centripetal forces during rotation; axial (longitudinal) vibrations, due to bouncing of the drilling bit on the rock during rotation, and hydraulic vibrations in the circulation system, stemming from pump pulsations.

Extensive research on the subject of friction-induced torsional vibrations in drill-string systems has already been conducted. Many of those papers consider vibrations in drill-string systems [Brett, 1991, 1992; Germaý, 2002; Jansen, 1993; Jansen and Van den Steen, 1995; Kreuzer and Kust, 1996a,b, 1997; Kust, 1998; Kyllingstad and Halsey, 1988; Leine, 2000; Leine et al., 2002; Mihajlović et al., 2005a,b, 2004a,b; Van de Wouw et al., 2005a; Van den Steen, 1997]. In most papers, it is concluded that torsional vibrations are caused by negative damping in the friction force present at the contact between the bit and the borehole (see for example [Brett, 1991, 1992; Kreuzer and Kust, 1996a; Mihajlović et al., 2004a]). A number of experimental results provide additional evidence for such conclusion [Brett, 1991, 1992; Leine, 2000; Leine et al., 2002; Mihajlović et al., 2005a,b, 2004a,b; Van de Wouw et al., 2005a; Van den Steen, 1997]. Based on that conclusion, in [Jansen, 1993; Jansen and Van den Steen, 1995] a control strategy is suggested to avoid torsional vibrations in drill-string systems.

It should be noted that Germaý [2002] and Richard et al. [2004] have concluded that torsional vibrations in drilling systems can appear due to coupling between torsional and axial dynamics of the system. Moreover, according to them, such interaction effectively leads to a Stribeck effect.

In this thesis, we also investigate a negative damping in a friction-velocity curve as a cause for torsional vibrations in drill-string systems. Moreover, since the sticking phenomenon is observed in the experimental set-up, the dynamical model of the set-up incorporates a set-valued force law for the friction, and, consequently, is of Filippov-type [Filippov, 1988; Leine, 2000; Leine and Nijmeijer, 2004].



## 1.2 Vibrations in Rotor Systems

### 1.2.1 Vibrations in Various Rotor Systems

Rotating machinery such as turbines, pumps and fans are very important components in many machines and systems. Some examples are aircraft engines, power stations, large flywheels in a hybrid transmission of motorcars, etc. Therefore, the behaviour of these rotor-dynamic components can influence the performance of the whole system. Namely, for certain ranges of rotational speed, such systems can exhibit various types of vibration which can be so violent that they can cause significant damage.

There are many possible causes for such behaviour. Some examples are friction or fluid forces in the bearings in which a shaft is borne, mass-unbalance in the rotor which can lead to whirling motions, flexibilities present in the system, etc. Consequently, the understanding of the dynamic behaviour of such systems is very important and can be very complex (see for example [Lee, 1993; Tondl, 1965; Van de Vorst, 1996; Van de Vorst et al., 1994; Van de Vrande, 2001]).

Krauter [1981] analyzed torsional vibrations in water lubricated bearings. As in many papers on drilling systems, he concluded that those vibrations are due to a negative damping in the bearings.

Lateral vibrations in rotor systems have been analyzed extensively by Fritz [1970a,b]; Lee [1993]; Muszynska [1986]; Tondl [1965]; Van de Vrande [2001]. Lee [1993], Tondl [1965] and Van de Vrande [2001] considered different types of rotor systems; but in all those systems, lateral vibrations are induced by the mass-unbalance in a rotor. On the other hand, Fritz [1970a,b] and Muszynska [1986] derived expressions for fluid forces which can also induce lateral vibrations in systems with a long vibrating rotor which rotates in a stator.

Interaction between torsional and lateral vibrations in different rotor systems is studied in [Gunter et al., 1983; Lee, 1993; Tondl, 1965; Van de Vorst, 1996; Van de Vorst et al., 1994]. In various mechanical systems it is noticed that increase of mass-unbalance can have both stabilizing and destabilizing effects in the considered system. For example, Tondl [1965] and Lee [1993] consider a simple disc with a mass-unbalance connected to a shaft which is elastic in both torsional and lateral direction (see figure 1.2). They noticed that in such systems, under certain conditions, instabilities can appear if the unbalance increases. On the other hand, in [Gunter et al., 1983; Van de Vorst, 1996; Van de Vorst et al., 1994] the opposite effect has been noticed. Namely, the behaviour of flexible rotor-bearing systems is analyzed and it is concluded that the mass-unbalance can stabilize some rotor systems.

### 1.2.2 Vibrations in Drill-String Systems

Many researchers study the dynamic behaviour of rotary drill-string systems. As we already mentioned, in such systems different types of vibrations appear during drilling [Jansen, 1991, 1993; Leine, 2000; Leine et al., 2002; Van den Steen, 1997].

A literature overview about torsional vibrations in drilling systems is given in the previous section. Lateral vibrations are studied in [Jansen, 1991, 1993; Leine, 2000; Leine et al., 2002; Van der Heijden, 1993, 1994]. In [Leine, 2000; Leine et al., 2002], it is assumed that fluid forces induce lateral vibrations. Namely, Leine et al. [2002] have used the expressions for fluid forces derived in [Fritz, 1970a,b; Muszynska, 1986] and analyzed lateral vibrations in drill-string systems caused by those forces. However,

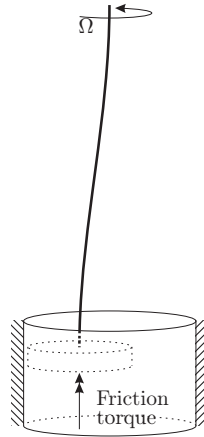


Figure 1.2: A simplified flexible rotor system.

it is widely accepted that lateral vibrations are mainly caused by pipe eccentricity and such vibrations have been analyzed by Jansen [1991, 1993] and Van der Heijden [1993, 1994].

The coupling between various types of vibrations in drilling systems is also studied. For example, the coupling mechanisms between axial and torsional vibrations have been studied in [Bailey and Finnie, 1960; Finnie and Bailey, 1960; Gernay, 2002; Richard et al., 2004]. Then, in [Jansen, 1991, 1993; Van der Heijden, 1993, 1994] not only lateral vibrations due to mass-unbalance in drilling collars have been studied, but also the influence of the drilling fluid, stabilizer clearance and stabilizer friction is taken into account. What is more, Tucker and Wang [1999] discussed the stability of drill-string configurations in vertical boreholes taking into account torsional, axial and lateral perturbations. The interaction between torsional and lateral vibrations in drilling systems is addressed in [Leine, 2000; Leine et al., 2002]. It is assumed that torsional vibrations are induced by the negative slope in the friction curve at the bit and that lateral vibrations are caused by fluid forces. Under these assumptions, a model of a simplified drill-string system (as shown in figure 1.2) is derived, and a bifurcation analysis is performed. As a result of this analysis, it is noticed that for higher angular velocity  $\Omega$  (see figure 1.2), torsional vibrations can disappear and backward whirl appears, which can also happen in real drilling systems.

However, although it is widely accepted that the main cause for torsional vibrations in drill-string systems is negative damping in the friction-velocity curve on the bit and the main cause for lateral vibrations is the mass-unbalance in the drill collars, the interaction between those two types of vibrations is not studied yet. Moreover, not a lot of experimental work has been done on interaction of various types of vibrations these systems. In order to study both types of vibrations and their interaction, an experimental set-up was built which will be described later.

### 1.3 Goals and Main Contribution of the Thesis

Although a lot of theoretical research has been performed on vibrations in flexible rotor systems, a rather limited number of papers is available which include experimental

results on the interaction between different types of vibrations. Therefore, the aim of this thesis is not only to include results of theoretical research, but the focus is on the experimental validation of the obtained results. For that purpose, we have designed an experimental set-up. The set-up consists of a DC-motor which is connected to a disc (the upper disc) via a gear box. The upper disc is connected via a low stiffness string to another disc (the lower disc) and at the lower disc an additional brake is used. The lower disc can rotate around its geometric center and can also move in both lateral directions. Consequently, such drill-string system can undergo torsional vibrations induced by the friction force, lateral vibrations due to an additional mass-unbalance which can be established at the lower disc and a combination of those two types of vibrations.

The set-up is modelled, the parameters of the model are estimated and the system dynamics are analyzed. The focus of the analysis is on the steady-state behaviour of the system when a constant input voltage is applied at the motor. Both in the model and the experiments the steady-state performance undergoes various qualitative changes when the input voltage is changed. These qualitative changes are typically captured in a bifurcation diagram that features the changes of equilibrium points into limit cycling (vibrations) and vice versa.

The main contributions of the thesis can be described as follows:

- Torsional vibrations, lateral vibrations and the interaction between those vibrations in flexible rotor systems with friction are modelled and analyzed. Those vibrations are analyzed using appropriate analytical and numerical tools. As a result of such analysis appropriate bifurcation diagrams are constructed. All this analysis is aiming at improved understanding for the cause of friction-induced limit cycling and effects of interaction which influence this type of limit cycling, and for limit cycling induced by the interaction.
- The fact that theoretically obtained results are validated experimentally, gives an opportunity to recognize which element or nonlinearity in the dynamics is responsible for certain behaviour. This allows to generalize the results, at least qualitatively, to more general types of systems.
- The dynamic model of the set-up is described by differential equations with discontinuous right-hand side (due to the presence of friction) and the bifurcations of such systems are not entirely understood. Moreover, an experimental study of discontinuous bifurcations is still rare. In the set-up, we encounter an equilibrium set, equilibria and stick-slip limit cycling; phenomena typical for systems with such a discontinuity. Moreover, we also observe a "discontinuous Hopf bifurcation" and a "discontinuous fold bifurcation" both in simulations and experiments. These observations provide the opportunity to analyze and to gain a better understanding of discontinuous bifurcations and other phenomena typical for Filippov systems.

## 1.4 Outline of the Thesis

Chapter 2 gives some basic definitions and theorems on nonlinear and non-smooth dynamics and describes several analytical and numerical tools which are used through

the thesis. In Section 2.1, we define phenomena which appear in discontinuous nonlinear systems. Analytical and numerical tools which are used for stability analysis and the prediction and estimation of steady-state behaviour of nonlinear systems are described in Section 2.2. Since we analyze discontinuous systems, we also describe the adaptations which need to be made to those analytical tools in order to use them for the analysis of discontinuous systems. Finally, in Section 2.3, we discuss the notion of bifurcation and introduce several basic bifurcations of periodic solutions, which are important in the remainder of the thesis.

Chapter 3 is devoted to the experimental set-up which is used in this thesis. In Section 3.1, we describe the set-up where friction-induced torsional vibrations, lateral vibrations due to a mass-unbalance and a combination of those types of vibration can occur. In Section 3.2, the model of the set-up is presented. The identification technique, which is used for the parameter estimation of the model and the estimated parameters for the experimental set-up are given in Section 3.3.

Chapter 4 addresses only torsional vibrations in flexible rotor systems. Therefore, we induce only torsional, and no lateral, vibrations by applying certain normal force at the brake at the lower disc of the set-up and, in Section 4.1, we estimate the friction torque at the lower disc. In Section 4.2, we determine equilibrium points (sets), periodic solutions and discuss related stability properties. As a result of such analysis we construct a bifurcation diagram based on the proposed model and the estimated parameters. We also discuss how different characteristics of the friction force at the lower disc influence the steady-state behaviour of the system. In Section 4.3, the bifurcation diagram is compared to experimentally obtained results. Furthermore, we present and discuss results obtained for different contact situations in the brake of the experimental set-up. This chapter we finish with a summary which is presented in Section 4.4.

In Chapter 5 we analyze the interaction between torsional and lateral vibrations in flexible rotor systems. Consequently, we induce both torsional and lateral vibrations in the set-up. In Section 5.1, we validate the obtained model. Next, in Section 5.2 we determine the equilibrium points (sets) and periodic solutions of the estimated model and elaborate on the related stability properties. Moreover, we discuss how various parameters of the set-up influence the vibrations in the system. In Section 5.3, based on the estimated model, a bifurcation diagram is presented and compared to experimentally obtained results. Furthermore, we discuss the experimental results obtained for various mass-unbalance levels present at the lower disc. Finally, a short summary of this chapter is given in Section 5.4.

Finally, in Chapter 6 we present conclusions which can be derived from this thesis and recommendations for future research, inspired by the results presented in the thesis.



# Chapter 2

## Preliminaries

In this thesis, we analyze the steady-state behaviour of flexible rotor systems with friction, modelled by a set-valued force law. Such systems belong to the class of discontinuous nonlinear dynamical systems. That is why, in Section 2.1, we define phenomena which appear in discontinuous nonlinear systems. Most of those definitions can be found in [Khalil, 2000; Parker and Chua, 1989; Sastry, 1999]. In Section 2.2, analytical and numerical tools are described which are used for the stability analysis, prediction and estimation of the steady-state behaviour of nonlinear systems. Most of those tools are described in more detail in [Nayfeh and Balachandran, 1995; Parker and Chua, 1989]. We also describe the adaptations which need to be made to those analytical tools in order to use them for the analysis of discontinuous systems. We also describe the Switch Model [Leine and Nijmeijer, 2004], a method which is used for numerical simulation of certain discontinuous systems. Finally, in Section 2.3 the notion of bifurcation is introduced and bifurcation diagrams are described as being a graphical tool to visualize the changes in the qualitative behaviour of differential equations as a parameter is varied.

### 2.1 Steady-State Behaviour of Nonlinear Mechanical Systems

In this thesis, we analyze the steady-state behaviour of autonomous systems. An  $n$ th-order autonomous, nonlinear dynamical system is defined by the following differential equation:

$$\dot{\mathbf{x}} = \mathbf{f}(\mathbf{x}), \quad (2.1)$$

with the initial condition

$$\mathbf{x}(t_0) = \mathbf{x}_0, \quad (2.2)$$

where  $\mathbf{x} \in \mathbb{R}^n$  represents the state,  $t \in \mathbb{R}$  represents time and  $\mathbf{f} : \mathbb{R}^n \rightarrow \mathbb{R}^n$  is called a *vector field*. The solution of (2.1) and (2.2) is called the *flow* and can be written as  $\mathbf{x}(t, \mathbf{x}_0)$  in order to show the explicit dependency on the initial condition. The set  $\{\mathbf{x}(t, \mathbf{x}_0) \mid -\infty < t < \infty\}$  is called the *trajectory* passing through  $\mathbf{x}_0$  at  $t_0$ . Very often, when no confusion arises, the solution of (2.1) and (2.2) is simply denoted as  $\mathbf{x}(t)$ .

Since we model friction with a discontinuous friction law, the vector field  $\mathbf{f}$  in (2.1) is discontinuous. In order to analyze such systems, these are often described by

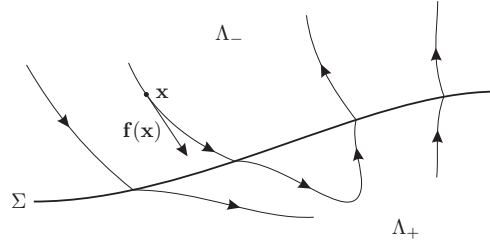


Figure 2.1: A vector field of a discontinuous system.

differential inclusions. Assume that the system (2.1) exhibits a discontinuous right-hand side:

$$\dot{\mathbf{x}} = \mathbf{f}(\mathbf{x}) = \begin{cases} \mathbf{f}_-(\mathbf{x}) & \text{for } \mathbf{x} \in \Lambda_-, \\ \mathbf{f}_+(\mathbf{x}) & \text{for } \mathbf{x} \in \Lambda_+, \end{cases} \quad (2.3)$$

with the initial condition (2.2). Then, assume that the vector field  $\mathbf{f}$  is piecewise continuous and smooth on  $\Lambda_-$  and  $\Lambda_+$  and is discontinuous on a hyper-surface  $\Sigma$  (see figure 2.1), with

$$\begin{aligned} \Sigma &= \{\mathbf{x} \in \mathbb{R}^n \mid g(\mathbf{x}) = 0\}, \\ \Lambda_- &= \{\mathbf{x} \in \mathbb{R}^n \mid g(\mathbf{x}) < 0\}, \\ \Lambda_+ &= \{\mathbf{x} \in \mathbb{R}^n \mid g(\mathbf{x}) > 0\}, \end{aligned} \quad (2.4)$$

where the smooth mapping  $g : \mathbb{R}^n \rightarrow \mathbb{R}$  defines the switching surface  $\Sigma$ . It is not required that  $\mathbf{f}_-(\mathbf{x})$  and  $\mathbf{f}_+(\mathbf{x})$  agree on  $\Sigma$ , i.e.  $\mathbf{f}_-(\mathbf{x}) \neq \mathbf{f}_+(\mathbf{x})$ ,  $\forall \mathbf{x} \in \Sigma$ . The system, described by (2.3), is not defined if  $\mathbf{x}$  is on  $\Sigma$ . We can overcome this problem with the following set-valued extension  $\mathbf{F}(\mathbf{x})$  (of  $\mathbf{f}(\mathbf{x})$ ):

$$\dot{\mathbf{x}} \in \mathbf{F}(\mathbf{x}) = \begin{cases} \mathbf{f}_-(\mathbf{x}) & \text{for } \mathbf{x} \in \Lambda_-, \\ [\mathbf{f}_-(\mathbf{x}), \mathbf{f}_+(\mathbf{x})] & \text{for } \mathbf{x} \in \Sigma, \\ \mathbf{f}_+(\mathbf{x}) & \text{for } \mathbf{x} \in \Lambda_+, \end{cases} \quad (2.5)$$

where  $[\mathbf{f}_-(\mathbf{x}), \mathbf{f}_+(\mathbf{x})]$  is a convex set for  $\mathbf{x} \in \Sigma$ :

$$[\mathbf{f}_-(\mathbf{x}), \mathbf{f}_+(\mathbf{x})] = \{(1 - q)\mathbf{f}_-(\mathbf{x}) + q\mathbf{f}_+(\mathbf{x}), \forall q \in [0, 1]\}.$$

The extension (2.5) of a discontinuous system (2.3) is called a *differential inclusion* [Filippov, 1988; Leine, 2000; Leine and Nijmeijer, 2004]. In the remainder of this thesis, we adopt Filippov's solutions concept to define solution of (2.3).

In the sequel, by *steady-state behaviour* we indicate the asymptotic behaviour of a system as  $t \rightarrow \infty$ . In this thesis, we are specifically interested in the steady-state behaviour of the systems under investigation. Therefore, we define different types of steady-state solutions encountered in nonlinear systems.

**Definition 2.1 (Equilibrium point).** *An equilibrium point  $\mathbf{x}_{eq}$  of (2.1) is a constant solution of the system. At an equilibrium point  $\mathbf{x}_{eq}$  the vector field  $\mathbf{f}$  vanishes:*

$$\mathbf{f}(\mathbf{x}_{eq}) = \mathbf{0}. \quad (2.6)$$

If the vector field  $\mathbf{f}$  is discontinuous, then an equilibrium point represents a solution of

$$\mathbf{0} \in \mathbf{F}(\mathbf{x}_{eq}), \quad (2.7)$$

where  $\mathbf{F}$  represent a differential inclusion (2.5). A solution of the algebraic inclusion (2.7) can be also an *equilibrium set*.

**Definition 2.2 (Periodic solution).** A solution  $\mathbf{x}_p(t, \mathbf{x}_{p0})$  is a periodic solution of an autonomous system (2.1) or (2.5) if

$$\mathbf{x}_p(t, \mathbf{x}_{p0}) = \mathbf{x}_p(t + T, \mathbf{x}_{p0}) \quad (2.8)$$

for all  $t \in \mathbb{R}$ .

The minimal period  $T > 0$  such that  $\mathbf{x}_p(t, \mathbf{x}_{p0}) = \mathbf{x}_p(t + T, \mathbf{x}_{p0})$  for every  $0 \leq t < T$  is called the period time of the periodic solution. A periodic solution is isolated if there is a neighborhood that contains no other periodic solution. In the autonomous case, an isolated periodic solution is called a *limit cycle*. Consequently, every limit cycle is a periodic solution. The converse, however, is not true. For instance, a linear time-invariant system may have periodic solutions, when it has a pair of eigenvalues on the imaginary axis ( $\pm j\omega$ ), but it has no limit cycles. In fact, one important difference between linear and nonlinear systems is that nonlinear systems can exhibit limit cycles, whereas linear systems cannot.

Assume that a steady-state solution of a nonlinear system is a function of two periodic functions: one with period  $T_1$  and another with period  $T_2$ . If it is possible to find a time  $T$  such that  $T = nT_1 = mT_2$ , where  $n$  and  $m$  are positive integers, then the motion is periodic with period  $T$ . If, however,  $T_1/T_2$  is an irrational number then no period time can be found and such motion is called *quasi-periodic*. Generally speaking, a quasi-periodic solution is a solution formed by the sum of periodic functions with incommensurate periods.

When analyzing the steady-state behaviour of a dynamical system, the stability properties of these steady-state solutions are often investigated because these are crucial for the global dynamics of the system. Various stability definitions exist with which the stability of these steady-state solutions can be assessed. In this thesis, *stability in the sense of Lyapunov* is considered.

**Definition 2.3 (Stability in the sense of Lyapunov).** A steady-state solution  $\mathbf{x}_s(t, \mathbf{x}_{s0})$  of a system (2.1), satisfying the initial condition  $\mathbf{x}_{s0} = \mathbf{x}_s(t_0, \mathbf{x}_{s0})$ , is defined to be stable in the sense of Lyapunov if for any  $\epsilon > 0$ , there exists a number  $\delta = \delta(\epsilon)$ , such that

$$\|\mathbf{x}_0 - \mathbf{x}_{s0}\| < \delta(\epsilon) \Rightarrow \|\mathbf{x}(t, \mathbf{x}_0) - \mathbf{x}_s(t, \mathbf{x}_{s0})\| < \epsilon, \text{ for all } t \geq t_0.$$

If, additionally the solution is attractive, i.e.

$$\|\mathbf{x}_0 - \mathbf{x}_{s0}\| < \delta(\epsilon) \Rightarrow \lim_{t \rightarrow \infty} \|\mathbf{x}(t, \mathbf{x}_0) - \mathbf{x}_s(t, \mathbf{x}_{s0})\| = 0,$$

then the solution  $\mathbf{x}_s(t, \mathbf{x}_{s0})$  is defined to be asymptotically stable in the sense of Lyapunov. The solution  $\mathbf{x}_s(t, \mathbf{x}_{s0})$  is unstable if it is not stable.

In figure 2.2, an illustration of the concept of the stability in the sense of Lyapunov is presented.

In nonlinear systems the coexistence of several (quasi-)periodic solutions and/or equilibrium points can appear. Assume, for example, that the nonlinear system (2.1) has two stable steady-state solutions: a stable equilibrium point and a stable periodic



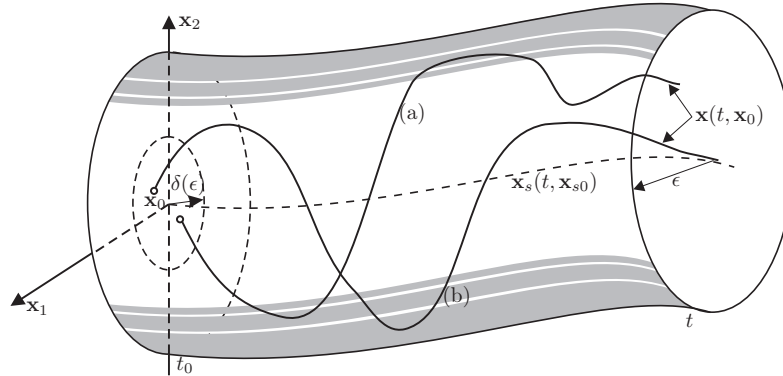


Figure 2.2: Graphical representation of (a) a stable trajectory, (b) an asymptotically stable trajectory  $\mathbf{x}_s(t, \mathbf{x}_{s0})$ .

solution. Then, the solution  $\mathbf{x}(t, \mathbf{x}_0)$  of the system converges to one of those solutions, depending on the initial condition  $\mathbf{x}_0$ . In that case we refer to the *local asymptotic stability* of the equilibrium point and the periodic solution. The collection of all initial conditions  $\mathbf{x}_0$  such that all solutions  $\mathbf{x}(t, \mathbf{x}_0)$  of (2.1) move towards the equilibrium point (periodic solution) as time proceeds, is referred to as the *domain of attraction* or the *basin of attraction* of the equilibrium point (periodic solution). If the solutions of (2.1) tend to the steady-state solution as time proceeds, for all initial conditions  $\mathbf{x}_0 \in \mathbb{R}^n$ , then we refer to the *global asymptotic stability* of the solution.

## 2.2 Tools for Prediction and Estimation of Steady-State Behaviour

### 2.2.1 Equilibrium Points and Tools for Related Stability Analysis

An equilibrium point  $\mathbf{x}_{eq}$  of an autonomous system (2.1) can be found by solving the set of algebraic equations (2.6) if the system is continuous or by solving the algebraic inclusions (2.7) for a discontinuous system (2.5). To prove that an equilibrium point is stable in the Lyapunov sense, there exist a number of methods. Further in the text, we describe Lyapunov's indirect method which can be used to determine the local stability properties of an equilibrium point. Furthermore, Lyapunov's stability theorem is given, which can be used to prove both local and global stability of an equilibrium point. Since, in this thesis we analyze discontinuous systems, we also explain under which conditions those theorems can be used for the stability analysis of the equilibrium points and equilibrium sets.

According to the Hartman-Grobman theorem [Sastry, 1999], the local behaviour of a nonlinear system (2.1) near its equilibrium point  $\mathbf{x}_{eq}$  is determined by its linearization around  $\mathbf{x}_{eq}$ . As a consequence the local stability can be studied using *Lyapunov's indirect method*.

**Theorem 2.1 (Lyapunov's indirect method).** [Khalil, 2000; Sastry, 1999] *Let  $\mathbf{x} = \mathbf{x}_{eq}$  be an equilibrium point of (2.1) where  $\mathbf{f} : D \rightarrow \mathbb{R}^n$  is continuously differentiable*

and  $D$  is a neighborhood of the equilibrium point. Let

$$\dot{\tilde{\mathbf{x}}} = \mathbf{A}\tilde{\mathbf{x}}, \quad \mathbf{A} = \frac{\partial \mathbf{f}}{\partial \mathbf{x}}(\mathbf{x}_{eq}), \quad \tilde{\mathbf{x}} = \mathbf{x} - \mathbf{x}_{eq} \quad (2.9)$$

represent the linearization of the nonlinear system (2.1) around the equilibrium point. Then,

1. the equilibrium point  $\mathbf{x}_{eq}$  is stable if all eigenvalues of  $\mathbf{A}$  have a negative real part,
2. the equilibrium point  $\mathbf{x}_{eq}$  is unstable if at least one eigenvalue has a positive real part,
3. no conclusions can be drawn if  $\mathbf{A}$  has an eigenvalue with a zero real part.

In (2.9), matrix  $\mathbf{A}$  represents the *Jacobian matrix* evaluated at the equilibrium point  $\mathbf{x}_{eq}$ . The stability of the equilibrium point can be tested by calculating the roots of the characteristic polynomial of (2.9). The characteristic polynomial can be found as

$$P(s) = \det(s\mathbf{I} - \mathbf{A}),$$

with

$$P(s) = a_n s^n + a_{n-1} s^{n-1} + \dots + a_1 s + a_0.$$

It should be noted that it is not necessary to actually find the zeros of the characteristic polynomial to determine stability, but only to determine whether there exists a zero with a positive real part. For such purposes, the Routh-Hurwitz method is useful. With that method the number of zeros with positive real part can be determined using only the coefficients of the characteristic polynomial, without actually solving the characteristic equation  $P(s) = 0$  itself [Driels, 1995].

If the equilibrium point  $\mathbf{x}_{eq}$  is not hyperbolic, i.e. if  $\mathbf{A}$  in (2.9) has at least one eigenvalue with a zero real part, whereas the rest of the eigenvalues have negative real parts, then the linearization fails to determine the stability properties of the equilibrium point. In that case, the *center manifold theory* may be applied [Khalil, 2000; Sastry, 1999]. Using that theory, the stability property of the equilibrium can be determined by analyzing a lower-order nonlinear system, whose order is exactly equal to the number of eigenvalues of  $\mathbf{A}$  with zero real parts. In that case, the  $n$ th-order nonlinear system (2.1) has to be analyzed to determine the stability of the equilibrium. However, since this theory is not used in this thesis, we do not present it here.

Since in this thesis we deal with discontinuous systems and therefore with differential inclusions, we should note that, due to non-differentiability of set-valued extension  $\mathbf{F}(\mathbf{x})$  on the discontinuity  $\Sigma$ , Lyapunov's indirect method can only be applied to assess the local stability of  $\mathbf{x}_{eq}$  if  $\mathbf{x}_{eq} \in \Lambda_- \cup \Lambda_+$  in system (2.5). However, if  $\mathbf{x}_{eq}$  is on the discontinuity, i.e.  $\mathbf{x}_{eq} \in \Sigma$ , then *Lyapunov's direct method* (also called the second method of Lyapunov) may be used for the stability analysis of such equilibrium points [Shevitz and Paden, 1994]. That method allows to analyze the stability properties of a solution of a system without explicitly solving the differential equation (2.1). The method is a generalization of the idea that if there is some measure of energy in a system which can be used, then we can study the rate of change of the energy of the system to ascertain stability. Moreover, Lyapunov showed that other functions

could be used instead of energy to determine the stability properties of an equilibrium point.

**Theorem 2.2 (Lyapunov's stability theorem).** [Khalil, 2000; Sastry, 1999] *Let  $\mathbf{x} = \mathbf{x}_{eq}$  be an equilibrium point of (2.1). Let  $V(\mathbf{x}) : D \rightarrow \mathbb{R}$  be a continuously differentiable function defined such that*

$$V(\mathbf{x}_{eq}) = 0 \text{ and } V(\mathbf{x}) > 0, \forall \mathbf{x} \in D - \{\mathbf{x}_{eq}\}, \quad (2.10)$$

$$\dot{V}(\mathbf{x}) \leq 0, \forall \mathbf{x} \in D. \quad (2.11)$$

*Then,  $\mathbf{x} = \mathbf{x}_{eq}$  is stable. Moreover, if*

$$\dot{V}(\mathbf{x}) < 0, \forall \mathbf{x} \in D - \{\mathbf{x}_{eq}\}, \quad (2.12)$$

*then equilibrium point  $\mathbf{x} = \mathbf{x}_{eq}$  is asymptotically stable.*

A continuously differentiable function  $V(\mathbf{x})$  which satisfies (2.10) and (2.11) is called a *Lyapunov function*. A function  $V(\mathbf{x})$  satisfying only condition (2.10) is said to be *positive definite* on  $D$ . If  $V(\mathbf{x})$  satisfies the weaker condition  $V(\mathbf{x}) \geq 0$  for  $\mathbf{x} \neq 0$ , then it is called *positive semidefinite*. A function  $V(\mathbf{x})$  is considered to be *negative definite* or *negative semidefinite* if  $-V(\mathbf{x})$  is positive definite or positive semidefinite, respectively. A function  $V(\mathbf{x})$  is *indefinite* if it does not have a definite sign.

The equilibrium point  $\mathbf{x}_{eq}$  is globally (asymptotically) stable in the sense of Lyapunov if the conditions of Theorem 2.2 hold in  $D = \mathbb{R}^n$  and  $V(\mathbf{x})$  is *radially unbounded* i.e.

$$\|\mathbf{x}\| \rightarrow \infty \Rightarrow V(\mathbf{x}) \rightarrow \infty.$$

Theorem 2.2 only gives sufficient conditions for the stability of the equilibrium point. This means that if a certain Lyapunov function does not satisfy the conditions of Theorem 2.2, then this fact does not imply that the equilibrium point is unstable. However, the theorem does not give a method for determining the Lyapunov function  $V(\mathbf{x})$ . On the other hand, it is a remarkable fact that the converse of Theorem 2.2 also exists: *if an equilibrium point is (asymptotically) stable, then there exists a function  $V(\mathbf{x})$  satisfying the conditions of the theorem.* However, the application of this and other converse theorems is limited by the lack of a technique for generating Lyapunov functions.

An extension of the basic Lyapunov theory is given in *LaSalle's invariance principle*. LaSalle's theorem enables one to conclude asymptotic stability of an equilibrium point even when  $V(\mathbf{x})$  does not satisfy (2.12). Moreover, the theorem can be used to prove the attractivity of an equilibrium set of a discontinuous system [Van de Wouw and Leine, 2004]. To introduce the theorem, we first introduce the definition of an invariant set.

**Definition 2.4 (Invariant set).** *The set  $M \subset \mathbb{R}^n$  is said to be an invariant set for system (2.1) if for all  $\mathbf{x}_0 \in M$  and  $t_0 \geq 0$ , we have that for the solution  $\mathbf{x}(t, \mathbf{x}_0)$  of (2.1), with  $\mathbf{x}_0 = \mathbf{x}(t_0)$ , the following holds:*

$$\mathbf{x}(t, \mathbf{x}_0) \in M, \forall t \in \mathbb{R}.$$

We can now state LaSalle's invariance principle and an additional corollary.

**Theorem 2.3 (LaSalle's invariance principle).** [Khalil, 2000; Sastry, 1999] *Let  $V : D \rightarrow \mathbb{R}$  be a continuously differentiable positive definite function on a domain  $D$  such that on the compact set  $D_c = \{\mathbf{x} \in D \mid V(\mathbf{x}) \leq c\}$  we have  $\dot{V}(\mathbf{x}) \leq 0$ . Define  $S = \{\mathbf{x} \in D_c \mid \dot{V}(\mathbf{x}) = 0\}$ . Then, every solution of (2.1), starting in  $D_c$  approaches the largest invariant set inside  $S$  as  $t \rightarrow \infty$ .*

**Corollary 2.1.** *Let  $\mathbf{x}_{eq}$  be an equilibrium point of (2.1). Let  $V : D \rightarrow \mathbb{R}$  be a continuously differentiable positive definite function on a domain  $D$  containing the equilibrium point, such that  $\dot{V}(\mathbf{x}) \leq 0$  in  $D$ . Define  $S = \{\mathbf{x} \in D_c \mid \dot{V}(\mathbf{x}) = 0\}$  and suppose that no solution, other than the solution  $\mathbf{x}(t) = \mathbf{x}_{eq}$ , can stay in  $S$ . In other words, suppose that  $\mathbf{x}_{eq}$  is the largest invariant set in  $S$ . Then,  $\mathbf{x}_{eq}$  is asymptotically stable. If all conditions hold for  $D = \mathbb{R}^n$  then the origin is globally asymptotically stable.*

## 2.2.2 Periodic Solutions and Tools for Related Stability Analysis

In order to determine a periodic solution  $\mathbf{x}_p(t, \mathbf{x}_{p0})$  of the system (2.1), we need to find a period  $T$  and a value for  $\mathbf{x}_{p0}$  such that (2.1) and (2.8) are satisfied for every  $t$ .

Various techniques exist for the prediction of such solutions. In the middle of the previous century, some approximating methods have appeared, e.g. the method of harmonic balance, the describing function method, and perturbation methods. More details about these methods can be found in [Khalil, 2000], [Nayfeh and Mook, 1979] and [Nayfeh, 1973], respectively. These methods have been useful in those times due to the fact that at that time the possibilities for extensive numerical computations were virtually absent.

Nowadays, numerical methods are used for the determination of a periodic solutions. In order to find a periodic solution, the most common first step is the manual search for such solution using a numerical simulation. When the approximate location of an interesting periodic solution is found, then more sophisticated numerical methods can be applied to calculate it more precisely. Some of those methods are the shooting method, the finite difference method and the multiple shooting method [Ascher et al., 1995; Leine and Van de Wouw, 2001; Nayfeh and Balachandran, 1995; Parker and Chua, 1989; Van Campen, 2000].

Further in the text, we first describe Floquet theory which explains how to determine the stability of a periodic solution and, next, the shooting method is described, since we use that method when computing periodic solutions throughout this thesis. Moreover, we also describe the method we use to numerically compute solutions of discontinuous systems.

### Floquet Theory

Suppose that an autonomous nonlinear dynamical system (2.1) has a periodic solution  $\mathbf{x}_p(t, \mathbf{x}_{p0})$ , where  $\mathbf{x}_{p0} = \mathbf{x}_p(t_0, \mathbf{x}_{p0})$ . Then, any other point on the periodic solution  $\mathbf{x}_p(t)$  is determined with  $\mathbf{x}_p(t) = \mathbf{x}_p(t, \mathbf{x}_{p0})$ .

To derive stability conditions for the periodic solution, we linearize system (2.1) around  $\mathbf{x}_p(t)$ . A perturbed solution  $\mathbf{x}(t) = \mathbf{x}_p(t) + \Delta\mathbf{x}(t)$  must also satisfy (2.1),

which leads to the following approximate differential equation for the perturbation:

$$\Delta \dot{\mathbf{x}}(t) = \mathbf{A}(t)\Delta \mathbf{x}(t), \quad \mathbf{A}(t) = \left. \frac{\partial \mathbf{f}}{\partial \mathbf{x}} \right|_{\mathbf{x}=\mathbf{x}_p(t)}, \quad (2.13)$$

where higher-order terms are neglected. Note that  $\mathbf{A}(t)$  is time-dependent (implicitly through  $\mathbf{x}_p(t)$ ) in a periodic fashion. The local stability of the periodic solution of (2.1) can now be assessed by assessing the stability of the equilibrium point  $\Delta \mathbf{x} = \mathbf{0}$  of (2.13). Moreover, the solution of (2.13) satisfies

$$\Delta \mathbf{x}(t) = \Phi(t, t_0, \mathbf{x}_{p0})\Delta \mathbf{x}(t_0), \quad \Phi(t_0, t_0, \mathbf{x}_{p0}) = \mathbf{I}, \quad (2.14)$$

where  $\Phi(t, t_0, \mathbf{x}_{p0})$  represents the fundamental solution matrix of system (2.13). In (2.14),  $\Delta \mathbf{x}(t)$  and  $\Delta \mathbf{x}(t_0)$  represent perturbations around the periodic solution at time instants  $t$  and  $t_0$ , respectively. According to (2.14), the fundamental solution matrix  $\Phi(t, t_0, \mathbf{x}_{p0})$  relates how an infinitesimally small perturbation at time  $t_0$  evolves to an infinitesimally small perturbation at time  $t$  (see figure 2.3).

Since we consider an autonomous system, the fundamental solution matrix only depends on the time span  $t - t_0$ , i.e.

$$\Phi(t, t_0, \mathbf{x}_0) = \Phi(t + t_a, t_0 + t_a, \mathbf{x}_0), \quad (2.15)$$

where  $\mathbf{x}_0$  is not necessarily on a periodic solution. Furthermore, because the solution  $\mathbf{x}_p(t, \mathbf{x}_{p0})$  is periodic with period time  $T$ , the following can be obtained:

$$\Delta \mathbf{x}(t_0 + kT) = \Phi^k(t_0 + T, t_0, \mathbf{x}_{p0})\Delta \mathbf{x}(t_0) = \Phi_T^k \Delta \mathbf{x}(t_0). \quad (2.16)$$

Herein,  $\Phi_T = \Phi(t_0 + T, t_0, \mathbf{x}_{p0})$  is the so-called *monodromy matrix*. From (2.16), it can be concluded that monodromy matrix maps an initial perturbation  $\Delta \mathbf{x}(t_0)$  to the perturbation  $\Delta \mathbf{x}(t_0 + T)$ , one period later, see figure 2.3. The eigenvalues of the monodromy matrix are called the *Floquet multipliers*. From (2.15) and (2.16) the following can be derived:

$$\Phi(t + kT, t_0, \mathbf{x}_{p0}) = \Phi(t + (k-1)T, t_0, \mathbf{x}_{p0})\Phi_T = \dots = \Phi(t, t_0, \mathbf{x}_{p0})\Phi_T^k. \quad (2.17)$$

The consequence of this equation is that  $\Phi(t, t_0, \mathbf{x}_{p0})$  is known at any time if it is known for  $t_0 \leq t \leq t_0 + T$ .

According to (2.17), it can be concluded that the long-term behaviour of the fundamental solution matrix is determined by the monodromy matrix, more specifically by its eigenvalues – the Floquet multipliers. The growth or decay of a perturbation follows from (2.14). If a Floquet multiplier has a magnitude larger (smaller) than one, then a perturbation grows (decays) in the direction of the corresponding eigenvector after one period.

The fundamental solution matrix can be obtained by solving the following initial value problem:

$$\dot{\Phi}(t, t_0, \mathbf{x}_{p0}) = \mathbf{A}(t)\Phi(t, t_0, \mathbf{x}_{p0}), \quad \Phi(t_0, t_0, \mathbf{x}_{p0}) = \mathbf{I}, \quad (2.18)$$

(see [Parker and Chua, 1989]). However, since we deal with discontinuous systems, then the monodromy matrix  $\Phi_T$  cannot be determined using (2.18). Instead, the monodromy matrix is determined by applying a sensitivity analysis to the periodic

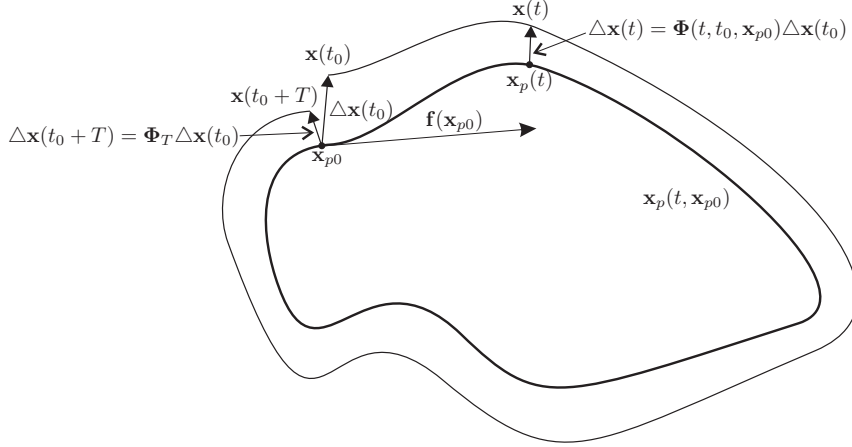


Figure 2.3: Periodic solution  $\mathbf{x}_p(t, \mathbf{x}_{p0})$  with related fundamental solution matrix  $\Phi(t, t_0, \mathbf{x}_{p0})$  and monodromy matrix  $\Phi_T = \Phi(t_0 + T, t_0, \mathbf{x}_{p0})$ .

solution using the relation (2.14) in the following way [Leine et al., 1998]. First, we perturb one component of the initial state vector  $\mathbf{x}_0$  (for example component  $j$ ), which is in the neighborhood of the periodic solution  $\mathbf{x}_p(t, \mathbf{x}_{p0})$ , with a small perturbation and leave other components unchanged, i.e.

$$\mathbf{x}_{0j} = \mathbf{x}_0 + \Delta \mathbf{x}_{0j},$$

with

$$\mathbf{x}_0 = [x_0^1 \quad \dots \quad x_0^j \quad \dots \quad x_0^n]^T$$

$$\Delta \mathbf{x}_{0j} = [0 \quad \dots \quad 0 \quad \xi \quad 0 \quad \dots \quad 0]^T,$$

where  $\xi \ll x_0^j$ . Second, we integrate the system (2.5) over the period time  $T$  with  $\mathbf{x}_{0j}$  as initial vector state and obtain  $\mathbf{x}_{Tj} = \mathbf{x}(t_0 + T, \mathbf{x}_{0j})$ . The perturbation of the final state vector, caused by the perturbation of the initial state vector, is:

$$\Delta \mathbf{x}_{Tj} = \mathbf{x}_{Tj} - \mathbf{x}_T,$$

with  $\mathbf{x}_T = \mathbf{x}(t_0 + T, \mathbf{x}_0)$ . The columns  $\Phi_T^j$  of the monodromy matrix  $\Phi_T$  can be obtained by

$$\Phi_T^j = \frac{\Delta \mathbf{x}_{Tj}^i}{\xi}.$$

Finally, we will also discuss a property which *only* holds for autonomous systems. Consider system (2.1) and introduce an infinitesimally small perturbation on the initial condition (which lies on the periodic solution) in the direction:  $\Delta \mathbf{x}(t_0) = \alpha \mathbf{f}(\mathbf{x}_{p0})$ ,  $\alpha \ll 1$ . Then, the resulting perturbation after one period will be identical to the initial perturbation  $\Delta \mathbf{x}(t_0 + T) = \Delta \mathbf{x}(t_0) = \alpha \mathbf{f}(\mathbf{x}_{p0})$ , due to the periodicity of the periodic solution, and then the fact that  $\Delta \mathbf{x}(t_0 + T) = \Phi(t_0 + T, t_0, \mathbf{x}_{p0}) \Delta \mathbf{x}(t_0)$  leads to  $\mathbf{f}(\mathbf{x}_{p0}) = \Phi_T \mathbf{f}(\mathbf{x}_{p0})$ . This means that one Floquet multiplier  $\lambda$  always equals 1 with a corresponding eigenvector  $\mathbf{f}(\mathbf{x}_{p0})$ .

### The Shooting Method

The shooting method is a widely used numerical method for the computation of periodic solutions of nonlinear systems [Ascher et al., 1995; Leine and Van de Wouw, 2001; Nayfeh and Balachandran, 1995; Parker and Chua, 1989; Van Campen, 2000]. In order to find a periodic solution of an autonomous system (2.1), we need to find the period time  $T$  and an initial condition  $\mathbf{x}_{p0}$  such that (2.8) is satisfied. In other words, we need to find zeros of the vector function  $\mathbf{H}$  with

$$\mathbf{H}(\mathbf{x}_{p0}, T) = \mathbf{x}_p(t_0 + T) - \mathbf{x}_{p0}, \quad (2.19)$$

where  $\mathbf{x}_{p0} = \mathbf{x}_p(t_0, \mathbf{x}_{p0})$  and  $\mathbf{x}_p(t_0 + T) = \mathbf{x}_p(t_0 + T, \mathbf{x}_{p0})$  are points on the periodic solution at time instants  $t_0$  and  $t_0 + T$ , respectively.

Assuming that a periodic solution exists, a zero of  $\mathbf{H}(\mathbf{x}_{p0}, T)$  can be found using the Newton-Raphson procedure [Leine and Van de Wouw, 2001; Parker and Chua, 1989]. If we apply it to  $\mathbf{H}(\mathbf{x}_{p0}, T)$  the following equation is obtained

$$\frac{\partial \mathbf{H}}{\partial \mathbf{x}_{p0}} \Delta \mathbf{x}_{p0} + \frac{\partial \mathbf{H}}{\partial T} \Delta T = -\mathbf{H}(\mathbf{x}_{p0}, T),$$

which, after evaluation of the partial derivatives, gives

$$(\Phi_T(\mathbf{x}_{p0}) - \mathbf{I}) \Delta \mathbf{x}_{p0} + \mathbf{f}(\mathbf{x}_p(t_0 + T, \mathbf{x}_{p0})) \Delta T = \mathbf{x}_{p0} - \mathbf{x}_p(t_0 + T, \mathbf{x}_{p0}). \quad (2.20)$$

Equation (2.20) represents a system of  $n$  equations with  $n+1$  unknowns ( $n$  components of  $\mathbf{x}_{p0}$  and the period  $T$ ), which means that it cannot be solved uniquely. The reason for this fact is that the phase of a periodic solution, belonging to an autonomous system, is not fixed. Any point on the periodic solution is a zero of (2.19). In order to remove this arbitrariness, some suggestions are done by Nayfeh and Balachandran [1995]. One suggestion is the use of an additional equation of the form

$$\mathbf{f}^T(\mathbf{x}_{p0}) \Delta \mathbf{x}_{p0} = 0. \quad (2.21)$$

This means that the update  $\Delta \mathbf{x}_{p0}$  is restricted to be orthogonal to the vector field  $\mathbf{f}$  at  $\mathbf{x}_{p0}$ . Therefore, condition (2.21) is called an orthogonality condition. Then, the combination of (2.21) and (2.20) gives the following  $n+1$  linear equations

$$\begin{bmatrix} \Phi_T(\mathbf{x}_{p0}^{(i)}) - \mathbf{I} & \mathbf{f}(\mathbf{x}_p(t_0 + T^{(i)}, \mathbf{x}_{p0}^{(i)})) \\ \mathbf{f}^T(\mathbf{x}_{p0}^{(i)}) & 0 \end{bmatrix} \begin{bmatrix} \Delta \mathbf{x}_{p0}^{(i)} \\ \Delta T^{(i)} \end{bmatrix} = \begin{bmatrix} \mathbf{x}_{p0}^{(i)} - \mathbf{x}_p(t_0 + T^{(i)}, \mathbf{x}_{p0}^{(i)}) \\ 0 \end{bmatrix} \quad (2.22)$$

for the  $n+1$  unknowns  $\Delta \mathbf{x}_{p0}^{(i)}$  and  $\Delta T^{(i)}$ . The shooting method solves in each iteration step the set of equations (2.22) and then updates the state and period time by

$$\begin{bmatrix} \mathbf{x}_{p0}^{(i+1)} \\ T^{(i+1)} \end{bmatrix} = \begin{bmatrix} \mathbf{x}_{p0}^{(i)} \\ T^{(i)} \end{bmatrix} + \begin{bmatrix} \Delta \mathbf{x}_{p0}^{(i)} \\ \Delta T^{(i)} \end{bmatrix},$$

with initial guesses  $\mathbf{x}_{p0}^{(0)}$  and  $T^{(0)}$ . This scheme is reiterated until some predefined convergence criterion with respect to  $\mathbf{x}_{p0}^{(i)}$  and  $T^{(i)}$  is satisfied. As we already mentioned, the monodromy matrix  $\Phi_T(\mathbf{x}_{p0}^{(i)})$  is obtained using a sensitivity analysis of

relation (2.14) [Leine et al., 1998], since we deal with discontinuous systems. When we find values for  $\mathbf{x}_0$  and  $T$  using the shooting method, it should be checked whether  $T$  is the minimum period of the solution, since it may also be a multiple of the actual period.

The most important drawback of all numerical methods for computing periodic solutions (and therefore also of the shooting method) is that these methods only converge if the initial guess  $\mathbf{x}_{p0}$  is close enough to the periodic solution. This means that those methods do not find periodic solutions, but refine an already good guess of the periodic solution. Nevertheless, with this method it is also possible to find an unstable periodic solution.

### 2.2.3 Switch Model

While pursuing numerical solutions of differential inclusions a range of computational problems can be encountered around a discontinuity. Therefore, a number of numerical techniques exists for the numerical solution of differential inclusions. The smoothing method, for example, approximates the discontinuous vector field by a smooth vector field (see for example [Van de Vrande et al., 1999]). The main disadvantage of this method is that it yields stiff differential equations which are numerically expensive to solve especially near the discontinuity. The so-called Switch Model solves the problems which appear in the smoothing method. However, the main disadvantage of the Switch Model technique is that the complexity of the simulation model rapidly increases with increasing number of discontinuity surfaces [Leine, 2000; Leine and Nijmeijer, 2004; Leine et al., 1998]. In such systems more sophisticated simulation methods can be used such as event-driven integration methods [Pfeiffer and Glocker, 1996] and the time-stepping method [Leine and Nijmeijer, 2004]. Since in this thesis we consider a system which does not have many discontinuous surfaces, the Switch Model is used for the numerical simulation of the considered system.

The Switch Model was presented for the first time by Leine et al. [1998] and a detailed description of the numerical method can be found in [Leine and Nijmeijer, 2004]. The Switch Model represents an improved version of the Karnopp model [Karnopp, 1985; Olsson, 1996]. In order to numerically integrate the differential inclusion (2.5), the Switch Model introduces a boundary layer with thickness  $2\eta$  around the hypersurface  $\Sigma$  (defined in (2.4)) to allow for an efficient numerical approximation. Then, within that boundary layer, a vector field is introduced such that the state of the system is pushed towards  $\Sigma$ , if an attractive sliding mode appears, avoiding numerical instabilities (chattering around the discontinuity surface). Consequently, using this method the space  $\mathbb{R}^n$  is divided into the following subspaces:

$$\begin{aligned}\Sigma' &= \{\mathbf{x} \in \mathbb{R}^n \mid |g(\mathbf{x})| \leq \eta\}, \\ \Lambda'_- &= \{\mathbf{x} \in \mathbb{R}^n \mid g(\mathbf{x}) < -\eta\}, \\ \Lambda'_+ &= \{\mathbf{x} \in \mathbb{R}^n \mid g(\mathbf{x}) > \eta\}.\end{aligned}\tag{2.23}$$

Then, the subspace  $\Sigma'$  is divided into subspaces  $\mathcal{A}$ ,  $\mathcal{R}$ ,  $\mathcal{T}_-$  and  $\mathcal{T}_+$  depending on direction of the vector fields  $\mathbf{f}_+(\mathbf{x})$  and  $\mathbf{f}_-(\mathbf{x})$  with respect to  $\Sigma$  (see figure 2.4). The subspace  $\mathcal{A}$  is a subset of the subspace  $\Sigma'$  which contains an attractive sliding mode,  $\mathcal{R}$  is a subset of  $\Sigma'$  which contains a repulsive sliding mode and  $\mathcal{T}_-$  and  $\mathcal{T}_+$  are the subspaces where the solution has a transversal intersection from  $\Lambda'_+$  to  $\Lambda'_-$  and  $\Lambda'_-$



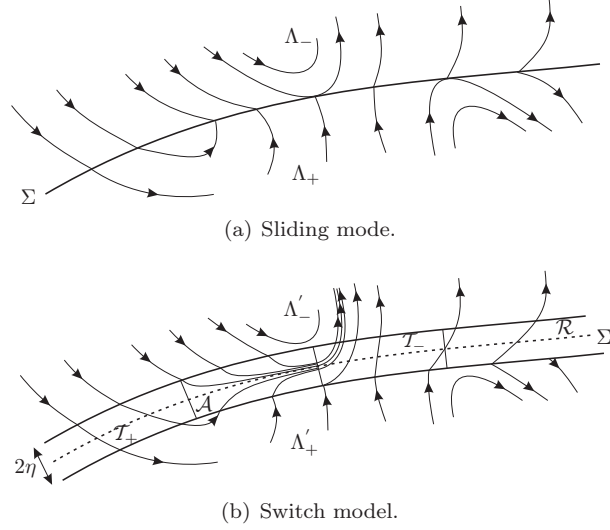


Figure 2.4: Numerical approximation of a sliding mode using the Switch Model.

to  $\Lambda'_+$ , respectively. For the differential inclusion (2.5), the subspaces  $\mathcal{A}$ ,  $\mathcal{R}$ ,  $\mathcal{T}_-$  and  $\mathcal{T}_+$  are defined by:

$$\begin{aligned}
 \mathcal{A} &= \{\mathbf{x} \in \mathbb{R}^n \mid |g(\mathbf{x})| \leq \eta, \mathbf{n}^\top(\mathbf{x})\mathbf{f}_+(\mathbf{x}) < 0, \mathbf{n}^\top(\mathbf{x})\mathbf{f}_-(\mathbf{x}) > 0\}, \\
 \mathcal{R} &= \{\mathbf{x} \in \mathbb{R}^n \mid |g(\mathbf{x})| \leq \eta, \mathbf{n}^\top(\mathbf{x})\mathbf{f}_+(\mathbf{x}) > 0, \mathbf{n}^\top(\mathbf{x})\mathbf{f}_-(\mathbf{x}) < 0\}, \\
 \mathcal{T}_- &= \{\mathbf{x} \in \mathbb{R}^n \mid |g(\mathbf{x})| \leq \eta, \mathbf{n}^\top(\mathbf{x})\mathbf{f}_+(\mathbf{x}) < 0, \mathbf{n}^\top(\mathbf{x})\mathbf{f}_-(\mathbf{x}) < 0\}, \\
 \mathcal{T}_+ &= \{\mathbf{x} \in \mathbb{R}^n \mid |g(\mathbf{x})| \leq \eta, \mathbf{n}^\top(\mathbf{x})\mathbf{f}_+(\mathbf{x}) > 0, \mathbf{n}^\top(\mathbf{x})\mathbf{f}_-(\mathbf{x}) > 0\},
 \end{aligned} \tag{2.24}$$

where  $\mathbf{n}(\mathbf{x})$  is the normal perpendicular to the switching hyper-surface  $\Sigma$ :

$$\mathbf{n}(\mathbf{x}) = \nabla g(\mathbf{x}). \tag{2.25}$$

Consequently, the differential inclusion (2.5) can be defined in the following way:

$$\dot{\mathbf{x}} = \begin{cases} \mathbf{f}_-(\mathbf{x}) & \text{for } \mathbf{x} \in \Lambda'_-, \\ \mathbf{f}_+(\mathbf{x}) & \text{for } \mathbf{x} \in \Lambda'_+, \\ \alpha\mathbf{f}_+(\mathbf{x}) + (1-\alpha)\mathbf{f}_-(\mathbf{x}) & \text{for } \mathbf{x} \in \mathcal{A}, \\ \mathbf{f}_-(\mathbf{x}) \text{ or } \mathbf{f}_+(\mathbf{x}) & \text{for } \mathbf{x} \in \mathcal{R}, \\ \mathbf{f}_-(\mathbf{x}) & \text{for } \mathbf{x} \in \mathcal{T}_-, \\ \mathbf{f}_+(\mathbf{x}) & \text{for } \mathbf{x} \in \mathcal{T}_+, \end{cases} \tag{2.26}$$

where

$$\alpha = \frac{\mathbf{n}^\top(\mathbf{x})\mathbf{f}_-(\mathbf{x}) + \tau g(\mathbf{x})}{\mathbf{n}^\top(\mathbf{x})(\mathbf{f}_-(\mathbf{x}) - \mathbf{f}_+(\mathbf{x}))}.$$

The parameter  $\tau$  determines how fast the solution is pushed towards the switching boundary  $g(\mathbf{x}) = 0$  when the current state is in  $\mathcal{A}$  (the higher value for  $\tau$ , the faster the solution is pushed towards  $g(\mathbf{x}) = 0$ ). In (2.23),  $\eta$  should be chosen sufficiently small such that  $Tol < \eta \ll 1$ , where  $Tol$  represents the tolerance of the numerical integration method used for the simulation of the system. Sufficiently small means that  $\eta$  is small enough to have no qualitative influence on the numerical solution of the system of equations.

## 2.3 Bifurcation Diagrams

A nonlinear dynamical system can evolve towards different steady-states such as an equilibrium point/set, a periodic solution or a quasi-periodic solution, depending on the initial condition of the system. Moreover, those steady-state solutions can be asymptotically stable, thereby attracting neighboring solutions, or unstable. Very often it is desirable to know how the steady-state behaviour of a system changes when a certain parameter of the system is changed, since some parameters of a system are not known precisely, or they can be subject to variation.

Consider a parameterized variant of (2.1)

$$\dot{\mathbf{x}} = \mathbf{f}(\mathbf{x}, \mu), \quad (2.27)$$

where  $\mu$  represents a parameter of the system which is a constant. If  $\mu$  changes, the steady-state solution  $\mathbf{x}_s(t, \mathbf{x}_{s0})$  may also change. Although, usually a small change in  $\mu$  produces only small quantitative changes in the steady-state solutions, a slight change can also cause a drastic qualitative change in the steady-state behaviour. For example, while varying the parameter  $\mu$ , the number and/or the stability of equilibrium points or (quasi-)periodic solutions can be changed. Such a qualitative change is called a *bifurcation* and the value of  $\mu$  at which a bifurcation occurs is called a *bifurcation point*. In [Khalil, 2000; Leine, 2000; Leine and Nijmeijer, 2004; Sastry, 1999; Van Campen, 2000] some classification of bifurcation points can be found.

In order to illustrate graphically such qualitative and quantitative changes in  $\mathbf{x}_s(t, \mathbf{x}_{s0})$  when  $\mu$  changes, we need a scalar measure  $[\mathbf{x}_s]$  of  $\mathbf{x}_s(t, \mathbf{x}_{s0})$ . Continuous curves representing the measure  $[\mathbf{x}_s]$  as a function of  $\mu$  are called *branches*. Moreover, the endpoints of a branch are always bifurcation points. A branch can consist of equilibrium points or periodic solutions; such branch will be called an *equilibrium branch* or a *periodic branch*, respectively. Some examples of bifurcation diagrams are shown in figures 2.5 and 2.7(a), where  $e_i$ ,  $i = 1, 2$  represent equilibrium branches and  $p_i$ ,  $i = 1, 2$  represent periodic branches. Since in this thesis we consider both Hopf and fold bifurcation points, we will describe them in the sequel.

At a *Hopf bifurcation* point the equilibrium point changes its stability and a periodic solution is born. There are three types of Hopf bifurcation points: supercritical, subcritical and degenerate bifurcations [Strogatz, 2000]. Suppose that a nonlinear system (2.27) settles down to equilibrium through an exponentially damped oscillation, i.e. small disturbances decay after a while. Then suppose that the decay rate depends on the parameter  $\mu$ . If the decay becomes slower and slower, and finally at a critical value  $\mu = \mu_c$ , small disturbances start to grow, the equilibrium state will lose stability. If the resulting motion is a small-amplitude stable oscillation around the former steady-state, then we say that the system undergoes a *supercritical Hopf bifurcation* for  $\mu = \mu_c$  (see figure 2.5(a)). Suppose that for certain value of  $\mu$  a nonlinear system (2.27) has an unstable equilibrium point. Then suppose that for  $\mu = \mu_c$  the equilibrium point becomes stable and an unstable limit cycle appears. Then we say that the system undergoes a *subcritical Hopf bifurcation* (see figure 2.5(b)). The subcritical bifurcation is much more dramatic than the supercritical, since after the bifurcation, the trajectory must jump to a distant attractor (e.g. an equilibrium point, a periodic solution, infinity, etc.). A *degenerate Hopf bifurcation* typically arises when a nonconservative system suddenly becomes conservative at the bifurcation point. Some examples of such systems can be found in [Strogatz, 2000]. In

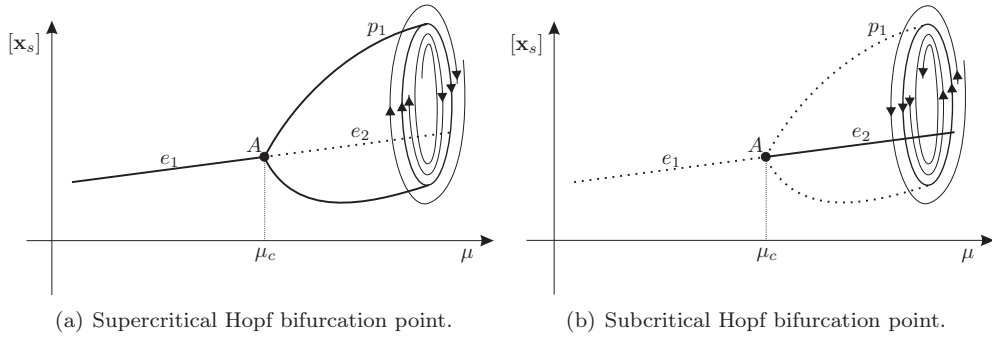


Figure 2.5: Hopf bifurcation points.

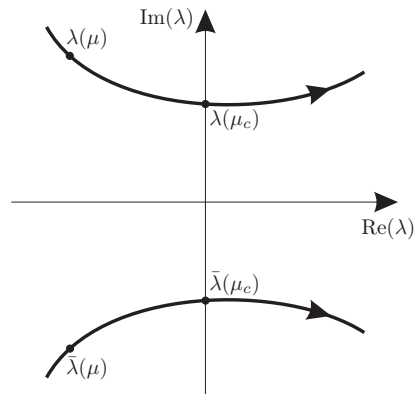


Figure 2.6: Two eigenvalues of a Hopf bifurcation point.

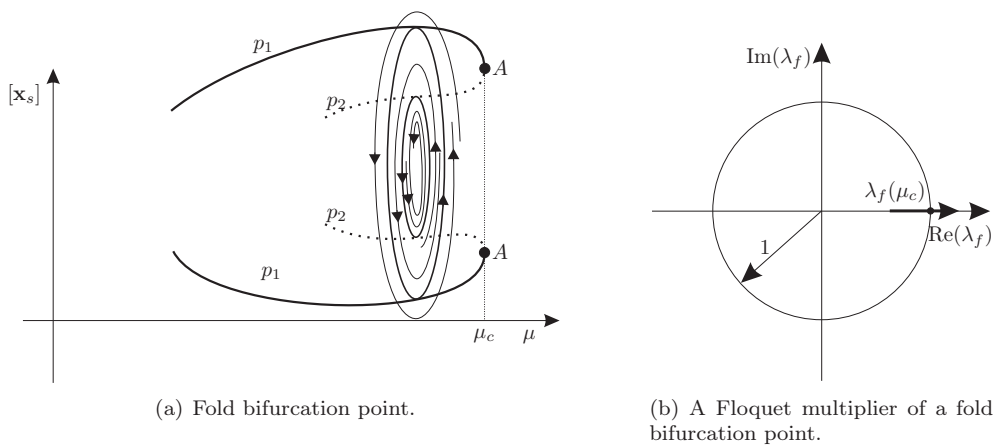


Figure 2.7: Fold bifurcation point and a related Floquet multiplier.

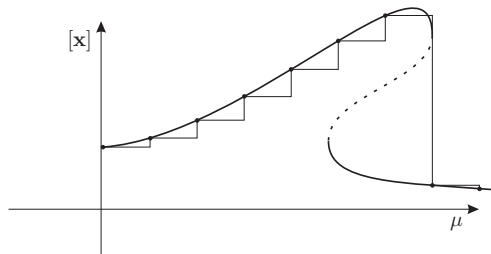


Figure 2.8: Graphical interpretation of sequential continuation method.

general, in a Hopf bifurcation point, the linearization of the nonlinear system (2.27) around the equilibrium has two complex conjugate eigenvalues which simultaneously cross the imaginary axis, for  $\mu = \mu_c$ , from the left to the right half-plane or vice versa (see figure 2.6) [Sastry, 1999; Strogatz, 2000].

At a *fold bifurcation point* (or *saddle-node bifurcation point of cycles*) a stable and an unstable limit cycle fuse together and annihilate each other for  $\mu = \mu_c$ . Moreover, at the bifurcation point (for  $\mu = \mu_c$ ) one Floquet multiplier  $\lambda_f$  leaves the unit circle in the complex plane through the point  $+1$  as shown in figure 2.7(b).

Since we model friction with a discontinuous friction law, equilibrium branches which consist of equilibrium sets can also appear in bifurcation diagrams. Furthermore, due to the discontinuity, some *discontinuous bifurcation points* can also appear. The analysis of various discontinuous bifurcation points in specific systems can be found in [Leine, 2000; Leine and Nijmeijer, 2004]. However, a classification of a bifurcation points for discontinuous systems does not exist to this date as it does for continuous systems. In this thesis, we encounter "discontinuous" variants of the Hopf and fold bifurcations both in simulations and experiments.

To find an equilibrium branch of a differential inclusion (2.5) we need to solve the following system of nonlinear algebraic inclusions

$$\mathbf{F}(\mathbf{x}_{eq}, \mu) \ni \mathbf{0},$$

for every possible value of  $\mu$  and to determine the stability properties of each equilibrium point (or set)  $\mathbf{x}_{eq} = \mathbf{x}_{eq}(\mu)$ . That system of inclusions can be solve analytically or numerically (using, for example, the Newton-Raphson algorithm).

Finding a periodic branch is not so straightforward as finding an equilibrium branch. However, first using the shooting method or some other numerical method, a periodic solution can be found for a certain parameter value  $\mu = \mu^*$ . Then, a periodic solution at  $\mu = \mu^* + \Delta\mu$  may be found using the solution at  $\mu = \mu^*$  as an initial guess. The periodic solver is likely to converge for small  $\Delta\mu$ . This type of continuation is called sequential continuation [Nayfeh and Balachandran, 1995].

The sequential continuation method proceeds in a step-wise fashion, due to the fact that each previous periodic solution is an initial guess for finding the next periodic solution. With this method, it is possible to follow branches of both stable and unstable periodic solutions. Nevertheless, a problem may occur at bifurcation points. If a periodic branch undergoes a fold bifurcation, at which the branch turns around (as shown in figure 2.8), the previous periodic solution is not a good guess for the next periodic solution. In such a case, it may happen that for a very small  $\Delta\mu$  the periodic solver does not converge. However, even if the periodic solver converges, a

part of the branch is not followed. This means that the method do not follow the entire branch.

There are some improvements of the sequential continuation method that can overcome the problem of following the branch around such bifurcation points [Nayfeh and Balachandran, 1995]. The arclength continuation method is one of these improved methods. Such a method can indeed go around a turning point, which is not the case with the sequential continuation method. The arclength continuation method does not only have to solve for the new update  $\Delta \mathbf{x}_0$  and  $\Delta T$  but also for  $\Delta \mu$ . More details on this method, which is used through the thesis, can be found in [Nayfeh and Balachandran, 1995].

## Chapter 3

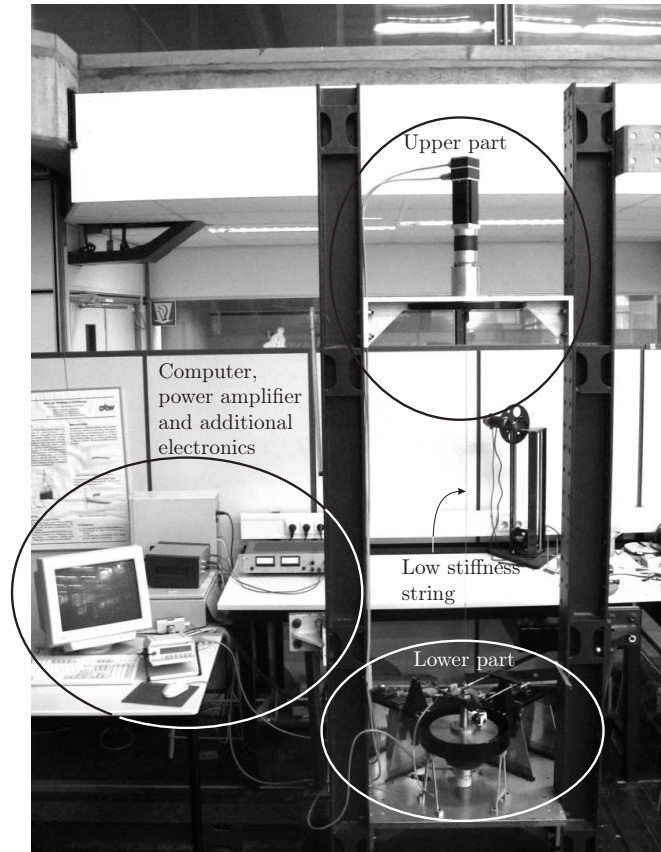
# The Experimental Drill-String Set-Up

In this chapter, we first describe the experimental drill-string set-up in Section 3.1. In the set-up torsional friction-induced vibrations, lateral vibrations and a combination of those types of vibration can be observed. This property makes this experimental set-up particularly suitable to address the main research goals of this thesis as formulated in Section 1.3. Second, in Section 3.2, the model of the set-up is presented. In this modelling part, special attention is given to the friction model and the model of the DC motor. Based on those two models, the full model of the set-up is given. Finally, in Section 3.3, we describe the technique, which is used for the parameter estimation of the model, and give the estimated parameters for the experimental set-up.

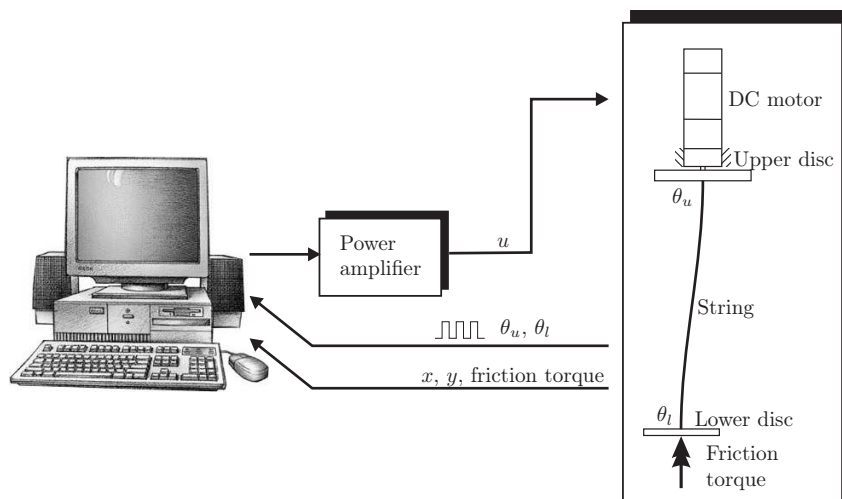
### 3.1 Description of the Set-Up

The experimental drill-string set-up is shown in figure 3.1. The set-up consists of a power amplifier, a DC-motor, two rotational (upper and lower) discs, a low-stiffness string and an additional brake applied to the lower disc. The input voltage from the computer ( $u$  in figure 3.1(b)), which is limited to the range  $[-5\text{ V}, 5\text{ V}]$ , is fed into the DC-motor via the power amplifier (see figure 3.2). The motor is connected, via the gear box, to the upper steel disc as shown in figure 3.3. The upper disc and the lower disc (figure 3.4) are connected through a low stiffness steel string. The lower disc can rotate around its geometric center and is also free to move in lateral directions.

In order to induce torsional vibrations at the lower disc, a brake and a small oil-box with felt stripes are fixed to the upper bearing housing of the lower part of the set-up, as shown in figure 3.5. With the brake, a range of normal forces can be applied and the contact between the brake and the brake disc produces a friction force exerted on the brake disc. The brake contact material is bronze. The steel brake disc is connected to the lower brass disc via a very stiff shaft. The oil-box with the felt stripes is constructed in order to add oil to the brake disc in a reproducible way. Namely, when some liquid is present in the box, the liquid can be added to both sides of the brake disc due to the capillary effect of the felt. This oil lubrication will prove to be crucial for the existence of torsional vibrations in the set-up.



(a) Photo.



(b) Schematic representation.

Figure 3.1: Experimental drill-string set-up.

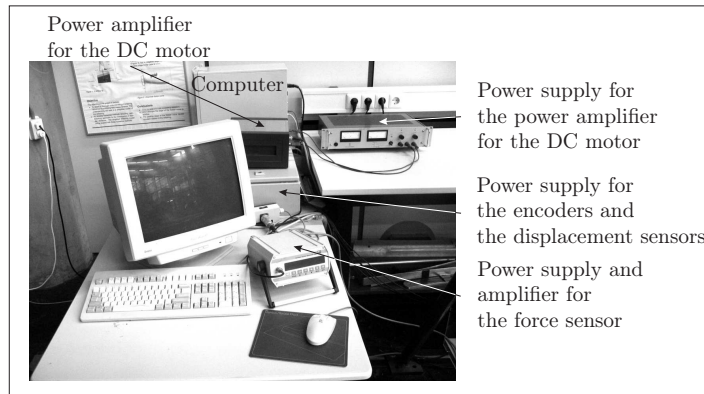


Figure 3.2: The power amplifier, the computer and electronics for the encoders and the sensors.

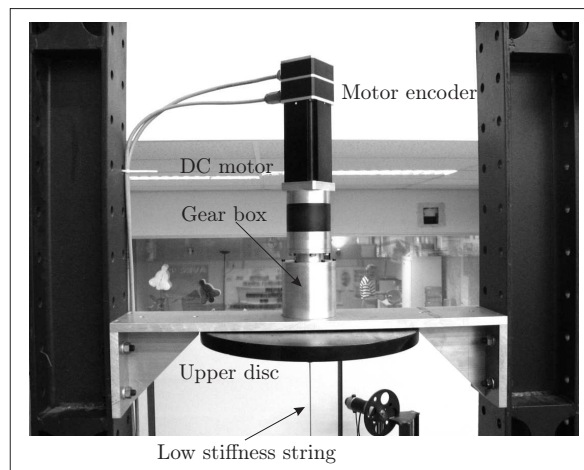


Figure 3.3: The upper part of the experimental drill-string set-up.

Lateral vibrations are induced by fixing an additional mass at the lower brass disc (figure 3.4). Consequently, a mass-unbalance is introduced to the disc which leads to motions in the lateral plane (whirl type motion). However, to limit the complexity of the system, tilting of the lower disc is avoided by means of two constraints; one in  $x$ - and one in  $y$ -direction as shown in figure 3.4. A front and a back view of the constraint in  $x$ -direction is shown in figure 3.6. That constraint consists of three flexible rods, a rigid body and two leaf springs. Two upper flexible rods are, at one end, connected to the upper bearing housing and, at the other end, to the rigid body of the constraint. These (upper) two rods suppress rotation of the upper bearing housing around the vertical axis; note in this respect that the brake is implemented at the bearing housing. The third (lower) flexible rod connects the lower bearing housing to the rigid body of the constraint. The combination of these rods suppresses tilting of the lower disc around the  $y$ -axis. The rigid body of the constraint is connected to the fixed world via two leaf-springs, which allow movement in  $x$ -direction. The construction of the



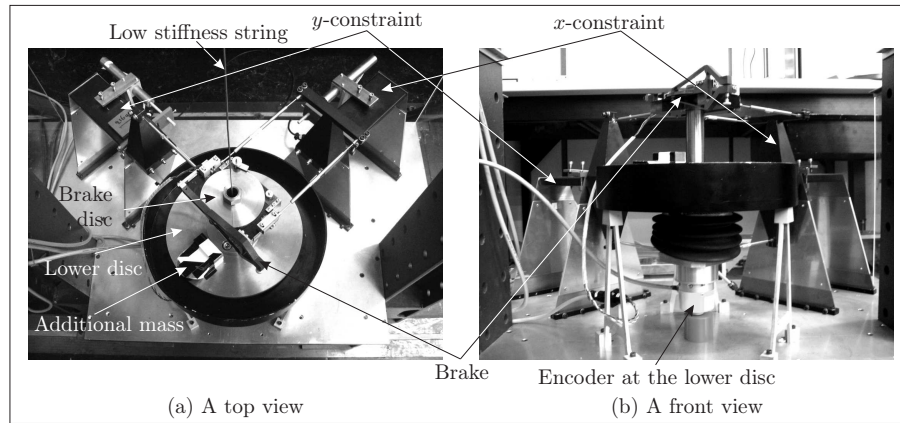


Figure 3.4: The lower part of the experimental drill-string set-up.

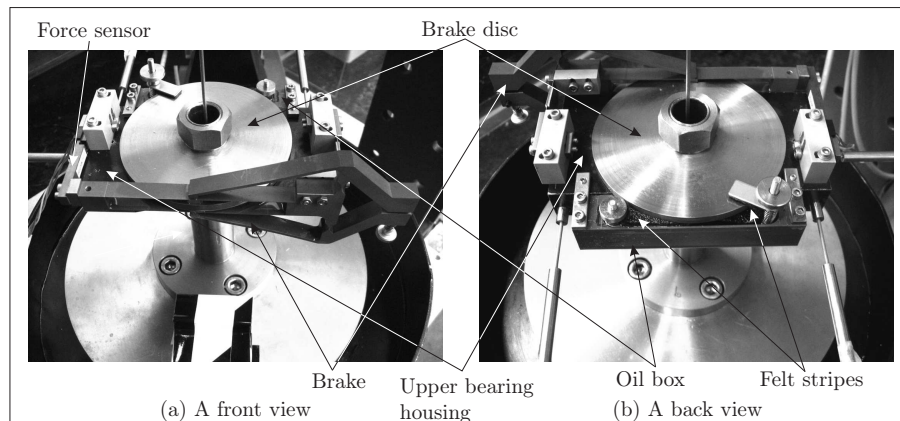


Figure 3.5: The brake and the oil box with the felt stripes.

constraint in  $y$ -direction is similar (see figure 3.7), except that just two flexible rods are implemented here: one fixed to the upper bearing housing and another to the lower bearing housing of the lower part. These rods suppress tilting of the lower disc around the  $x$ -axis.

Both constraints can be fixed using appropriate mechanisms, as shown in figures 3.6 and 3.7, and, when effected, the lower disc cannot move in lateral direction but can only rotate around its geometric center. In such a way, a drill-string set-up is created, which can undergo only torsional vibrations (by fixing the constraints and applying the brake), only lateral vibrations (by opposite means) and a combination of those two types of vibration.

The angular positions of the upper and lower disc ( $\theta_u$  and  $\theta_l$ , respectively in figure 3.1(b)) are measured using incremental encoders (see figures 3.3 and 3.4). The motor encoder has 1000 counts per revolution. The signal from the encoder is connected to a so-called quadrature decoder, an electronic circuit placed in the computer, which has the possibility to increase the number of measured encoder counts four times. Then, the signal from the quadrature decoder goes into a digital counter, which counts the

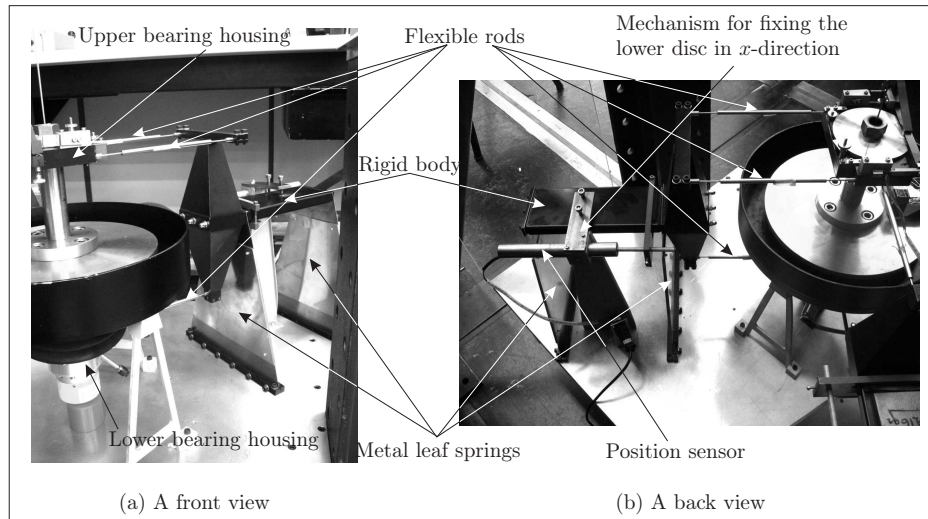


Figure 3.6: (a) A front and (b) a back view of the  $x$ -constraint.

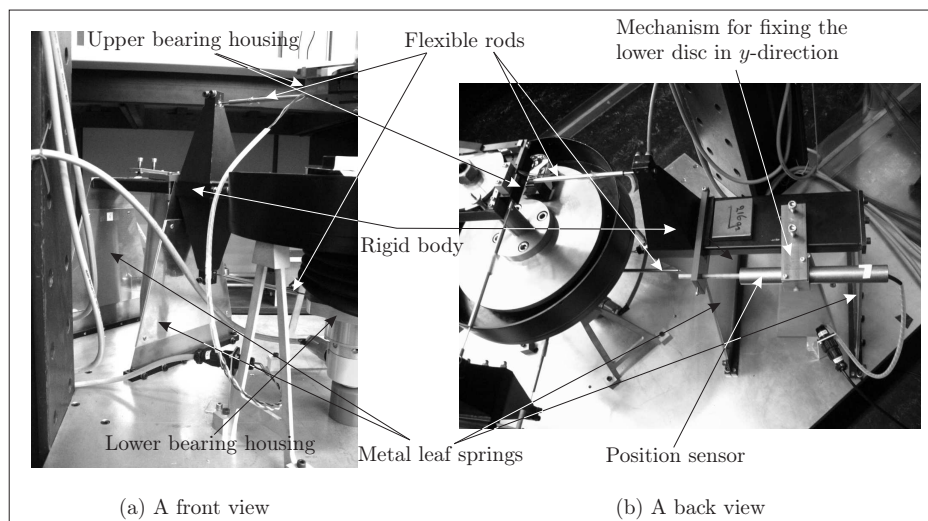


Figure 3.7: (a) A front and (b) a back view of the  $y$ -constraint.

number of pulses. Moreover, since the motor encoder is connected to the motor shaft before the gear box and the reduction ratio of the gear box is  $n = 3969/289$ , the computer measures the angular position at the upper disc with  $4 \cdot 1000 \cdot n = 54934.26$  counts per revolution. The encoder at the lower disc has 10000 counts per revolution and the computer measures the angular position at the lower disc (via a quadrature decoder) with 40000 counts per revolution. The angular velocities of both discs are obtained by numerical differentiation of the angular positions and filtering the resulting signals using a low-pass filter with a cut-off frequency of 200 rad/s (31.8 Hz). The displacements of the geometric center of the lower disc in  $x$ - and  $y$ -directions are measured with two LVDT (Linear Variable Differential Transformer) displacement

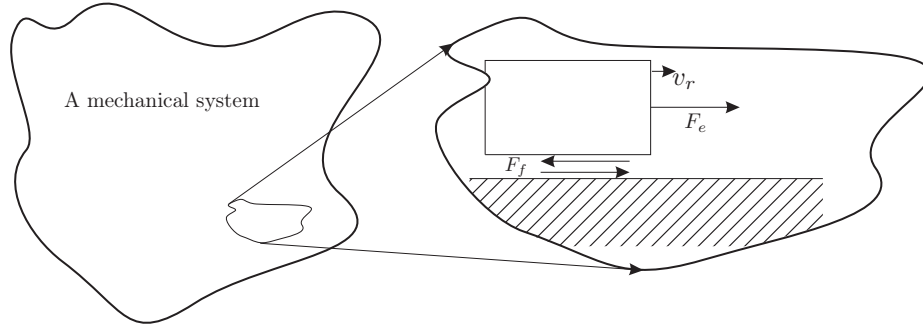


Figure 3.8: An example of a mechanical system with friction.

sensors 500 HR-DC [Schaevitz, 2004]. The displacement sensors measure, in fact, the displacements of the rigid bodies of the constraints in  $x$ - and  $y$ -direction which equal the displacement of the lower disc in those two directions (see figures 3.6 and 3.7). Since measurements obtained from the LVDTs contain a lot of measurement noise, the signals are filtered off-line with a digital low-pass filter with a cut-off frequency of 5 Hz and the obtained signal is compensated for the resulting phase lag. In order to measure the applied friction force, a force sensor LQB 630 [Cooperinstruments, 2002] is fixed at one side of the brake as shown in figure 3.5.

## 3.2 Model of the Set-Up

### 3.2.1 Friction Modelling

We are mainly interested in the steady-state behaviour of flexible rotor systems with friction and we are not interested in the detailed dynamic modelling of the friction for very small angular velocities. That is why we choose a static friction model when modelling friction forces at the experimental set-up. Moreover, both at the upper and at the lower part of the set-up the sticking phenomenon is observed. Consequently, the friction forces are modelled with

$$F_f(v_r) \in \begin{cases} F_c(v_r)\text{sgn}(v_r) & \text{for } v_r \neq 0, \\ [-F_s, F_s] & \text{for } v_r = 0, \end{cases} \quad (3.1)$$

i.e. with a set-valued friction force law, indicated by the fact that (3.1) is an algebraic inclusion. In (3.1),  $v_r$  represents the relative velocity between two contacting surfaces where the friction force  $F_f$  appears.

When the relative velocity  $v_r$  is zero, the bodies *stick* to each other. In the stick phase, the friction force adjusts to enforce equilibrium with the external forces acting on the bodies ( $F_e$  in figure 3.8). Consequently, the friction force  $F_f$  lies in the interval  $-F_s \leq F_f \leq F_s$  when the bodies stick to each other. In general, the maximum static friction force  $F_s$  can be higher than  $F_c(0)$  (the so-called Coulomb friction). If the friction force in the stick phase exceeds a threshold  $F_s$  (the so-called the break-away friction force) the bodies begin to *slip*, i.e. attain a non-zero relative velocity with respect to each other. In the slip phase ( $v_r \neq 0$ ), the friction force is a function of velocity, i.e.  $F_f(v_r) = F_c(v_r)$  in (3.1). In general,  $F_c(v_r)$  is a nonlinear function such

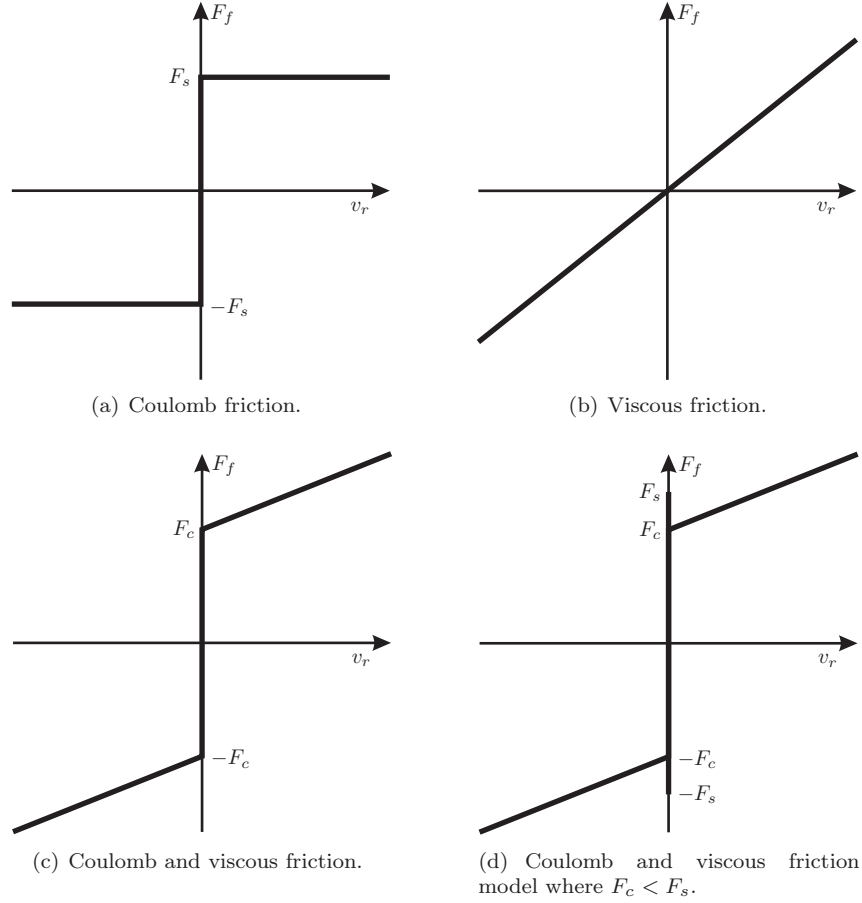


Figure 3.9: Examples of friction models.

that

$$F_c(v_r) \geq 0, \quad \forall v_r \in \mathbb{R} \setminus \{0\}, \quad (3.2)$$

which means that the friction force is dissipative. In order to describe the stick phase properly, the friction force (3.1) is represented in the following way:

$$F_f(v_r) \in \begin{cases} F_c(v_r) \operatorname{sgn}(v_r) & \text{for } v_r \neq 0, \\ \min(|F_e|, F_s) \operatorname{sgn}(F_e) & \text{for } v_r = 0. \end{cases} \quad (3.3)$$

The most commonly used friction model is the Coulomb friction model. In that model

$$F_c(v_r) = F_s = \text{const},$$

in (3.3), as shown in figure 3.9(a). To describe also the friction force caused by the viscosity of lubricants, viscous friction is usually described with

$$F_f = b_v v_r,$$

(see figure 3.9(b)). However, such description of viscous friction is not always correct and often a more general relation is  $F_f = b_v |v_r|^{\delta_v} \operatorname{sgn}(v_r)$  where  $\delta_v$  depends on the

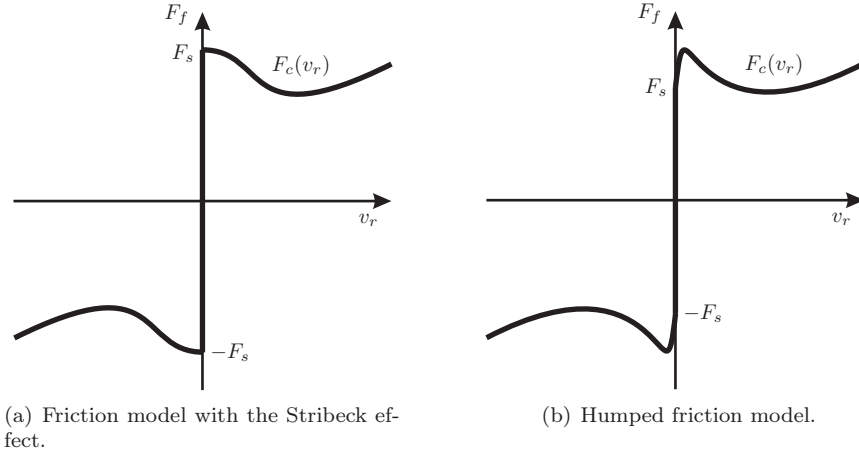


Figure 3.10: Friction models with negative damping.

geometry of the application [Olsson, 1996]. Coulomb friction with viscous friction is shown in figure 3.9(c). For such a friction model,

$$F_c(v_r) = F_s + b_v|v_r|,$$

in (3.3). The friction model shown in figure 3.9(d) can be described with (3.3), where

$$F_c(v_r) = F_c + b_v|v_r|$$

and the Coulomb friction force  $F_c$  is smaller than the static friction force  $F_s$ . However, Leine [2000] discussed such a friction model and concluded that solutions of the resulting differential inclusion with such a friction model can be non-unique. In order to avoid such difficulties, we do not use friction models where the static friction is higher than the Coulomb friction.

In this thesis, in order to predict torsional vibrations in the experimental drill-string system, a negative damping in the friction force should be present. Two friction models that include such effect are, firstly, a friction model with the Stribeck effect (see figure 3.10(a)) and, secondly, a humped friction model (see figure 3.10(b)). Some examples of nonlinear functions  $F_c(v_r)$  (in (3.3)) which exhibit the Stribeck effect can be found in [Armstrong-Hélouvy et al., 1994a; Canudas de Wit et al., 1991; Hensen, 2002; Olsson, 1996; Olsson et al., 1998]. The most common function is

$$F_c(v_r) = F_c + (F_s - F_c)e^{-|v_r/v_s|^{\delta_s}} + b_v|v_r|, \quad (3.4)$$

where  $F_c$ ,  $F_s$  and  $b_v$  have already been described,  $v_s$  is called the Stribeck velocity and  $\delta_s$  is the Stribeck shape parameter. Moreover, some examples of functions  $F_c(v_r)$  for a humped friction model are given in [Brockley et al., 1967; Brockley and Ko, 1970]. Very often, the nonlinear function  $F_c(v_r)$  is described using a neural network model [Hensen, 2002; Hensen et al., 2000; Mihajlović et al., 2004a,b; Narendra and Parthasarathy, 1990], since it can describe both friction models. Herewith, the friction force is modelled with (3.3), where

$$F_c(v_r) = T_s + \sum_{i=1}^n T_i \left( 1 - \frac{2}{1 + e^{2w_i v_r}} \right) + b_v|v_r|, \quad (3.5)$$

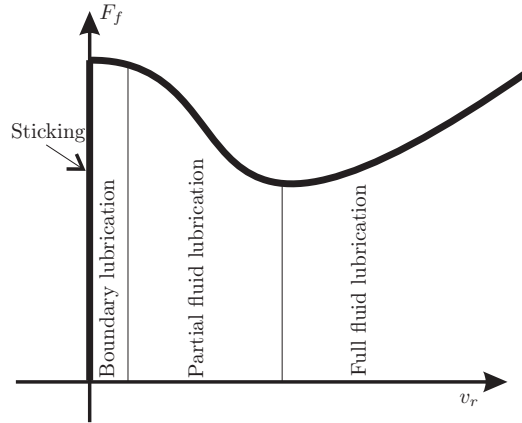


Figure 3.11: Different regimes in the friction force.

where  $n$  represents the number of nodes of the neural network model,  $T_s$ ,  $T_i$  and  $w_i$ , with  $i = 1, \dots, n$ , are additional parameters of the friction model

### 3.2.2 Negative Damping in the Friction Force

When lubrication is present between two contacting surfaces, the mechanisms behind friction can roughly be divided into four regimes in terms of the relative velocity between the contacting surfaces. According to Armstrong-Hélouvy [1991] and Armstrong-Hélouvy et al. [1994a] the regimes are sticking, boundary lubrication, partial fluid lubrication and full fluid lubrication (see figure 3.11). These regimes depend on the relative velocity between the contacting surfaces.

In the sticking regime, the friction force is due to elastic and plastic deformation of the asperity contacts [Armstrong-Hélouvy, 1991; Armstrong-Hélouvy et al., 1994a; Olsson, 1996]. It is often assumed that in this regime there is no motion between the contact surfaces. However, there is a displacement, the so-called presliding displacement. When the applied force is higher than the so-called break-away force, true (gross) sliding begins and the system enters the boundary lubrication regime.

In the boundary lubrication regime, the relative velocity between the contacting surfaces is very low and hardly any lubricant is present in the contact. Therefore, the friction force is due to the shearing resistance of the asperity contacts.

If the sliding velocity increases further, more lubricant is brought into contact which increases the separation of the surfaces and the system enters a partial fluid lubrication regime. This represents a transitional regime before full fluid lubrication appears. The friction force is partly due to asperity contacts and partly due to the lubricant and its viscosity and it is influenced by the interaction between lubricant viscosity, motion speed and contact geometry. As the sliding velocity increases, the solid-to-solid contact decreases, reducing friction and increasing the acceleration of the moving part.

Finally, when the sliding velocity increases even further, the two surfaces are completely separated by the lubricant and full fluid lubrication occurs. Then, the friction force is due to the hydrodynamic behaviour of the lubricant and the viscosity of the lubricant becomes a dominant factor.

Table 3.1: Description of the parameters and variables used in the model of the upper part of the set-up.

Symbol	Description	Unit
$u$	Input voltage to the power amplifier	V
$i_r$	Rotor current	A
$\theta_u$	Angular position of the upper disc	rad
$\omega_u = \dot{\theta}_u$	Angular velocity of the upper disc	rad/s
$a$	Amplification factor of the power amplifier	-
$R_i$	Output resistance of the amplifier	$\Omega$
$L_r$	Inductance of the rotor circuit	V s/A
$R_r$	Resistance of the rotor circuit	$\Omega$
$n$	Reduction ratio of the gear box ( $n = 3969/289$ )	-
$k_{em}$	Electromotive force constant	V s/rad
$k_{me}$	Torque constant	N m/A
$T_{fm}$	Friction torque in the DC motor and in the bearings of the motor shaft	N m
$T_{fu}$	Equivalent friction torque present at the upper part of the set-up	N m
$k_m$	Motor constant	N m/V
$J_u$	Moment of inertia of the upper disc with respect to its center of mass	kg m <sup>2</sup>

### 3.2.3 Model of the DC Motor

The DC motor, the gear box and the upper steel disc together represent the upper part of the set-up. The model of the upper part of the set-up can be described by the following differential equations:

$$\begin{aligned} a u &= L_r i_r + (R_i + R_r) i_r + n k_{em} \dot{\theta}_u, \\ J_u \ddot{\theta}_u + T_{fm}(\dot{\theta}_u) &= n k_{me} i_r, \end{aligned} \quad (3.6)$$

where all variables and parameters are defined in table 3.1. In (3.6), and further in the text, a dot above a variable indicates a time derivative (e. g.  $i_r = di_r/dt$ ).

In the sequel, the inductance of the rotor circuit is neglected ( $L_r = 0$ ), since the electrical part of the system has a much faster dynamics than the mechanical part. With this assumption the model of the motor is of lower order and can be formulated as:

$$J_u \ddot{\theta}_u + \frac{n^2 k_{em} k_{me}}{R_i + R_r} \dot{\theta}_u + T_{fm}(\dot{\theta}_u) = \frac{a n k_{me}}{R_i + R_r} u. \quad (3.7)$$

Next, by introduction of an equivalent friction torque at the upper part defined by  $T_{fu}(\dot{\theta}_u)$  by

$$T_{fu}(\dot{\theta}_u) = \frac{n^2 k_{em} k_{me}}{R_i + R_r} \dot{\theta}_u + T_{fm}(\dot{\theta}_u) \quad (3.8)$$

and by defining the motor constant  $k_m$  as

$$k_m = \frac{a n k_{me}}{R_i + R_r}, \quad (3.9)$$



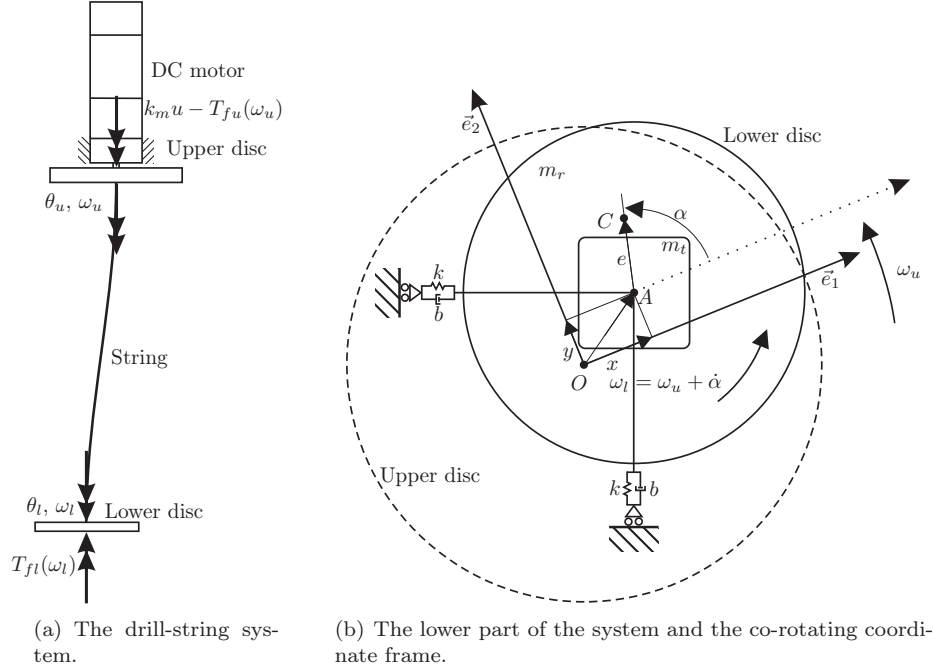


Figure 3.12: The drill-string system.

the following model of the upper part of the set-up can be obtained:

$$J_u \ddot{\theta}_u + T_{fu}(\dot{\theta}_u) = k_m u. \quad (3.10)$$

From (3.8), it can be concluded that the equivalent friction torque  $T_{fu}(\dot{\theta}_u)$  consists of the friction torque  $T_{fm}(\dot{\theta}_u)$  due to the friction in the bearings and the additional term  $(n^2 k_{em} k_{me}) \dot{\theta}_u / (R_i + R_r)$ , which has the nature of a viscous friction and is due to the electro-magnetic characteristics of the DC-motor. As mentioned before, the friction torque  $T_{fu}$  is modelled using a set-valued force law (as in (3.1)).

### 3.2.4 The Full Model of the Set-Up

When deriving a model of the entire set-up the following assumptions are adopted:

- The radial displacement  $r$  of the geometric center of the lower disc (point  $A$  in figure 3.12(b)) is much smaller than the length of the string. Consequently, it is assumed that the lower disc does not move in vertical direction.
- The lower disc is always in horizontal position when moving in the lateral direction - there is no tilt in the lower brass disc. This is guaranteed by the design of the constraints in  $x$ - and  $y$ -direction implemented at the lower part of the set-up.
- The constraints are weakly coupled and therefore such coupling effects are neglected.



- The sticking behaviour is present in lateral direction due to friction in the LVDTs. However, since the corresponding break-away friction level is very small it is neglected.
- The mass, damping and stiffness characteristics of the set-up in lateral direction (i.e.  $m$ ,  $b$  and  $k$  in table 3.2) are isotropic.
- The torsional damping coefficient, related the material damping in the steel string, is very small compared to the damping at the upper and lower part (due to friction) of the set-up. Therefore, it is neglected.
- The coordinate frame, used to describe the translational motion of the system, is fixed to and rotates with the upper disc, i.e. a co-rotating coordinate frame is used, see figure 3.12(b).

In order to derive a model of the system shown in figure 3.12, the Euler-Lagrange equations are used:

$$\frac{d}{dt} \left( \frac{\partial \mathcal{T}}{\partial \dot{\mathbf{q}}}(\mathbf{q}, \dot{\mathbf{q}}) \right) - \frac{\partial \mathcal{T}}{\partial \mathbf{q}}(\mathbf{q}, \dot{\mathbf{q}}) + \frac{\partial \mathcal{V}}{\partial \mathbf{q}}(\mathbf{q}) = (\mathbf{Q}^{nc})^T \quad (3.11)$$

where  $\mathcal{T}(\mathbf{q}, \dot{\mathbf{q}})$  is the kinetic energy,  $\mathcal{V}(\mathbf{q})$  is the potential energy and  $\mathbf{Q}^{nc}$  represents the generalized non-conservative forces and  $\mathbf{q}$  are the generalized coordinates. If we choose the following generalized coordinates:

$$\mathbf{q} = [ \theta_u \quad x \quad y \quad \alpha ]^T, \quad (3.12)$$

then for the system in figure 3.12 we obtain that kinetic and potential energies are:

$$\begin{aligned} \mathcal{T}(\mathbf{q}, \dot{\mathbf{q}}) &= \frac{1}{2} m_r (\dot{x} - e \dot{\alpha} \sin(\alpha) - y \dot{\theta}_u - e \dot{\theta}_u \sin(\alpha))^2 \\ &\quad + \frac{1}{2} m_r (\dot{y} + e \dot{\alpha} \cos(\alpha) + x \dot{\theta}_u + e \dot{\theta}_u \cos(\alpha))^2 \\ &\quad + \frac{1}{2} m_t (\dot{x} - y \dot{\theta}_u)^2 + \frac{1}{2} m_t (\dot{y} + x \dot{\theta}_u)^2 + \frac{1}{2} J_u \dot{\theta}_u^2 + \frac{1}{2} J_C (\dot{\theta}_u + \dot{\alpha})^2, \\ \mathcal{V}(\mathbf{q}) &= \frac{1}{2} k (x^2 + y^2) + \frac{1}{2} k_\theta \alpha^2, \end{aligned} \quad (3.13)$$

and the nonconservative forces are described with:

$$\mathbf{Q}^{nc} = \begin{bmatrix} k_m u - T_{fu}(\dot{\theta}_u) - T_{fl}(\dot{\theta}_u + \dot{\alpha}) - b x (\dot{y} + x \dot{\theta}_u) + b y (\dot{x} - y \dot{\theta}_u) \\ -b (\dot{x} - y \dot{\theta}_u) \\ -b (\dot{y} + x \dot{\theta}_u) \\ -T_{fl}(\dot{\theta}_u + \dot{\alpha}) \end{bmatrix}. \quad (3.14)$$

All symbols and variables are described in tables 3.1 and 3.2. A detailed derivation of (3.13) and (3.14) is presented in Appendix A. If we substitute (3.13) and (3.14) in (3.11), the following equations of motion are obtained:

$$\mathbf{M}(\mathbf{q}) \ddot{\mathbf{q}} + \mathbf{h}(\mathbf{q}, \dot{\mathbf{q}}) + \mathbf{W}_T(\mathbf{q}) \boldsymbol{\Lambda}_T = \mathbf{K}_m u, \quad (3.15)$$

with

$$\mathbf{M}(\mathbf{q}) = \begin{bmatrix} M_{11}(\mathbf{q}) & M_{12}(\mathbf{q}) & M_{13}(\mathbf{q}) & M_{14}(\mathbf{q}) \\ M_{12}(\mathbf{q}) & m_r + m_t & 0 & -m_r e \sin(\alpha) \\ M_{13}(\mathbf{q}) & 0 & m_r + m_t & m_r e \cos(\alpha) \\ M_{14}(\mathbf{q}) & -m_r e \sin(\alpha) & m_r e \cos(\alpha) & m_r e^2 + J_C \end{bmatrix},$$

$$M_{11}(\mathbf{q}) = (m_r + m_t)(x^2 + y^2) + m_r e(2y \sin(\alpha) + 2x \cos(\alpha) + e) + J_u + J_C,$$

$$M_{12}(\mathbf{q}) = -(m_r + m_t)y - m_r e \sin(\alpha),$$

$$M_{13}(\mathbf{q}) = (m_r + m_t)x + m_r e \cos(\alpha),$$

$$M_{14}(\mathbf{q}) = m_r e(y \sin(\alpha) + x \cos(\alpha) + e) + J_C,$$

$$\mathbf{h}(\mathbf{q}, \dot{\mathbf{q}}) = \begin{bmatrix} 2(m_r + m_t)\dot{\theta}_u(x\dot{x} + y\dot{y}) + m_r(2e\dot{x}\dot{\theta}_u \cos(\alpha) + 2e\dot{y}\dot{\theta}_u \sin(\alpha) + 2ye\dot{\alpha}\dot{\theta}_u \cos(\alpha) + ey\dot{\alpha}^2 \cos(\alpha) - 2xe\dot{\alpha}\dot{\theta}_u \sin(\alpha) - ex\dot{\alpha}^2 \sin(\alpha)) + b(x\dot{y} - y\dot{x} + x^2\dot{\theta}_u + y^2\dot{\theta}_u) \\ -(m_r + m_t)\dot{\theta}_u(2\dot{y} + x\dot{\theta}_u) + m_r(-2e\dot{\alpha}\dot{\theta}_u \cos(\alpha) - e\dot{\alpha}^2 \cos(\alpha) - e\dot{\theta}_u^2 \cos(\alpha)) + b(\dot{x} - y\dot{\theta}_u) + kx \\ (m_r + m_t)\dot{\theta}_u(2\dot{x} - y\dot{\theta}_u) + m_r(-2e\dot{\alpha}\dot{\theta}_u \sin(\alpha) - e\dot{\alpha}^2 \sin(\alpha) - e\dot{\theta}_u^2 \sin(\alpha)) + b(\dot{y} + x\dot{\theta}_u) + ky \\ m_r(2e\dot{x}\dot{\theta}_u \cos(\alpha) + 2e\dot{y}\dot{\theta}_u \sin(\alpha) - ey\dot{\theta}_u^2 \cos(\alpha) + ex\dot{\theta}_u^2 \sin(\alpha)) + k_\theta \alpha \end{bmatrix}, \quad (3.16)$$

$$\mathbf{W}_T(\mathbf{q}) = \begin{bmatrix} 1 & 1 \\ 0 & 0 \\ 0 & 0 \\ 0 & 1 \end{bmatrix}, \quad \mathbf{\Lambda}_T = \begin{bmatrix} T_{fu}(\dot{\theta}_u) \\ T_{fl}(\dot{\theta}_u + \dot{\alpha}) \end{bmatrix}, \quad \mathbf{K}_m = \begin{bmatrix} k_m \\ 0 \\ 0 \\ 0 \end{bmatrix}.$$

The dynamics of the eighth-order system (3.15) and (3.16) is independent of the angular position of the discs ( $\theta_u$  and  $\theta_l$ ), but only depends on the difference  $\alpha$  between these two angular positions. That is why, we replace  $\dot{\theta}_u$  with  $\omega_u$  in (3.16). Then, if we perform some equivalent transformations to (3.15), the following seventh-order system of differential equations can be obtained.

$$J_u \dot{\omega}_u - k_\theta \alpha + T_{fu}(\omega_u) = k_m u,$$

$$(m_r + m_t)\ddot{x} - m_r e \ddot{\alpha} \sin(\alpha) - (m_r + m_t)\dot{\omega}_u y - m_r e \dot{\omega}_u \sin(\alpha) + b\dot{x} - 2(m_r + m_t)\omega_u \dot{y} - 2m_r e \omega_u \dot{\alpha} \cos(\alpha) - m_r e \dot{\alpha}^2 \cos(\alpha) + kx - (m_r + m_t)\omega_u^2 x - b\omega_u y - m_r e \omega_u^2 \cos(\alpha) = 0,$$

$$(m_r + m_t)\ddot{y} + m_r e \ddot{\alpha} \cos(\alpha) + (m_r + m_t)\dot{\omega}_u x + m_r e \dot{\omega}_u \cos(\alpha) + b\dot{y} + 2(m_r + m_t)\omega_u \dot{x} - 2m_r e \omega_u \dot{\alpha} \sin(\alpha) - m_r e \dot{\alpha}^2 \sin(\alpha) + ky - (m_r + m_t)\omega_u^2 y + b\omega_u x - m_r e \omega_u^2 \sin(\alpha) = 0, \quad (3.17)$$

$$-m_r \ddot{x} e \sin(\alpha) + m_r \ddot{y} e \cos(\alpha) + (m_r e^2 + J_C)(\ddot{\alpha} + \dot{\omega}_u) + m_r \dot{\omega}_u e(x \cos(\alpha) + y \sin(\alpha)) + 2m_r e \dot{x} \omega_u \cos(\alpha) + 2m_r e \dot{y} \omega_u \sin(\alpha) + T_{fl}(\omega_u + \dot{\alpha}) + m_r x e \omega_u^2 \sin(\alpha) - m_r y e \omega_u^2 \cos(\alpha) + k_\theta \alpha = 0.$$

As mentioned before, the friction torques  $T_{fu}(\omega_u)$  and  $T_{fl}(\omega_l)$  are modelled using

Table 3.2: Description of the parameters and the variables used in the model of the lower part of the set-up.

Symbol	Description	Unit
$J_C$	Moment of inertia of the lower disc with respect to its center of mass (point $C$ in figure 3.12(b)).	kg m <sup>2</sup>
$J_A$	Moment of inertia of the lower disc with respect to its geometric center (point $A$ in figure 3.12(b)).	kg m <sup>2</sup>
$k$	Bending stiffness coefficient in lateral direction.	N/m
$b$	Damping coefficient in lateral direction.	kg/s
$k_\theta$	Torsional stiffness coefficient.	N m/rad
$x, y$	Displacement of the geometric center of the lower disc in the Cartesian co-rotating coordinate frame.	m
$\alpha$	Angle which represents the twist of the string. ( $\alpha = \theta_l - \theta_u$ ),	rad
$\theta_l$	Angular position of the lower disc.	rad
$\omega_l = \dot{\theta}_l$	Angular velocity of the lower disc.	rad/s
$e$	Distance between the center of the mass $E$ of the lower disc and its geometric center $A$ .	m
$m_r$	Mass of all parts of the lower part of the set-up which can rotate around the center of the disc.	kg
$m_t$	Mass of all parts of the lower part of the set-up which do not rotate around the center of the disc (one constraint, the brake, the oil box, the upper bearing housing, the lower bearing housing and the encoder at the lower discs).	kg
$T_{fl} = T_{flb} + T_{fla}$	Equivalent friction torque present at the lower disc which is caused by the friction between the brake disc and the brake and the friction in the bearings.	N m
$T_{flb}$	Friction torque caused by the friction between the brake disc and the brake.	N m
$T_{fla}$	Friction torque in the bearings.	N m

set-valued force laws:

$$\begin{aligned}
 T_{fu}(\omega_u) &\in \begin{cases} T_{cu}(\omega_u)\text{sgn}(\omega_u) & \text{for } \omega_u \neq 0, \\ [-T_{cu}(0^-), T_{cu}(0^+)] & \text{for } \omega_u = 0, \end{cases} \\
 T_{fl}(\omega_l) &\in \begin{cases} T_{cl}(\omega_l)\text{sgn}(\omega_l) & \text{for } \omega_l \neq 0, \\ [-T_{cl}(0^-), T_{cl}(0^+)] & \text{for } \omega_l = 0. \end{cases}
 \end{aligned} \tag{3.18}$$

Consequently, the model of the system, constituted by (3.17) and (3.18), is a set of differential inclusions. It should also be stressed that the friction torque at the lower disc  $T_{fl}(\omega_l)$  consists of the friction between the brake disc and the brake  $T_{flb}(\omega_l)$ , and the friction in the bearings  $T_{fla}(\omega_l)$ . Both friction torques are modelled using set-valued force laws:

$$\begin{aligned}
T_{fla}(\omega_l) &\in \begin{cases} T_{cla}(\omega_l)\text{sgn}(\omega_l) & \text{for } \omega_l \neq 0, \\ [-T_{cla}(0^-), T_{cla}(0^+)] & \text{for } \omega_l = 0, \end{cases} \\
T_{flb}(\omega_l) &\in \begin{cases} T_{clb}(\omega_l)\text{sgn}(\omega_l) & \text{for } \omega_l \neq 0, \\ [-T_{clb}(0^-), T_{clb}(0^+)] & \text{for } \omega_l = 0. \end{cases}
\end{aligned} \tag{3.19}$$

### 3.3 Parameter Estimation

In order to analyze the dynamics of the experimental set-up, we need to estimate the parameters of the nonlinear model (3.17) ( $k_m, J_u, k_\theta, J_C, e, m_r, m_t, k, b$ ), to choose nonlinear functions  $T_{cu}(\omega_u), T_{cl}(\omega_l)$  in (3.18) and to estimate their parameters. Several techniques are available for parameter estimation of nonlinear systems. In [Gelb et al., 1978] the following two techniques are described: minimum variance and nonlinear least-squares estimation. The most popular minimum variance estimator is the so-called Extended Kalman filter. Such estimator is often used for an on-line estimation of states and parameters of a nonlinear system. However, in this thesis we are only interested in estimating the parameters of the model (3.17) and (3.18). That is why we have chosen to use the nonlinear least-squares technique.

#### 3.3.1 Nonlinear Least-Squares Technique

Assume that a state-space model of the experimental system is given by:

$$\begin{aligned}
\dot{\mathbf{x}} &= \mathbf{f}(\mathbf{x}, \mathbf{u}^{(k)}, \mathbf{p}), \\
\mathbf{y}^{(k)} &= \mathbf{g}(\mathbf{x}, \mathbf{u}^{(k)}), \\
k &= 1, \dots, N,
\end{aligned} \tag{3.20}$$

where  $\mathbf{x} \in \mathbb{R}^{N_x}$ ,  $\mathbf{u} \in \mathbb{R}^{N_u}$ ,  $\mathbf{y} \in \mathbb{R}^{N_y}$ ,  $\mathbf{p} \in \mathbb{R}^{N_p}$  represent the states, inputs, outputs and parameters of the system, respectively. In (3.20), the superscripts in  $\mathbf{u}^{(k)}$  and  $\mathbf{y}^{(k)}$  indicate that the input and the output are discretized signals, since  $\mathbf{u}$  and  $\mathbf{y}$  are measured at discrete time instants  $t_k$ . Using nonlinear least-squares estimation, we aim to find optimal values for the parameters  $\mathbf{p}$  such that the performance index, defined by

$$J(\mathbf{p}) = \sum_{k=1}^N (\hat{\mathbf{y}}^{(k)} - \mathbf{y}^{(k)}(\mathbf{p}))^T \mathbf{W}^{(k)} (\hat{\mathbf{y}}^{(k)} - \mathbf{y}^{(k)}(\mathbf{p})), \tag{3.21}$$

is minimal. In (3.21),  $\mathbf{W}^{(k)}$  is a sequence of weighting matrices,  $\hat{\mathbf{y}}^{(k)}$  represents the measured data and  $\mathbf{y}^{(k)}$  the simulation data obtained when the input  $\mathbf{u}^{(k)}$  is applied both to the system and to the model (3.20), respectively.

In order to minimize  $J(\mathbf{p})$ , it is not possible to find optimal values for the parameters  $\mathbf{p}$  using elementary matrix algebra as it is possible for linear least-squares estimation. Consequently, an iterative process must be used [Coleman et al., 2002; Mayers, 1989]. However, for any type or iterative process we need good starting values for the parameters. Poor starting values may result in convergence to a local minimum of  $J(\mathbf{p})$ . Therefore, when estimating the parameters of a nonlinear system, more information about the system is needed in order to have good initial estimates for the parameters, which need to be estimated.

To estimate parameters of a system, the measured data  $\hat{\mathbf{y}}^{(k)}$  need to represent sufficient information about the dynamics of the system. In other words, we need

to choose an appropriate input signal  $\mathbf{u}^{(k)}$  which will excite all the system dynamics we are interested in. The property of an input signal which gives a measure about the "variation" that is present in the signal is called *persistence of excitation* [Ljung, 1999].

Finally, to give an objective judgement on the accuracy of the estimated parameters, the following  $R_y^2$ -criterion is introduced [Mayers, 1989]:

$$R_y^2 = 1 - \frac{\sum_{k=1}^{N_y} (\hat{y}^{(k)} - y^{(k)})^2}{\sum_{k=1}^{N_y} (\hat{y}^{(k)} - \bar{y})^2}, \quad \bar{y} = \frac{1}{N_y} \sum_{k=1}^{N_y} \hat{y}^{(k)}. \quad (3.22)$$

In (3.22),  $y \in \mathbb{R}$  is an output signal of the system (3.20), i.e. if  $\mathbf{y} = [y_1, y_2, \dots, y_{N_y}]^T$ , then  $y \in \{y_1, y_2, \dots, y_{N_y}\}$ . Furthermore, from (3.22) it can be seen that the maximum value for  $R_y^2$  is 1. Namely, if  $R_y^2$  is close to 1, then this indicates the high quality of the obtained parameter estimates.

### 3.3.2 Parameter Estimation of the Set-Up

In order to obtain a predictive model of the drill-string set-up, the parameters  $k_m$ ,  $J_u$ ,  $J_C$ ,  $k_\theta$ ,  $m_r$ ,  $m_t$ ,  $e$ ,  $k$ ,  $b$  in (3.17) and the nonlinear functions  $T_{cu}(\omega_u)$ ,  $T_{cl}(\omega_l)$  in (3.18) need to be estimated. Since good starting values are needed for the parameters of the set-up, we perform the estimation procedure in the following way:

1. We disconnect the upper disc from the lower disc and estimate the parameters of the upper part of the set-up ( $k_m$ ,  $J_u$ ) and the related friction torque ( $T_{cu}(\omega_u)$ ).
2. We connect upper and lower disc, fix the lower disc in order to avoid motion in lateral direction, and do not apply any normal force at the brake at the lower part of the set-up. Then, we estimate the stiffness parameter of the string ( $k_\theta$ ), the moment of inertia of the lower disc ( $J_A$ ) and the friction torque in the bearings at the lower disc ( $T_{cla}(\omega_l)$ ) - the estimation of the friction at the lower disc when the normal force on the brake is applied, is performed in Chapter 4.
3. We release the lower disc - so it can move in the lateral direction - and estimate the remaining parameters of the model ( $e$ ,  $m_r$ ,  $m_t$ ,  $k$  and  $b$ ). Based on those estimates, we determine  $J_C$  using

$$J_C = J_A - e^2 m_r. \quad (3.23)$$

In order to estimate the parameters of the set-up using the nonlinear least-squares method, we use a quasi-random input signal  $u$  as shown in figure 3.13(a) and to validate the model we use the signal as shown in figure 3.13(b) which both contain enough information to excite the important dynamics of the system.

#### Parameter Estimation of the Upper Part of the Set-Up ( $k_m$ , $J_u$ and $T_{cu}(\omega_u)$ )

The model of the upper part of the set-up is described with (3.10). Further in the thesis, we assume that the exact value of the moment of inertia of the upper disc is known and is determined using the following relation:

$$J_u = \rho_u \frac{\pi}{32} d_u^4 l_u^4, \quad (3.24)$$

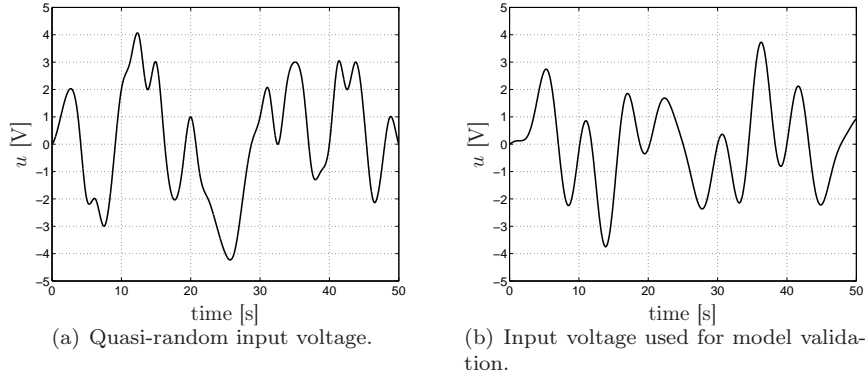


Figure 3.13: Input signals used for parameter estimation and validation of the model of the set-up.

where the description of all parameters and related (measured) values is given in table 3.3. According to the values given in table 3.3 and according to (3.24), the moment of inertia of the upper disc is:

$$J_u = 0.4765 \text{ kg m}^2. \quad (3.25)$$

In order to determine the non-linear function  $T_{cu}(\omega_u)$ , the starting values for  $k_m$  and for the parameters of  $T_{cu}(\omega_u)$ , different constant input voltages  $u$  are applied and the rotor current  $i_r$ , the angular velocity of the upper disc  $\omega_u$  and the voltage from the power amplifier to the motor ( $a u - R_r i_r$  in (3.6)) are measured in steady-state [Van Veggel, 2002]. According to those measurements the behaviour of the upper part of the set-up is analyzed and the following is noticed:

- A negative damping is not present in the friction torque at the upper disc. An explanation for this can be recognized in (3.8). Namely, this equation expresses that the friction in the bearings of the upper disc  $T_{fm}(\omega_u)$  may very well be small with respect to the viscous friction term due to the electro-magnetic forces in the DC-motor. Experiments show that that is indeed the case. Therefore, the friction torque at the upper disc  $T_{fu}(\omega_u)$  is modelled as Coulomb friction with viscous friction as shown in figure 3.9(c).
- The friction torque at the upper disc is asymmetric. This means that  $T_{cu}(\omega_u) \neq T_{cu}(-\omega_u)$  in (3.18).

Table 3.3: Description and (measured) parameter values of the upper disc of the set-up.

Symbol	Description	Value and unit
$\rho_u$	Density of the material of the upper disc (steel)	7900 kg/m <sup>3</sup>
$d_u$	Diameter of the upper disc	0.4 m
$l_u$	Thickness of the upper disc	0.024 m

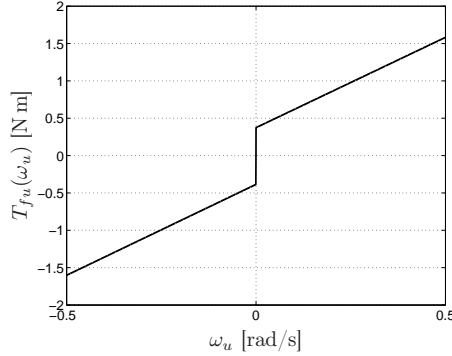


Figure 3.14: Estimated friction torque at the upper part of the set-up.

Summarizing, the friction torque at the upper part of the set-up is modelled as in (3.18) with

$$T_{cu}(\omega_u) = T_{su} + \Delta T_{su} \text{sgn}(\omega_u) + b_u |\omega_u| + \Delta b_u \omega_u. \quad (3.26)$$

In (3.26),  $T_{cu}(0^+) = T_{su} + \Delta T_{su}$  and  $-T_{cu}(0^-) = -T_{su} + \Delta T_{su}$  represent the maximum and minimum value of the friction torque for zero angular velocities and  $b_u + \Delta b_u$  and  $b_u - \Delta b_u$  are the viscous friction coefficients for positive and negative velocities, respectively.

Moreover, using those steady-state measurements, the starting values for  $k_m$  and for the parameters of  $T_{cu}(\omega_u)$  in (3.26) are determined [Van Veggel, 2002]. Next, using those values, the quasi-random input signal, shown in figure 3.13(a), is applied and the following performance index is minimized:

$$J = \sum_{k=1}^N (\hat{\theta}_u^{(k)} - \theta_u^{(k)})^2, \quad (3.27)$$

where  $\hat{\theta}_u$  and  $\theta_u$  represent measured and simulated data for the angular position of the upper disc. The identification procedure yields the following parameter values:

$$\begin{aligned} k_m &= 4.3228 \frac{\text{N m}}{\text{V}}, \quad T_{su} = 0.37975 \text{ N m}, \quad \Delta T_{su} = -0.00575 \text{ N m}, \\ b_u &= 2.4245 \frac{\text{kg m}^2}{\text{rad s}}, \quad \Delta b_u = -0.0084 \frac{\text{kg m}^2}{\text{rad s}}. \end{aligned} \quad (3.28)$$

The estimated friction torque is shown in figure 3.14. The measured and simulated angular position signals obtained for the applied quasi-random signal are shown in figure 3.15 and the value of the related  $R_y^2$  criterion (3.22) is:  $R_{\hat{\theta}_u}^2 = 1.0000$ . A model validation is performed for the input signal shown in figure 3.13(b); the appropriate measured and simulated responses are shown in figure 3.16, where  $R_{\hat{\theta}_u}^2 = 0.9993$ . The comparison between the responses of the experimental set-up and estimated model indicates the high quality of the obtained parameter estimates.

Here we like to mention that the parameter  $k_m$  and the parameters of the friction  $T_{fu}(\omega_u)$  can slightly change over time. These changes can be caused by changing conditions in the laboratory (temperature, humidity) in which the set-up is placed. From equations (3.8) and (3.9) it can be concluded that changes in  $k_m$  are mainly due to a change of the parameters of the motor ( $k_{em}$ ,  $k_{m\epsilon}$  and  $R_r$ ) or of the parameters of the power amplifier ( $a$ ,  $R_i$ ).

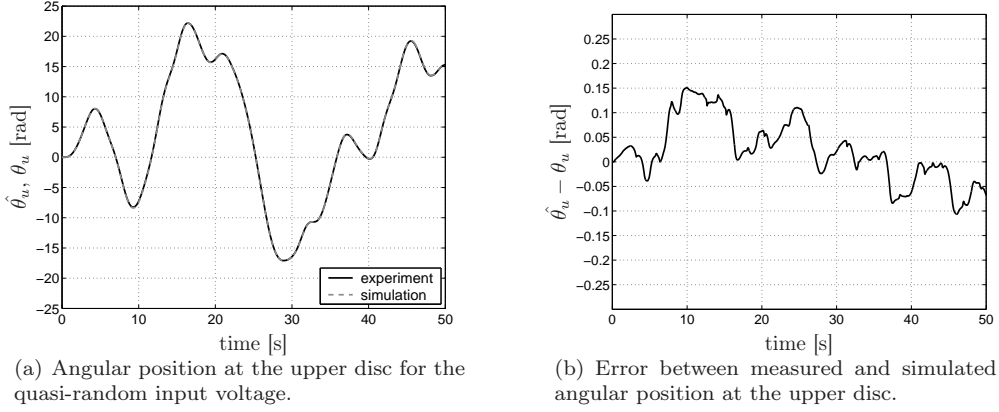


Figure 3.15: Estimation signals for the upper part of the set-up ( $R_{\theta_u}^2 = 1.0000$ ).

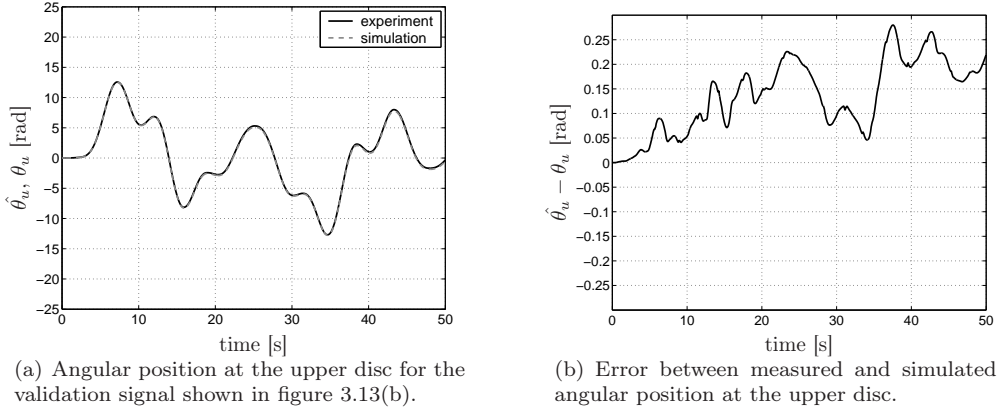


Figure 3.16: Validation signals for the upper part of the set-up ( $R_{\theta_u}^2 = 0.9993$ ).

### Parameter Estimation of the Lower Part of the Set-Up in Torsional Direction ( $k_\theta$ , $J_A$ and $T_{cla}(\omega_l)$ )

To estimate the parameters  $k_\theta$ ,  $J_A$  and the friction torque  $T_{fla}(\omega_l)$  in the bearings at the lower part, the upper and lower disc are connected by means of the low-stiffness string, the lower disc is fixed in such a way that it cannot move in lateral direction (using the  $x$ - and  $y$ -constraint mechanisms shown in figures 3.6 and 3.7) and no normal force is applied at the brake (shown in figure 3.5). The model of that system can be derived from (3.17), assuming that  $x = \dot{x} = \ddot{x} = y = \dot{y} = \ddot{y} = 0$ :

$$\begin{aligned} J_u \dot{\omega}_u - k_\theta \alpha + T_{fu}(\omega_u) &= k_m u, \\ J_A (\ddot{\alpha} + \dot{\omega}_u) + T_{fla}(\omega_u + \dot{\alpha}) + k_\theta \alpha &= 0. \end{aligned} \quad (3.29)$$

In order to determine initial values for  $k_\theta$  and  $J_A$  for the nonlinear least-squares algorithm, the following relations are used [Fenner, 1989]:

$$\begin{aligned} k_\theta &= G_s \frac{I_s}{l_s}, \text{ with } I_s = \frac{\pi}{32} d_s^4 \text{ and } G_s = \frac{E_s}{2(1+\nu_s)} \\ J_A &= \rho_l \frac{\pi}{32} d_l^4 l_l^4 + l_m^2 \Delta m, \end{aligned} \quad (3.30)$$



Table 3.4: Description and (measured) parameter values of the string and the lower disc.

Symbol	Description	Value and unit
$E_s$	Elasticity modulus for the steel string	$2.0 \cdot 10^{11} \text{ N/m}^2$
$\nu_s$	Poisson ratio for steel	1/3
$d_s$	The diameter of the string	0.002 m
$I_s$	Polar second-moment of the string cross-section about its axis	$\text{m}^4$
$l_s$	The length of the string	1.47 m
$\rho_l$	The density of the material of the lower disc (brass)	$8500 \text{ kg/m}^3$
$d_l$	The diameter of the lower disc	0.25 m
$l_u$	The thickness of the lower disc	0.01 m
$\Delta m$	The added mass to the lower disc	0.45 kg
$l_m$	The distance between the geometric center of the lower disc and the added mass	0.1 m

where the description of all parameters and related (measured) values are given in table 3.4.

In order to determine the friction torque  $T_{fla}(\omega_l)$  in the bearings, the non-linear function  $T_{cla}(\omega_l)$  should be determined. Therefore, the behaviour of the friction torque is analyzed and it is concluded that it can be modelled as in (3.18), with

$$T_{cla}(\omega_l) = T_{sla} + b_{la}|\omega_l|, \quad (3.31)$$

where  $T_{sla}$  is the Coulomb friction in the bearings and  $b_{la}$  is the related viscous friction coefficient.

To obtain the starting values for the parameters of  $T_{cla}(\omega_l)$ , the upper disc is fixed. Then, break-away experiments are performed to determine  $T_{sla}$ . Namely, a force transducer is attached to the lower disc, a force is applied to the disc at a certain radius from its center and the force at which the lower disc starts to move is measured. Using those measurements,  $T_{sla}$  in (3.31) is determined. Next, after removing the force transducer, a certain initial angle is given to the lower disc; consequently the string is deformed elastically. Subsequently the lower disc is released and the transient response of  $\theta_l$  is measured. Based on that response, a starting value for  $b_{la}$  is determined [Van Veggel, 2002].

Using those starting values, a quasi-random input signal is applied (see figure 3.13(a)) and the following performance index is minimized:

$$J = \sum_{k=1}^N (\hat{\theta}_l^{(k)} - \theta_l^{(k)})^2, \quad (3.32)$$

( $\hat{\theta}_l$  and  $\theta_l$  are measured and simulated data for angular position of the lower disc, respectively). The identification procedure yields the following parameter values for the torsional stiffness coefficient and for the moment of inertia of the lower disc:

$$J_A = 0.0414 \text{ kg m}^2, \quad k_\theta = 0.0775 \frac{\text{N m}}{\text{rad}}, \quad (3.33)$$

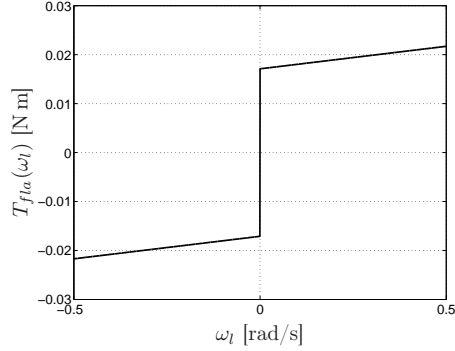


Figure 3.17: Estimation friction torque in the bearings at the lower part of the set-up.

and for the parameters of the friction torque in the bearings:

$$T_{sla} = 0.0171 \text{ N m}, \quad b_{la} = 0.0092 \frac{\text{kg m}^2}{\text{rad s}}. \quad (3.34)$$

The estimated friction torque is shown in figure 3.17. The measured and simulated angular position obtained for the applied quasi-random signal are shown in figure 3.18 and the related performance criterium (3.22) is  $R_{\theta_i}^2 = 0.9997$ . A model validation is performed for the input signal shown in figure 3.13(b) and the related measured and simulated responses are shown in figure 3.19 with  $R_{\theta_i}^2 = 0.9994$ . The comparison between the responses of the experimental set-up and estimated model indicates the high quality of the obtained parameter estimates.

### Parameter Estimation of the Lower Part of the Set-Up in Lateral Direction ( $e$ , $m_r$ , $m_t$ , $k$ and $b$ )

To estimate the parameters  $e$ ,  $m_r$ ,  $m_t$ ,  $k$  and  $b$ , the lower disc is released using the  $x$ - and  $y$ -constraint mechanisms shown in figure 3.6 and 3.7. Consequently, it can move in lateral direction. The model of that system is given by the equations (3.17).

The starting values for  $e$ ,  $m_r$  and  $m_t$  are determined by measuring the masses of all related components of the lower part of the set-up. To determine the starting values for  $k$  and  $b$ , the lower disc is fixed in one direction and a certain initial displacement is prescribed to the lower disc. Then the lower disc is released and the transient response (of the displacement) of the lower disc is measured. Based on this response, starting values for  $k$  and  $b$  are determined [Hendriks, 2004].

In order to estimate the parameters  $e$ ,  $m_r$ ,  $m_t$ ,  $k$  and  $b$  accurately, the quasi-random input signal is applied and the following performance index is minimized:

$$J = \sum_{k=1}^N (\hat{r}^{(k)} - r^{(k)})^2, \quad (3.35)$$

where  $\hat{r}$  and  $r$  are measured and simulated values of the radial displacement of the geometric center of the lower disc, respectively. Here, we stress the following:

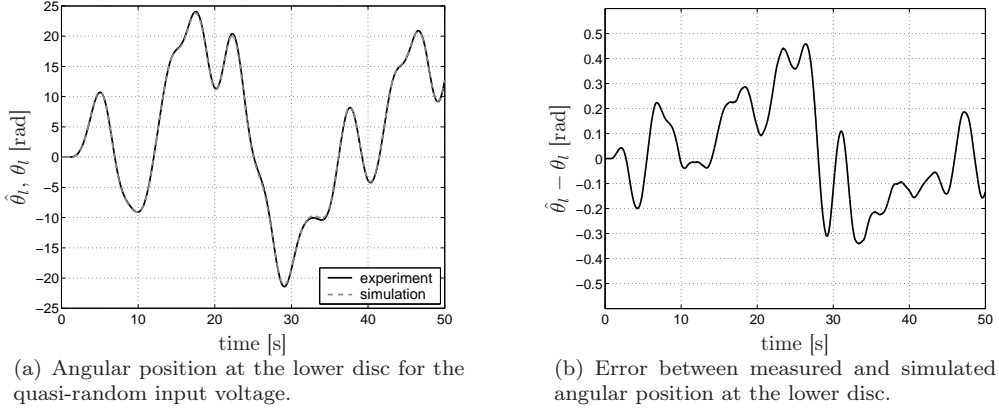


Figure 3.18: Estimation signals for the lower part of the set-up ( $R_{\theta_l}^2 = 0.9997$ ).

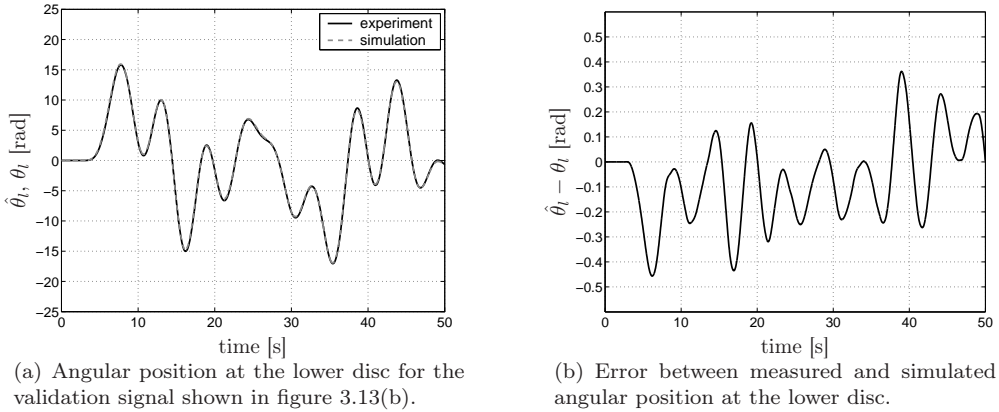


Figure 3.19: Validation signals for the lower part of the set-up ( $R_{\theta_l}^2 = 0.9994$ ).

- In the set-up, we measure the displacement of the lower disc in the fixed coordinate frame, i.e. we measure coordinates  $x^0$  and  $y^0$  in figure 3.20. Therefore, using those measurements we obtain  $\hat{r} = \sqrt{(\hat{x}^0)^2 + (\hat{y}^0)^2}$ .
- The model of the set-up is given in the co-rotating coordinate frame (see equation (3.17), table 3.2, and figure 3.12(b)). The simulated radial displacement can be computed with  $r = \sqrt{x^2 + y^2} = \sqrt{(x^0)^2 + (y^0)^2}$ , with

$$\begin{bmatrix} x^0 \\ y^0 \end{bmatrix} = \begin{bmatrix} \cos(\alpha) & -\sin(\alpha) \\ \sin(\alpha) & \cos(\alpha) \end{bmatrix} \begin{bmatrix} x \\ y \end{bmatrix}. \quad (3.36)$$

- When estimating the parameters of the lower part of the set-up, we minimize the quadratic error with respect to  $r$  and not with respect to the displacements in  $x$ - and  $y$ -direction, since, in the sequel, we are interested in the behaviour of the lower disc in radial direction. Moreover, it is noticed that unmodelled

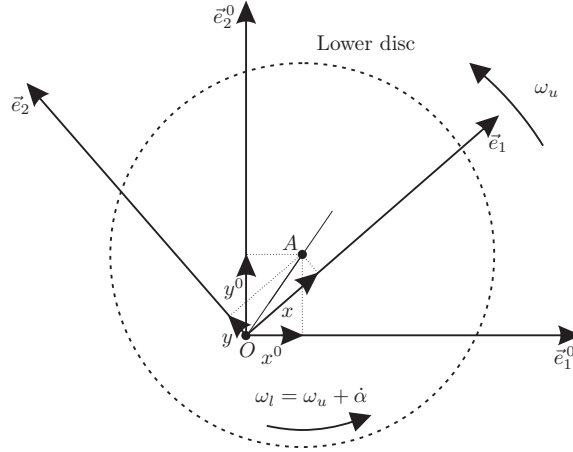


Figure 3.20: The co-rotating and the fixed coordinate frame.

dynamics influences much more the phase shift of the center of the lower disc during lateral movements (thus  $\hat{x}^0$  and  $\hat{y}^0$ ) than the radial displacement  $r$ .

The identification procedure yields the following parameter values:

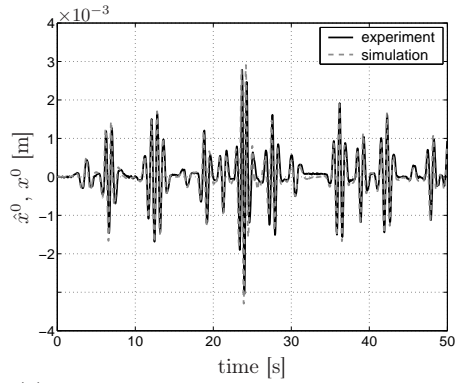
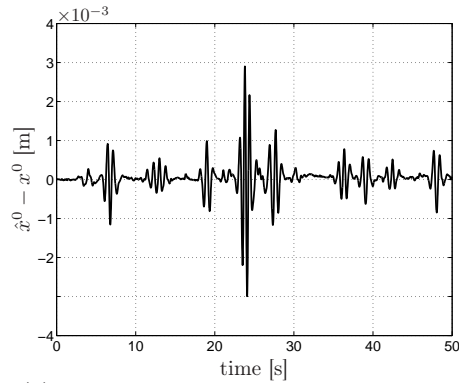
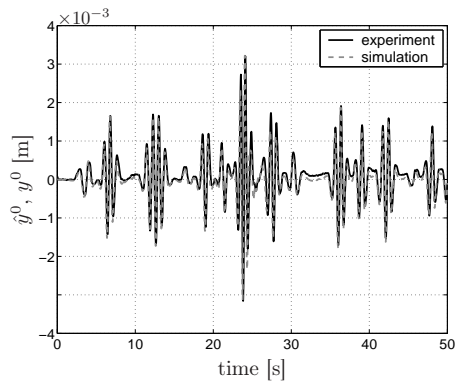
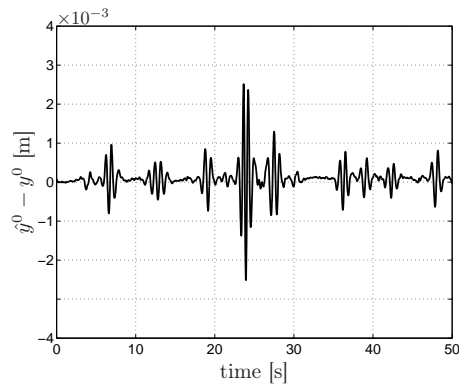
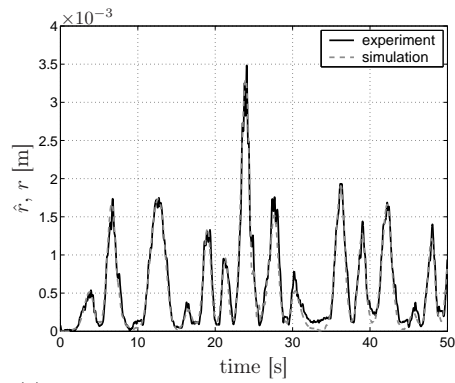
$$\begin{aligned} e &= 0.00489 \text{ m}, \quad m_r = 9.9137 \text{ kg}, \quad m_t = 3.3202 \text{ kg}, \\ k &= 2974.25 \frac{\text{N}}{\text{m}}, \quad b = 25 \frac{\text{kg}}{\text{s}}, \end{aligned} \quad (3.37)$$

with

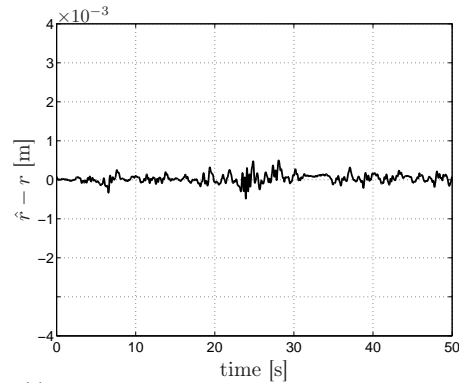
$$J_C = 0.0412 \text{ kg m}^2 \quad (3.38)$$

which is computed using expression (3.23). The measured ( $\hat{x}^0$ ,  $\hat{y}^0$  and  $\hat{r}$ ) and simulated lateral displacements ( $x^0$ ,  $y^0$  and  $r$ ), obtained when the quasi-random signal is applied, are shown in figures 3.21(a), 3.21(c), 3.21(e) and the related  $R^2$  criteria are  $R_x^2 = 0.5300$ ,  $R_y^2 = 0.6498$  and  $R_r^2 = 0.9653$ . A model validation is performed for the input signal shown in figure 3.13(b). The obtained signals are shown in figures 3.22(a), 3.22(c), 3.22(e), with  $R_x^2 = 0.6231$ ,  $R_y^2 = 0.6960$  and  $R_r^2 = 0.8747$ . According to these values, it can be concluded that the matching between simulations and experiments in radial direction is very good while the matching between corresponding signals in  $x^0$  and  $y^0$  directions are of a somewhat lower quality. However, from figures 3.21(a), 3.21(c), 3.22(a) and 3.22(c) it can be concluded that our model predicts very well even the behaviour of the set-up in  $x$ - and  $y$ -directions.

This slightly worse correspondence between simulation and experimental results can be due to several reasons. First, this is due to unmodelled effects which are not included in the model and which are mentioned in Section 3.2.4. Second, the mechanisms for fixing the disc in  $x$ - and  $y$ -direction (see figures 3.6 and 3.7), where also the position sensors are fixed, are not stiff enough. Namely, they can produce small vibrations, especially when the lower disc makes large movements in lateral direction. However, even with those imperfections in the construction of the set-up, the model (3.17), (3.18), (3.19), (3.26), (3.31) with the parameter estimates (3.25), (3.28), (3.33), (3.34), (3.37) and (3.38) predict very well the dynamics of the set-up.

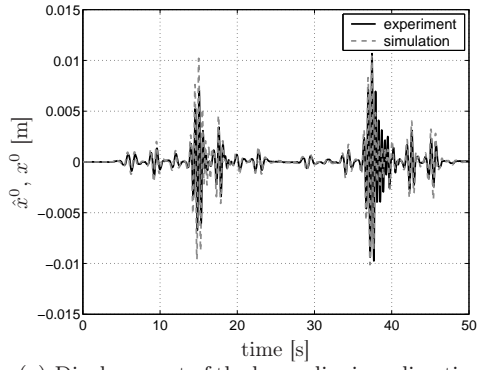
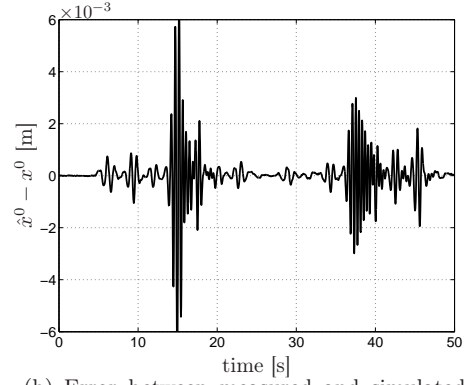
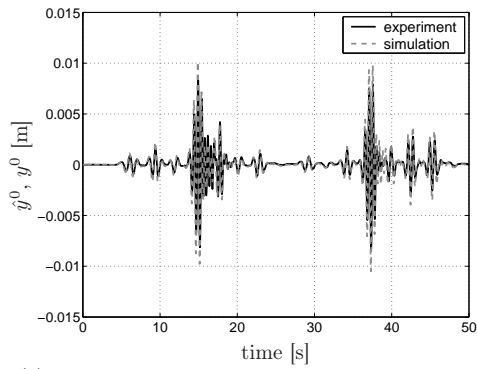
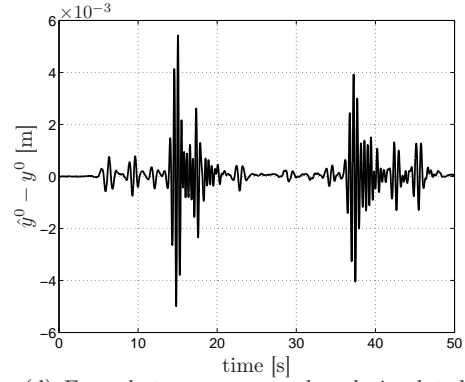
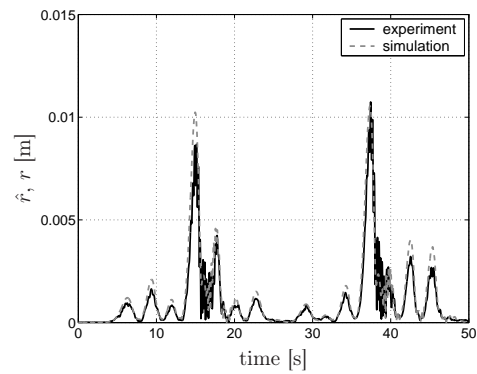
(a) Displacement of the lower disc in  $x$ -direction.(b) Error between measured and simulated displacements in  $x$ -direction.(c) Displacement of the lower disc in  $y$ -direction.(d) Error between measured and simulated displacement in  $y$ -direction.

(e) Displacement of the lower disc in radial direction.

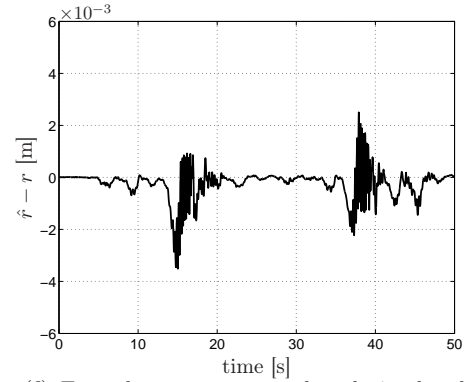


(f) Error between measured and simulated displacement in radial direction.

Figure 3.21: Estimation signals in  $x^0$ -,  $y^0$ - and  $r$ -direction:  $R_x^2 = 0.5300$ ,  $R_y^2 = 0.6498$  and  $R_r^2 = 0.9653$ .

(a) Displacement of the lower disc in  $x$ -direction.(b) Error between measured and simulated displacements in  $x$ -direction.(c) Displacement of the lower disc in  $y$ -direction.(d) Error between measured and simulated displacement in  $y$ -direction.

(e) Displacement of the lower disc in radial direction.



(f) Error between measured and simulated displacement in radial direction.

Figure 3.22: Validation signals in  $x^0$ -,  $y^0$ - and  $r$ -direction:  $R_x^2 = 0.6231$ ,  $R_y^2 = 0.6960$  and  $R_r^2 = 0.8747$ .



## Chapter 4

# Torsional Vibrations in Drill-String Systems

In order to obtain only torsional and no lateral vibrations in the experimental set-up, the lower disc is fixed using the  $x$ - and  $y$ -constraints (shown in figures 3.6 and 3.7). Subsequently, we applied a normal force to the brake and the contact between the brake and the brake disc produces a friction force on the lower disc (see figure 3.5). For several levels of normal forces and no lubrication between the brake and the disc, no torsional vibrations in steady-state are noticed when a constant input voltage is applied. However, when ondina oil 68 [Shell, 1997] is added as a lubrication fluid between the brake disc and the contact material of the brake, torsional steady-state vibrations appear for constant input voltages. Since we are interested in the investigation of torsional vibrations of drill-string systems, we proceed with the analysis of the system when ondina oil 68 is added in a reproducible fashion (using the felt stripes as shown in figure 3.5).

In Section 4.1, we estimate the friction torque at the lower disc  $T_{fl}(\omega_l)$ , when ondina oil 68 is used and a 20.5 N normal force is applied to the brake. Then, in Section 4.2, based on the estimated parameters of the set-up and the estimated friction torque, we determine the equilibrium points (sets), periodic solutions and discuss related stability properties. As a result of such analysis we construct a bifurcation diagram based on the proposed model and the estimated parameters. Moreover, we discuss how different characteristics of the friction force at the lower disc, influence the steady-state behaviour of the system. In Section 4.3, based on the proposed model and estimated parameters, a bifurcation diagram is presented and compared to the experimentally obtained results. Furthermore, we present and discuss results obtained for different contact situations in the brake of the experimental set-up (various normal force levels, various temperatures, and various types of contact material and lubrication). Finally, we finish with a summary in Section 4.4.

### 4.1 Parameter Estimation of the Friction Model

The model of the set-up when only torsional vibrations appear in the system is similar to the model (3.29), (3.18), (3.26) and (3.4), and it can be represented by the following



system of equations [Mihajlović et al., 2005a,b; Van de Wouw et al., 2005a]:

$$\begin{aligned}
J_u \dot{\omega}_u - k_\theta \alpha + T_{fu}(\omega_u) &= k_m u, \\
J_A(\ddot{\alpha} + \dot{\omega}_u) + T_{fl}(\omega_u + \dot{\alpha}) + k_\theta \alpha &= 0, \\
T_{fu}(\omega_u) &\in \begin{cases} T_{cu}(\omega_u) \text{sgn}(\omega_u) & \text{for } \omega_u \neq 0, \\ [-T_{su} + \Delta T_{su}, T_{su} + \Delta T_{su}] & \text{for } \omega_u = 0, \end{cases} \\
T_{cu}(\omega_u) &= T_{su} + \Delta T_{su} \text{sgn}(\omega_u) + b_u |\omega_u| + \Delta b_u \omega_u, \\
T_{fl}(\omega_l) &\in \begin{cases} T_{cl}(\omega_l) \text{sgn}(\omega_l) & \text{for } \omega_l \neq 0, \\ [-T_{sl}, T_{sl}] & \text{for } \omega_l = 0, \end{cases} \\
T_{cl}(\omega_l) &= T_{cl} + (T_{sl} - T_{cl}) e^{-|\omega_l/\omega_{sl}|^{\delta_{sl}}} + b_l |\omega_l|, \\
\omega_l &= \omega_u + \dot{\alpha}.
\end{aligned} \tag{4.1}$$

As already described in Section 3.2.1,  $T_{cl}$  and  $T_{sl}$  represent the Coulomb friction and static friction levels, respectively,  $\omega_{sl}$  is the Stribeck velocity,  $\delta_{sl}$  the Stribeck shape parameter and  $b_l$  the viscous friction coefficient. For the estimation of the parameters of the friction model, we use the already estimated parameters (3.25), (3.28) and (3.33). Next, a quasi-random signal, shown in figure 3.13(a), is applied to the experimental set-up. Then, using a nonlinear least-squares technique we ensure a close match between the experimentally obtained angular position  $\hat{\theta}_l$  and the corresponding model prediction  $\theta_l$  (i.e. we minimize the performance index (3.32)). This leads to the following parameter estimates for the friction model at the lower disc:

$$\begin{aligned}
T_{sl} &= 0.2781 \text{ N m}, \quad T_{cl} = 0.0473 \text{ N m}, \quad \omega_{sl} = 1.4302 \frac{\text{rad}}{\text{s}}, \\
\delta_{sl} &= 2.0575, \quad b_l = 0.0105 \frac{\text{N m s}}{\text{rad}}.
\end{aligned} \tag{4.2}$$

The estimated friction torque is shown in figure 4.1. In such a friction model, positive damping is present for very small angular velocities, see figure 4.1(b), for higher angular velocities, negative damping occurs and for even higher angular velocities positive damping is again present in the friction (a humped friction model). The measured and simulated angular positions obtained for the applied quasi-random signal are shown in figure 4.2, and the related criterium (3.22) is  $R_{\theta_l}^2 = 0.9991$ . A model validation is performed for the input signal shown in figure 3.13(b) and the appropriate measured and simulated responses are shown in figure 4.3 with  $R_{\theta_l}^2 = 0.9702$ . The comparison between the responses of the experimental set-up and estimated model indicates the good quality of the obtained parameter estimates.

To summarize, the parameters of the model (4.1) are given in table 4.1 and further in this chapter we use them as the referent values. Since the steady-state behaviour of the set-up is of interest, in the sequel we analyze the behaviour of the system described by (4.1) with the parameters in table 4.1.

## 4.2 Analysis of the Nonlinear Dynamic Behaviour

Since both equilibria (constant velocity at the upper and lower disc) and limit cycles (torsional vibrations at the lower disc) are observed in the experimental set-up, in this section we analyze these equilibrium points (sets) and limit cycles of the model as well as the related stability properties.

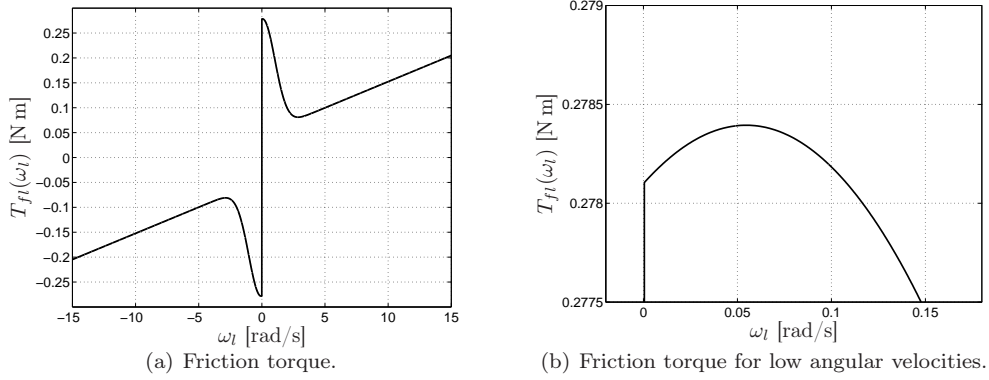


Figure 4.1: Estimated friction torque at the lower disc when ondina oil 68 and a 20.5 N normal force are applied.

Table 4.1: Estimated parameters of the set-up.

Parameter	unit	Estimated value
$J_u$	[kg m <sup>2</sup> ]	0.4765
$k_m$	[N m/V]	4.3228
$T_{su}$	[N m]	0.37975
$\Delta T_{su}$	[N m]	-0.00575
$b_u$	[kg m <sup>2</sup> /rad s]	2.4245
$\Delta b_u$	[kg m <sup>2</sup> /rad s]	-0.0084
$k_\theta$	[N m/rad]	0.0775
$J_A$	[kg m <sup>2</sup> ]	0.0414
$T_{sl}$	[N m]	0.2781
$T_{cl}$	[N m]	0.0473
$\omega_{sl}$	[rad/s]	1.4302
$\delta_{sl}$	[-]	2.0575
$b_l$	[kg m <sup>2</sup> /rad s]	0.0105

### 4.2.1 Equilibria and Related Stability Analysis

#### Equilibrium Points and Equilibrium Sets

In the equilibrium points, the time derivatives of all variables in (4.1) are zero, i.e.  $\dot{\omega}_u = \ddot{\alpha} = \dot{\alpha} = 0$ , for  $u = u_c$ , with  $u_c$  a constant. If we insert  $(\omega_u, \alpha) = (\omega_{eq}, \alpha_{eq})$  into (4.1), then  $\omega_{eq}$  and  $\alpha_{eq}$  should satisfy

$$\begin{aligned} -k_\theta \alpha_{eq} + T_{fu}(\omega_{eq}) &= k_m u_c, \\ T_{fl}(\omega_{eq}) + k_\theta \alpha_{eq} &= 0, \end{aligned} \quad (4.3)$$

which is equivalent to the following system of equations:

$$\begin{aligned} T_{fu}(\omega_{eq}) + T_{fl}(\omega_{eq}) &= k_m u_c, \\ T_{fl}(\omega_{eq}) + k_\theta \alpha_{eq} &= 0. \end{aligned} \quad (4.4)$$

Moreover, it also holds that  $\omega_l = \omega_{eq}$  in steady-state, since  $\omega_l = \omega_u + \dot{\alpha}$ . Then, since friction torques  $T_{fu}(\omega_u)$  and  $T_{fl}(\omega_l)$  are both modelled using a set-valued friction

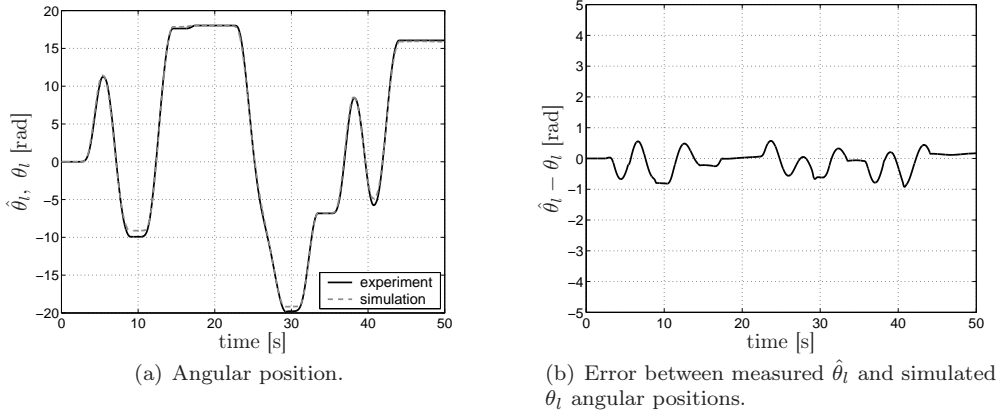


Figure 4.2: Estimation signals at the lower disc obtained for the quasi-random input voltage shown in figure 3.13(a):  $R_{\hat{\theta}_l}^2 = 0.9991$ .

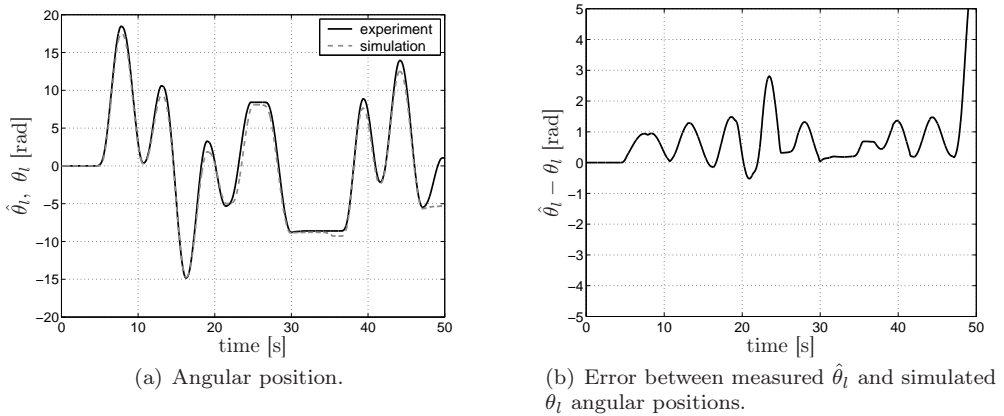


Figure 4.3: Validation signals at the lower disc obtained for the input voltage shown in figure 3.13(b):  $R_{\hat{\theta}_l}^2 = 0.9702$ .

model, the following two cases should be considered:

- equilibrium points for  $\omega_{eq} \neq 0$ , i.e. both the lower and the upper disc rotate with the same constant angular velocity  $\omega_{eq}$  and
- equilibrium points for  $\omega_{eq} = 0$ , i.e. both the lower and the upper disc stand still.

For  $\omega_{eq} > 0$ ,  $T_{fu}(\omega_{eq}) = T_{cu}(\omega_{eq})$  and  $T_{fl}(\omega_{eq}) = T_{cl}(\omega_{eq})$  (see (4.1)). Therefore, such equilibrium points satisfy the following set of nonlinear algebraic equations

$$\begin{aligned} k_m u_c - (T_{su} + \Delta T_{su}) - (b_u + \Delta b_u) \omega_{eq} - T_{cl}(\omega_{eq}) &= 0, \\ \alpha_{eq} &= -\frac{T_{cl}(\omega_{eq})}{k_\theta}. \end{aligned} \quad (4.5)$$

From (4.1), the first algebraic equation of (4.5) and since  $\omega_{eq} > 0$ , it can be concluded that the system exhibits only an equilibrium point for

$$u_c > u_{\mathcal{E}p}, \quad (4.6)$$

with

$$u_{\mathcal{E}p} = \frac{T_{su} + \Delta T_{su} + T_{sl}}{k_m}. \quad (4.7)$$

In general, the first equation in (4.4) can have more than one solution. However, for the estimated parameters given in table 4.1, it holds that

$$-b_u - \Delta b_u - \left. \frac{dT_{cl}}{d\omega_l} \right|_{\omega_l = \omega_{eq}} \leq 0, \quad \forall \omega_{eq} > 0, \quad (4.8)$$

which means that the system has only one equilibrium point for a given  $u_c > u_{\mathcal{E}p}$  ( $\omega_{eq} > 0$ ).

In a similar way, for  $\omega_{eq} < 0$ , it follows that (4.1) has one equilibrium point which is a solution of

$$\begin{aligned} k_m u_c + (T_{su} - \Delta T_{su}) - (b_u - \Delta b_u) \omega_{eq} + T_{cl}(\omega_{eq}) &= 0, \\ \alpha_{eq} &= \frac{T_{cl}(\omega_{eq})}{k_\theta}, \end{aligned} \quad (4.9)$$

for

$$u_c < u_{\mathcal{E}n}, \quad (4.10)$$

with

$$u_{\mathcal{E}n} = -\frac{T_{su} - \Delta T_{su} + T_{sl}}{k_m}. \quad (4.11)$$

The equilibrium points (sets) for  $\omega_{eq} = 0$  exist only when the input voltage satisfies the condition

$$u_{\mathcal{E}n} \leq u_c \leq u_{\mathcal{E}p}. \quad (4.12)$$

Then, from (4.3) the following can be derived:

$$\begin{aligned} \alpha_{eq} &\in \left[ \frac{-k_m u_c - (T_{su} - \Delta T_{su})}{k_\theta}, \frac{-k_m u_c + (T_{su} + \Delta T_{su})}{k_\theta} \right] \text{ and} \\ \alpha_{eq} &\in \left[ \frac{-T_{sl}}{k_\theta}, \frac{T_{sl}}{k_\theta} \right]. \end{aligned} \quad (4.13)$$

Consequently, it can be concluded that when (4.12) is satisfied, equilibrium points are such that  $(\omega_{eq}, \alpha_{eq}) \in \mathcal{E}$ , where  $\mathcal{E}$  is defined by

$$\mathcal{E} = \left\{ (\omega_{eq}, \alpha_{eq}) \in \mathbb{R}^2 \mid \omega_{eq} = 0, \alpha_{eq} \in \left[ -\frac{T_{sl}}{k_\theta}, \frac{T_{sl}}{k_\theta} \right] \cap [\alpha_1, \alpha_2] \right\},$$

with

$$\alpha_1 = \frac{-k_m u_c - (T_{su} - \Delta T_{su})}{k_\theta}, \quad \alpha_2 = \frac{-k_m u_c + (T_{su} + \Delta T_{su})}{k_\theta},$$

i.e.  $\mathcal{E}$  can also be described by

$$\mathcal{E} = \{ (\omega_{eq}, \alpha_{eq}) \in \mathbb{R}^2 \mid \omega_{eq} = 0, \alpha_{eq} \in [\alpha_{min}, \alpha_{max}] \}, \quad (4.14)$$

with

$$\begin{aligned}\alpha_{min} &= \max\left(\frac{-k_m u_c - (T_{su} - \Delta T_{su})}{k_\theta}, -\frac{T_{sl}}{k_\theta}\right), \\ \alpha_{max} &= \min\left(\frac{-k_m u_c + (T_{su} + \Delta T_{su})}{k_\theta}, \frac{T_{sl}}{k_\theta}\right).\end{aligned}\quad (4.15)$$

### Analysis of Local Stability Properties

In order to obtain local stability conditions for the equilibrium points, we use Lyapunov's indirect method which is presented in Section 2.2.1 (Theorem 2.1). The method can be applied only when

$$u_c \in (-\infty, u_{\mathcal{E}n}) \cup (u_{\mathcal{E}p}, \infty), \quad (4.16)$$

i.e. for  $\omega_{eq} \neq 0$ . In order to obtain the stability conditions when (4.6) is satisfied ( $\omega_{eq} > 0$ ), the nonlinear system (4.1) is linearized around the equilibrium point. Then, according to the Routh-Hurwitz criterion the equilibrium point of the system is locally asymptotically stable if and only if all the parameters  $R_i$ ,  $i = 1, 2, 3, 4$ , defined by

$$\begin{aligned}R_1 &= J_u J_A, \\ R_2 &= d_l J_u + (b_u + \Delta b_u) J_A, \\ R_3 &= d_l^2 J_u (b_u + \Delta b_u) + d_l J_u^2 k_\theta + d_l (b_u + \Delta b_u)^2 J_A + (b_u + \Delta b_u) J_A^2 k_\theta, \\ R_4 &= k_\theta ((b_u + \Delta b_u) + d_l),\end{aligned}\quad (4.17)$$

have the same sign [Mihajlović et al., 2005a]. In (4.17),  $d_l$  represents the friction damping present at the lower disc when  $\omega_l = \omega_{eq}$ , i.e.

$$d_l = \left. \frac{dT_{cl}}{d\omega_l} \right|_{\omega_l = \omega_{eq}}. \quad (4.18)$$

From (4.17) it follows that the equilibrium point of the system is locally asymptotically stable when

$$d_l > d_{min}, \quad (4.19)$$

with

$$\begin{aligned}d_{min} &= \max(d_1, d_2, d_3) \\ d_1 &= -\frac{(b_u + \Delta b_u) J_A}{J_u}, \\ d_2 &= \frac{-J_u^2 k_\theta - (b_u + \Delta b_u)^2 J_A + \sqrt{(J_u^2 k_\theta + (b_u + \Delta b_u)^2 J_A)^2 - 4 J_u J_A^2 k_\theta (b_u + \Delta b_u)^2}}{2 J_u (b_u + \Delta b_u)}, \\ d_3 &= -b_u - \Delta b_u.\end{aligned}\quad (4.20)$$

Then, for the system parameters given in table 4.1, it is obtained that

$$d_{min} = \frac{-J_u^2 k_\theta - (b_u + \Delta b_u)^2 J_A + \sqrt{(J_u^2 k_\theta + (b_u + \Delta b_u)^2 J_A)^2 - 4 J_u J_A^2 k_\theta (b_u + \Delta b_u)^2}}{2 J_u (b_u + \Delta b_u)}, \quad (4.21)$$

i.e.  $d_{min} = -0.00124 \frac{\text{kg m}}{\text{rad s}}$ . The same analysis can be performed when (4.10) is satisfied ( $\omega_{eq} < 0$ ).

In order to analyze (non-local) stability properties of the equilibrium points and sets, we use Lyapunov's stability theorem (Theorem 2.2 in Section 2.2.1).

### Analysis of Global Stability Properties

In order to apply the Lyapunov's stability theorem, the following Lyapunov candidate function is considered [Miha]lović et al., 2005a]:

$$V_t(\mathbf{x}_t, \mathbf{x}_{teq}) = \frac{1}{2}k_\theta(\alpha - \alpha_{eq})^2 + \frac{1}{2}J_u(\omega_u - \omega_{eq})^2 + \frac{1}{2}J_A(\omega_u + \dot{\alpha} - \omega_{eq})^2, \quad (4.22)$$

where  $\mathbf{x}_t$  and  $\mathbf{x}_{teq}$  represents the states and equilibrium point of the system (4.1), i.e.

$$\mathbf{x}_t = [\omega_u \quad \alpha \quad \dot{\alpha}]^T, \quad \mathbf{x}_{teq} = [\omega_{eq} \quad \alpha_{eq} \quad 0]^T. \quad (4.23)$$

Then, according to (4.1), the time derivative of  $V_t$  obeys:

$$\begin{aligned} \dot{V}_t(\mathbf{x}_t, \mathbf{x}_{teq}) = & -(\omega_u - \omega_{eq})(T_{fu}(\omega_u) - T_{fu}(\omega_{eq})) \\ & -(\omega_u + \dot{\alpha} - \omega_{eq})(T_{fl}(\omega_u + \dot{\alpha}) - T_{fl}(\omega_{eq})). \end{aligned} \quad (4.24)$$

For the sake of simplicity, we replace  $\omega_u + \dot{\alpha}$  by  $\omega_l$  in expressions (4.22) and (4.24) when analyzing the (non-local) stability properties of the equilibrium points and sets.

According to Lyapunov's stability theorem, in order to have an (asymptotically) stable equilibrium,  $\dot{V}_t(\mathbf{x}_t, \mathbf{x}_{teq})$  should be negative (semi)definite. Since the friction torque at the upper disc is a monotonically increasing function (see figure 3.14), it follows that the following incremental sector condition is satisfied:

$$-(\omega_u - \omega_{eq})(T_{fu}(\omega_u) - T_{fu}(\omega_{eq})) \leq 0, \quad (4.25)$$

for every  $\mathbf{x}_t \in \mathbb{R}^3$  and  $\omega_{eq} \in \mathbb{R}$ . On the other hand, the friction torque at the lower disc  $T_{fl}(\omega_l)$  is not a monotonically increasing function, as is the case shown in figure 4.1. Consequently, the following condition does not hold for every  $\mathbf{x}_t \in \mathbb{R}^3$  and  $\omega_{eq} \in \mathbb{R}$ :

$$-(\omega_l - \omega_{eq})(T_{fl}(\omega_l) - T_{fl}(\omega_{eq})) \leq 0. \quad (4.26)$$

Nevertheless, one should realize that the friction torque at the lower disc can change (due to changing temperature, lubrication conditions, contact materials and geometry). Therefore, in the sequel we will discuss stability properties of equilibrium points and sets for the following possible friction situations at the lower disc:

1. the friction model  $T_{fl}(\omega_l)$  is a monotonically increasing function (see figure 4.4(a)),
2. the friction model exhibits a region of negative damping and a region of positive damping for very small and for very high velocities (so-called humped friction model as shown in figures 4.5(a) and 4.5(c)),
3. the friction model exhibits the Stribeck effect and positive damping exists only for high velocities (as shown in figure 4.6(a)).

For all types of friction situations, mentioned above, the following can be concluded. When condition (4.16) is satisfied ( $\omega_{eq} \neq 0$ ), then isolated equilibrium points represent the solution of the system of algebraic equations (4.5) for  $\omega_{eq} > 0$ , or the solution of (4.9) for  $\omega_{eq} < 0$ . Moreover, for  $\omega_{eq} = 0$  the equilibrium points  $\mathbf{x}_{teq}$  are such that they jointly constitute an equilibrium set  $\mathcal{E}_t$  described with:

$$\mathcal{E}_t = \{\mathbf{x}_t \in \mathbb{R}^3 \mid \omega_u = \dot{\alpha} = 0, \alpha \in [\alpha_{min}, \alpha_{max}]\}, \quad (4.27)$$

( $\alpha_{min}$  and  $\alpha_{max}$  are defined by (4.15)).

Let us now discuss, for each of the friction models mentioned above, the stability properties of the isolated equilibrium points and the equilibrium sets of the system (for detailed stability proofs the reader is referred to Appendix B):

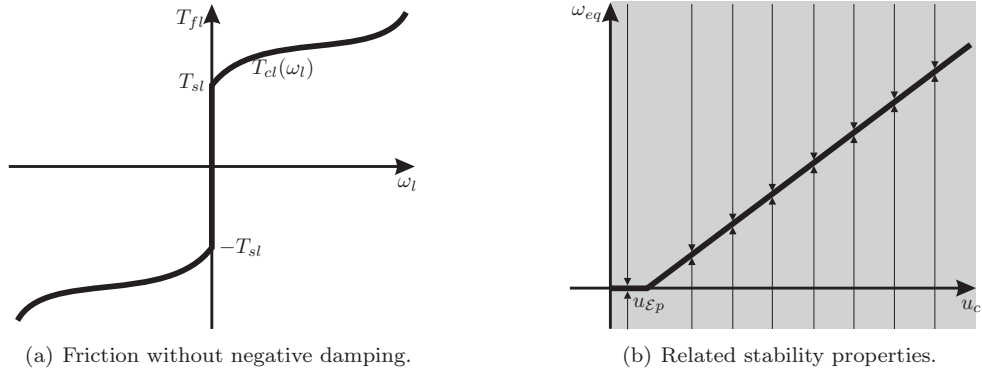


Figure 4.4: A friction model  $T_{fl}(\omega_l)$  without negative damping and graphical representation of stability properties of related equilibrium points and sets.

1. If the friction torque is as shown in figure 4.4(a), we prove in Appendix B that the equilibrium set  $\mathcal{E}_t$ , described with (4.27), and the isolated equilibrium points of the system are globally asymptotically stable. These stability properties are schematically depicted in figure 4.4(b) by the arrows and a gray area spanning the entire range in vertical direction indicates global asymptotic stability.
2. The equilibrium set  $\mathcal{E}_t$  is also globally asymptotically stable when the friction torque  $T_{fl}(\omega_l)$  is as shown in figure 4.5(a), since  $T_{sl} < |T_{fl}(\omega_l)|$ ,  $\forall \omega_l \neq 0$ . However, this is not the case for all isolated equilibrium points when  $\omega_{eq} \neq 0$ . In Appendix B, we prove that for  $\omega_{eq} > 0$  the equilibrium points are locally asymptotically stable when

$$u_c \in (u_{g1}, u_{s1}) \cup (u_{s2}, u_{g2}), \quad (4.28)$$

and they are globally asymptotically stable when

$$u_c \in (u_{\mathcal{E}p}, u_{g1}) \cup (u_{g2}, \infty), \quad (4.29)$$

where  $u_{\mathcal{E}p}$  is defined by (4.7),

$$u_{s1} = \frac{T_{cu}(\omega_{s1}) + T_{cl}(\omega_{s1})}{k_m}, \quad u_{s2} = \frac{T_{cu}(\omega_{s2}) + T_{cl}(\omega_{s2})}{k_m}, \quad (4.30)$$

$$\left. \frac{dT_{cl}}{d\omega_l} \right|_{\omega_l \in \{\omega_{s1}, \omega_{s2}\}} = d_{min},$$

( $d_{min}$  is defined by (4.20)). Moreover, in (4.28) and (4.29),

$$u_{g1} = \frac{T_{cu}(\omega_{g1}) + T_{cl}(\omega_{g1})}{k_m}, \quad u_{g2} = \frac{T_{cu}(\omega_{g2}) + T_{cl}(\omega_{g2})}{k_m}, \quad (4.31)$$

where  $\omega_{g1}$  and  $\omega_{g2}$  are chosen such that  $T_{cl}(\omega_{g1}) = T_{cl}(\omega_{e1})$  and  $T_{cl}(\omega_{g2}) = T_{cl}(\omega_{e2})$ , respectively, with

$$\left. \frac{dT_{cl}}{d\omega_l} \right|_{\omega_l \in \{\omega_{e1}, \omega_{e2}\}} = 0, \quad \omega_{e1} < \omega_{e2}, \quad (4.32)$$

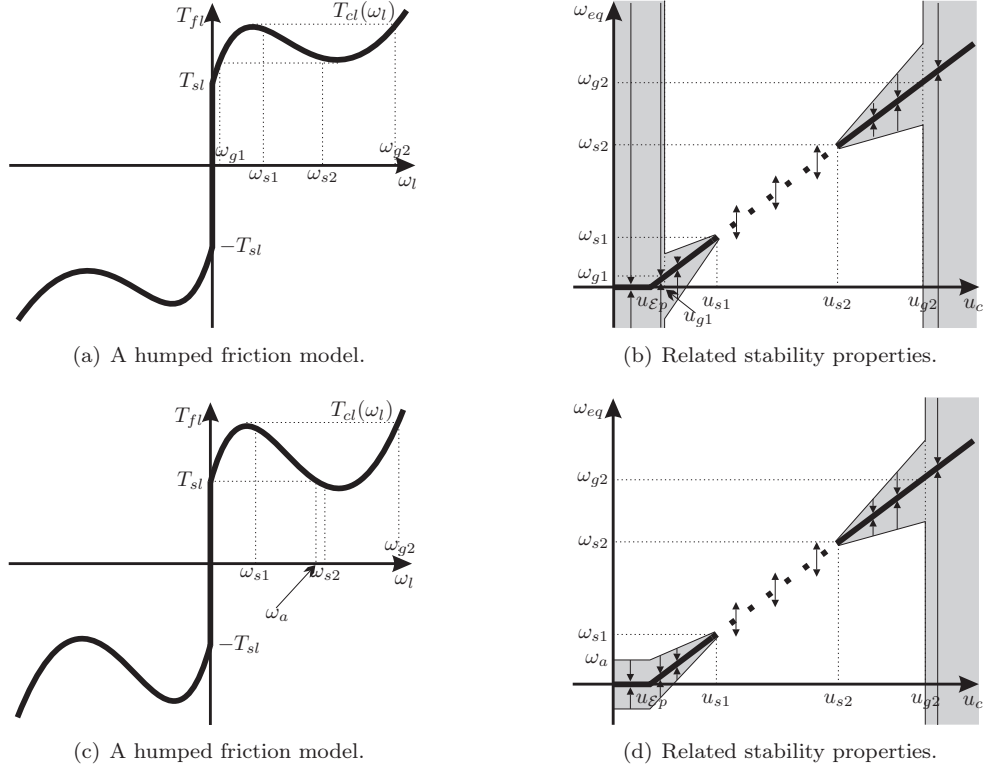


Figure 4.5: Various types of a humped friction model  $T_{fl}(\omega_l)$  and graphical representation of stability properties of related equilibrium points and sets.

(see figure 4.5 and figure B.1 in Appendix B). Moreover, for locally stable equilibria we have a "semi-global" region of attraction. The graphical interpretation of this result is presented in figure 4.5(b). Moreover, in Appendix B we also conclude that if  $u_c$  satisfies (4.28) and is moved towards to  $u_{s1}$  or  $u_{s2}$  then the basin of attraction of the equilibrium point decreases. Similar conditions can be derived for  $\omega_{eq} < 0$ .

If the friction torque is as shown in figure 4.5(c), then the equilibrium set  $\mathcal{E}_t$  is locally asymptotically stable (see for the proof Appendix B) and the isolated equilibrium points are globally asymptotically stable when  $u_c \geq u_{g2}$ , where  $u_{g2}$  is defined by (4.31). For locally stable equilibrium sets and points we have a "semi-global" region of attraction. The graphical interpretation of this result is presented in figure 4.5(d). Similar conditions can be derived for  $\omega_{eq} < 0$ .

3. If the friction torque  $T_{fl}(\omega_l)$  is as shown in figure 4.6(a), the isolated equilibrium points are globally asymptotically stable when  $u_c \geq u_{g2}$  ( $u_{g2}$  is defined by (4.31)) for  $\omega_{eq} > 0$  and similar results hold when  $\omega_{eq} < 0$ .

When  $\omega_{eq} = 0$ , then, since  $d_{l0} < 0$ , with

$$d_{l0} = \left. \frac{dT_{cl}}{d\omega_l} \right|_{\omega_l=0^+}, \quad (4.33)$$



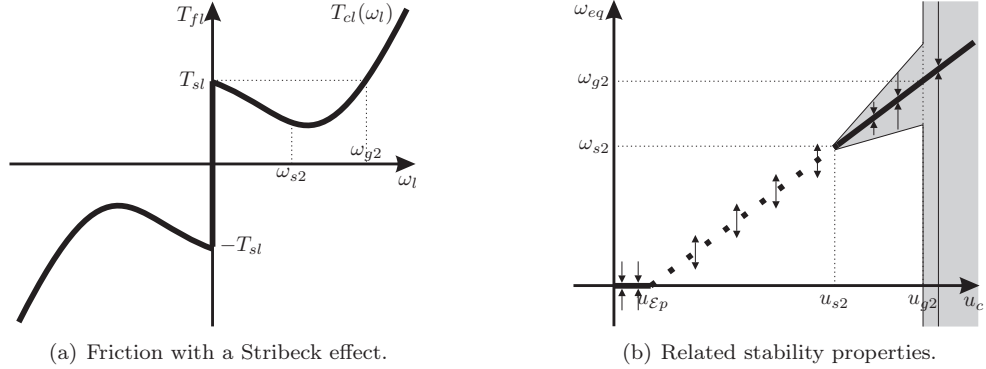


Figure 4.6: A friction model  $T_{fl}(\omega_l)$  with a Stribeck effect and graphical representation of stability properties of related equilibrium points and sets

we can only prove that every equilibrium point  $\mathbf{x}_{teq} \in \mathcal{E}_t$  is stable except the equilibrium points for which  $\alpha_{eq} = -T_{sl}/k_\theta$  or  $\alpha_{eq} = T_{sl}/k_\theta$ , which are present only if  $\alpha_{min} = -T_{sl}/k_\theta$  or  $\alpha_{max} = T_{sl}/k_\theta$  in (4.15), respectively. Namely,  $\dot{V}_t(\mathbf{x}_t, \mathbf{x}_{teq})$  is not negative semidefinite in the neighborhood of such equilibria. However, using Lyapunov's indirect method we have already concluded that equilibrium points, for  $\omega_{eq} \neq 0$  are locally stable when (4.19) holds. Therefore, for our system, all such equilibrium points which are in the neighborhood of the sticking region are locally asymptotically stable even when  $d_{l0}$  is negative (i.e. when  $d_{l0} > d_{min}$ , with  $d_{min}$  defined with (4.20)). Consequently, it can also be expected that equilibrium point  $\mathbf{x}_{teq}$  for which  $\alpha_{eq} \in \{-T_{sl}/k_\theta, T_{sl}/k_\theta\}$  is also stable in the sense of Lyapunov for  $d_{l0} > d_{min}$ . However, a similar conclusion cannot be derived when  $d_{l0} \leq d_{min}$ . Therefore, we cannot provide a definite conclusion about stability properties of the equilibrium set  $\mathcal{E}_t$ .

### Equilibrium Branches

Since the estimated friction is described as shown in figure 4.5(c) (compare that figure with figure 4.1), in the sequel we consider that friction situation. Based on the performed stability analysis of the isolated equilibria and equilibrium sets, in figure 4.7 a sketch of the equilibrium branches for different constant input voltages  $u_c$  is plotted. Although we are particularly interested in the behaviour of the velocity of the lower disc for different constant input voltages (figure 4.7(b)), in figure 4.7(a) also the phase lag of the upper disc with respect to the lower disc  $-\alpha_{eq}$  ( $\alpha = \theta_l - \theta_u$ ) is shown for different  $u_c$ . We have chosen to show  $-\alpha_{eq}$  (in stead of  $\alpha_{eq}$ ) since  $-\alpha_{eq} = T_{cl}(\omega_{eq})/k_\theta$  and, thus, this has a similar form as the friction torque  $T_{fl}(\omega_l)$  for nonzero velocities.

In figure 4.7, solid lines represent stable and dotted lines unstable equilibrium branches. If we use the results of the steady-state analysis of system (4.1) for  $u = u_c \geq 0$ , with  $u_c$  constant, and take into account that the friction torque, present at the lower disc, is of the type shown in figure 4.8, the following can be concluded:

- For  $u_c \leq u_{\epsilon p}$ , with  $u_{\epsilon p}$  given by (4.7), the system is in the stick phase in steady-state; i.e. the system has a locally asymptotically stable equilibrium set described by (4.14) and (4.15) (equilibrium branch  $e_1$  in figure 4.7). Namely,

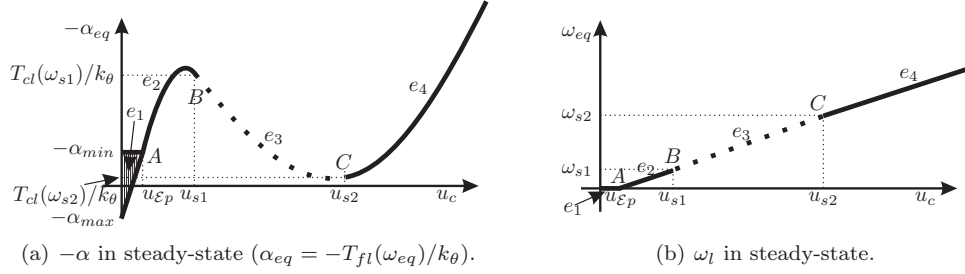
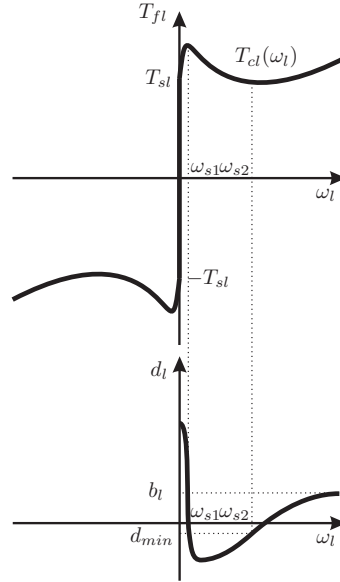


Figure 4.7: A sketch of equilibrium branches of the set-up.


 Figure 4.8: A sketch of the friction torque  $T_{fl}(\omega_l)$  with the friction damping  $d_l$  at the lower part of the set-up.

both the lower and the upper disc do not rotate since the input voltage is not large enough to overcome the static friction torques at the upper and lower disc at zero velocity. Moreover, from (4.14) and (4.15) it can be seen that if  $u_c$  increases, the size of equilibrium set  $\mathcal{E}_t$  decreases. Then, for  $u_c = u_{\mathcal{E}p}$  (point  $A$  in figure 4.7)  $\mathcal{E}_t$  becomes a locally asymptotically stable equilibrium point  $A$ .

- For  $u_c = u_{\mathcal{E}p}$  (point  $A$  in figure 4.7) no change of stability properties occurs, since the locally asymptotically stable equilibrium set (4.14) becomes the locally asymptotically stable equilibrium point  $A$ .
- The system has one equilibrium point for  $u_c > u_{\mathcal{E}p}$  since condition (4.8) is satisfied. Given the fact that the friction torque at the lower disc is as shown in figure 4.8, it can be concluded that a stable equilibrium branch  $e_2$  appears (figure 4.7). Namely, for an increasing (but constant)  $u_c > u_{\mathcal{E}p}$  the system leaves the stick phase, the steady-state velocity at the lower disc increases, the friction damping  $d_l$  of the friction torque at the lower disc is positive and starts

to decrease (see figure 4.8). For a certain angular velocity  $\omega_{eq} = \omega_{s1}$ , the friction damping  $d_l = d_{min}$  and the equilibrium point becomes unstable (see conditions (4.19) and (4.20)). From (4.30), the corresponding input voltage  $u_c = u_{s1}$  can be found for given  $\omega_{eq} = \omega_{s1}$  (point  $B$  in figure 4.7). Therefore, for  $u_{\mathcal{E}p} < u_c < u_{s1}$  system has asymptotically stable equilibrium points (equilibrium branch  $e_2$  in figure 4.7). The global and local stability conditions have already been discussed in this section.

- If  $u_c$  increases from  $u_c = u_{s1}$ , the system has an unstable equilibrium point and the corresponding  $\omega_{eq}$  increases as well. Next, for a certain value of  $\omega_{eq}$  the friction damping  $d_l$  (which is negative) starts to increase and for  $\omega_{eq} = \omega_{s2}$  (see figure 4.8) and for  $u_c = u_{s2}$  (point  $C$  in figure 4.7),  $d_l$  reaches the value  $d_l = d_{min}$  and the equilibrium point becomes asymptotically stable again. Therefore, for  $u_{s1} < u_c < u_{s2}$  the system has an unstable equilibrium point (equilibrium branch  $e_3$  in figure 4.7).
- For  $u_c > u_{s2}$ , the system has both locally and globally asymptotically stable equilibrium points (equilibrium branch  $e_4$  in figure 4.7) depending on the value of  $u_c$  (see stability proof earlier in this section).
- For  $u_c = u_{s1}$  (point  $B$  in figure 4.7) and for  $u_c = u_{s2}$  (point  $C$  in figure 4.7) a change in stability properties occurs. Namely, a pair of complex conjugate eigenvalues, related to the linearisation of the nonlinear dynamics of (4.1) around the equilibrium point, crosses the imaginary axis to the right-half complex plane. Therefore, Hopf bifurcations occur at these points.

## 4.2.2 Bifurcation Diagram of the Set-Up

Here we analyze the steady-state behaviour of the estimated model. According to the previous analysis, Hopf bifurcation points occur for  $u_c = u_{s1}$  and  $u_c = u_{s2}$ . Next, using a path following technique in combination with a shooting method [Ascher et al., 1995; Parker and Chua, 1989], limit cycles are computed numerically for the estimated model of the system. The results are shown in a bifurcation diagram, with  $u_c$  as a bifurcation parameter, in figure 4.9. In those figures, the maximal and minimal values of  $\omega_l$  are plotted when a limit cycle is found. Floquet multipliers, corresponding to these limit cycles, are computed numerically and used to determine the local stability properties of these limit cycles. With respect to the obtained results, the following remarks can be made:

- From the bifurcation point  $B$  for  $u_c > u_{s1}$  an unstable equilibrium branch  $e_3$  arises (as discussed in this section). Moreover, from point  $B$  an unstable periodic branch  $p_1$  (see figure 4.9(b)) arises. The periodic branch  $p_1$  consists of unstable limit cycles without stick-slip, hence, point  $B$  represents a smooth subcritical Hopf bifurcation point [Khalil, 2000; Sastry, 1999; Strogatz, 2000].
- The unstable periodic branch  $p_1$  is connected to a locally stable periodic branch  $p_2$  at point  $D$ , which represents a fold bifurcation point. Since the periodic branch  $p_2$  consists of limit cycles which represent torsional vibrations with stick-slip (see figure 4.9(b)), point  $D$  represents a discontinuous fold bifurcation.

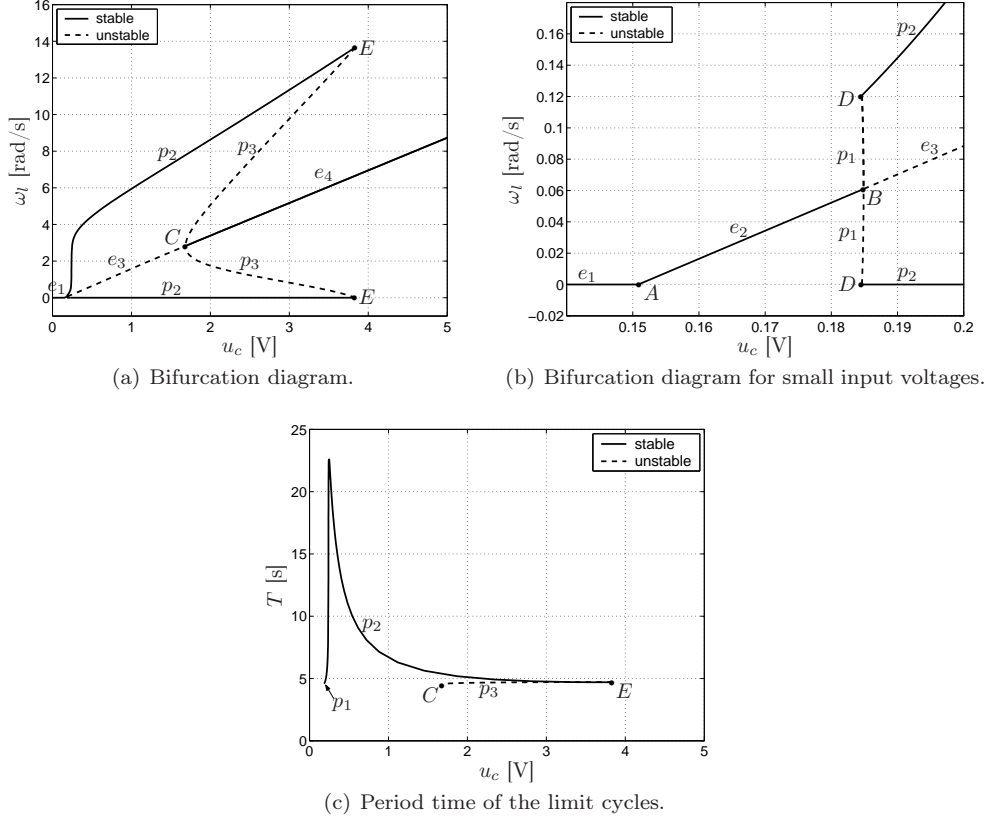


Figure 4.9: Bifurcation diagram of the experimental set-up when only torsional and no lateral vibrations are present.

- The periodic branch  $p_2$  consists only of locally stable limit-cycles with stick-slip, due to the non-smooth nonlinearities in the friction torque at the lower disc. For some higher constant input voltage  $u_c$  (point  $E$  in figure 4.9) the locally stable periodic branch  $p_2$  disappears again through a discontinuous fold bifurcation (see figure 4.9(a)). At this fold bifurcation point the stable periodic branch  $p_2$  merges with an unstable periodic branch  $p_3$ .
- The unstable periodic branch  $p_3$  is connected to the equilibrium branches  $e_3$  and  $e_4$  in the Hopf bifurcation point  $C$ . Moreover, in figure 4.9(a) point  $C$  represents a smooth subcritical Hopf bifurcation point.

The existence of the fold bifurcation point  $E$  is expected to appear, from the analysis of the global stability properties of equilibrium points (see figure 4.5(d)). Namely, using Lyapunov's indirect and direct method (Theorems 2.1 and 2.2 in Section 2.2.1) we conclude that the equilibrium points are locally asymptotically stable for  $u_{s2} < u_c < u_{g2}$  and are globally asymptotically stable for  $u_c > u_{g2}$ . Furthermore, we estimated numerically that for input voltages which are in the region between the Hopf bifurcation point  $C$  (for  $u_c = u_{s2}$ ) and the fold bifurcation point  $E$ , both equilibrium points (constant velocity at the lower disc) and limit cycles (torsional

vibrations) exist. Consequently,  $u_c = u_{g2}$  represents an estimate of the voltage where fold bifurcation point  $E$  occurs. However, since the value for  $u_{g2}$  is obtained using Lyapunov's direct method, and the method gives only sufficient conditions, the fold bifurcation points can appear for  $u_{s2} < u_c < u_{g2}$ .

### 4.2.3 The Influence of Friction Characteristics on the Steady-State Behaviour

Here we analyze how various friction characteristics influence the steady-state behaviour of the drill-string system. Hereto, we discuss the influence of various friction characteristics of  $T_{fi}(\omega_l)$  on the bifurcation diagram shown in figure 4.9, for the model of the system described by (4.1), with parameters estimates given in table 4.1.

#### Changes in the Static Friction Torque

In order to analyze the influence of the static friction level on the steady-state behaviour of the drill-string system (4.1) we consider the following friction torque at the lower disc:

$$T_{fi}(\omega_l) \in \begin{cases} (\Delta T_{sl} + T_{cl}(\omega_l))\text{sgn}(\omega_l) & \text{for } \omega_l \neq 0, \\ [- (T_{sl} + \Delta T_{sl}), T_{sl} + \Delta T_{sl}] & \text{for } \omega_l = 0. \end{cases} \quad (4.34)$$

where  $T_{cl}(\omega_l)$  represents the estimated (nominal) friction with parameters (4.2) and  $\Delta T_{sl}$  represent a change in the static friction level which is such that the friction at the lower part of the set-up remains dissipative, i.e.

$$(\Delta T_{sl} + T_{cl}(\omega_l)) \geq 0, \quad \forall \omega_l \in \mathbb{R} \setminus \{0\}. \quad (4.35)$$

Therefore, such friction torques are presented in figure 4.10(a), where  $\Delta T_{sl} > 0$  for the friction torque plotted with a dark-grey line and  $\Delta T_{sl} < 0$  for the friction torque plotted with a black line. The nominal friction model is depicted by the light-grey line. Related bifurcation diagrams are shown in figures 4.10(b), 4.10(c) 4.10(d) with matching colors. According to the analysis performed in Section 4.2.1 and from figure 4.10 the following can be concluded:

- If the static friction torque is lower (black line in figure 4.13(a)), then the value of input voltage  $u_{\mathcal{E}p}$  at which the lower disc starts to rotate is lower. This can be explained knowing that  $u_{\mathcal{E}p}$  is defined by (4.7).
- A lower static friction torque also influences the position of both Hopf bifurcation points (points  $B'$ ,  $B''$  and  $C'$ ,  $C''$  in figures 4.10(b), 4.10(c) and 4.10(d)). Note that the angular velocities  $\omega_{s1}$  and  $\omega_{s2}$  in (4.30), at which Hopf bifurcation points appear, do not change. However, for a lower static friction, the Hopf bifurcation points appear for lower voltages  $u_{s1}$  and  $u_{s2}$ , according to (4.30) and (4.34). Similarly, for a higher static static friction level, the Hopf bifurcation points shift to a higher voltages.
- From figure 4.10, we see that a lower static friction torque causes a higher angular velocity in steady-state  $\omega_{eq}$  (see figures 4.10(b), 4.10(c) and 4.10(c)). Namely, when static friction is lower, then the friction is also lower (see figure 4.10(a)), hence, the dissipation of the energy due to such friction is lower.

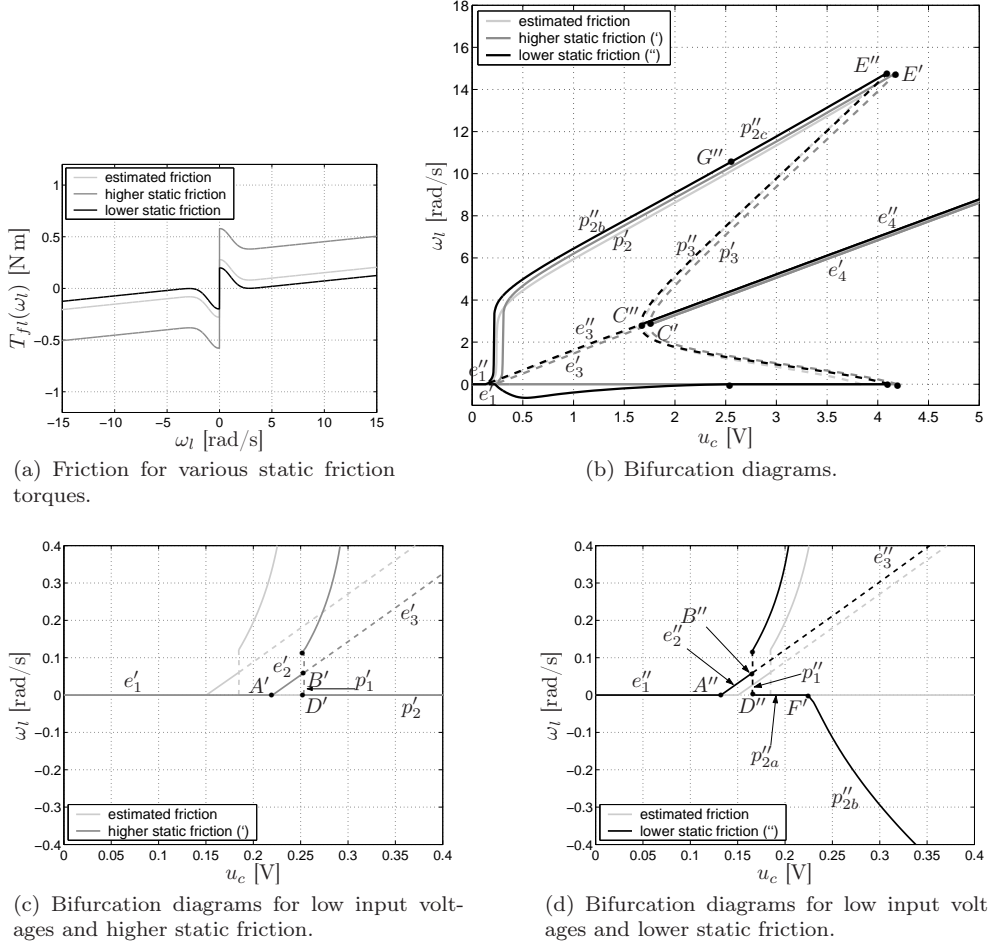


Figure 4.10: Friction torques at the lower disc for various static friction levels and related bifurcation diagrams.

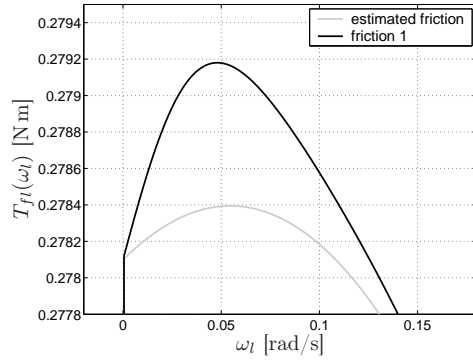
- We can also see that if the static friction torque is very low, then the lower disc can rotate both in positive and in negative direction for certain input voltages, as is the case for limit cycles depicted with the periodic branch  $p_{2b}''$ .
- Finally, according to the (local and global) stability proofs which we have discussed in Section 4.2.1, we can conclude that for all friction situations shown in figure 4.10(a) the angular velocity at which Hopf bifurcation points appear  $\omega_{s1}$  and  $\omega_{s2}$  (see (4.30)), and the angular velocity at which limit cycles cannot appear  $\omega_{g2}$  (see (4.31)) are identical. However, the corresponding input voltages  $u_{s1}$ ,  $u_{s2}$  and  $u_{g2}$  change slightly, due to the different static friction level, such that those voltages are lower for the friction with lower static friction (black line) and higher for higher static friction (dark-grey line). This is only the case according to the performed analysis for the Hopf bifurcations and not for the fold bifurcation points.

### Changes in the Low-Velocity Characteristics

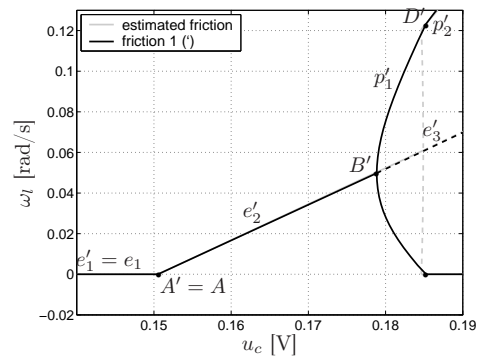
To analyze the influence of the low-velocity characteristics of  $T_{fi}(\omega_l)$  on the steady-state behaviour of the set-up (4.1), we consider various friction situations which differ only for very low angular velocities (the static friction level  $T_{sl}$  is the same), as shown in figure 4.11. Namely, the friction damping  $d_{l0}$ , defined by (4.33), is varied. For such friction torques, the related bifurcation diagrams are constructed. It appears that the obtained bifurcation diagrams differ only for very low velocities.

Since all friction situations have the same static friction  $T_{sl}$ , the equilibrium branches  $e'_1$ ,  $e''_1$  and  $e'''_1$  in figures 4.11(b), 4.11(d) and 4.11(f), respectively, are all identical to the branch  $e_1$  shown in figure 4.9(a). When we compare the obtained bifurcation diagrams the following can be concluded:

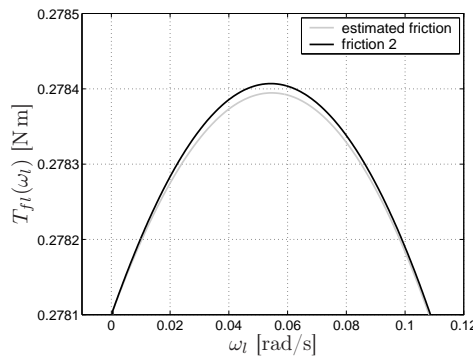
- If the friction damping at very low velocities  $d_{l0}$  is high enough ('friction 1' in figure 4.11(a)), then from bifurcation point  $B'$  a locally unstable equilibrium branch  $e'_3$  and a locally *stable* periodic branch  $p'_1$  arise through a *supercritical* Hopf bifurcation. The periodic branch  $p'_1$  consists of limit-cycles which represent torsional vibrations without stick-slip. Therefore, point  $B'$  represents a *smooth* supercritical Hopf bifurcation point. At point  $D'$  torsional vibrations with stick-slip appear (branch  $p'_2$  in figure 4.11(b)), due to the non-smooth nonlinearities in the friction torque at the lower disc. Since both  $p'_1$  and  $p'_2$  represent locally stable periodic branches, point  $D'$  is not considered to be a bifurcation point by many scientists (see for example [Leine, 2000; Leine and Nijmeijer, 2004]). However, some others classify this point as being a C-bifurcation point [Feigin, 1978, 1994] marking the transition from a limit cycle which does not touch the discontinuity to a limit cycle which touches the discontinuity.
- If the friction damping  $d_{l0}$  decreases ('friction 2' in figure 4.11(c)), then the stable periodic branch  $p'_1$  ('friction 1') splits into stable and unstable periodic branches, represented by  $p''_{1a}$  and  $p''_{1b}$  in figure 4.11(d), respectively. Consequently, an additional fold bifurcation point  $F''$  appears. Moreover, the C-bifurcation point  $D'$  becomes a discontinuous fold bifurcation point  $D''$  since at this point the unstable branch  $p''_{1b}$ , consisting of torsional vibrations without stick-slip, and the stable branch  $p''_2$ , consisting of torsional vibrations with stick-slip, are connected.
- For even lower  $d_{l0}$ , the fold bifurcation point  $F''$  and stable limit cycle  $p''_{1a}$  disappear (see light-grey line in figures 4.11(d) and 4.11(f)). Consequently, a smooth supercritical Hopf bifurcation point  $B''$  transforms to a smooth subcritical Hopf bifurcation point  $B$  in figure 4.9(b).
- If we decrease  $d_{l0}$  even further, then for  $d_{l0} = d_{min}$  ( $d_{min}$  represents the minimum value of friction damping at the lower disc for which locally stable equilibrium points appear (see expression (4.20))) torsional vibrations appear immediately when the system leaves the sticking region, i.e. for  $u_c > u_{\mathcal{E}_p}$  ( $u_{\mathcal{E}_p}$  is described by (4.7)). Consequently, the stable equilibrium branch  $e_2$ , the unstable periodic branch  $p_1$  and the bifurcation point  $B$  in figure 4.9(b) disappear and in point  $A'''$  a stable equilibrium branch  $e'''_1$ , an unstable equilibrium branch  $e'''_3$  and a stable periodic branch  $p'''_2$  are connected as shown in figure 4.11(f). A stable equilibrium branch  $e'''_1$  consists of locally stable equilibrium sets (which



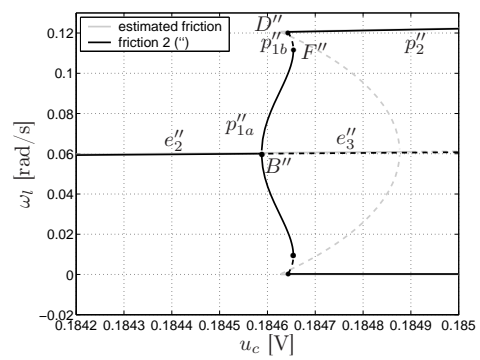
(a) Friction torque 1 with a positive damping for low angular velocities.



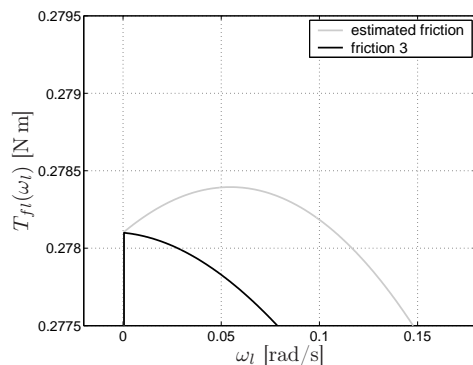
(b) Bifurcation diagram.



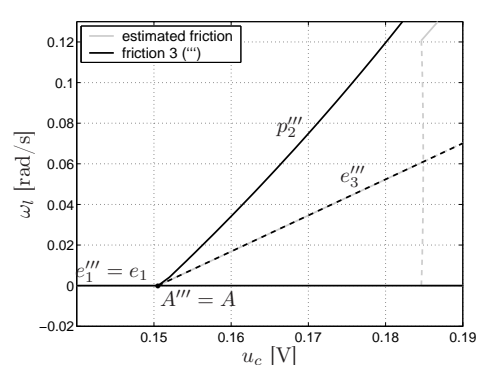
(c) Friction torque 2 with a positive damping for low angular velocities.



(d) Bifurcation diagram.



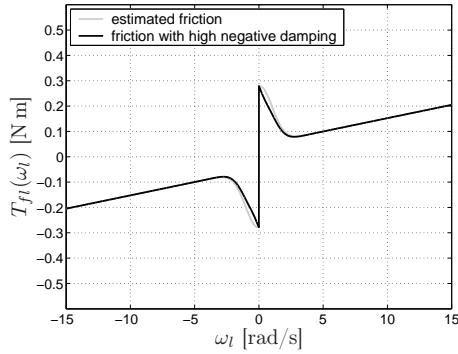
(e) Friction torque with a negative damping for low angular velocities:  $d_{l0} = d_{min}$ .



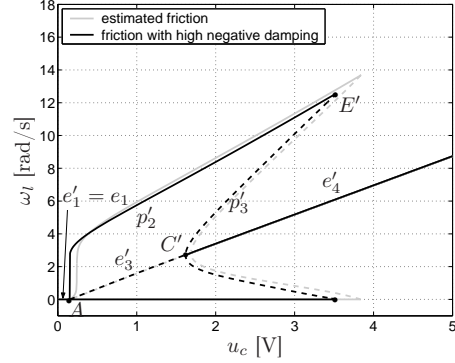
(f) Bifurcation diagram.

Figure 4.11: Friction torques at the lower disc for various low-velocity friction characteristics and related bifurcation diagrams.

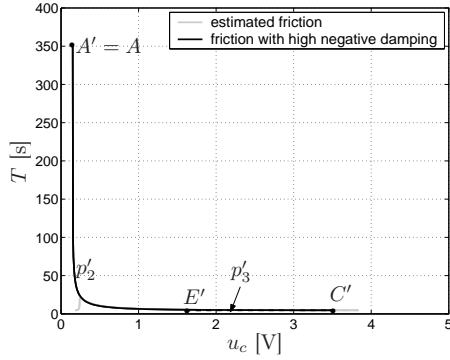




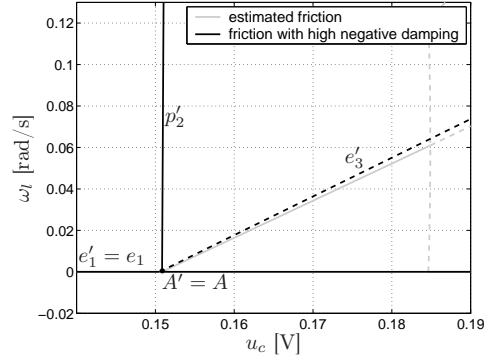
(a) Friction torque with a high negative damping at low velocities.



(b) Bifurcation diagram.



(c) Period time of the periodic solutions.

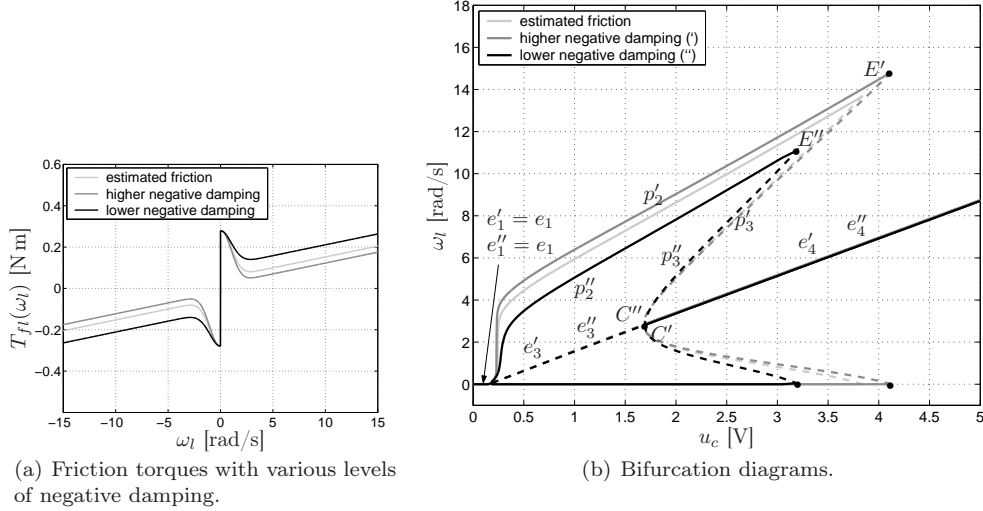


(d) Bifurcation diagram for low input voltages

Figure 4.12: Estimated friction torque and friction torque with high negative damping at low velocities with related bifurcation diagrams.

exist due to sticking phenomenon) and the periodic branch  $p_2'''$  consists of limit cycles which represent torsional vibrations with stick-slip. Therefore, point  $A'''$  represents a discontinuous bifurcation point. Moreover, such bifurcation point looks like a kind of discontinuous supercritical Hopf bifurcation point described in [Leine, 2000; Leine and Nijmeijer, 2004]. However, since  $e_1'''$  consists of equilibrium sets and of equilibrium point  $A'''$ , and not only of equilibrium points, this is not the case here.

If  $d_{l0}$  is even lower, as shown in figure 4.12(a), then the period time of the periodic solutions increases dramatically when  $u_c$  is close to the bifurcation point  $A'$  as shown in figure 4.12(c). However, for such low  $d_{l0}$ , the friction characteristic does not change only for very low velocities but the change is significant for even higher velocities. That is why we see that the position of the Hopf  $C'$  and the fold bifurcation point  $E'$  slightly differs from the position of the same bifurcation points in the nominal case. No other qualitative change appears with respect to the bifurcation diagram shown in figure 4.11(f) when  $d_{l0} = d_{min}$  ('friction 3'-case).



(a) Friction torques with various levels of negative damping.

(b) Bifurcation diagrams.

Figure 4.13: Friction torques with various negative damping levels and related bifurcation diagrams.

### Changes in the Negative Damping

In order to analyze the influence of various negative damping levels in  $T_{fl}(\omega_l)$  on the steady-state behaviour of the drill-string system (4.1), we consider two friction situations, as shown in figure 4.13(a), with respect to the estimated friction torque  $T_{fl}(\omega_l)$ . In both friction situations the static friction level  $T_{sl}$  is the same as in the estimated friction torque. The angular velocities  $\omega_{s1}$  and  $\omega_{s2}$  at which  $d_l = d_{min}$  are such that Hopf bifurcation points appear at approximately the same input voltages  $u_{s1}$  and  $u_{s2}$  (see expression (4.30) and figure 4.13(b)) as in the experimental set-up. However, in one friction situation the negative damping is higher (dark-grey line in figure 4.13(a)) and in the second friction situation the negative damping is lower (black line in figure 4.13(a)) than in the estimated friction torque (light-grey line in figure 4.13(a)). Related bifurcation diagrams together with the bifurcation diagram obtained for the estimated model of the set-up are shown in figure 4.13(b).

When we compare the obtained bifurcation diagrams the following can be concluded:

- If the negative damping is lower (black line in figure 4.13(a)), then torsional vibrations disappear for lower constant input voltages (compare the discontinuous fold bifurcation points  $E'$  and  $E''$  in figure 4.13(b)). In other words, if the negative damping in the friction torque at the lower disc is lower, then torsional vibrations can appear for a smaller range of input voltages  $u_c$ . This can be explained using the analysis of the global stability properties of the equilibrium points performed in Section 4.2.1. In that section, we have proven that for  $u_c > u_{g2}$  ( $u_{g2}$  is defined with (4.31) and figure 4.5(a)), equilibrium points of the system are globally asymptotically stable and, hence, no torsional vibrations can appear. We also conclude that  $u_{g2}$  does not represent the exact position of a fold bifurcation point, but only a conservative estimate of the constant voltage at which torsional vibrations disappear. If we determine  $u_{g2}$  for each friction

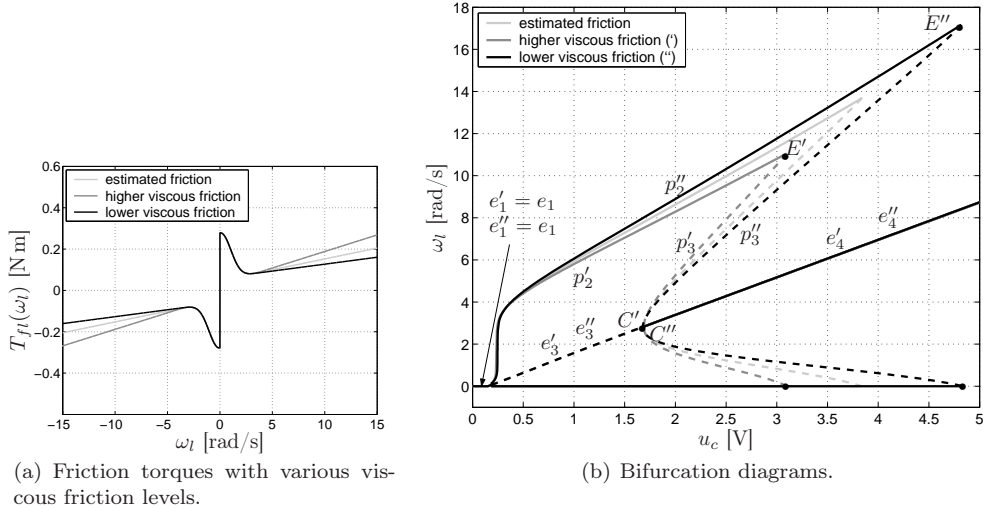


Figure 4.14: Friction torques with various viscous friction levels and related bifurcation diagrams.

situation shown in figure 4.13(a) we obtain that  $u'_{g2} = 13.9890$  V for the friction shown with the dark-grey line and  $u''_{g2} = 9.2941$  V for the friction shown with the black line. Indeed, figure 4.13 shows that if the range of angular velocities defined by  $\omega_l \in [\omega_{c2}, \omega_{g2}]$  decreases (increases) due to a lower (higher) negative damping level, then the region (in terms of input voltages) of co-existence decreases (increases).

- From figure 4.13 we see that lower negative damping causes a smaller amplitude of the torsional vibrations in the drill-string system. When the negative damping is lower, than the friction is higher (see figure 4.13(a)), hence, the dissipation of the energy due to such friction is higher and therefore, the amplitude of torsional vibrations is smaller.

### Changes in the Viscous Friction

In order to discuss the influence of various viscous friction levels in  $T_{fl}(\omega_l)$  on the steady-state behaviour of the drill-string system (4.1), we consider two friction situations in comparison with the estimated friction torque of the set-up as shown in figure 4.14(a). In all friction situations, the static friction level  $T_{sl}$  is the same and the friction torques differ only for high angular velocities  $\omega_l$ . In one friction situation, the viscous friction level is higher (dark-grey line in figure 4.14(a)) and, in the second friction situation, the viscous friction level is lower (black line in the same figure) than in the estimated friction torque (light-grey line). Related bifurcation diagrams together with the bifurcation diagram obtained for the estimated friction model of the set-up are shown in figure 4.14(b).

When we compare the obtained bifurcation diagrams, the following can be concluded:

- If the viscous friction level is lower, then the fold bifurcation point  $E''$  appears for higher constant input voltages: i.e. in such a case torsional vibrations can appear

for bigger range of input voltages  $u_c$  (compare discontinuous fold bifurcation points  $E'$  and  $E''$  in figure 4.14(b)). This can be explained in a similar fashion as we explained the influence of various negative damping levels on the bifurcation diagram using the analysis of global stability properties of equilibrium points performed in Section 4.2.1. Namely, when the viscous friction level is lower, then  $u_{g2}$  is higher (see expression (4.31) and figure 4.5) and, therefore, voltages at which no torsional vibrations can appear ( $u_c > u_{g2}$ ) are higher ( $u'_{g2} = 8,8290$  V for the friction plotted by the dark-grey line and  $u''_{g2} = 18.3156$  V for the friction plotted by the black line).

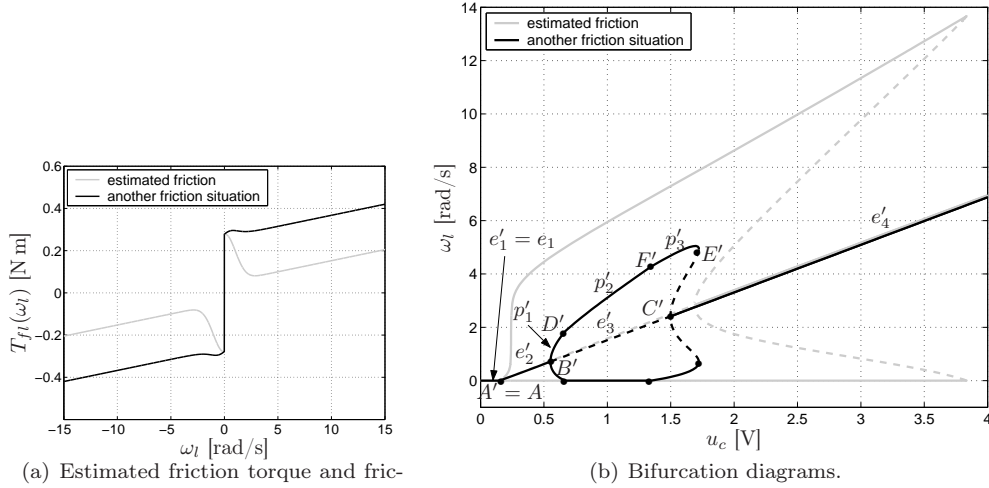
Based on the results presented in figures 4.13 and 4.14 it can be concluded that a subtle interplay of negative damping characteristics at low velocities and viscous friction at higher velocities determines the occurrence and the range of input voltages for which limit cycles occur.

- In figure 4.14(b), we observe that a lower viscous friction level causes higher amplitudes of the torsional vibrations in the system. Namely, when the viscous friction level is lower, then the friction is also lower (see figure 4.14(a)); hence, the dissipated energy is lower and the amplitude of torsional vibrations is higher.
- Stable equilibrium branches  $e'_2$  and  $e''_2$  and unstable periodic solutions  $p'_1$  and  $p''_1$  are also present in the bifurcation diagrams in figure 4.14(b) and these branches are almost identical to  $e_2$  and  $p_1$  in figure 4.9(b).

### Friction Situation when only Smooth Fold and Hopf Bifurcations Appear

Here, we discuss the steady-state behaviour of the system (4.1) when a friction torque as shown in figure 4.15(a) (with black line) is present at the lower part of the set-up. As a result of a steady-state analysis the bifurcation diagram in figure 4.15(b) is constructed. With respect to the obtained results the following remarks can be made:

- From bifurcation point  $B'$ , a locally unstable equilibrium branch  $e'_3$  arises (as discussed in Section 4.2.1) as well as a stable periodic branch  $p_1$ . Therefore, point  $B'$  represents a supercritical Hopf bifurcation point.
- Close to the bifurcation points, the periodic branch  $p'_1$  consists of locally stable limit-cycles which represent torsional vibrations *without* stick-slip. Therefore, bifurcation point  $B'$  represents a smooth supercritical Hopf bifurcation point.
- At point  $D'$ , torsional vibrations with stick-slip appear (branch  $p'_2$  in figure 4.15(b)), due to the non-smooth nonlinearities in the friction torque at the lower disc. Moreover, the periodic branch  $p'_2$  is also locally stable. As previously discussed  $D'$  is considered to be a C-bifurcation point [Feigin, 1978, 1994].
- For some higher constant input voltage  $u_c$  (point  $F'$  in figure 4.15(b)) torsional vibrations without stick-slip appear once more (locally stable periodic branch  $p'_3$ ) through a C-bifurcation point.
- Then, for even higher  $u_c$ , the locally stable periodic branch  $p'_3$  loses its stability and an unstable periodic branch appears (periodic branch  $p'_4$  in figure 4.15(b)).



(a) Estimated friction torque and friction torque with a positive damping for low velocities followed by a small region of negative damping.

(b) Bifurcation diagrams.

Figure 4.15: Estimated friction torque, friction torque with a positive damping for low velocities followed by a small region of negative damping and related bifurcation diagrams.

- The point where the stable periodic branch  $p'_3$  is connected to the unstable branch  $p'_4$  represents a smooth fold bifurcation point (point  $F'$  in figure 4.15(b)). The unstable periodic branch  $p'_4$  is connected to the equilibrium branches  $e'_3$  and  $e'_4$  in the Hopf bifurcation point  $C'$ . In figure 4.15(b) point  $C'$  represents a (smooth) subcritical Hopf bifurcation point.

If positive damping is present in  $T_{fl}(\omega_l)$  for very low velocities, this does not mean that torsional vibrations without stick-slip can appear in the set-up. For example, positive damping is present in the estimated friction model (see figure 4.1) but no torsional vibrations without stick-slip appear (see related bifurcation diagram in figure 4.9(b)). However, according to the results shown in figures 4.11(a) and 4.11(b) we see that such torsional vibrations appear when the damping at the lower velocities is high enough with respect to the following negative damping. Therefore, the combination of a low negative damping in the friction torque shown in figure 4.15(a) together with high positive damping at a very low velocities is responsible for the appearance of torsional vibrations without stick-slip.

## 4.3 Experimental Results

### 4.3.1 Validation of Steady-State Behaviour of the Set-Up

In order to check the validity of the obtained model of the drill-string set-up when ondina oil 68 is used as a lubrication fluid, a 20.5 N normal force is applied at the brake and the  $x$ - and  $y$ -constraints are fixed, experimental results are compared with the numerical results. As already mentioned earlier, the evidence about the predictive quality of the estimated model in steady-state is of great interest. Therefore, when

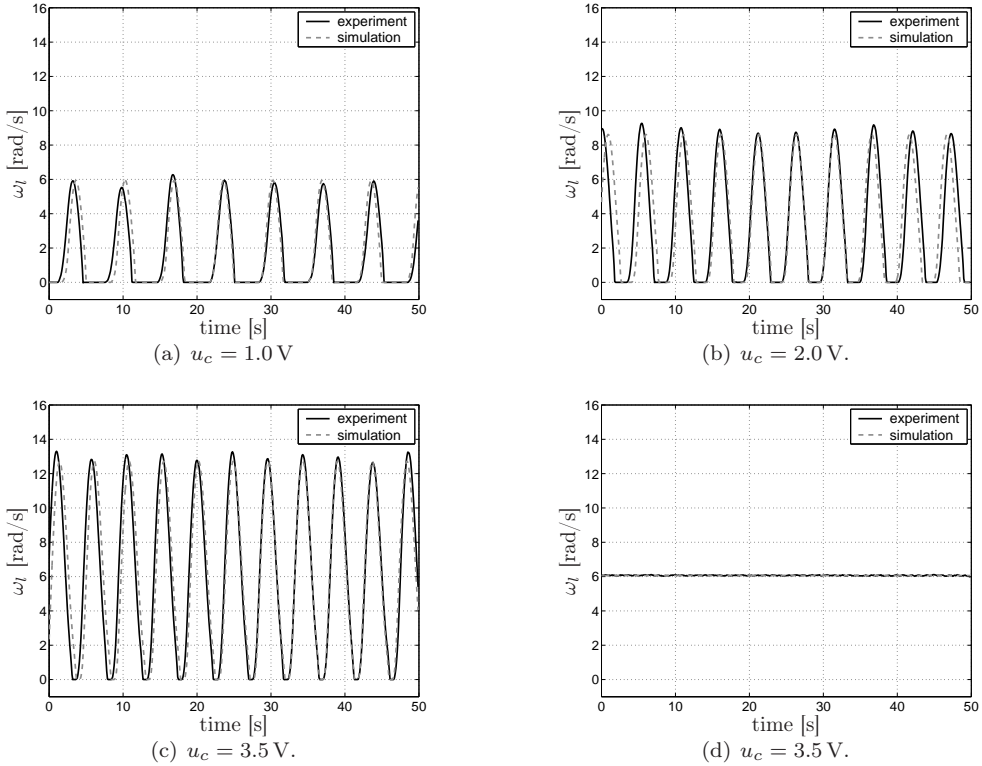


Figure 4.16: Experimental and simulated angular velocity at the lower disc for various constant input voltages and various initial conditions.

a constant voltage is applied at the input of the set-up, each experiment lasted long enough to guarantee that all transient effects have disappeared and the last 50 and sometimes 100 seconds (mainly for low input voltages) of the angular velocity signal  $\omega_l$  are recorded<sup>1</sup>. Some of the obtained results are shown in figure 4.16. In this figure, the experimental angular velocity (solid black line) and the angular velocity obtained using the estimated model (dashed grey line) in steady-state are shown for different constant input voltages. Namely, the signals presented in figures 4.16(a), 4.16(b) and 4.16(c) represent stick-slip limit-cycling (torsional vibrations) and figure 4.16(d) represents an equilibrium point. Clearly, the combination of figures 4.16(c) and 4.16(d) confirms that in the experiments a region exists for which both stable equilibria and stable limit cycles exist. From the comparison between numerical and experimental results, it can be concluded that with the proposed model the steady-state behaviour of the set-up is accurately predicted.

Next, the same type of bifurcation diagram, as shown in figure 4.9, is constructed experimentally. In order to construct such experimental bifurcation diagram, different constant input voltages are applied to the set-up. When no torsional vibrations are observed (as in figure 4.16(d)), the mean value of the recorded angular velocity is computed and obtained data are plotted using the symbol "x". Next, when torsional vibrations are observed at the lower disc (as in figures 4.16(a), 4.16(b) and 4.16(c)), the

<sup>1</sup>When presenting those signals in time domain, we always start from 0 on the time scale.

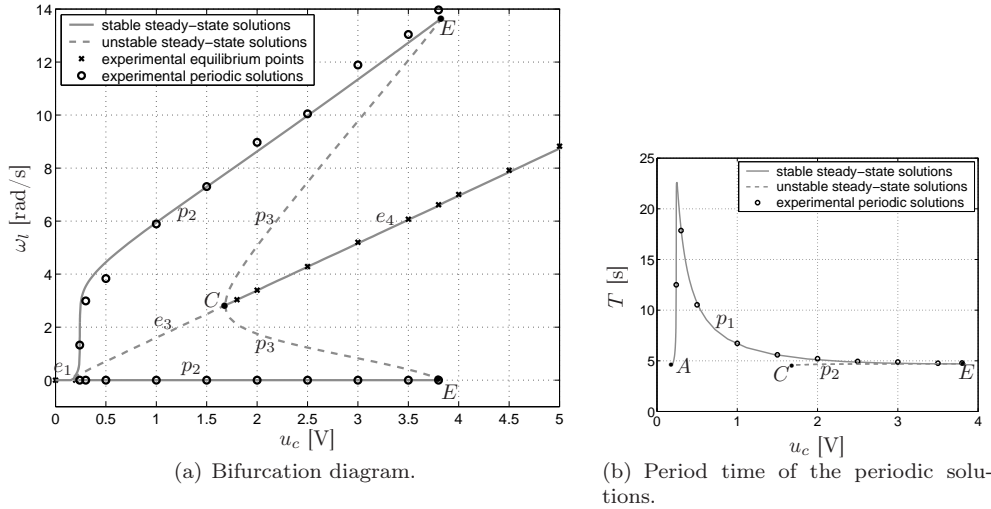


Figure 4.17: Comparison of the numerical and experimental bifurcation diagram.

mean value of local maxima and minima of the vibrations are computed. Then, these experimentally obtained data are plotted using the symbol "o". Such experimental results, together with the bifurcation diagram obtained by numerical analysis of the estimated model, are shown in figure 4.17(a). Moreover, when torsional vibrations are observed in the set-up, the period time  $T$  of the vibrations is determined as well. In figure 4.17(b) such experimental results are compared to the period time of the numerically obtained limit cycles. The results, shown in figure 4.17, illustrate the predictive quality of the obtained model.

Both in the numerical and the experimental bifurcation diagram we notice qualitatively different behaviour of the system when the constant input voltage is changed:

- For very low input voltages, the system is in a sticking phase. In figure 4.18(a), an experimental angular velocity is shown for  $u_c = 0.1$  V: the system is in the sticking phase.
- If the input voltage is increased, the system enters the region where only torsional vibrations (i.e. stable limit cycles) appear. The result shown in figure 4.18(b) gives evidence about the existence of such region in the experimental set-up. Namely, when we apply constant input voltage  $u_c = 1.6$  V we observe a stick-slip limit cycle ( $0 < t < t_1$ ). Moreover, when we perturb the lower disc (at  $t = t_1$ ) in order to bring the system in the vicinity of the equilibrium point, the system converges toward the stick-slip vibrations. In figure 4.18(b), we perturbed the system at the time instants  $t_1$  and  $t_2$ . After each perturbation, torsional stick-slip vibrations reappear in steady-state.
- If the input voltage is even higher, then the input voltage is in the region where both torsional vibrations (limit cycles) and a constant angular velocity at the lower disc (equilibrium points) can appear in the set-up. In figure 4.18(c), we show the angular velocity obtained as a result of the following experiment. When we apply a constant input voltage  $u_c = 3.6$  V, the lower disc converges to stick-slip vibrations. At the time instant  $t_1$ , we disturb the system such that

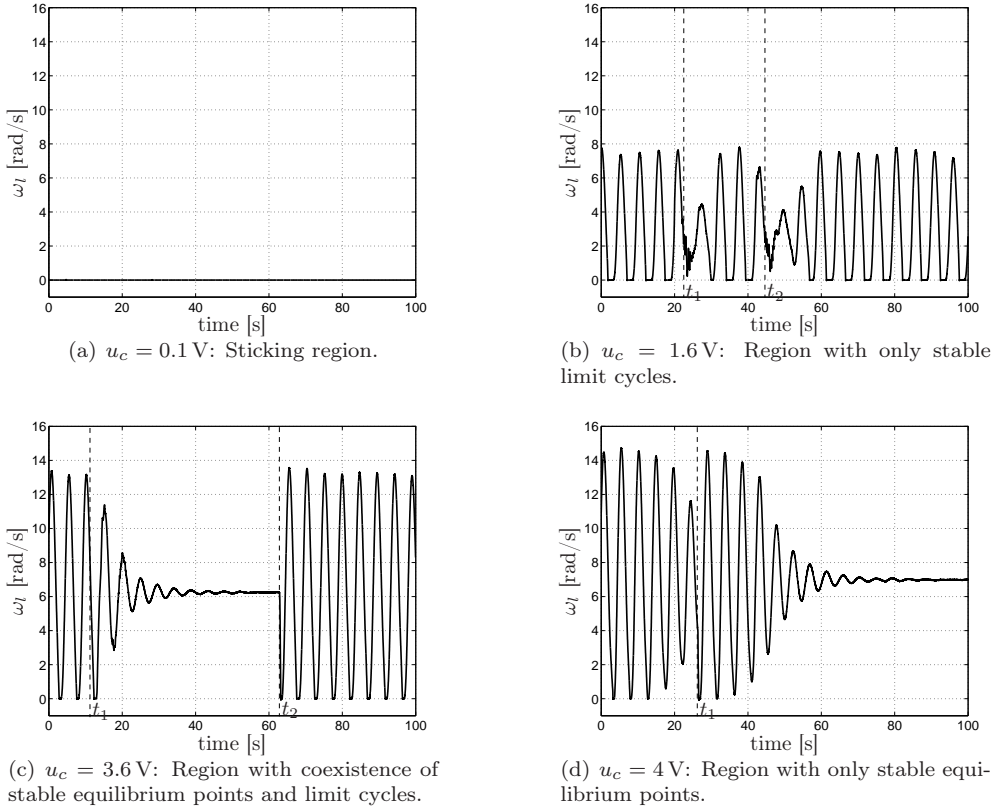


Figure 4.18: Experimental time series in various regions of the bifurcation diagram.

the lower disc, after a while, starts to rotate with a constant angular velocity. Then, at the time instant  $t_2$  we stopped the lower disc for a very short period (in other words the system is manually brought close to the stick-slip limit cycle) and the system continues with stick-slip vibrations. This experimental result shows that a stable limit cycle (torsional vibrations) and a stable equilibrium point (constant velocity) coexist in the experimental set-up for  $u_c = 3.6 \text{ V}$ . This can also be seen in figure 4.17(a).

- If the input voltage is high enough ( $u_c > 3.8 \text{ V}$ ), the system enters a region where no torsional vibrations can appear in the system in steady-state. From figure 4.18(d), we can conclude that when we apply an input voltage  $u_c = 4 \text{ V}$  to the system, torsional vibrations disappear even though at the time instant  $t_1$  we tried to induce those vibrations manually. Therefore, this result represents an indication for the fact that for  $u_c = 4 \text{ V}$  no torsional vibrations can appear in the set-up.

### Unmodelled Dynamics

Although various validation procedures show that the model constituted by (4.1), with parameter estimates in table 4.1, represents a very good model of the set-up, when



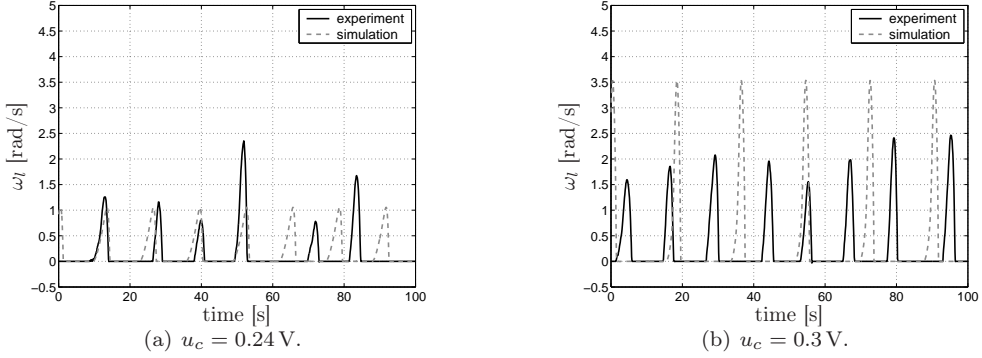


Figure 4.19: Experimental and simulated angular velocities at the lower disc for  $u_c = 0.24$  V and  $u_c = 0.3$  V.

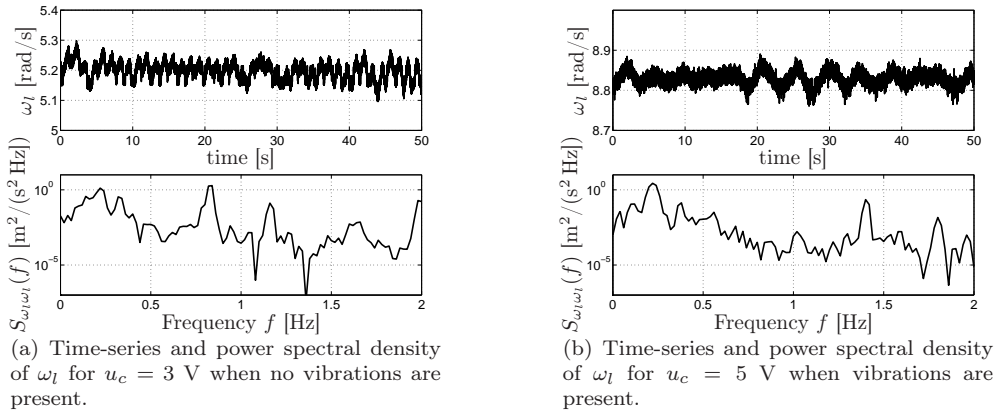


Figure 4.20: Power spectral density of various velocity signals in steady-state.

the lower disc only rotates (and cannot move in lateral direction), some unmodelled dynamics is present in the set-up:

- In figure 4.19, we see that when a very low constant voltage is applied to the motor, torsional vibrations which appear at the lower disc do not have a constant amplitude as it should be the case according to the estimated model. This is due to the presence of position-dependent friction at the lower disc, which is not modelled. In other words, the friction force induced by the brake on the lower disc is not the same at each angular position of the disc. The same conclusion can be derived from the power spectral density of experimental time-series as shown in figure 4.20. These measured time-series are obtained, while applying constant input voltages  $u_c = 3$  V and  $u_c = 5$  V and waiting long enough to obtain constant velocities at the lower disc. Then the last 50 seconds of the measurements are recorded and the power spectral density of the obtained signals are determined. If we analyze the power spectral density  $S_{\omega_l \omega_l}(f)$  shown in figure 4.20(a), it can be noticed that some dominant spectral components are present at the frequencies  $f = 0.22$  Hz and  $f = 0.83$  Hz. The first spectral

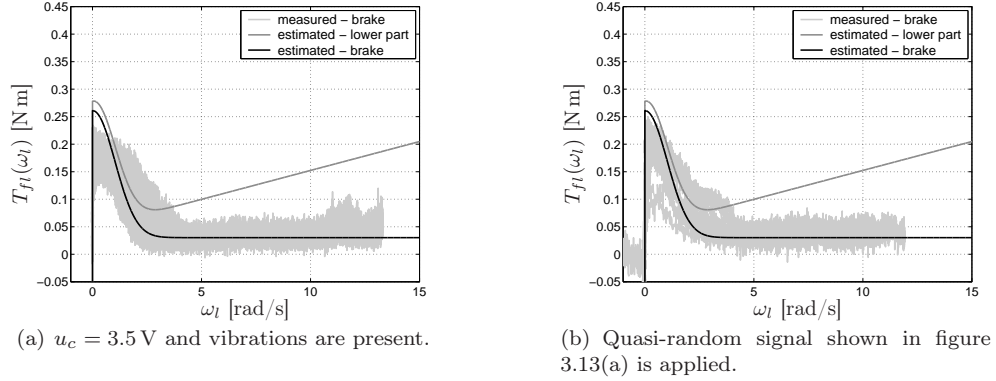


Figure 4.21: Measured and estimated friction torque on the brake and estimated friction torque at the lower part of the set-up.

component is close to the mechanical resonance frequency of the system. In order to understand the second important spectral component, we should analyze the angular velocity shown in figure 4.20(a). Namely, for  $u_c = 3$  V the experimentally obtained velocity is  $\omega_l = 5.1964$  rad/s = 0.8270 Hz which is very close to the second important spectral component. Similarly, for  $u_c = 5$  V we notice important spectral components for  $f = 0.22$  Hz and  $f = 1.4$  Hz as shown in figure 4.20(b). The first spectral component is the same as for  $u_c = 3$  V and is due to the mechanical resonance of the set-up which is independent of the angular velocity. Moreover, at  $u_c = 5$  V the obtained angular velocity  $\omega_l = 8.8272$  rad/s = 1.4049 Hz is close to the second dominant spectral component (see figure 4.20(b)). Consequently, this represents clear evidence for the presence of the position-dependent friction at the lower disc.

- Since the brake at the lower part of the set-up is connected to the force sensor (see figure 3.5), we can also measure the friction force which the brake produces at the lower disc. Then knowing the distance from the geometric center of the lower disc to the place where the friction force is applied to the disc (which equals 4.2 cm), we can compute the friction torque applied by the brake to the lower disc. The measured and estimated friction torques on the brake ( $T_{flb}$  in table 3.2) and the estimated friction torque at the lower part of the set-up ( $T_{fla} + T_{flb}$  in table 3.2) are shown in figure 4.21. From that figure, it can be seen that negative damping is indeed present in the set-up. However, it can also be seen that some other unmodelled effects are also present in the friction force. Moreover, we observe that the estimated friction model describes the measured friction better for higher than for lower velocities. This can be due to the fact that the friction sensor needs more accurate calibration, but it can also be due to the fact that static friction models do not describe very accurately all friction phenomena for small relative velocities.

Finally, from figure 4.21 it can be observed that, in the working region of the set-up, the viscous friction is mainly due to the friction in the bearing and negative damping is mainly due to the brake.

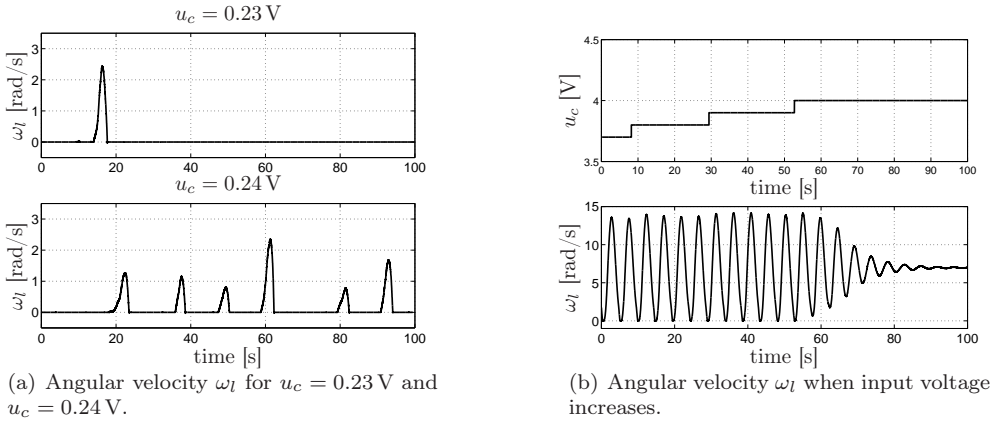


Figure 4.22: Indication of the existence of the discontinuous fold bifurcation points for (a) very small and (b) very high constant input velocities.

### Fold Bifurcation Points

From the steady-state analysis of the estimated model of the set-up, it appears that the model exhibits two discontinuous fold bifurcation points: one for  $u_c = 0.1846$  V (point  $D$  in figure 4.9(b)) and another for  $u_c = 3.835$  V (point  $E$  in figures 4.9(a), 4.9(c) and 4.17).

From the measurements of the angular velocity  $\omega_l$ , shown in figure 4.22(a), we can conclude that the discontinuous fold bifurcation point is present for an input voltage  $u_c \in (0.23$  V,  $0.24$  V). The difference between our estimates and experimentally obtained results is due to unmodelled dynamics and mainly due to the position dependent friction which is observed at the lower disc and which is not modelled. Moreover, according to the steady-state analysis and from figure 4.9(b), we also expect that for very small input voltages, a constant velocity can appear at the lower disc (equilibrium branch  $e_2$  in figure 4.9(b)). However, this equilibrium branch cannot be observed experimentally due to the existence of the position dependent friction.

In order to show that the second fold bifurcation point (point  $E$  in figures 4.9(a), 4.9(c) and 4.17) is present in the experimental set-up we perform the following experiment. We apply a constant input voltage and wait long enough to obtain torsional vibrations. Then we increase the input voltage in order to see when the torsional vibrations disappear. In other words, we follow the periodic branch  $p_2$  in figure 4.17(a) in a step-wise fashion in order to estimate the position of the fold bifurcation point  $E$  experimentally. Such experiment shows that torsional vibrations disappear when we increase the input voltage  $u_c$  from 3.9 V to 4 V (see figure 4.22(b)). The very small difference between experimental analytical obtained results can be due to the presence of unmodelled dynamics.

### Hopf Bifurcation Points

According to the bifurcation diagram shown in figure 4.9 we have two smooth sub-critical Hopf bifurcation points: one for  $u_c = 0.1849$  V (point  $B$  in figure 4.9(b)) and another one for  $u_c = 1.6865$  V (point  $C$  in figures 4.9(a) and 4.17(a)).

We have already mentioned that, mainly due to position-dependent friction, we

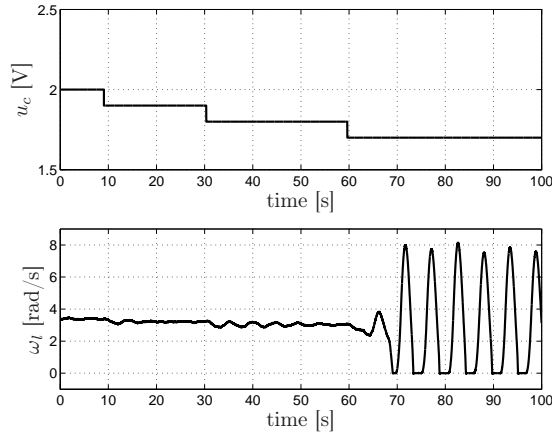


Figure 4.23: Indication of existence of the subcritical Hopf bifurcation point  $C$ .

cannot observe the equilibrium branch  $e_2$  in figure 4.9(b) in experiments and, therefore, we cannot observe the Hopf bifurcation point  $B$  for lower input voltages separately from the discontinuous fold bifurcation at point  $D$ .

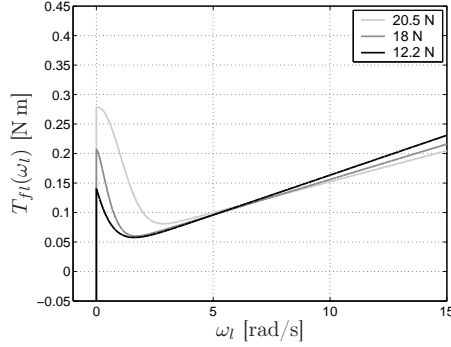
In order to show that the second Hopf bifurcation point is present (point  $C$  in figure 4.17(a)) in the experimental set-up, we perform the following experiment. We apply a constant input voltage and perturb the system in order to bring it to the equilibrium point (constant velocity at the lower disc). Then we slowly decrease the input voltage in order to see when the torsional vibrations appear. In other words, we follow the equilibrium branch  $e_4$  in figure 4.17(a) in order to estimate the location of the smooth subcritical Hopf bifurcation point  $C$ . Such an experiment shows that torsional vibrations appear when we decrease the input voltage  $u_c$  from 1.8 V to 1.7 V (see figure 4.23). The very small difference between the experimentally and the numerically obtained location of the Hopf bifurcation point is due to the fact that the region of attraction of the equilibrium point is very small near the Hopf bifurcation point. Namely, when we decrease the input voltages in even smaller steps we noticed that even for  $u_c = 1.6$  V system can rotate with constant velocity in steady-state.

### 4.3.2 Various Friction Situations

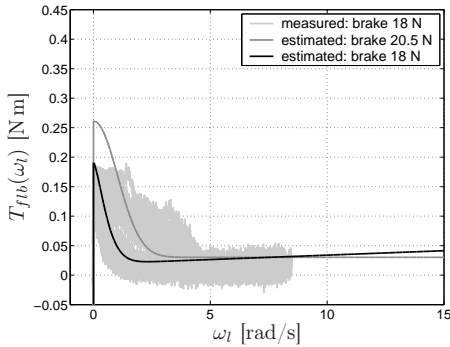
In Section 4.2.3, we have analyzed how various changes in the friction characteristics can influence torsional vibrations in drill-string systems. Here, we investigate how various friction conditions influence these friction characteristics and, in turn, the torsional vibrations in the experimental set-up.

#### Changes in the Applied Normal Force

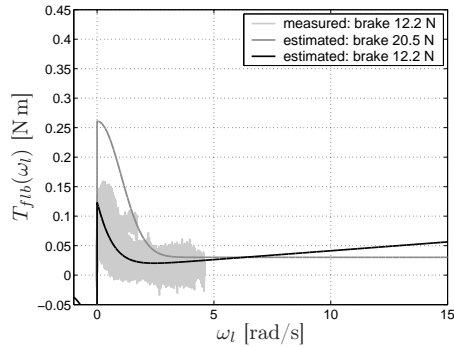
In order to analyze how changes in normal force, which is applied to the brake, influence the steady-state behaviour of the set-up, we applied a 18 N and a 12.2 N normal force to the brake (ondina oil 68 is present between the brake blocks and brake disc). Next, the parameters of the model of the obtained friction torques are estimated, as described in Section 4.1, the obtained models are validated and numerical and experimental bifurcation diagrams are constructed for both normal force levels. The estimated friction model at the lower part of the set-up ( $T_{fl}(\omega_l) = T_{fla}(\omega_l) + T_{flb}(\omega_l)$ )



(a) Estimated friction models for the friction at the lower disc for various normal force levels applied at the brake.



(b) Measured and estimated friction torque at the brake for 18 N normal force.



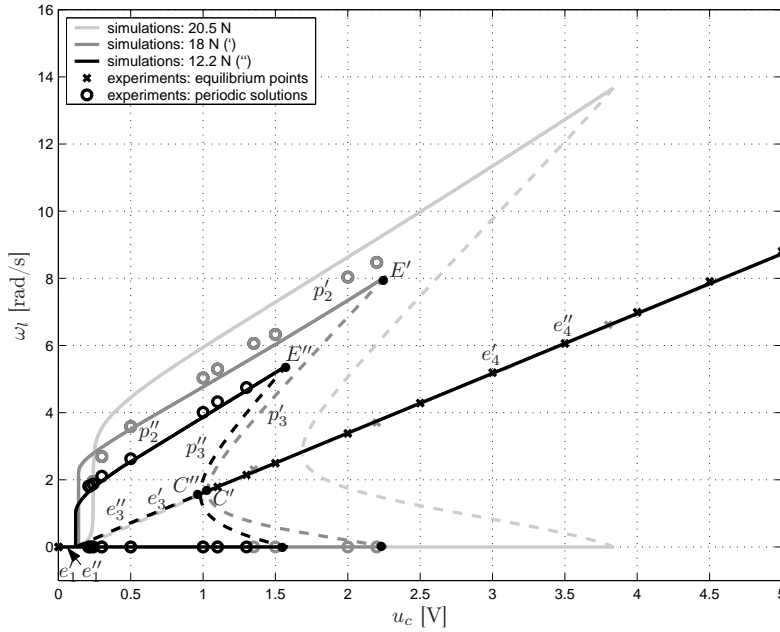
(c) Measured and estimated friction torque at the brake for 12.2 N normal force.

Figure 4.24: Measured and estimated friction torques at the lower disc and on the brake for various normal force levels.

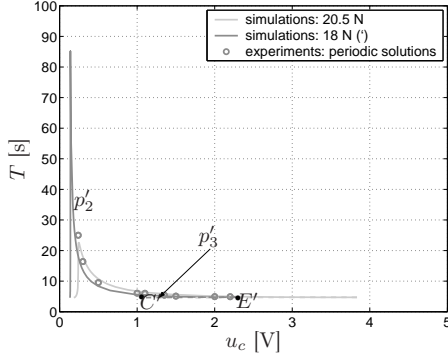
in table 3.2), caused by the friction in the bearings ( $T_{fla}(\omega_l)$ ) and by the friction between the brake disc and the brake ( $T_{flb}(\omega_l)$ ), are shown in figures 4.24(a). The measured and estimated friction torques in the brake are shown in figures 4.24(b) and 4.24(c) and the related bifurcation diagrams are shown in figure 4.25.

When a lower normal force is applied to the brake, the static friction level is lower, the sticking region decreases and the lower disc starts to rotate for lower input voltages. In the set-up, the lower disc starts to rotate (with torsional vibrations) for  $u_c = 0.24$  V when normal forces of 20.5 N and 18 N are applied, and for  $u_c = 0.21$  V when 12.2 N normal force was applied. The fact that no decrease in the sticking region is observed when we apply a normal force 18 N can be due to the fact that we collected experimental results for  $u_c = 0.23$  V and  $u_c = 0.24$  V and such resolution is not small enough to distinguish the difference between in the sticking regions for those two normal forces. However, from the results obtained for a 12.2 N normal force it is clear that the sticking region decreases when the normal force is lower.

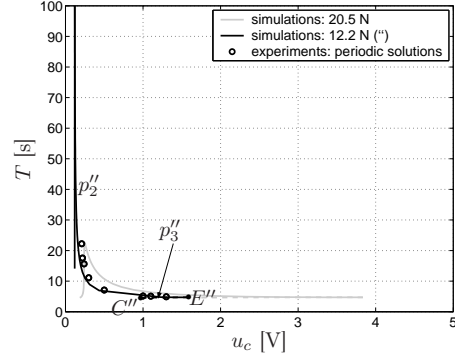
For lower normal force levels, the separation process between the contacting surfaces (brake disc and the brake blocks) and the full fluid lubrication regime occur for lower velocities (the friction regimes are depicted in figure 3.11). Moreover, in Sec-



(a) Bifurcation diagrams.



(b) Period time of the periodic solutions for 18 N normal force.

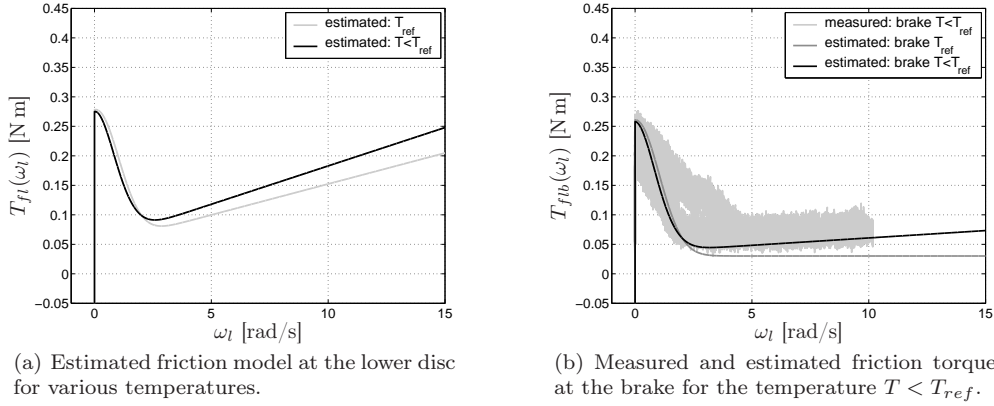


(c) Period time of the periodic solutions for 12.2 N normal force.

Figure 4.25: Simulated and experimental bifurcation diagrams for various normal force levels applied to the brake.

tion 4.2.1 we have concluded that the position of the second Hopf bifurcation points is determined by the point on the  $T_{fl}(\omega_l)$ -curve where the negative damping reaches the value  $d_{min}$  ( $\omega_l = \omega_{s2}$  figure 4.8). This, in fact, corresponds to the point where full fluid lubrication appears (see figure 3.11). Consequently, for lower normal force levels, the Hopf bifurcation points  $C'$  and  $C''$  in figure 4.25 appear for lower input voltages and the region, where a constant velocity at the lower disc can appear, decreases.

From figures 4.24(a), 4.24(b) and 4.24(c) it can be seen that we estimate a higher viscous friction coefficient for the lower normal force levels. Namely, when a lower normal force is applied, full fluid lubrication appears at the lower angular velocities. Then, for higher normal forces and high enough  $u_c$  the system is closer to the tran-



(a) Estimated friction model at the lower disc for various temperatures.

(b) Measured and estimated friction torque at the brake for the temperature  $T < T_{ref}$ .

Figure 4.26: Measured and estimated friction torques at the lower disc and on the brake for temperatures  $T \in (17^\circ\text{C}, 22^\circ\text{C})$  and  $T_{ref} \in (25^\circ\text{C}, 30^\circ\text{C})$ .

sition between partial and full fluid lubrication than when the normal force is lower. Consequently, this effect is, in the range of input voltages which can be applied to the system, modelled with lower viscous friction for higher normal forces. However, if the normal force is low enough, the effects which cause the negative damping in friction disappear (effects are described in Section 3.2.2) and the torsional vibrations in the drill-string system also disappear. In the considered experimental drill-string set-up torsional vibrations disappear when the normal force is smaller than 7.8 N. An important observation is that the normal force influences the friction characteristics in a rather complex way, which can be explained using the friction regimes in figure 3.11. By no means the normal force forms a mere scaling factor for the friction force.

### Temperature Changes

The results, which are analyzed in Section 4.3.1, are obtained when the temperature in the laboratory, where the set-up is placed, is between  $25^\circ\text{C}$  and  $30^\circ\text{C}$ . The same results are collected when the temperature in the laboratory is between  $17^\circ\text{C}$  and  $22^\circ\text{C}$ , for the same normal force applied at the brake (20.5 N). The parameters of the obtained friction torque are estimated (as described in Section 4.1), the obtained model is validated and both numerical and experimental bifurcation diagrams are constructed. The estimated friction torque at the lower part of the set-up ( $T_{fla} + T_{flb}$  in table 3.2) is shown in figure 4.26(a). The measured and estimated friction torque at the brake ( $T_{flb}$ ) is shown in figure 4.26(b). The related bifurcation diagrams are shown in figure 4.27.

When the temperature is lower, the viscosity of the oil becomes higher. With a more viscous lubricant, the separation between the contacting surfaces (brake disc and the brake blocks in the experimental set-up) and the full fluid lubrication process occur for lower velocities. In Section 4.2.1, we have concluded that the position of the second Hopf bifurcation point is determined by the point where the negative damping reaches the value  $d_{min}$  (see figure 4.8), which, in fact, corresponds to the point when the full fluid lubrication appears (see figure 3.11). Consequently, the Hopf bifurcation point  $C'$ , in figure 4.27, appears for lower input voltages than it does in the set-up

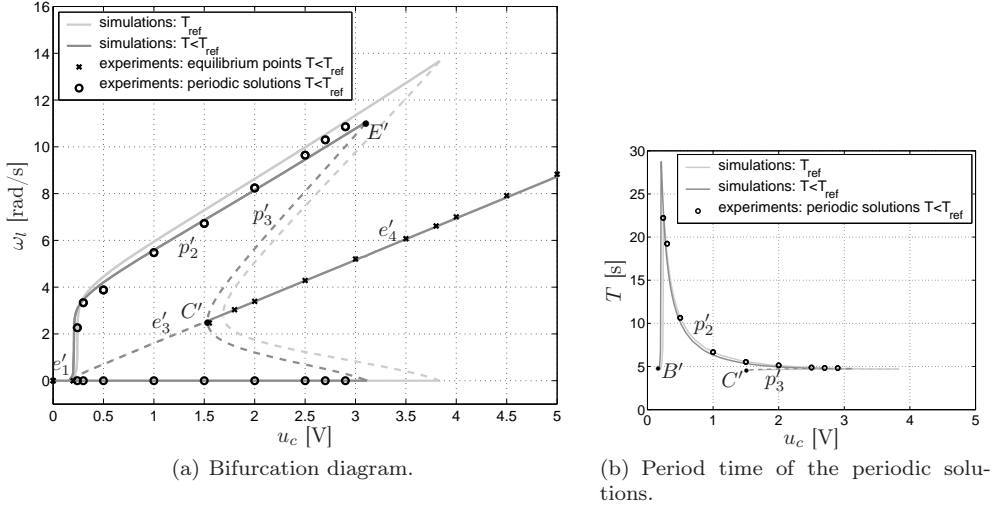


Figure 4.27: Simulated and experimental bifurcation diagram for various temperatures.

when the temperature in the laboratory is higher.

Moreover, in Section 4.2.3 we have concluded that a higher viscous friction level causes a decrease of the amplitude of the torsional vibrations and that the range of voltages in which torsional vibrations can appear is smaller (compare figure 4.14 with figures 4.26(a) and 4.27(a)).

### Changes in the Contact Material

In Section 3.1, we mention that in order to obtain torsional vibrations, a brake and a small oil-box are fixed to the lower part of the set-up, as shown in figure 3.5. The brake material is bronze, the brake disc is made of steel and ondina oil 68 [Shell, 1997] is added to the brake disc in order to obtain torsional vibrations. The set-up, described in Section 3.1, is obtained by redesigning the lower part of an existing drill-string set-up. In the previous set-up, torsional vibrations are obtained when a brake, with a rubber brake material, is applied to the lower brass disc and when water is added between the lower disc and the contact material of the brake. Then, using a Neural Network friction model (3.5) with two nodes ( $n = 2$  in (3.5)), the parameters of the friction model are estimated. The estimated friction model is shown in figure 4.28. Then, both experimental and numerical bifurcation diagrams are constructed [Mihajlović et al., 2004a,b] (see figure 4.29). Since the input voltage is limited to 5 V, the experimental data are only available in that range. In [Mihajlović et al., 2004a,b] the estimated parameters of the previous set-up are slightly different than the parameters of the set-up considered in this thesis due to the following reasons. Firstly, the amplification of the power amplifier can easily be changed and during the redesigning of the old set-up we changed the amplification of the amplifier. Secondly, temperature, humidity can also influence the parameters of the upper part of the set-up. Finally, during the redesigning of the set-up, we changed the lower part of the set-up, hence, the inertia and the friction torque in the bearings at the lower disc has also been changed. However, such difference has no qualitative influence to the



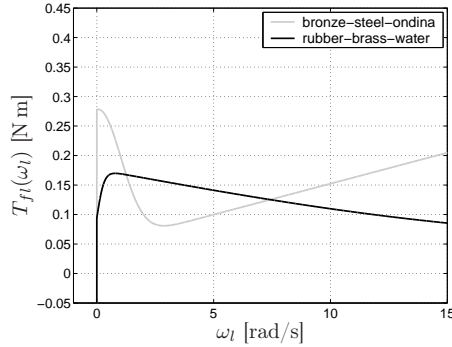


Figure 4.28: Estimated friction torque at the lower disc for different contact materials.

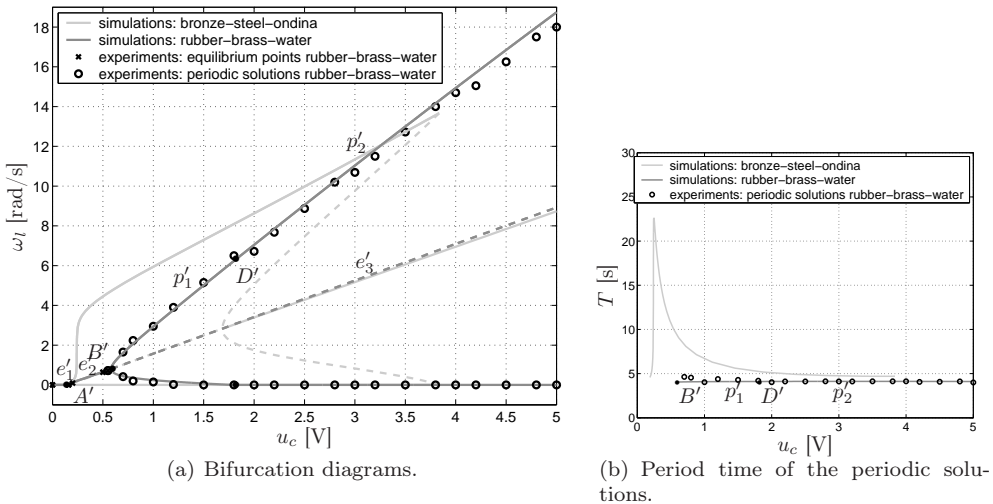


Figure 4.29: Simulated and experimental bifurcation diagrams for different contact materials.

steady-state results presented here, since the torsional vibrations are due to a negative damping in the friction characteristics.

A comparison of numerical and experimental bifurcation diagrams indicates the predictive quality of the model (see figure 4.29(a)). For very low velocities, the set-up resides in the sticking phase in steady-state (equilibrium branch  $e_1$ ). Then for higher input voltages  $u_c$  the system has one equilibrium point (equilibrium branch  $e_2$ ). When  $u_c$  increases further, torsional vibrations without stick-slip appear (periodic branch  $p_1$ ) and finally for even higher  $u_c$  torsional vibrations with stick-slip appear.

In order to model torsional vibrations with and without stick-slip a humped friction model (see figure 3.10(b)), was used. Namely, in the estimated friction model a positive damping is present for very small angular velocities and for higher angular velocities negative damping occurs as shown in figure 4.28. Moreover, for even higher angular velocities positive damping is expected to occur. However, due to the limited input voltage to the DC motor, the maximal angular velocity, which can be achieved, was limited. Therefore, this region was not observed in the friction.

An explanation for the appearance of positive damping for very low angular velocities can be provided when we analyze the various friction regimes described in Section 3.2.2. Namely, for very low angular velocities hardly any lubricant is present in the contact (boundary lubrication regime in figure 3.11). Then the friction is mainly due to the shearing resistance of the asperity contact, i.e. it is mainly determined by the contact between brake material (rubber) and lower disc (brass). Since brass is much stiffer than the rubber, the small positive damping in the friction characteristics is mainly caused by the damping characteristics of the rubber.

Finally, the estimated friction torque shown in figure 4.1 has a positive damping at the lower velocities, but no torsional vibrations without stick-slip. According to the results shown in figures 4.11(a) and 4.11(b) we see that such torsional vibrations appear when the damping at the lower velocities is high enough with respect the following negative damping. Consequently, the combination of a low negative damping in the friction torque shown in figure 4.28 together with a high positive damping at a very low velocities is responsible for the appearance of torsional vibrations without stick-slip.

## 4.4 Summary

The aim of this chapter is to give an improved understanding for the causes of torsional vibrations in rotor systems with flexibility. For that purpose, we have analyzed an experimental drill-string set-up in which torsional vibrations occur. However, the results obtained here can apply to many other engineering systems with friction and flexibility. Namely, the set-up represents a configuration of two masses, coupled by a flexibility, of which one is subject to friction and the other is driven by an actuator. In this context, one can think of applications such as printers, pick and place machines, industrial and domestic robots, braking mechanisms and many others. According to the presented results the following can be concluded:

- Based on theoretical, numerical and experimental results torsional vibrations, in the type of systems considered in this chapter, are mainly due to the friction present at the lower disc, i.e. the friction characteristic, modelled with a negative damping in a friction-velocity curve, is responsible for those vibrations. When the disc rotates with a (steady-state) velocity, at which negative damping is present in the friction, instability is induced in the system. Consequently, the lower disc cannot rotate with a constant velocity any more and torsional vibrations occur. However, for even higher input voltages, corresponding to a region where a positive damping is present in the friction, both a constant velocity (stable equilibrium point) and torsional vibrations (limit cycles) coexist in the system. The size of this region is determined by a level of negative damping at low velocities in comparison to a level of viscous friction at higher velocities. Moreover, the velocity at which the friction attains its minimum is also important. Namely, if this velocity increases, the second fold bifurcation (point  $E$  in figure 4.9(a)) and the second Hopf bifurcation point (point  $C$  in figure 4.9(a)) shifts to high input voltages.

The friction characteristics that induce torsional vibrations is not present when only a normal force is applied to the brake at the lower disc and no lubrication fluid is added. Namely, torsional vibrations are induced when a certain lubrica-

tion is added between the brake disc and the brake material. When a lubrication is present in the contact, the friction force is partly due to the contact of two surfaces and partly due to the lubricant and its viscosity. As the sliding velocity increases, the solid-to-solid contact decreases, reducing friction and increasing the acceleration of the moving part. Consequently, negative damping occurs in the friction-velocity curve, which is responsible for the occurrence of torsional vibrations in the set-up.

- When torsional vibrations are present in the system, then vibrations with and/or without stick-slip can appear. In this chapter we conclude that these types of vibrations are determined by the level of positive damping in the friction at very small velocities in relation to the level of negative damping appearing for slightly higher velocities. Namely, if the positive damping at very low velocities is small with respect to the negative damping level, then only torsional vibrations with stick-slip can occur. However, if the positive damping level at very low velocities is high enough with respect to the negative damping level, then torsional vibrations with and without stick-slip can occur.

In the set-up, torsional vibrations with stick-slip are obtained as a result of a contact between a bronze brake and a steel brake disc with ondina oil 68 as a lubricant. Furthermore, torsional vibrations with and without stick-slip are obtained when the friction torque is produced as a result of a contact between a rubber brake and a brass disc, with a water as a lubricant. For very low angular velocities, the friction is mainly due to the contact between the contacting materials. Consequently, the friction is determined by characteristics of the materials and the appearance of a positive damping for lower velocities in the friction model is connected to the types of contact material which produce friction; not so much to the type of lubricant.

- The results on theoretical, numerical and experimental level confirm that the sticking phenomenon, which is modelled with a set-valued force law for the friction, plays a crucial role in describing the steady-state phenomena observed in the set-up. With this friction model, the dynamics of the set-up is described by differential equations with discontinuous right-hand side. Consequently these equations successfully model equilibrium sets, equilibria and stick-slip limit cycling; phenomena which are also observed in the set-up. Moreover, we observe a discontinuous fold bifurcation both in simulations and experiments. The performed analysis confirms that the discontinuous bifurcations play a crucial role in the creation and destruction of the observed limit cycling (i.e. torsional vibrations).
- Finally, in this chapter we consider only an experimental set-up with a very low stiffness which is not the case in many mechanical systems. According to the presented stability analysis, it can be concluded that if the two inertias (the lower disc and upper disc) are coupled by a higher stiffness and friction force with negative damping is present, then the higher stiffness level does not influence significantly the size of the instability region and, thus, the appearance of torsional vibrations. However, a higher stiffness level is expected to influence quantitatively torsional vibrations, e.g. the amplitude of the vibrations, the size of the region in which constant velocity and torsional vibrations co-exist and the type of torsional vibrations (with/without stick-slip).

## Chapter 5

# Interaction Between Torsional and Lateral Vibrations in Drill-String Systems

In order to obtain both torsional and lateral vibrations in the experimental set-up, first, the  $x$ - and  $y$ -constraints shown in figures 3.6 and 3.7 are released, second, a normal force of 20.5 N is applied to the brake and, third, ondina oil 68 is added between the brake disc and the contact material of the brake (as in Chapter 4). We have already derived a model of the set-up and estimated and validated all parameters of the model in Chapter 3. In Chapter 4, we also estimated and validated the parameters of the friction torque at the lower part of the set-up (see (4.2)) when a 20.5 N normal force and ondina oil is applied.

Therefore, in Section 5.1, first we present the full model of the set-up and subsequently validate the obtained model using the signals shown in figure 3.13. In Section 5.2, we determine equilibrium points (sets) and periodic solutions of the estimated model and assess the related stability properties. Moreover, we discuss how different levels of mass-unbalance at the lower disc and several other parameters of the lower part of the set-up influence the steady-state behaviour of the system. Then, in Section 5.3 a bifurcation diagram based on the estimated model is presented and compared to experimentally obtained results. Furthermore, we discuss the experimental results obtained for several mass-unbalance levels present at the lower disc. Finally, in Section 5.4 we give a brief summary of this chapter.

### 5.1 Model Validation

The model of the set-up, when both torsional and lateral vibrations are present, is given by (3.17), (3.18), (3.26) and with  $T_{cl}(\omega_l)$  as in (4.1), i.e. it can be represented by the following system of equations:

Table 5.1: Estimated parameters of the set-up.

Parameter	unit	Estimated value
$J_u$	[kg m <sup>2</sup> ]	0.4765
$k_m$	[N m/V]	4.3228
$T_{su}$	[N m]	0.37975
$\Delta T_{su}$	[N m]	-0.00575
$b_u$	[kg m <sup>2</sup> /rad s]	2.4245
$\Delta b_u$	[kg m <sup>2</sup> /rad s]	-0.0084
$k_\theta$	[N m/rad]	0.0775
$J_C$	[kg m <sup>2</sup> ]	0.0412
$e$	[m]	0.00489
$m_r$	[kg]	9.9137
$m_t$	[kg]	3.3202
$k$	[N/m]	2974.25
$b$	[N s/m]	25
$T_{sl}$	[N m]	0.2781
$T_{cl}$	[N m]	0.0473
$\omega_{sl}$	[rad/s]	1.4302
$\delta_{sl}$	[-]	2.0575
$b_l$	[kg m <sup>2</sup> /rad s]	0.0105

$$\begin{aligned}
& J_u \dot{\omega}_u - k_\theta \alpha + T_{fu}(\omega_u) = k_m u, \\
& (m_r + m_t) \ddot{x} - m_r e \ddot{\alpha} \sin(\alpha) - (m_r + m_t) \dot{\omega}_u y - m_r e \dot{\omega}_u \sin(\alpha) + b \dot{x} \\
& - 2(m_r + m_t) \omega_u \dot{y} - 2 m_r e \omega_u \dot{\alpha} \cos(\alpha) - m_r e \dot{\alpha}^2 \cos(\alpha) + k x \\
& - (m_r + m_t) \omega_u^2 x - b \omega_u y - m_r e \omega_u^2 \cos(\alpha) = 0, \\
& (m_r + m_t) \ddot{y} + m_r e \ddot{\alpha} \cos(\alpha) + (m_r + m_t) \dot{\omega}_u x + m_r e \dot{\omega}_u \cos(\alpha) + b \dot{y} \\
& + 2(m_r + m_t) \omega_u \dot{x} - 2 m_r e \omega_u \dot{\alpha} \sin(\alpha) - m_r e \dot{\alpha}^2 \sin(\alpha) + k y \\
& - (m_r + m_t) \omega_u^2 y + b \omega_u x - m_r e \omega_u^2 \sin(\alpha) = 0, \\
& -m_r \ddot{x} e \sin(\alpha) + m_r \ddot{y} e \cos(\alpha) + (m_r e^2 + J_C)(\ddot{\alpha} + \dot{\omega}_u) + \\
& m_r \dot{\omega}_u e (x \cos(\alpha) + y \sin(\alpha)) + 2 m_r e \dot{x} \omega_u \cos(\alpha) + 2 m_r e \dot{y} \omega_u \sin(\alpha) \\
& + T_{fl}(\omega_u + \dot{\alpha}) + m_r x e \omega_u^2 \sin(\alpha) - m_r y e \omega_u^2 \cos(\alpha) + k_\theta \alpha = 0, \tag{5.1} \\
& T_{fu}(\omega_u) \in \begin{cases} T_{cu}(\omega_u) \text{sgn}(\omega_u) & \text{for } \omega_u \neq 0, \\ [-T_{su} + \Delta T_{su}, T_{su} + \Delta T_{su}] & \text{for } \omega_u = 0, \end{cases} \\
& T_{cu}(\omega_u) = T_{su} + \Delta T_{su} \text{sgn}(\omega_u) + b_u |\omega_u| + \Delta b_u \omega_u, \\
& T_{fl}(\omega_l) \in \begin{cases} T_{cl}(\omega_l) \text{sgn}(\omega_l) & \text{for } \omega_l \neq 0, \\ [-T_{sl}, T_{sl}] & \text{for } \omega_l = 0, \end{cases} \\
& T_{cl}(\omega_l) = T_{cl} + (T_{sl} - T_{cl}) e^{-|\omega_l / \omega_{sl}|^{\delta_{sl}}} + b_l |\omega_l|, \\
& \omega_l = \omega_u + \dot{\alpha}.
\end{aligned}$$

The parameters of the model are given in the table 5.1 and further in this thesis we use these parameter values as reference values.

The model of the set-up is validated using the quasi-random and the validation signal shown in figure 3.13. The measured and simulated angular position  $\theta_l$  and

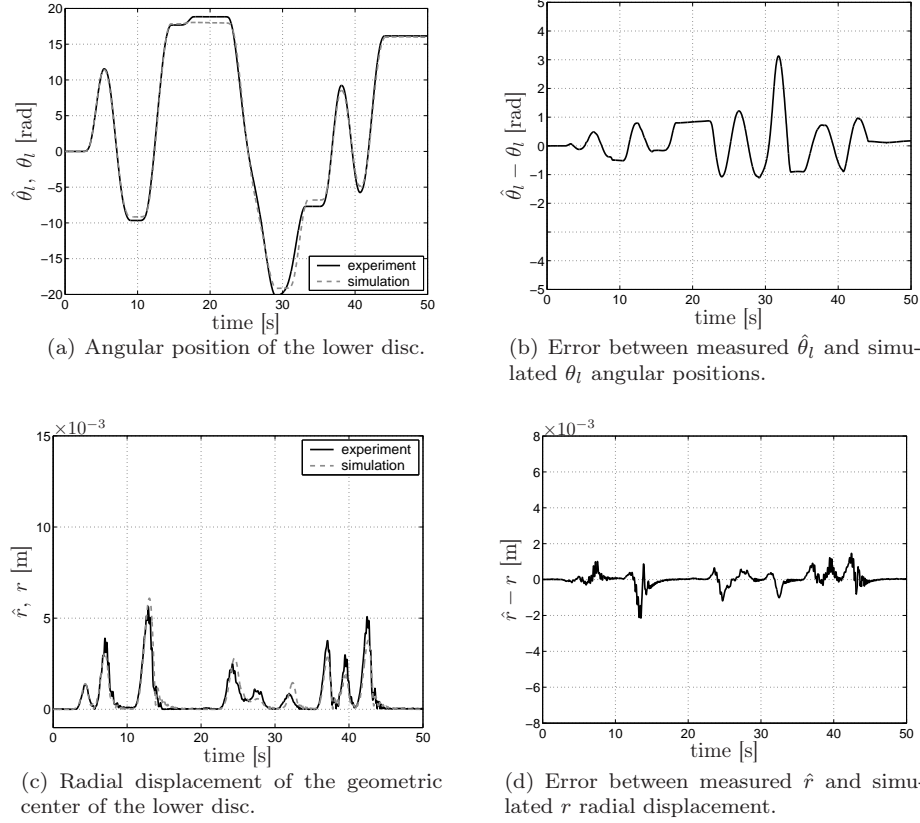


Figure 5.1: Validation signals in terms of  $\theta_l$  and  $r$  obtained for the quasi-random input voltage shown in figure 3.13(a):  $R_{\theta_l}^2 = 0.9962$ ,  $R_r^2 = 0.8859$ .

radial displacement  $r$ , when the quasi-random input signal is applied, are shown in figure 5.1 and the related  $R^2$  performance criteria (3.22) are  $R_{\theta_l}^2 = 0.9962$  and  $R_r^2 = 0.8859$ . The model is also validated using the validation signal, as shown in figure 3.13(b). The corresponding measured and simulated responses are shown in figure 5.2 with  $R_{\theta_l}^2 = 0.9667$  and  $R_r^2 = 0.6939$ . The comparison between the responses of the experimental set-up and estimated model indicates a good quality of the obtained parameter estimates. The reasons for the slightly weaker results for  $R_r^2$  are addressed in Section 5.3.1.

In the sequel, we analyze the steady-state behaviour of the set-up, when a constant input voltage  $u = u_c = \text{const}$  is applied, since such behaviour is of special interest.

## 5.2 Analysis of Nonlinear Dynamics Behaviour

When both the upper and lower disc rotate with constant velocity, a forward whirling motion is performed by the lower disc (lateral vibrations), i.e. the center of the lower disc moves in the same direction as the rotation of the disc, and this represents a periodic solution in the fixed coordinate frame (with coordinates  $x^0$  and  $y^0$  in figure 3.20). The period time of such periodic solution corresponds to the angular velocity

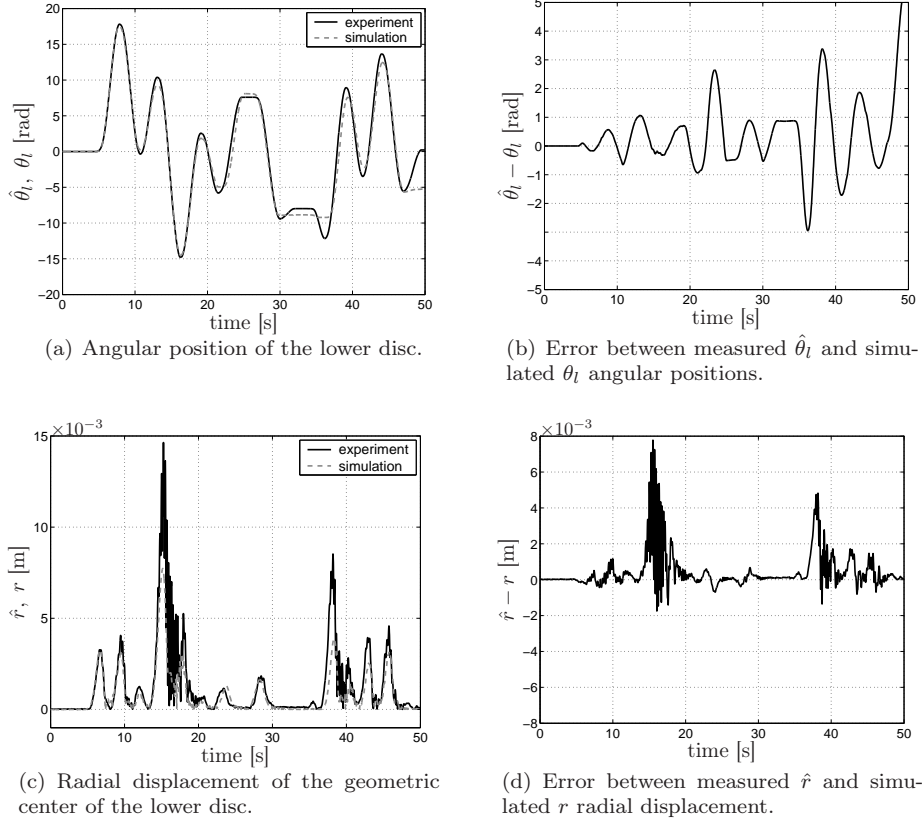


Figure 5.2: Validation signals in terms of  $\theta_l$  and  $r$  obtained for the input voltage shown in figure 3.13(b):  $R_{\theta_l}^2 = 0.9667$ ,  $R_r^2 = 0.6939$ .

of the discs. Moreover, when torsional vibrations appear in the system, then the ratio between period time of torsional vibrations and of whirling motion is, in general, an irrational number. Therefore, such motion represents a quasi-periodic motion in the fixed coordinate frame. However, in the co-rotating coordinate frame (with coordinates  $x$  and  $y$ ), in terms of which the model is formulated, the whirling motion represents an equilibrium point. Moreover, in terms of the co-rotating coordinate frame the quasi-periodic solution, in the case of fixed coordinates, appears as a periodic solution. Therefore, both the equilibrium points (sets) and the limit cycles of the model (in the co-ordinates  $x$  and  $y$ ) as well as the related stability properties are analyzed.

### 5.2.1 Equilibria and Related Stability Analysis

#### Equilibrium Points and Equilibrium Sets

In the equilibria, the time derivatives of all variables in (5.1) are zero, i.e.  $\dot{\omega}_u = \ddot{\alpha} = \dot{\alpha} = \ddot{x} = \dot{x} = \ddot{y} = \dot{y} = 0$ , for  $u = u_c$ , with  $u_c$  a constant. If we substitute this in (5.1),

then equilibria defined by  $(\omega_u, \alpha, x, y) = (\omega_{eq}, \alpha_{eq}, x_{eq}, y_{eq})$ , satisfy

$$\begin{aligned} -k_\theta \alpha_{eq} + T_{fu}(\omega_{eq}) &= k_m u_c, \\ k x_{eq} - (m_r + m_t) \omega_{eq}^2 x_{eq} - b \omega_{eq} y_{eq} - m_r e \omega_{eq}^2 \cos(\alpha_{eq}) &= 0, \\ k y_{eq} - (m_r + m_t) \omega_{eq}^2 y_{eq} + b \omega_{eq} x_{eq} - m_r e \omega_{eq}^2 \sin(\alpha_{eq}) &= 0, \\ T_{fl}(\omega_{eq}) + m_r e x_{eq} \omega_{eq}^2 \sin(\alpha_{eq}) - m_r e y_{eq} \omega_{eq}^2 \cos(\alpha_{eq}) + k_\theta \alpha_{eq} &= 0. \end{aligned}$$

Furthermore, since  $\omega_l = \omega_u + \dot{\alpha}$ , then  $\omega_l = \omega_{eq}$  in equilibrium. This system of equations is equivalent to the following system of equations:

$$\begin{aligned} & \frac{k_m u_c - T_{fu}(\omega_{eq}) - T_{fl}(\omega_{eq})}{b e^2 m_r^2 \omega_{eq}^5} \\ & - \frac{1}{(m_r + m_t)^2 \omega_{eq}^4 + b^2 \omega_{eq}^2 - 2k(m_r + m_t) \omega_{eq}^2 + k^2} = 0, \\ \alpha_{eq} &= -\frac{T_{fl}(\omega_{eq})}{k_\theta} - \frac{b e^2 m_r^2 \omega_{eq}^5}{k_\theta ((m_r + m_t)^2 \omega_{eq}^4 + b^2 \omega_{eq}^2 - 2k(m_r + m_t) \omega_{eq}^2 + k^2)}, \quad (5.2) \\ x_{eq} &= \frac{e m_r \omega_{eq}^2 (k - (m_r + m_t) \omega_{eq}^2) \cos(\alpha_{eq}) + b e m_r \omega_{eq}^3 \sin(\alpha_{eq})}{(m_r + m_t)^2 \omega_{eq}^4 + b^2 \omega_{eq}^2 - 2k(m_r + m_t) \omega_{eq}^2 + k^2}, \\ y_{eq} &= \frac{e m_r \omega_{eq}^2 (k - (m_r + m_t) \omega_{eq}^2) \sin(\alpha_{eq}) - b e m_r \omega_{eq}^3 \cos(\alpha_{eq})}{(m_r + m_t)^2 \omega_{eq}^4 + b^2 \omega_{eq}^2 - 2k(m_r + m_t) \omega_{eq}^2 + k^2}. \end{aligned}$$

Consequently, in order to find equilibria of the system, first  $\omega_{eq}$  should be computed by solving the first nonlinear equation in (5.2), then  $\alpha_{eq}$  can be computed using the second equation, and finally,  $x_{eq}$  and  $y_{eq}$  can be determined using the last two equations of (5.2). Since friction torques  $T_{fu}(\omega_u)$  and  $T_{fl}(\omega_l)$  are modelled using set-valued friction models, the following situations should be considered:

- equilibria for  $\omega_{eq} \neq 0$ , i.e. both the upper and the lower disc rotate with the same constant angular velocity  $\omega_{eq}$  and
- equilibria for  $\omega_{eq} = 0$ , i.e. both the upper and the lower disc stand still.

For  $\omega_{eq} > 0$ ,  $T_{fu}(\omega_{eq}) = T_{cu}(\omega_{eq})$  and  $T_{fl}(\omega_{eq}) = T_{cl}(\omega_{eq})$  (see expression (5.1)). Consequently, such an equilibrium point satisfies the algebraic equations

$$\begin{aligned} & \frac{k_m u_c - (T_{su} + \Delta T_{su}) - (b_u + \Delta b_u) \omega_{eq} - T_{cl}(\omega_{eq})}{b e^2 m_r^2 \omega_{eq}^5} \\ & - \frac{1}{(m_r + m_t)^2 \omega_{eq}^4 + b^2 \omega_{eq}^2 - 2k(m_r + m_t) \omega_{eq}^2 + k^2} = 0, \quad (5.3) \\ \alpha_{eq} &= -\frac{T_{cl}(\omega_{eq})}{k_\theta} - \frac{b e^2 m_r^2 \omega_{eq}^5}{k_\theta ((m_r + m_t)^2 \omega_{eq}^4 + b^2 \omega_{eq}^2 - 2k(m_r + m_t) \omega_{eq}^2 + k^2)}, \end{aligned}$$

and the last two equations of (5.2). From (5.1), the first algebraic equation of (5.3) and due to the fact that  $\omega_{eq} > 0$ , it can be concluded that system has such an equilibrium point when  $u_c > u_{\mathcal{E}p}$  where  $u_{\mathcal{E}p}$  is defined by (4.7). In general, the first equation in (5.3) can have more than one solution, but if

$$\begin{aligned} & \frac{b e^2 m_r^2 \omega_{eq}^4 ((m_r + m_t)^2 \omega_{eq}^4 + 3b^2 \omega_{eq}^2 - 6k(m_r + m_t) \omega_{eq}^2 + 5k^2)}{((m_r + m_t)^2 \omega_{eq}^4 + b^2 \omega_{eq}^2 - 2k(m_r + m_t) \omega_{eq}^2 + k^2)^2} \\ & - b_u - \Delta b_u - \left. \frac{dT_{cl}}{d\omega_l} \right|_{\omega_l = \omega_{eq}} \leq 0, \quad \forall \omega_{eq} > 0, \end{aligned} \quad (5.4)$$



then it has a unique solution. Since this is satisfied for the estimated model, the system has only one equilibrium point for  $u_c > u_{\mathcal{E}p}$ .

Similarly, for  $\omega_{eq} < 0$ , it follows that (5.2) has one equilibrium point, for the estimated model, and it is a solution of

$$k_m u_c + (T_{su} - \Delta T_{su}) - (b_u - \Delta b_u) \omega_{eq} + T_{cl}(\omega_{eq}) - \frac{b e^2 m_r^2 \omega_{eq}^5}{(m_r + m_t)^2 \omega_{eq}^4 + b^2 \omega_{eq}^2 - 2k(m_r + m_t) \omega_{eq}^2 + k^2} = 0,$$

$$\alpha_{eq} = \frac{T_{cl}(\omega_{eq})}{k_\theta} - \frac{b e^2 m_r^2 \omega_{eq}^5}{k_\theta ((m_r + m_t)^2 \omega_{eq}^4 + b^2 \omega_{eq}^2 - 2k(m_r + m_t) \omega_{eq}^2 + k^2)},$$

and the last two equations of (5.2). Moreover, the system has such equilibrium points for  $u_c < u_{\mathcal{E}n}$ , where  $u_{\mathcal{E}n}$  is defined by (4.11).

For  $\omega_{eq} = 0$ , equilibrium points are such that  $(\omega_{eq}, \alpha_{eq}, x_{eq}, y_{eq}) \in \mathcal{E}_i$  and they exist when the input voltage is  $u_{\mathcal{E}n} \leq u_c \leq u_{\mathcal{E}p}$ , where  $\mathcal{E}_i$  represents the equilibrium set defined by

$$\mathcal{E}_i = \{(\omega_{eq}, \alpha_{eq}, x_{eq}, y_{eq}) \in \mathbb{R}^4 \mid \omega_{eq} = x_{eq} = y_{eq} = 0, \alpha_{eq} \in [\alpha_{min}, \alpha_{max}]\}, \quad (5.5)$$

where  $\alpha_{min}$  and  $\alpha_{max}$  are defined by (4.15).

### Analysis of Local Stability Properties

In order to obtain local stability conditions for the equilibrium points (for  $\omega_{eq} \neq 0$ ) we can use Lyapunov's indirect method which is given in Section 2.2.1 (Theorem 2.1). The method can be only be applied when  $\omega_{eq} \neq 0$  (i.e. condition (4.16) should be satisfied). Therefore, the model of the system (5.1) is linearized around the equilibrium point and the following linear model is obtained

$$\dot{\bar{\mathbf{x}}} = \mathbf{A} \bar{\mathbf{x}},$$

with

$$\bar{\mathbf{x}} = [\omega_u - \omega_{eq} \quad x - x_{eq} \quad y - y_{eq} \quad \alpha - \alpha_{eq} \quad \dot{x} \quad \dot{y} \quad \dot{\alpha}]^T.$$

Matrix  $\mathbf{A}$  is defined by

$$\mathbf{A} = \begin{bmatrix} \mathbf{O} & \mathbf{I}' \\ -\bar{\mathbf{M}}^{-1} \bar{\mathbf{K}} & -\bar{\mathbf{M}}^{-1} \bar{\mathbf{C}} \end{bmatrix} \quad (5.6)$$

with

$$\mathbf{O} = \begin{bmatrix} 0 & 0 & 0 \\ 0 & 0 & 0 \\ 0 & 0 & 0 \end{bmatrix}, \quad \mathbf{I}' = \begin{bmatrix} 0 & 1 & 0 & 0 \\ 0 & 0 & 1 & 0 \\ 0 & 0 & 0 & 1 \end{bmatrix}.$$

The matrixes  $\bar{\mathbf{M}}$ ,  $\bar{\mathbf{C}}$  and  $\bar{\mathbf{K}}$  are obtained from the linearization of the model (5.1) for  $\omega_{eq} > 0$ :

$$\bar{\mathbf{M}} = \begin{bmatrix} J_u & 0 & 0 & 0 \\ \bar{m}_{21} & m_r + m_t & 0 & -m_r e \sin(\alpha_{eq}) \\ \bar{m}_{31} & 0 & m_r + m_t & m_r e \cos(\alpha_{eq}) \\ \bar{m}_{41} & -m_r e \sin(\alpha_{eq}) & m_r e \cos(\alpha_{eq}) & J_C + m_r e^2 \end{bmatrix},$$

$$\begin{aligned} \bar{m}_{21} &= -(m_r + m_t)y_{eq} - m_r e \sin(\alpha_{eq}), \\ \bar{m}_{31} &= (m_r + m_t)x_{eq} + m_r e \cos(\alpha_{eq}), \\ \bar{m}_{41} &= m_r e x_{eq} \cos(\alpha_{eq}) + m_r e y_{eq} \sin(\alpha_{eq}) + J_C + m_r e^2 \end{aligned}$$

$$\bar{\mathbf{C}} = \begin{bmatrix} b_u + \Delta b_u & 0 & 0 & 0 \\ \bar{c}_{21} & b & -2(m_r + m_t)\omega_{eq} & \bar{c}_{24} \\ \bar{c}_{31} & 2(m_r + m_t)\omega_{eq} & b & \bar{c}_{34} \\ \bar{c}_{41} & -\bar{c}_{24} & -\bar{c}_{34} & d_l \end{bmatrix},$$

$$\begin{aligned} \bar{c}_{21} &= -2 m_r e \omega_{eq} \cos(\alpha_{eq}) - 2(m_r + m_t)x_{eq}\omega_{eq} - b y_{eq}, \\ \bar{c}_{24} &= -2 m_r e \omega_{eq} \cos(\alpha_{eq}), \\ \bar{c}_{31} &= -2 m_r e \omega_{eq} \sin(\alpha_{eq}) - 2(m_r + m_t)y_{eq}\omega_{eq} + b x_{eq}, \\ \bar{c}_{34} &= -2 m_r e \omega_{eq} \sin(\alpha_{eq}), \\ \bar{c}_{41} &= \frac{2 m_r^2 e^2 \omega_{eq}^4 b}{(m_r + m_t)^2 \omega_{eq}^4 + b^2 \omega_{eq}^2 - 2 k(m_r + m_t)\omega_{eq}^2 + k^2} + d_l, \end{aligned}$$

$$\bar{\mathbf{K}} = \begin{bmatrix} 0 & 0 & -k_\theta \\ -(m_r + m_t)\omega_{eq}^2 + k & -b \omega_{eq} & m_r e \omega_{eq}^2 \sin(\alpha_{eq}) \\ b \omega_{eq} & -(m_r + m_t)\omega_{eq}^2 + k & -m_r e \omega_{eq}^2 \cos(\alpha_{eq}) \\ m_r e \omega_{eq}^2 \sin(\alpha_{eq}) & -m_r e \omega_{eq}^2 \cos(\alpha_{eq}) & k_{44} \end{bmatrix},$$

$$k_{44} = k_\theta + \frac{m_r^2 e^2 \omega_{eq}^4 (k - (m_r + m_t)\omega_{eq}^2)}{(m_r + m_t)^2 \omega_{eq}^4 + b^2 \omega_{eq}^2 - 2 k(m_r + m_t)\omega_{eq}^2 + k^2},$$

where  $d_l$  represents the friction damping present at the lower disc when  $\omega_l = \omega_{eq}$  (see expression (4.18)). Consequently, the nonlinear system (5.1) is asymptotically stable if matrix  $\mathbf{A}$  in (5.6) is Hurwitz.

In order to analyze the stability properties of the equilibrium set (5.5) we use Lyapunov's stability theorem (Theorem 2.2 in Section 2.2.1). Based on proposed the kinetic and potential energy of the system defined in (3.13), the following candidate Lyapunov function is considered:

$$V_i(\mathbf{x}_{i1}, \mathbf{x}_{i2}, \mathbf{x}_{i1eq}, \mathbf{x}_{i2eq}) = \mathcal{T}(\mathbf{x}_{i1}, \mathbf{x}_{i2} - \mathbf{x}_{i2eq}) + \mathcal{V}(\mathbf{x}_{i1} - \mathbf{x}_{i1eq}), \quad (5.7)$$

where:

$$\begin{aligned} \mathbf{x}_{i1} &= [x \quad y \quad \alpha]^T, \\ \mathbf{x}_{i2} &= [\omega_u \quad \dot{x} \quad \dot{y} \quad \dot{\alpha}]^T. \end{aligned} \quad (5.8)$$

From (3.13) we see that  $\mathcal{T}(\mathbf{q}, \dot{\mathbf{q}})$  and  $\mathcal{V}(\mathbf{q})$ , where  $\mathbf{q}$  represents generalized coordinates defined by (3.12), are not dependent on  $\theta_u$ . Consequently, they can be rewritten as  $\mathcal{T}(\mathbf{x}_{i1}, \mathbf{x}_{i2})$  and  $\mathcal{V}(\mathbf{x}_{i1})$ , where  $\mathbf{x}_{i1}$  and  $\mathbf{x}_{i2}$  are defined by (5.8). In Appendix C, we derive that the time derivative of  $V_i$  obeys:

$$\begin{aligned} \dot{V}_i(\mathbf{x}_{i1}, \mathbf{x}_{i2}, \mathbf{x}_{i1eq}, \mathbf{x}_{i2eq}) &= -(T_{fu}(\omega_u) - T_{fu}(0))\omega_u - (T_{fl}(\omega_l) - T_{fl}(0))\omega_l \\ &\quad - b \mathbf{x}'_i{}^T P(x, y) \mathbf{x}'_i, \end{aligned} \quad (5.9)$$

with

$$\mathbf{x}'_i = [\omega_u \quad \dot{x} \quad \dot{y}]^T, \quad P(x, y) = \begin{bmatrix} x^2 + y^2 & -y & x \\ -y & 1 & 0 \\ x & 0 & 1 \end{bmatrix}.$$

The friction torque  $T_{fu}(\omega_u)$  is a monotonically increasing function (see figure 3.14). Then, since 0, 1 and  $x^2 + y^2 + 1$  are the eigenvalues of matrix  $P(x, y)$ , matrix  $P(x, y)$  is positive semidefinite. Consequently, the following incremental sector condition is satisfied

$$-(T_{fu}(\omega_u) - T_{fu}(0))\omega_u - b\mathbf{x}'_i{}^T P(x, y)\mathbf{x}'_i \leq 0, \quad (5.10)$$

for every  $\omega_u$ ,  $\dot{x}$  and  $\dot{y}$ . From (5.9), we see that the sign of  $\dot{V}_i(\mathbf{x}_{i1}, \mathbf{x}_{i2}, \mathbf{x}_{i1eq}, \mathbf{x}_{i2eq})$ , thus the stability condition of the equilibrium set  $\mathcal{E}_i$ , depends only on the sign of  $-(T_{fl}(\omega_l) - T_{fl}(0))\omega_l$ . Therefore, the stability condition of the equilibrium set  $\mathcal{E}_i$  (5.5) can be discussed in a similar manner as discussed in Section 4.2.1 for the system when only torsional vibrations can occur, despite the fact that the system considered in this chapter is of a higher order. According to such discussion the following can be concluded:

- If the friction torque  $T_{fl}(\omega_l)$  is as shown in figure 4.4(a) (a monotonically increasing function), then the equilibrium set  $\mathcal{E}_i$  is globally asymptotically stable.
- If the friction torque  $T_{fl}(\omega_l)$  is as shown in figures 4.5(a) and 4.5(c) (a humped friction model), then the equilibrium set  $\mathcal{E}_i$  is locally asymptotically stable.
- If the friction torque  $T_{fl}(\omega_l)$  is as shown in figure 4.6(a), then almost all equilibrium points from the equilibrium set  $\mathcal{E}_i$  can be shown to be locally stable except the boundary points of the set where  $\alpha_{eq} = -T_{sl}/k_\theta$  or  $\alpha_{eq} = T_{sl}/k_\theta$ . However, we cannot show the stability property of the set as a whole. This degradation of the (proven) stability properties is directly related to the fact that negative damping occurs for infinitesimally small values of  $\omega_l$  in  $T_{fl}(\omega_l)$ .

### Equilibrium Branches

Since in the set-up both torsional and lateral vibrations appear, we are interested in the angular velocity  $\omega_l$  and radial displacement  $r$  of the lower disc in steady-state for different constant input voltages  $u_c$ . As already discussed, when  $u_c > u_{\mathcal{E}p}$  ( $\omega_{eq} > 0$ ),  $\omega_l$  in steady-state can be obtained by solving the first algebraic equation in (5.3). The corresponding radial displacement of the center of the lower disc (in equilibrium) can be derived from the third and fourth equation in (5.2) as:

$$r_{eq} = \sqrt{x_{eq}^2 + y_{eq}^2} = \frac{m_r e \omega_{eq}^2}{\sqrt{(m_r + m_t)^2 \omega_{eq}^4 + b^2 \omega_{eq}^2 - 2k(m_r + m_t)\omega_{eq}^2 + k^2}}, \quad (5.11)$$

since  $(m_r + m_t)^2 \omega_{eq}^4 + b^2 \omega_{eq}^2 - 2k(m_r + m_t)\omega_{eq}^2 + k^2 > 0$  for every  $\omega_{eq} \in \mathbb{R}$  for the estimated parameters of the set-up. If we analyze expression (5.11) the following is obtained:

$$\begin{aligned} r_{eq} &= 0, \quad \text{for } \omega_{eq} = 0, \\ r_{eq} &\rightarrow \frac{m_r e}{m_r + m_t}, \quad \text{for } \omega_{eq} \rightarrow \infty. \end{aligned}$$

Moreover, the so-called critical speed  $\omega_c$  [Lee, 1993], i.e. the angular velocity at which the amplitude of lateral vibrations due to an unbalance at the lower disc reaches a local maximum, is given by:

$$\omega_c = \sqrt{\frac{2k^2}{2k(m_r + m_t) - b^2}}. \quad (5.12)$$

For that angular velocity, radial displacement of the lower disc in steady-state is

$$r_c = \frac{2km_re}{b\sqrt{4k(m_r + m_t) - b^2}} \quad (5.13)$$

and the corresponding input voltage is

$$u_{cc} = \frac{(b_u + \Delta b_u)\omega_c + T_{su} + \Delta T_{su} + T_{cl}(\omega_c)}{k_m} + \frac{be^2m_r^2\omega_c^5}{k_m((m_r + m_t)^2\omega_c^4 + b^2\omega_c^2 - 2k(m_r + m_t)\omega_c^2 + k^2)}. \quad (5.14)$$

The equilibrium branches, with respect to  $\omega_{eq}$ , can be constructed by solving the first algebraic non-linear equation from (5.2), for various  $u_c$ . In general, that equation can only be solved numerically. Then based on the solution, we can construct the equilibrium branch with respect to  $r_{eq}$ .

In the sequel we consider the equilibrium branches of the estimated model. Based on the performed stability analysis of the equilibrium points and sets, in figures 5.3 and 5.4 equilibrium branches for different constant input voltages  $u_c > 0$  are plotted. Since we are interested in the behaviour of the velocity  $\omega_l$  and radial displacement  $r$  of the lower disc for different constant input voltages, we constructed equilibrium branches for both  $\omega_l$  (figure 5.3) and  $r$  (figure 5.4).

Given the fact that for very low input voltages the radial displacement of the lower disc is very small (see figure 5.4(b)), it can be expected that the influence of the dynamics in lateral direction to the dynamics in torsional direction, is very small. Consequently, it is expected that the equilibrium branches for low input voltages are almost identical to the equilibrium branches when only torsional vibrations appears (i.e. when lower disc is fixed in lateral direction). This is indeed the case. Namely, according to the results shown in figures 5.3 and 5.4 the following can be concluded:

- For  $u_c \leq u_{\mathcal{E}p}$ , with  $u_{\mathcal{E}p}$  given by (4.7) (point *A* in figures 5.3(b) and 5.4(b)), the system is in stick phase in steady-state, i.e. the system has a locally asymptotically stable equilibrium set described by (5.5) and (4.15) (equilibrium branch  $e_1$  in figures 5.3(b) and 5.4(b)).
- For  $u_c = u_{\mathcal{E}p}$  (point *A* in the bifurcation diagrams) the locally asymptotically stable equilibrium set (5.5) condenses to a locally asymptotically stable isolated equilibrium point and no change of stability properties occurs.
- The system has a unique equilibrium point for  $u_c > u_{\mathcal{E}p}$  since condition (5.4) is satisfied. Moreover, according to the stability analysis, a stable equilibrium branch  $e_2$  appears (figures 5.3(b) and 5.4(b)), for which  $\omega_{eq}$  and  $r_{eq}$  increase.

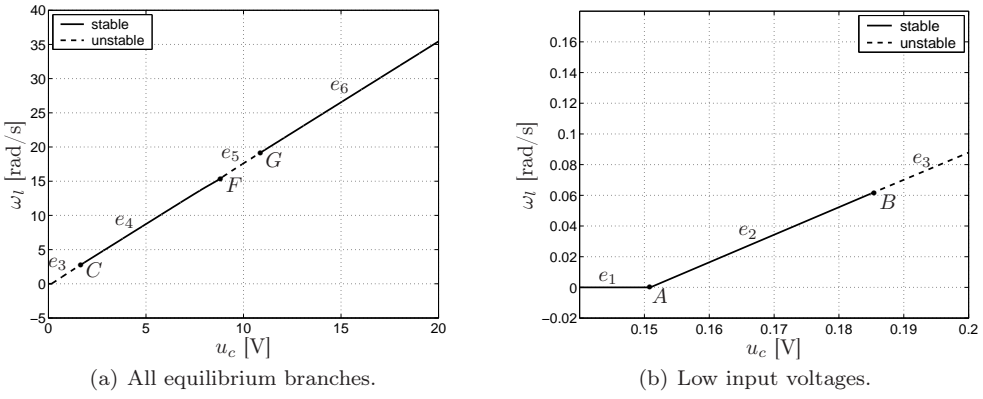


Figure 5.3: Equilibrium branches of the set-up - angular velocity  $\omega_l$ .

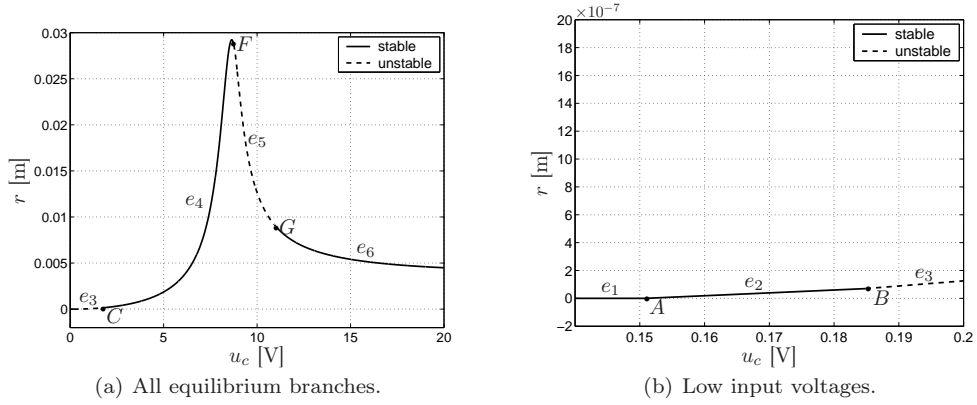


Figure 5.4: Equilibrium branches for low input voltages - radial displacement  $r$ .

- If  $u_c$  increases from point  $B$  in figures 5.3(b) and 5.4(b), the system exhibits an unstable equilibrium point (equilibrium branch  $e_3$ ) and the corresponding  $\omega_{eq}$  and  $r_{eq}$  increase again.
- At point  $C$ , the equilibrium point changes its stability and a stable equilibrium branch  $e_4$  appears (figures 5.3(a) and 5.4(a)). For an equilibrium point at the equilibrium branch  $e_4$ , more specifically for  $u_c = 3$  V, a trajectory of the center of the lower disc in steady-state is shown in figures 5.5(a) (fixed coordinate frame) and 5.5(b) (co-rotating coordinate frame). The time signals for  $\omega_l$ ,  $r$  and  $x^0$ ,  $y^0$  are shown in figures 5.5(c) and 5.5(d). From figure 5.5(d) it can be noticed that lateral vibrations are present in the system in  $x^0$  and  $y^0$  direction (fixed coordinate frame). Moreover, the period time of those vibrations is equal to the period time of the rotation of both discs.
- In points  $B$  and  $C$  a change in stability properties occurs. Namely, a pair of complex conjugate eigenvalues, related to the linearisation of the nonlinear dynamics of (5.1) around the equilibrium point, cross the imaginary axis. Therefore, Hopf bifurcations occur at these points.

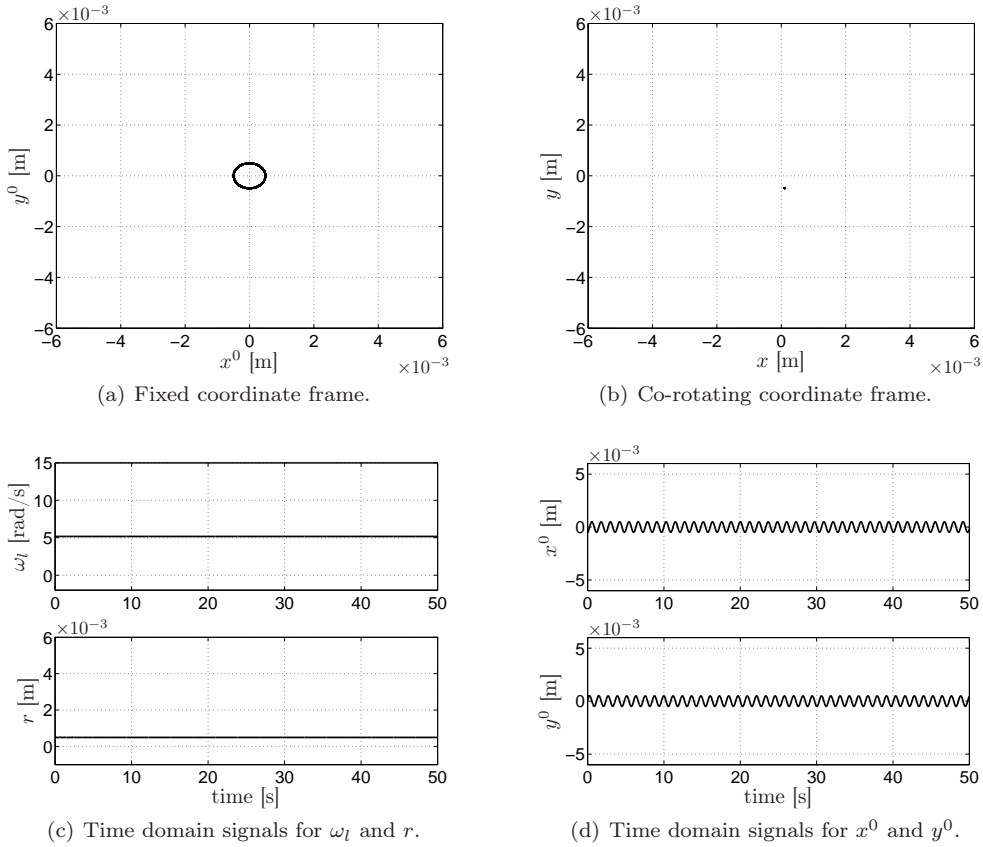


Figure 5.5: An equilibrium point on the equilibrium branch  $e_4$ :  $u_c = 3$  V.

- At point  $F$ , the equilibrium point loses stability and an unstable equilibrium branch  $e_5$  occurs (figures 5.3(a) and 5.4(a)).
- If  $u_c$  increases further, at point  $G$  a stable equilibrium branch  $e_6$  appears.
- In points  $F$  and  $G$  a change in stability properties occurs, i.e. a pair of complex conjugate eigenvalues related to the linearisation of the nonlinear dynamics of (5.1) around the equilibrium point, cross the imaginary axis. Therefore, Hopf bifurcations occur at these points.

The analysis shows that the unstable equilibrium branch  $e_3$ , in figure 5.3, is almost identical to the equilibrium branch  $e_3$  which appears when only torsional and no lateral vibrations are present in the set-up (see figure 4.9). Therefore, we can conclude that such unstable branch occurs due to the negative damping in the friction torque. For higher input voltages the velocity at the lower disc is such that viscous friction is dominant in the friction characteristic. However, even for those input voltages an unstable branch occurs (equilibrium branch  $e_5$ ). This represents an indication that such instability is due to the interaction between torsional and lateral dynamics in the system. In the sequel, we analyze the dynamics in that region in more details.

### 5.2.2 Bifurcation Diagram of the System

According to the previous analysis, Hopf bifurcation points occur at points  $B$ ,  $C$ ,  $F$  and  $G$ . Next, using a path following technique in combination with a shooting method [Ascher et al., 1995; Parker and Chua, 1989], limit cycles are computed numerically for the estimated model of the system. The results are shown in bifurcation diagrams in figure 5.6. Moreover, since equilibrium branches and bifurcation points that occur at low input voltages cannot be seen in figure 5.6, we present them in figure 5.7. In those figures, the maximal and minimal values of  $\omega_l$  (figures 5.6(a) and 5.7(a)) and  $r$  (figure 5.6(b) and 5.7(b)) are plotted when a limit cycle is found. The Floquet multipliers, corresponding to these limit cycles, are numerically computed and are used to determine the local stability properties of these limit cycles.

If we compare the obtained bifurcation diagram in figure 5.6(a), for  $u_c \in [0 \text{ V}, 5 \text{ V}]$ , with the bifurcation diagram shown in figure 4.9(a) of the set-up when only torsional and no lateral vibrations are present, we recognize the same type of periodic branches and bifurcation points:

- From bifurcation point  $B$  an unstable equilibrium branch  $e_3$  and an unstable periodic branch  $p_1$  arises (see figure 5.7). Point  $B$  represents a smooth subcritical Hopf bifurcation point [Khalil, 2000; Sastry, 1999; Strogatz, 2000] because the unstable periodic branch  $p_1$  consists of limit cycles without stick-slip.
- The unstable periodic branch  $p_1$  is connected to a locally stable periodic branch  $p_2$  at the point  $D$ , which represents a discontinuous fold bifurcation point, since the periodic branch  $p_2$  consists of stable limit cycles which represent torsional vibrations with stick-slip (see figure 5.7(a)). Moreover, a Floquet multiplier crosses through the point  $+1$  in the complex plane.
- The periodic branch  $p_2$  consists of locally stable limit-cycles with stick-slip due to the non-smooth nonlinearities in the friction torque at the lower disc. A trajectory of the center of the lower disc, when the system is on the periodic branch  $p_2$  ( $u_c = 3 \text{ V}$ ), is shown in figures 5.8(a) in the fixed coordinate frame, and 5.8(b) in the co-rotating coordinate frame. Time series of the angular velocity  $\omega_l$ , lateral displacements  $r$ ,  $x$  and  $y$  in the fixed coordinate frame are shown in figures 5.8(c) and 5.8(d). For  $u_c = 3 \text{ V}$ , the equilibrium point (the branch  $e_4$  - see figure 5.5) and the periodic branch (the branch  $p_2$  - see figure 5.8) coexist. If we compare results shown in figures 5.5 and 5.8, we see that torsional and lateral vibrations are significantly higher when the system is at the periodic branch  $p_2$ . Furthermore, since the ratio between period time of torsional vibrations and the period time which corresponds to angular velocity is an irrational number, a quasi-periodic solution occurs in the fixed coordinate frame (see figure 5.8(a) and compare it with 5.5(a) where pure whirling occurs). Moreover, while the lateral vibrations are periodic when the system is on the branch  $e_4$  (see figure 5.5(d)), lateral vibrations on the periodic branch  $p_2$  are quasi-periodic as shown in figures 5.8(a) and 5.8(d).
- For some higher constant input voltage  $u_c$  (point  $E$  in figure 5.6) the locally stable periodic branch  $p_2$  loses stability and an unstable periodic branch appears (periodic branch  $p_3$  in figure 5.6) through another discontinuous fold bifurcation (point  $E$  in figure 5.6).

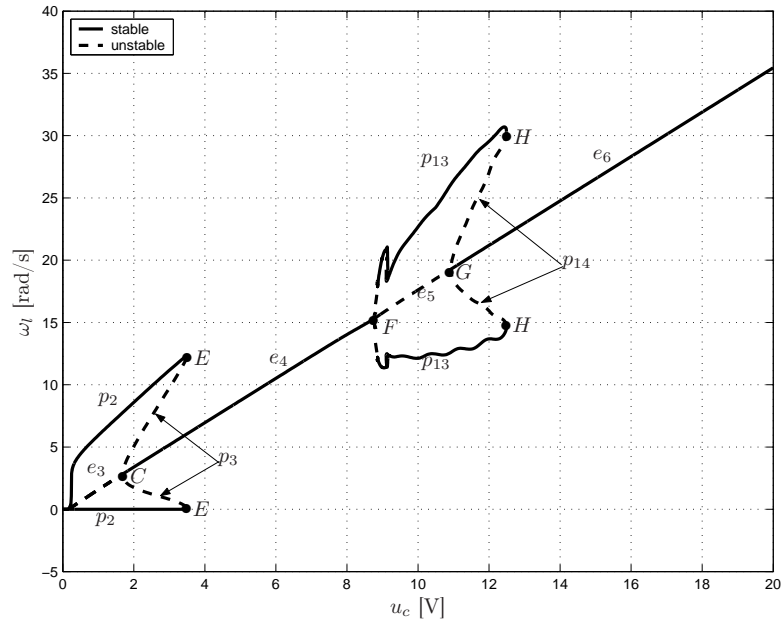
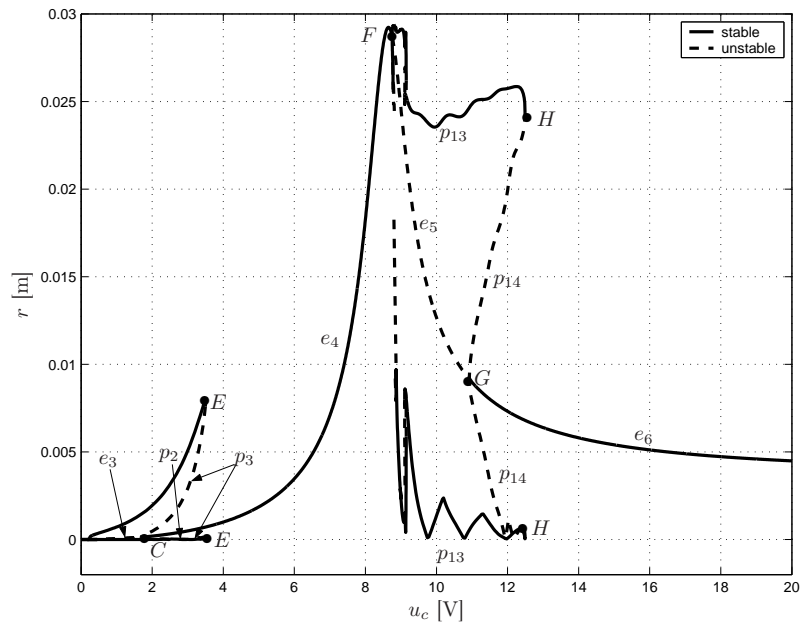
(a) Angular velocity  $\omega_1$ .(b) Radial displacement  $r$ .

Figure 5.6: Bifurcation diagram of the experimental set-up when both torsional and lateral vibrations are present.



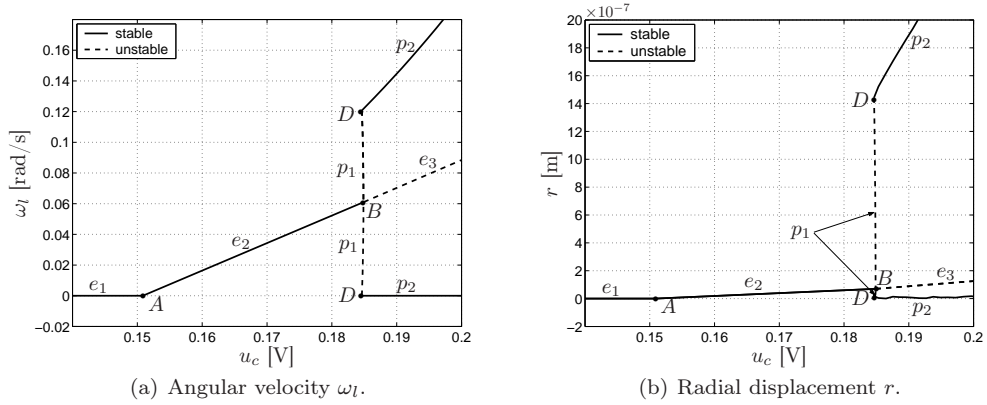


Figure 5.7: Bifurcation diagram for low input voltages.

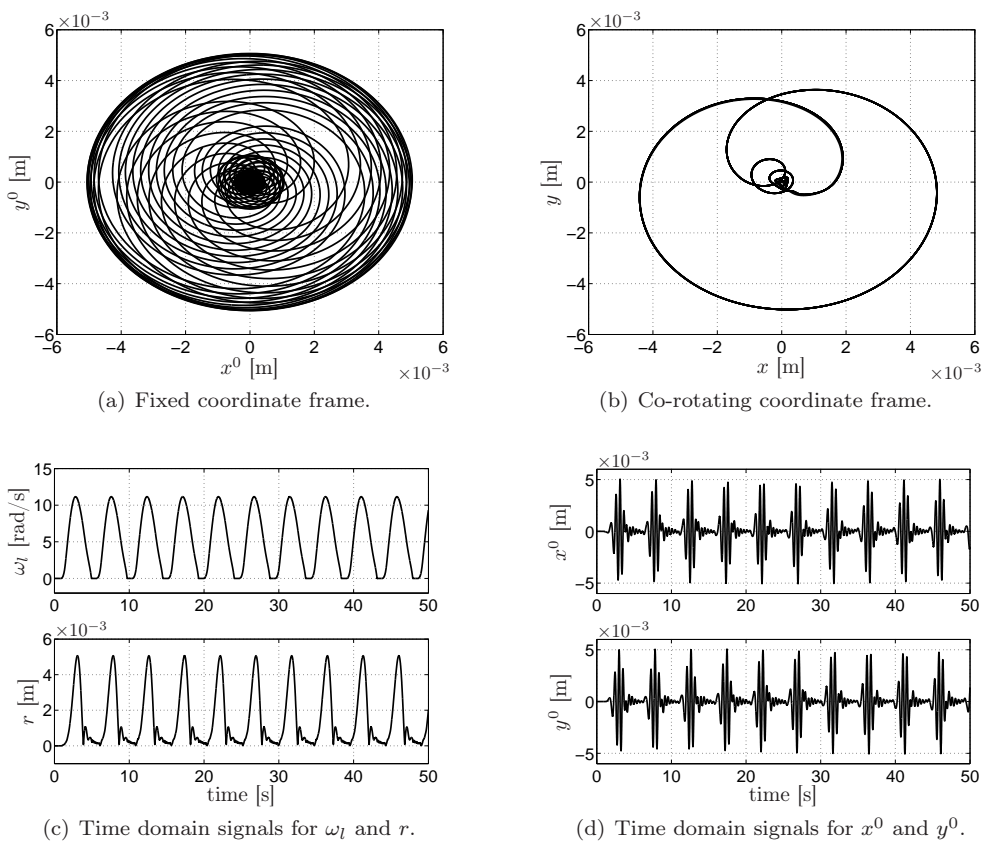
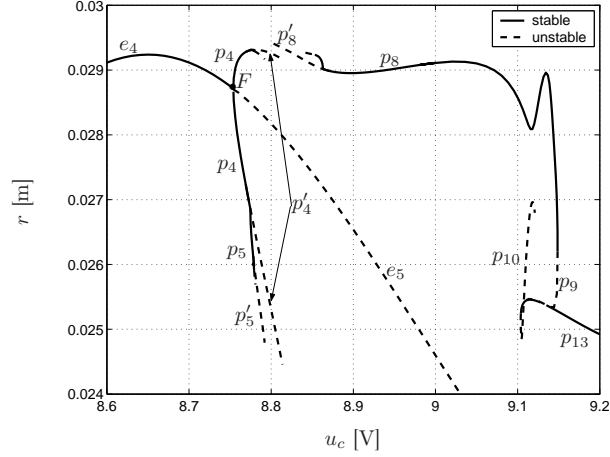
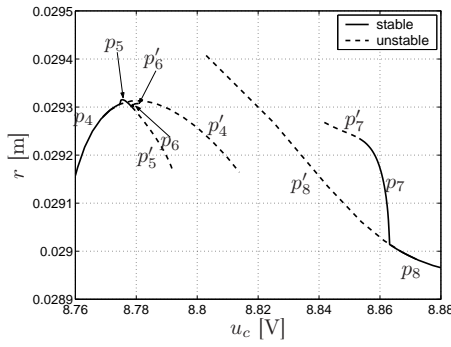
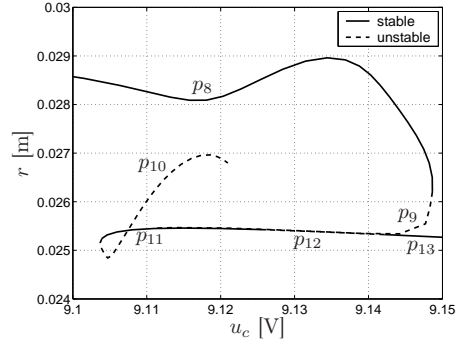


Figure 5.8: A periodic solution on the periodic branch  $p_2$ :  $u_c = 3$  V.

(a) Whole bifurcation diagram, for  $u_c \in (8.6 \text{ V}, 9.2 \text{ V})$ .(b)  $u_c \in (8.76 \text{ V}, 8.88 \text{ V})$ .(c)  $u_c \in (9.1 \text{ V}, 9.15 \text{ V})$ .Figure 5.9: Bifurcation diagram of radial displacement  $r$ , for  $u_c \in (8.6 \text{ V}, 9.2 \text{ V})$ .

- The unstable periodic branch  $p_3$  is connected to the equilibrium branches  $e_3$  and  $e_4$  in the smooth subcritical Hopf bifurcation point  $C$ .

For even higher input voltages, the velocity at the lower disc  $\omega_l$  in steady-state continues to increase. For such high angular velocities, viscous friction is dominant in the friction at the lower disc (see the estimated friction torque  $T_{f1}(\omega_l)$  in figure 4.1). However, according to the steady-state analysis the following periodic solutions are observed in the bifurcation diagrams in figure 5.6:

- From bifurcation point  $F$  an unstable equilibrium branch  $e_5$  arises as well as a stable periodic branch  $p_4$  (see figure 5.9(a)). Point  $F$  represents a supercritical Hopf bifurcation point. A trajectory of the center of the lower disc in steady-state, when the system is on the periodic branch  $p_4$ , is shown in figures 5.10(a), in the fixed coordinate frame, and 5.10(b), in the co-rotating coordinate frame. Time series of the radial displacement  $r$  and angular velocity  $\omega_l$  in steady-state are shown in figure 5.10(c).

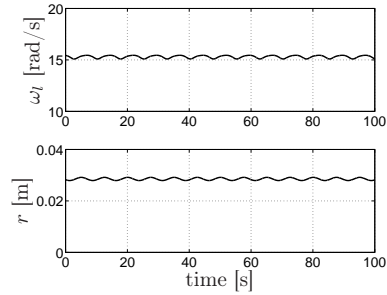
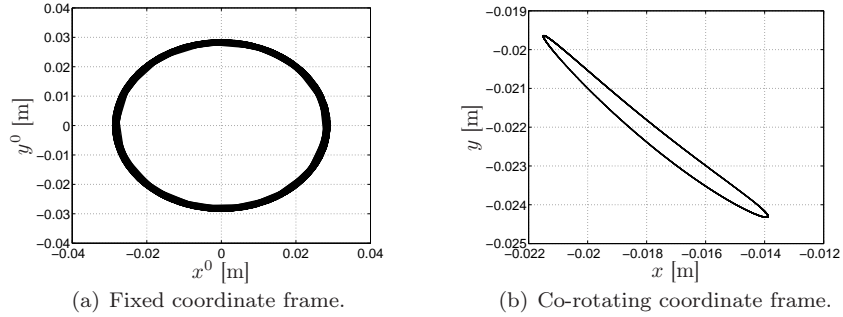


Figure 5.10: A periodic solution on the periodic branch  $p_4$ :  $u_c = 8.76$  V.

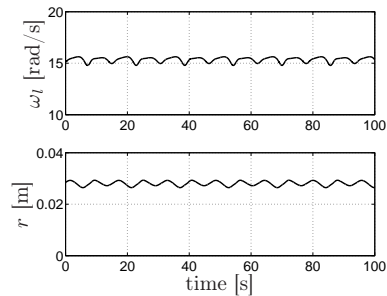
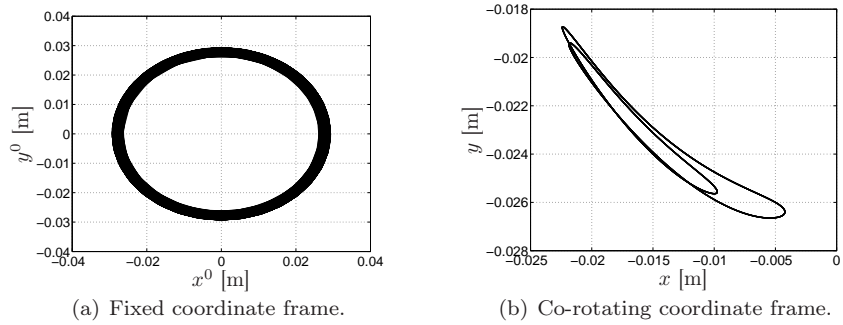


Figure 5.11: A period-2 solution on the periodic branch  $p_5$ :  $u_c = 8.776$  V.

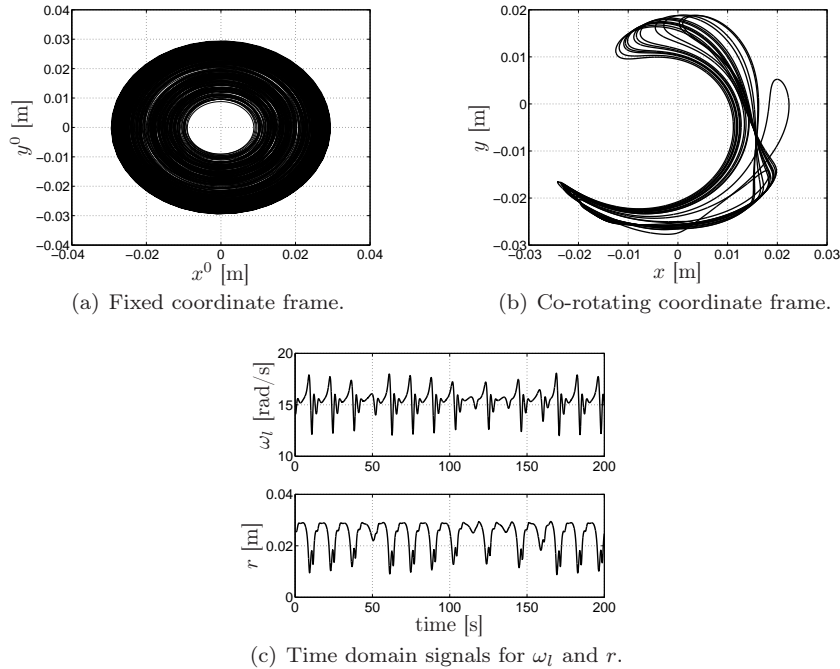


Figure 5.12: A solution reached via period doubling cascade  $p_4 - p_5 - p_6$ :  $u_c = 8.82$  V.

- The stable periodic branch  $p_4$  is connected to an unstable periodic  $p'_4$  via a period doubling bifurcation point [Khalil, 2000; Van Campen, 2000]. Consequently, from that point, a stable period-doubled branch  $p_5$  arises, as shown in figure 5.9(a). A related trajectory with the time-domain signals of a periodic solution from the branch  $p_5$  are shown in figure 5.11.
- The periodic branch  $p_5$  is connected to an unstable periodic branch  $p'_5$ , via another period doubling bifurcation point (figure 5.9(b)).
- Then, from that point, a stable period-doubled periodic branch  $p_6$  arises, which is again connected to an unstable branch  $p'_6$  via another period doubling bifurcation point (figure 5.9(b)).
- The periodic branches  $p_4 - p_5 - p_6$  form a so-called period doubling cascade which, according to Strogatz [2000], leads to a chaos. From that region, which is reached via the period doubling cascade, we present a trajectory of the center of the lower disc in steady-state in figures 5.12(a) (fixed coordinate frame) and in 5.12(b) (co-rotating coordinate frame). The related time signals for  $r$  and  $\omega$  are shown in figure 5.12(c).
- If we increase  $u_c$  even further, unstable periodic branches  $p'_7$  and  $p'_8$  appear. The unstable branch  $p'_7$  is connected to a stable branch  $p_7$  via an period doubling bifurcation point, as shown in figure 5.9(b).
- The unstable branch  $p'_8$  and the stable period-doubled branch  $p_7$  are connected to a stable periodic branch  $p_8$ , via another period doubling bifurcation ( $p_8$  and

$p'_8$  have the same period time in the bifurcation point). Consequently,  $p_8 - p_7$  represents a period doubling cascade which leads to chaos, see [Strogatz, 2000].

- The stable branch  $p_8$  is connected to an unstable periodic branch  $p_9$  via a fold bifurcation point, see figure 5.9(c).
- An unstable branch  $p_{10}$  is connected to a stable  $p_{11}$  branch, via a secondary Hopf bifurcation (figure 5.9(c)). Branches  $p_{10}$  and  $p_{11}$  consists of limit cycles which have the same period time in the bifurcation point.
- The stable branch  $p_{11}$  is connected to an unstable  $p_{12}$  branch, through a period doubling bifurcation. Then,  $p_{12}$  is connected to a stable periodic branch  $p_{13}$ , via another period doubling bifurcation point. The branches  $p_{11}$  and  $p_{12}$  have the same period time in the bifurcation point. The same holds for the branches  $p_{12}$  and  $p_{13}$ .
- At the point  $H$  the stable periodic branch  $p_{13}$  is connected to an unstable branch  $p_{14}$  through a fold bifurcation point (figure 5.6).
- The unstable periodic branch  $p_{14}$  is connected to the equilibrium branches  $e_5$  and  $e_6$  in the subcritical Hopf bifurcation point  $G$ .

Finally, since all periodic branches from  $p_4$  to  $p_{14}$  consists of periodic solutions which do not touch the line  $\omega_l = 0$ , all related bifurcation points in that region are smooth bifurcations.

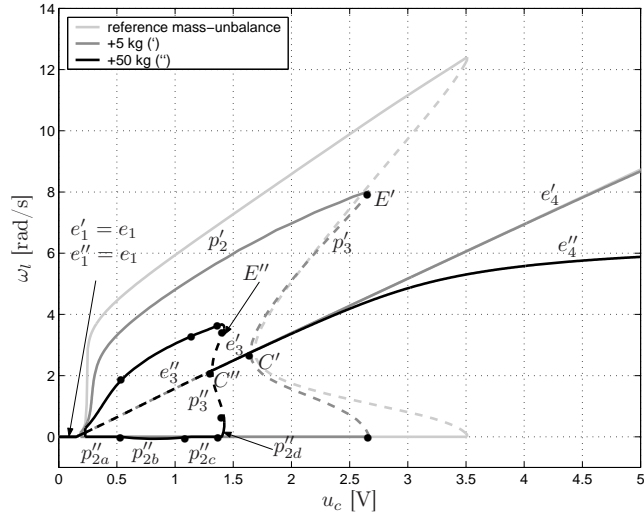
The bifurcation diagrams certainly do not show all periodic branches that exist. For example, not all period-doubled branches are calculated and also other branches may be missing in the bifurcation diagram. However, the presented bifurcation analysis shows that for input voltages  $u_c > 5$  V, which is in fact outside the working region of the experimental set-up, a rich variety of interesting qualitative changes in the dynamic behaviour can appear when the input voltage is changed.

### 5.2.3 Friction-Induced Vibrations

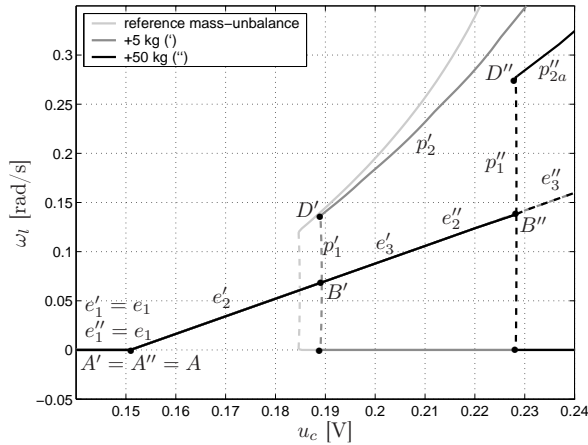
We have already concluded that the vibrations, which are observed in the model for  $u_c \in [0 \text{ V}, 5 \text{ V}]$ , are induced by friction. Such vibrations are analyzed in Chapter 4 when the lower disc is fixed in lateral direction. The main cause for lateral vibrations is a mass-unbalance. Therefore, we analyze the influence of the level of mass-unbalance to the steady-state behaviour of the system for  $u_c \in [0 \text{ V}, 5 \text{ V}]$ . Moreover, we investigate this type of parameter change since it will be shown that it affects significantly the friction-induced limit-cycling.

Hereto, we add additional mass  $\Delta m$  at a distance of  $d_\Delta = 0.1$  m from the center of the lower disc in the direction of the already existing unbalance. Consequently, the parameters  $e$ ,  $m_r$  and  $J_C$  of the estimated model (see table 5.1) are changed and the new related parameters  $e_\Delta$ ,  $m_{r\Delta}$  and  $J_{C\Delta}$  are:

$$\begin{aligned} e_\Delta &= \frac{m_r e + d_\Delta \Delta m}{m_r + \Delta m}, \\ m_{r\Delta} &= m_r + \Delta m, \\ J_{C\Delta} &= J_C + d_\Delta^2 \Delta m. \end{aligned} \tag{5.15}$$



(a) Bifurcation diagrams.



(b) Bifurcation diagrams at low input voltages.

Figure 5.13: Bifurcation diagrams for various levels of mass-unbalance - angular velocity  $\omega_l$ :  $u_c \in [0 \text{ V}, 5 \text{ V}]$ .

In figure 5.13 and 5.14, bifurcation diagrams are shown for the estimated system (light-grey line), for  $\Delta m = 5 \text{ kg}$  (dark-grey line), for  $\Delta m = 50 \text{ kg}$  (black line). Of course, adding an additional mass  $\Delta m = 50 \text{ kg}$  to the lower disc, with the estimated mass being  $m_r = 9.9137 \text{ kg}$ , is practically impossible. However, we analyze that case in order to observe the effect of additional mass-unbalance to the steady-state behaviour of the set-up. According to the obtained results the following can be concluded:

- Due to an additional mass-unbalance, the region (in terms of the input voltage) where friction-induced torsional vibrations appear, decreases (see figure 5.13). Namely, if mass-unbalance increases, the first fold and Hopf bifurcation points occur at the higher input voltages (compare the fold bifurcations  $D'$  and  $D''$  and the Hopf bifurcation points  $B'$  and  $B''$  in figure 5.13(b)). Furthermore,

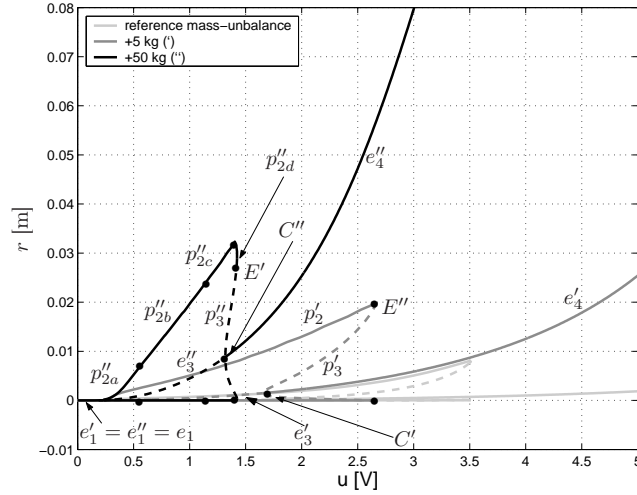


Figure 5.14: Bifurcation diagrams for various levels of mass-unbalance - radial displacement  $r$ :  $u_c \in [0 \text{ V}, 5 \text{ V}]$ .

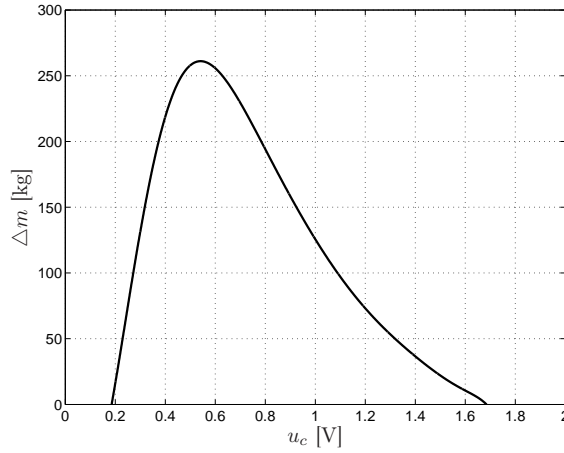


Figure 5.15: The regions for which the equilibrium points of the system are locally stable and unstable.

the second fold and Hopf bifurcation points occur at the lower input voltages (compare the fold bifurcation points  $E'$  and  $E''$ , and the Hopf bifurcations  $C'$  and  $C''$  in figure 5.13(a)). Therefore, the region in which the torsional vibrations can occur is smaller when the mass unbalance is increased. In figure 5.15 we presented the position of the first and the second Hopf bifurcations for various levels of the added mass-unbalance, i.e. we show the region, in which unstable equilibria occur for various  $\Delta m$  and for  $u_c \in [0 \text{ V}, 5 \text{ V}]$ . This figure clearly display the influence of the level of mass unbalance on friction induced instabilities in torsional direction.

- From figure 5.14 it can be concluded that when the mass-unbalance increases,

the amplitude of lateral vibrations increases both for the input voltages where torsional vibrations occur (compare periodic branch  $p'_2$  with periodic branches  $p''_{2a}$ ,  $p''_{2b}$ ,  $p''_{2c}$  and  $p''_{2d}$  in figure 5.14) and where no torsional vibrations appear (compare equilibrium branches  $e'_4$  and  $e''_4$  in the same figure).

- In figure 5.13, we see that the periodic branch  $p'_2$ , for  $\Delta m = 5$  kg, splits to four branches  $p''_{2a}$ ,  $p''_{2b}$ ,  $p''_{2c}$  and  $p''_{2d}$ , for  $\Delta m = 50$  kg. The periodic branches  $p''_{2a}$  and  $p''_{2c}$  consists of torsional vibrations with stick-slip, the branch  $p''_{2d}$  represents torsional vibrations without stick-slip. The branch  $p''_{2b}$  represents such torsional vibrations where the lower disc starts to rotate in the opposite direction during one period time (i.e.  $\min(\omega_l) < 0$  in a limit-cycle on  $p''_{2b}$ ).
- In figure 5.13(a) we notice that for  $\Delta m = 50$  kg  $\partial\omega_l/\partial u_c$  decreases in steady-state for increasing  $u_c$ , see the equilibrium branch  $e''_4$ . In the sequel we analyze that phenomenon when addressing the vibrations which occur at higher input voltages and are purely due to coupling between the torsional and lateral mode in the system.

The effect of decreasing of friction-induced torsional vibrations when the mass-unbalance is increased can be explained in the following way. When no mass-unbalance is present at the lower disc, the range in which friction-induced torsional vibrations can occur is determined by a subtle balance between negative damping at lower velocities and viscous friction at higher velocities. Namely, the energy which is released due to the negative damping in the friction characteristics at the lower disc is mainly transformed to the kinetic energy at the lower disc (i.e.  $\omega_l$ ) and to the potential energy in the low-stiffness string (i.e.  $\alpha$ ) and torsional vibrations occur. When a mass-unbalance is present at the lower disc, then the energy released due to the negative damping is also transformed to the potential energy stored in the leaf springs and rods (i.e.  $r$ ) and kinetic energy related to the translational motion of the lower disc. Consequently, less energy is transformed to the kinetic energy of the lower disc in torsional direction and torsional vibrations decrease. Moreover, when the level of mass-unbalance is higher, then lateral vibrations increase for angular velocities which are lower than the critical angular velocity and less energy can be transformed to the kinetic energy of the disc in torsional direction, hence, torsional vibrations decrease further or they even disappear.

#### 5.2.4 Vibrations due to Coupling Between Torsional and Lateral Dynamics

For input voltages  $u_c > 5$  V, we observe vibrations which are not friction-induced. Namely, when we remove the negative damping in the friction  $T_{fl}(\omega_l)$  and assume that only viscous friction is present at the lower disc, i.e.  $T_{fl}(\omega_l) = b_l\omega_l$ , with  $b_l$  as in table 5.1, torsional friction-induced vibrations disappear for  $u_c \in [0 \text{ V}, 5 \text{ V}]$ . However, the vibrations for  $u_c > 5$  V are practically unchanged. Therefore, in order to gain a better understanding of such vibrations, we discuss the influence of the following parameters to the steady-state behaviour of the system: an additional mass unbalance  $\Delta m$ , the damping coefficient in lateral direction  $b$ , the stiffness  $k$  in lateral direction and the string stiffness  $k_\theta$ .

According to the steady-state analysis performed for the estimated system, we observe a number of bifurcations of periodic solutions in that region, such as period



doubling, fold and secondary Hopf bifurcations (see figure 5.9). Moreover, we observe a period doubling cascade which, according to [Strogatz, 2000], can lead to a chaos (see figure 5.12). The occurrence of a periodic solution means that torsional vibrations appear in the system and that the whirling motion (lateral vibrations) is not periodic in the fixed coordinate frame (see, for example, figure 5.8(d)).

However, here we are not interested in a detailed bifurcation analysis of the system for various parameter changes, but in how various parameters influence the (dis)appearance of vibrations which are due to coupling of torsional and lateral motion in the system. Therefore, we only discuss the influence of the changes of various parameters to (the stability of) the equilibrium points of the system. For such purposes we discuss the behaviour of  $\omega_{eq}$ ,  $r_{eq}$  and  $-\alpha_{eq}$  for various constant input voltages  $u_c$ . The reason for considering  $-\alpha_{eq} = \theta_u - \theta_l$  is similar to the reason mentioned in Chapter 4 (see figure 4.7(a)). Namely, we concluded that a higher dissipative torque at the lower disc ( $T_{fl}(\omega_l)$  in Chapter 4) causes an increase in  $-\alpha_{eq}$ , i.e. an increase in the phase lag of the lower disc with respect to the upper disc in equilibrium.

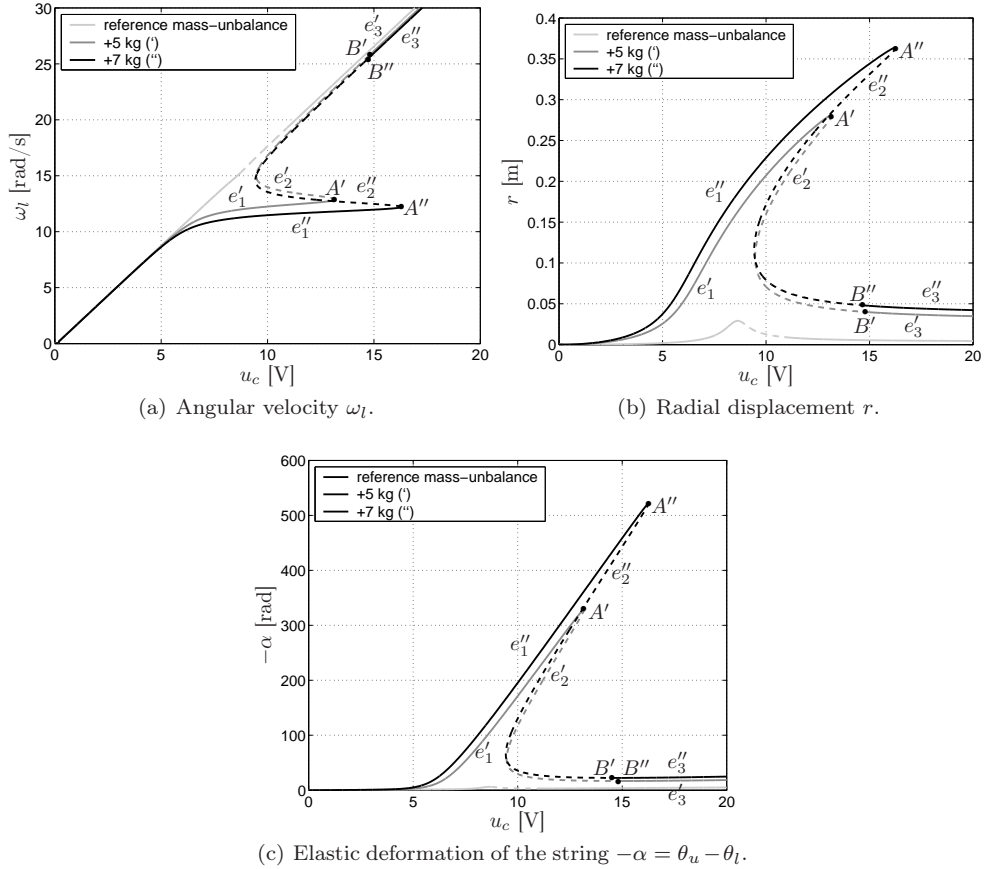
### Changes in Mass-Unbalance

In Section 5.2.3 we have already discussed how changes in mass-unbalance influence the friction-induced torsional vibrations and concluded that due to a higher mass-unbalance such torsional vibrations decrease and can even disappear. In figure 5.16, we show the results of a stability analysis of the equilibrium points of the considered system, with only viscous friction at the lower disc and an additional mass  $\Delta m$  added to the lower disc. In that figure, we show equilibrium branches for the nominal system (light-grey line), for  $\Delta m = 5$  kg (dark-grey line) and for  $\Delta m = 7$  kg (black line). According to the obtained results the following can be concluded:

- When the mass-unbalance is high enough, more than one equilibrium appears in the system. Then, condition (5.4) is not satisfied anymore and the first equation in (5.3) has more than one solution  $\omega_{eq}$ , for the given parameter set.

In order to understand the cause for the appearance of multiple equilibrium points, we should consider the model of the system (5.1). Assume that we drive the upper disc with a constant velocity  $\omega_u = \Omega$ . Then, the dynamics of such system can be described with the model (5.1) without the first equation, which describes the dynamics of the upper part of the set-up, and with  $\omega_u = \Omega = \text{const}$ . According to (5.3), the system has a unique equilibrium point  $(x, y, \alpha) = (x_{eq}, y_{eq}, \alpha_{eq})$  where  $\alpha_{eq}$ ,  $x_{eq}$  and  $y_{eq}$  can be computed using the second, third and fourth equation in (5.3), respectively, with  $\omega_{eq} = \Omega$ . Consequently, the degree of freedom which exists in the dynamics of the upper part of the set-up is responsible for the appearance of multiple equilibrium points.

- For  $\Delta m = 5$  kg and  $\Delta m = 7$  kg we observe a change in stability properties at points  $A'$ ,  $B'$  and  $A''$ ,  $B''$ , respectively; Hopf bifurcations occur at these points inducing limit cycling.
- For  $\Delta m = 5$  kg, bifurcation point  $A'$  occurs at a lower input voltage ( $u_c = 13.1865$  V) than bifurcation point  $B'$  ( $u_c = 14.741$  V, see figure 5.16). Consequently, there exists a region with only unstable equilibrium points. Moreover,

Figure 5.16: Equilibrium branches for various levels of the mass-unbalance  $\Delta m$ .

according to a numerical analysis, it is observed that point  $A'$  represents a supercritical Hopf bifurcation and point  $B'$  a subcritical Hopf bifurcation, which induce periodic solutions (torsional vibrations) in the system.

- For  $\Delta m = 7 \text{ kg}$ , bifurcation point  $A''$  occurs at a higher input voltage ( $u_c = 16.2907 \text{ V}$ ) than bifurcation point  $B''$  ( $u_c = 14.5113 \text{ V}$ , see figure 5.16). Therefore, there no region exists where only unstable equilibria occur. Furthermore, based on a numerical analysis, we can conclude that both points represent subcritical Hopf bifurcations and no stable periodic solutions are observed in the system.
- Assume that we apply a constant input voltage  $u_c$  to the system, which is lower than the critical input voltage  $u_{cc}$  related to the critical angular velocity inducing a resonance in lateral direction, see equation (5.14). For low input voltages, the radial displacement of the lower disc is very small and the energy which is added to the system (via  $u_c$ ) is mainly transformed to rotational kinetic energy of the lower disc, i.e.  $\omega_l$  increases. If we increase  $u_c$ , then radial displacement  $r$  starts to increase as  $u_c$  approaches the critical voltage  $u_{cc}$ . Moreover, if the mass-unbalance increases, then the level of lateral vibrations in the system also

increases and the energy which is added to the system mainly transforms to the potential energy stored in the leaf springs and rods, see figure 5.16(b), and to the potential energy stored in the low-stiffness spring (i.e.  $-\alpha$ ), see figure 5.16(c). Consequently, less energy can be transformed to kinetic energy of the lower disc in torsional direction and angular velocity  $\omega_l$  starts to increase much slower than it increases for lower input voltages (see equilibrium branches  $e'_1$  and  $e''_1$  in figure 5.16(a)). If  $u_c$  reaches  $u_{cc}$  ( $u_{cc} = 13.1712$  V for  $\Delta m = 5$  kg and  $u_{cc} = 16.2750$  V for  $\Delta m = 7$  kg) and continues to increase further, the lateral vibrations reach their (local) maximum level, and the amplitude of these lateral vibrations and the potential energy stored in lateral direction decreases, despite the fact that more energy is added to the system. Consequently, significantly more energy can be transformed to the kinetic energy of the lower disc in torsional direction. According to figure 5.16, for  $\Delta m = 5$  kg torsional vibrations occur and for  $\Delta m = 7$  kg the system jumps suddenly from the locally stable equilibrium branch  $e''_1$  to the locally stable branch  $e''_3$ . Furthermore, for  $\Delta m = 7$  kg the velocity at the lower disc suddenly increases, the amplitude of lateral vibrations (i.e.  $r$ ) and the phase lag between lower and upper disc (i.e.  $-\alpha_{eq}$ ) suddenly decreases, in steady-state, and no torsional vibrations occurs at the lower disc.

According to these observations it can be concluded that due to the mass-unbalance the vibrations due to coupling between the torsional and lateral mode can disappear, which is also concluded for the friction-induced vibrations. However, due to the degree of freedom at the upper part of the set-up multiple equilibria occur. Furthermore, for the input voltages which are slightly higher than  $u_{cc}$ , defined by (5.12) and (5.14), either torsional vibrations appear for low mass-unbalance or for higher levels of mass-unbalance no torsional vibrations occur, but the angular velocity in steady-state suddenly increases, while the amplitude of lateral vibrations suddenly decreases.

### Changes in Damping in Lateral Direction

To analyze the influence of various damping levels in lateral direction on the steady-state behaviour of the system, we vary the parameter  $b$ . Only a minor influence of  $b$  to  $\omega_{eq}$  is noticed, i.e.  $\omega_{eq}$  is almost the same as shown with light-gray line in figure 5.16(a) for the considered levels of the damping. Therefore, in figure 5.17 we only show  $r_{eq}$  and  $-\alpha_{eq}$  as a result of an equilibrium analysis. According to that analysis the following can be concluded:

- When the damping in lateral direction  $b$  increases, the region in which instabilities occur, decreases. Furthermore, if the damping is high enough, torsional vibrations can disappear as it is the case when the damping is 3 times higher (black line in figure 5.17) than the estimated  $b$ .
- Similarly as we have already noticed before, an instability region can occur for input voltages which are slightly higher than the critical voltage  $u_{cc}$ . Namely, for low input voltages, the radial displacement of the lower disc is very small and the energy which is added to the system (via  $u_c$ ) is mainly transformed to the kinetic energy of the lower disc, i.e.  $\omega_l$  increases. If we increase  $u_c$ , the radial displacement  $r$  starts to increase as  $u_c$  approaches  $u_{cc}$ . Then the lateral vibrations in the system also increase and the energy which is added to the system transforms to the potential energy stored in the leaf springs and rods

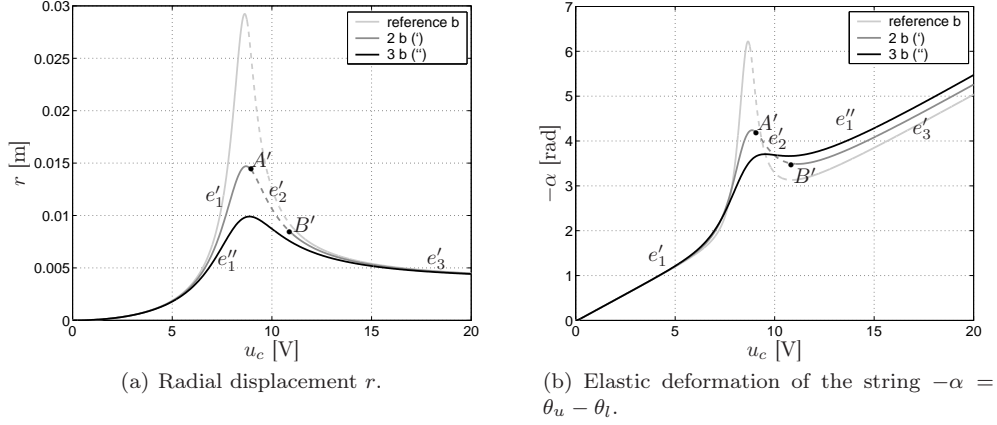


Figure 5.17: Equilibrium branches for various levels of damping  $b$  in lateral direction.

( $r$ ), to the kinetic energy of the lower disc in torsional direction ( $\omega_l$ ) and to the potential energy stored in the low-stiffness spring ( $\alpha$ ), see figure 5.17. If  $u_c$  reaches  $u_{cc}$  and continues to increase further, the lateral vibrations reach their local maximum and the amplitude of lateral vibrations, i.e. the potential energy stored in lateral direction decreases, despite the fact that more energy is added to the system. Moreover, instabilities (thus, torsional vibrations) appear at the input voltages which are higher than  $u_{cc}$ . Namely, at those input voltages, the energy which is supplied to the system (through  $u_c$ ) causes a significant decrease in the potential energy stored in the leaf sprigs and rods (i.e.  $r$ ) and the potential energy in the low-stiffness spring (i.e.  $-\alpha$ ). According to our observations, that energy is transformed to torsional vibrations (since such vibrations start occurring) and to lateral vibrations. However, for higher levels of damping in lateral direction, the potential energies does not decrease that much, and less energy is transformed to the vibrations, i.e. for a certain level of  $b$  torsional vibrations even disappear (no unstable equilibrium branch occurs) and lateral vibrations decrease ( $r_{eq}$  decreases).

### Changes in Stiffness in Lateral Direction

When discussing the influence of various stiffness levels in lateral direction we assumed that a non-dimensionless (material) damping of the construction, which is responsible for the stiffness in lateral direction, is constant. Since non-dimensionless damping is defined by

$$\zeta = \frac{b}{2\sqrt{k m}},$$

we assumed that the mass  $m$  of the construction and  $b/\sqrt{k}$  are constant, when changing the stiffness  $k$  in lateral direction. Under those assumptions we analyze the stability of equilibria of the system when the stiffness is 9 times higher (damping  $b$  is 3 times higher) and 9 times lower ( $b$  is 3 times lower) than the nominal (estimated) value. Since we noticed only a minor influence of such changes to  $\omega_{eq}$ , in figure 5.18 we only show  $r_{eq}$  and  $-\alpha_{eq}$ . According to this analysis the following conclusions can be drawn:

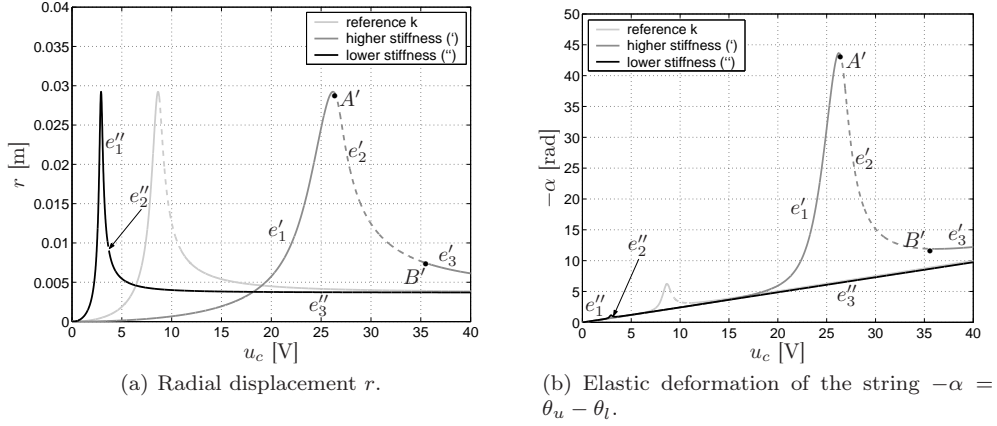


Figure 5.18: Equilibrium branches for various levels of stiffness in lateral direction with  $b/\sqrt{k} = \text{const}$ .

- Torsional vibrations can disappear if the stiffness of the construction in lateral direction is lower, i.e. the region in which torsional vibrations appear, becomes larger if the construction is stiffer in lateral direction.
- An instability region occurs for  $u_c > u_{cc}$ , where  $u_{cc}$  is the input voltage which corresponds to the critical velocity  $\omega_c$ . When the construction in lateral direction is stiffer, then  $u_{cc}$  is higher. Consequently, the instability region appears for higher input voltages. On the other hand, for a lower stiffness, critical speed occurs at a lower input voltage  $u_{cc}$  as shown in figure 5.18. Since the instability region decreases for a lower stiffness in lateral direction, then lower  $k$  may seem favorable to have in the considered system. However, since for lower  $k$  instabilities and  $u_{cc}$  (related to the critical angular velocity inducing a resonance in lateral direction) occur at lower input voltages, it may be undesirable.
- From figure 5.18(a) and from expression (5.13) it can be seen that the local maximum  $r_c$  in radial displacement does not change when the stiffness in lateral direction changes (given the fact that the dimensionless damping level stays the same).
- When analyzing  $-\alpha_{eq}$ , similar conclusions can be derived as derived when analyzing  $-\alpha_{eq}$  for various changes in  $b$ . Namely, instabilities appear almost immediately when the input voltage becomes higher than  $u_{cc}$ . At those input voltages, despite the fact that extra energy is supplied to the system (due to an increase of  $u_c$ ), the potential energy stored in the leaf springs and rods (i.e.  $r$  decreases) and in the potential energy stored in the low-stiffness spring (i.e.  $-\alpha$ ) both significantly decrease. The extra supplied energy is stored in torsional and lateral vibrations. For lower  $k$ , the potential energy in lateral direction decreases even more significantly, but almost no decrease occurs in the potential energy of the low-stiffness spring (i.e.  $-\alpha_{eq}$  slightly decreases for voltages  $u_c$  which are slightly higher than  $u_{cc}$ ). Consequently, the extra energy supplied to the system transforms mainly to the kinetic energy of the lower disc, since  $\omega_{eq}$  increases.

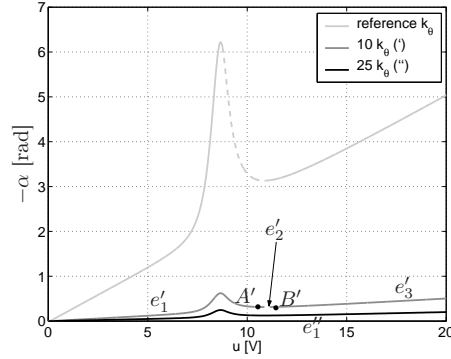


Figure 5.19: Equilibrium branches for various levels of string stiffness  $k_\theta$ : elastic deformation of the string  $-\alpha = \theta_u - \theta_l$ .

### Changes in String Stiffness

A low torsional stiffness is not always present in rotor systems. Therefore, we analyze the influence of a higher string stiffness to the stability properties of the system. According to (5.2), the string stiffness  $k_\theta$  influences elastic deformation of the string in steady-state ( $\alpha_{eq}$ ) and has no influence on  $\omega_{eq}$  and  $r_{eq}$ . Namely,  $\omega_{eq}$  is the same as shown with light-gray line in figure 5.16(a),  $r_{eq}$  is the same as shown with the light-gray line in figures 5.16(b), 5.17(a) and 5.18(a) and only the position of the fold bifurcation points ( $A$  and  $B$ ) change for various levels of  $k_\theta$ . Consequently, in figure 5.19 we only shown  $-\alpha_{eq}$  as a result of an analysis of the equilibria of the system. According to that analysis the following remarks can be made:

- When the string stiffness increases, the elastic deformation of the string  $-\alpha_{eq}$  decreases (compare  $-\alpha_{eq}$  for various levels of  $k_\theta$  in figure 5.19). Furthermore, the instability region which occurs for the input voltages higher than  $u_{cc}$  also decreases. What is more, if the string is stiff enough, the vibrations can disappear as is the case when the stiffness is 25 times higher than the estimated  $k_\theta$  (black line in figure 5.19).
- Similarly as we concluded in the previous situations, the instability region disappears when the decrease in  $-\alpha_{eq}$  is small enough for input voltages which are slightly higher than  $u_{cc}$ . Namely, for low input voltages, the radial displacement of the lower disc is very small and the extra energy which is supplied to the system (via  $u_c$ ) is mainly transformed to the kinetic energy of the lower disc, i.e.  $\omega_l$  increases. Next, for higher  $u_c$ , the radial displacement  $r$  starts to increase as  $u_c$  approaches  $u_{cc}$ , hence the extra energy supplied to the system mainly transforms to potential energy stored in the leaf springs and rods (i.e.  $r$ ), to kinetic energy of the lower disc in torsional direction (i.e.  $\omega_l$ ) and to potential energy stored in the low-stiffness spring (i.e.  $-\alpha$ ), see figure 5.19. Then, if  $u_c$  reaches  $u_{cc}$  and continues to increase further, lateral vibrations reach their (local) maximum and the amplitude of the lateral vibrations and the potential energy stored in lateral direction decreases, despite the fact that more energy is supplied to the system. Moreover, according to figure 5.19 potential energy which is stored in the low-stiffness string also decreases. Consequently, more energy is transformed to the kinetic energy of the lower disc in torsional direction.

However, if the decrease in the potential energy in torsional direction is high, instabilities occur in the system, and the released potential energy is transformed to energy sustaining torsional and lateral vibrations. On the other hand, when the string stiffness is high enough, the potential energy (in torsional direction) does not decrease that much and, consequently, no energy can be transformed to torsional vibrations and no torsional vibrations occur.

## 5.3 Experimental Results

### 5.3.1 Validation of Steady-State Behaviour of the Set-Up

The model of the drill-string set-up when ondina oil 68 is used as a lubrication fluid, 20.5 N normal force is applied at the brake and the  $x$ - and  $y$ -constraints are released is given by (5.1) and the parameter estimates are given in table 5.1. That set-up undergoes both torsional and lateral vibrations. As mentioned earlier, the predictive quality of the estimated model in steady-state is of great interest. Therefore, a constant voltage is applied at the input of the DC motor of the set-up and each experiment lasted long enough to guarantee that all transient effects have disappeared; the last 50 seconds of the angular velocity  $\omega_l$  and radial displacement signal  $r$  are recorded. However, due to the limited voltage range ( $u \in [-5 \text{ V}, 5 \text{ V}]$ ) we can only observe the friction-induced vibrations in the set-up. Some of the obtained results are shown in figure 5.20. In that figure, the experimental signals (solid black line) and the signals obtained using the estimated model (dashed grey line) in steady-state are shown for different constant input voltages. The time-series shown in figures 5.20(a), 5.20(b) and 5.20(c) represent stick-slip limit-cycling (torsional and lateral vibrations) and figure 5.20(d) represents an equilibrium point (constant velocity at the lower disc and whirling motion of the disc -  $r$  is constant). From the comparison between the numerical and experimental results, it can be concluded that with the suggested model the steady-state behaviour of the set-up is modelled accurately.

The same type of bifurcation diagrams, as shown in figure 5.6, are constructed experimentally. However, due to limitations in the DC motor, the experimental bifurcation diagram is constructed by applying different constant input voltages in the limited voltage range  $u_c \in [0 \text{ V}, 5 \text{ V}]$ . When no torsional vibrations are observed (as in figure 5.20(d)), the mean value of the recorded angular velocity and radial displacement are computed and the obtained data are plotted using the symbol "x". Next, when torsional vibrations are observed at the lower disc (as in figures 5.20(a), 5.20(b) and 5.20(c)), the mean values of local maxima and minima of the vibrations are computed. Then, these experimentally obtained data are plotted using the symbol "o". Experimental results, together with the bifurcation diagram obtained by numerical analysis of the estimated model, are shown in figures 5.21(a) and 5.21(b). Furthermore, when torsional vibrations are observed in the set-up, the period time  $T$  of the vibrations is determined as well. The experimental results are compared to the period time of the numerically obtained limit cycles in figure 5.21(c). The results, shown in figure 5.21, illustrate the predictive quality of the obtained model.

Both in the numerical and the experimental bifurcation diagram we recognize the regions which are also present when only torsional vibrations are possible in the set-up:

- a sticking region, for very low input voltages,



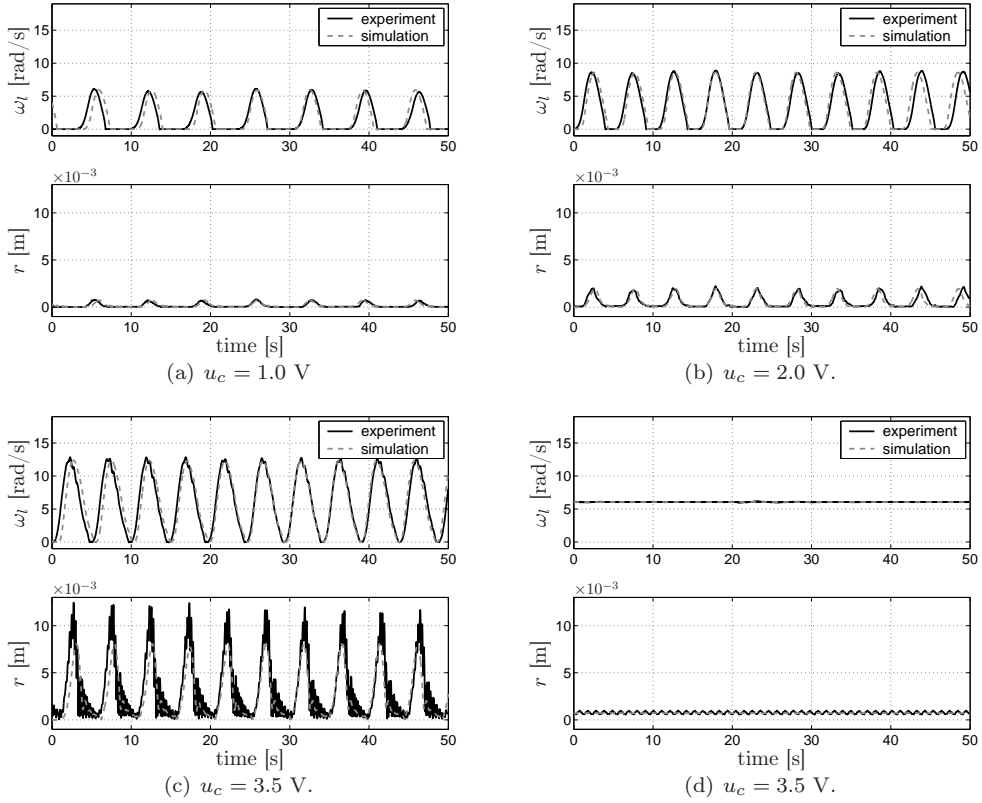


Figure 5.20: Experimental and simulated angular velocity  $\omega_l$  and radial displacement  $r$  for various constant input voltages and various initial conditions.

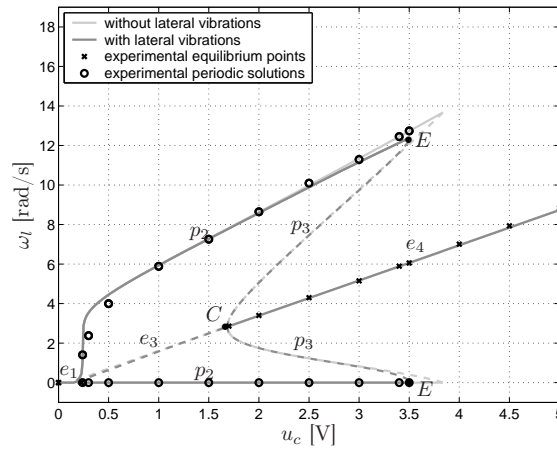
- a region in which only torsional vibrations (i.e. stable limit cycles) appear,
- a region in which torsional vibrations (stable limit cycles) and a constant angular velocity at the lower disc (stable equilibrium points) coexist, and
- a region in which no torsional vibrations can appear in the system in steady-state.

For the input voltages  $u_c \in [3 \text{ V}, 3.5 \text{ V}]$  we notice somewhat less quality of the estimated model (see specifically figure 5.21(b)). The reasons for this fact are discussed in the part of this section where we discuss the observed unmodelled dynamics in the set-up.

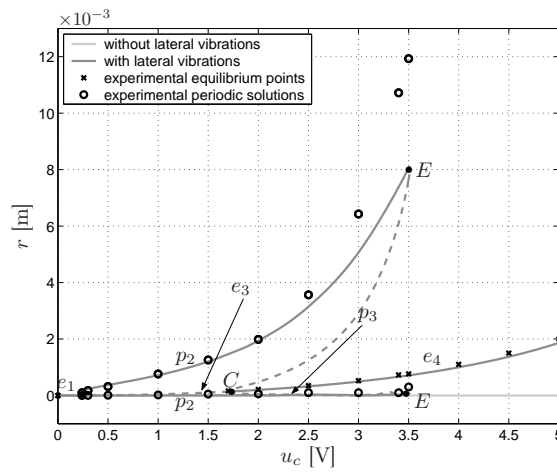
### Disappearance of Torsional Vibrations

In figure 5.21 with a light-grey line we show the bifurcation diagram of the set-up when only torsional and no lateral vibrations are possible, i.e. when  $x$ - and  $y$ -constraints are fixed. If we compare that bifurcation diagram with the bifurcation diagram obtained

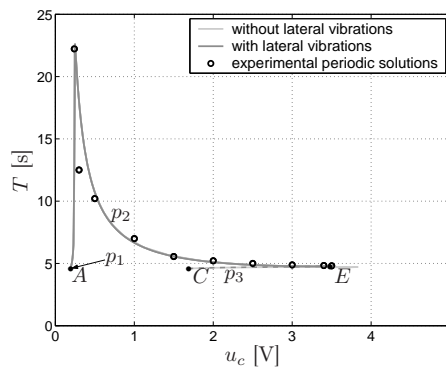




(a) Angular velocity  $\omega_l$  at the lower disc.



(b) Radial displacement  $r$  of the lower disc.



(c) Period time of the periodic solutions.

Figure 5.21: Comparison of the numerical and experimental bifurcation diagram.

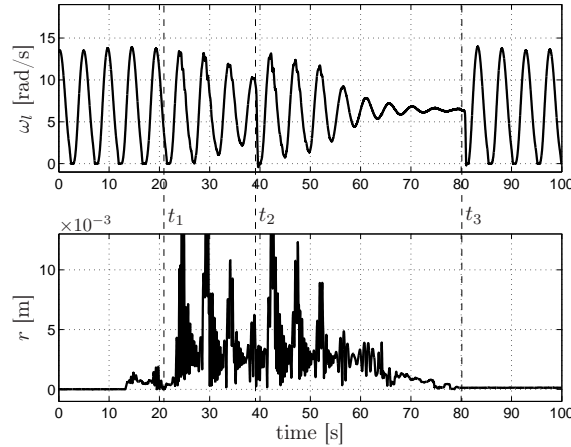


Figure 5.22: Indication of disappearance of torsional vibrations when the lower disc moves in lateral direction:  $u_c = 3.7$  V.

when lateral vibrations are present in the set-up (dark-grey line), we see that the second fold bifurcation point moves towards lower velocities when mass-unbalance and lateral vibrations are present in the system (as predicted in Section 5.2.3). Namely, when the constraints are fixed then the second fold bifurcation point is observed for  $u_c \in (3.9$  V, 4.0V) and when the constraints are released the second fold bifurcation point is observed for  $u_c \in (3.5$  V, 3.6V).

In order to show that torsional vibrations can really disappear, for some voltages, due to the existence of lateral vibrations, the following experiment is performed. We fix the constraints, apply a constant input voltage  $u_c = 3.7$  V and wait long enough to obtain torsional vibrations (see figure 5.22). Then, at time instant  $t_1$  we release the constraints and the lower disc starts to vibrate in lateral direction. After a while, the torsional vibrations disappear even though at time instant  $t_2$  we tried to induce those vibrations manually, by holding up the lower disc for a very short time. Finally, when we fix again the constraints and stop the lower disc manually (time instant  $t_3$  in figure 5.22), the system continues with stick-slip vibrations. This experiment provides additional evidence for the fact that torsional vibrations can indeed disappear due to the presence of lateral vibrations.

### Unmodelled Dynamics

Various validation procedures show that the model given by (5.1), with parameter estimates given in table 5.1, represents a high quality model of the set-up. Nevertheless, some unmodelled dynamics is present in the set-up:

- In the previous chapter we observe that position dependant friction and some other friction effects are present at the lower disc, which are not captured with the static friction model  $T_{fl}(\omega_l)$  in (5.1).
- From figures 5.2(c), 5.2(d), 5.20(c) and 5.21(b) we see that the quality of the estimated model is somewhat less, as far as the lateral dynamics is concerned, when large lateral displacements occur at the lower disc. Moreover, in figures 5.2(c), 5.2(d), 5.20(c) we see that in such case (unmodelled) high-frequency

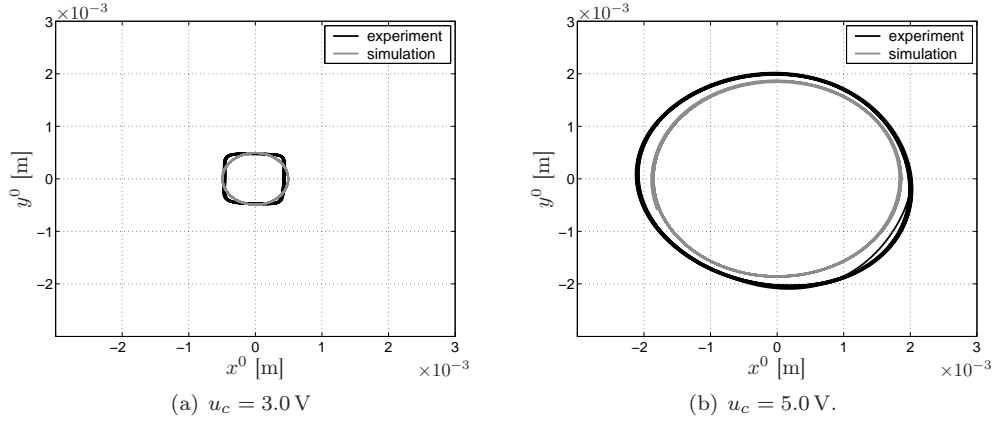


Figure 5.23: Experimental and simulated displacement of the lower disc in steady-state when the lower disc rotates with constant velocity (equilibrium point).

vibrations are induced. These high-frequency vibrations are due to the mechanisms for fixing the lower disc in  $x$ - and  $y$ -direction (see figures 3.6 and 3.7), which are appeared to be not stiff enough.

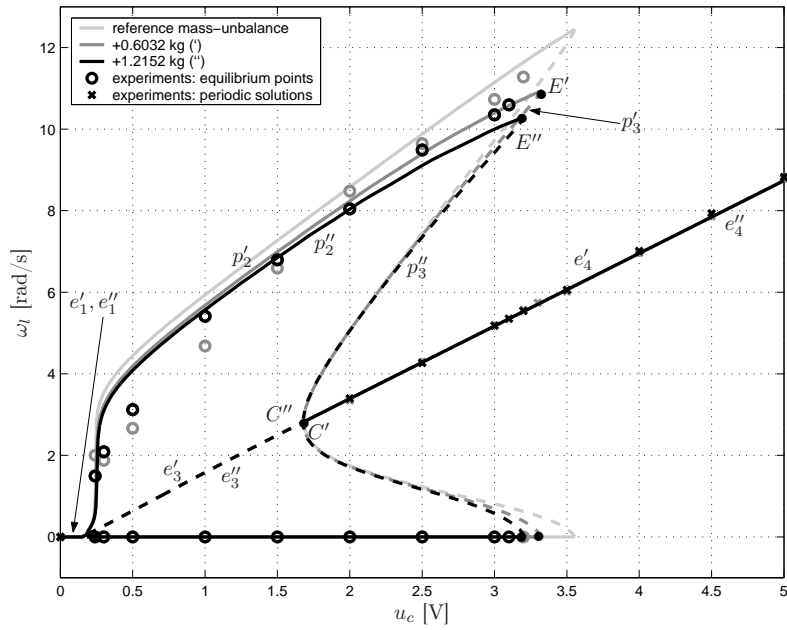
- If we apply an input voltage of  $u_c = 3.0\text{ V}$ , perturb the system such that the lower disc, after a while, starts to rotate with a constant angular velocity and then observe the trajectory of the center of the lower disc, we do not see a circular trajectory, as expected from the model, but a rectangular one (see figure 5.23(a)). This is due to the sticking behaviour present in lateral direction due to LVDT displacement sensors 500 HR-DC [Schaevitz, 2004] (see figures 3.6 and 3.7); friction between the core and the housing of the LVDT causes this sticking. If we perform the same experiment for  $u_c = 5.0\text{ V}$  and compare the obtained result (figure 5.23(b)) with the result obtained for  $u_c = 3.0\text{ V}$  we conclude that the sticking behaviour only occurs at low input voltages.
- From figure 5.23(b) we also see that the characteristics of the set-up in lateral direction is not entirely isotropic, since the trajectory in figure 5.23(b) is not a circle but an irregular ellipsoid.

However, despite all observed unmodelled effects, we obtain a vary good match between the estimated model and the experiments.

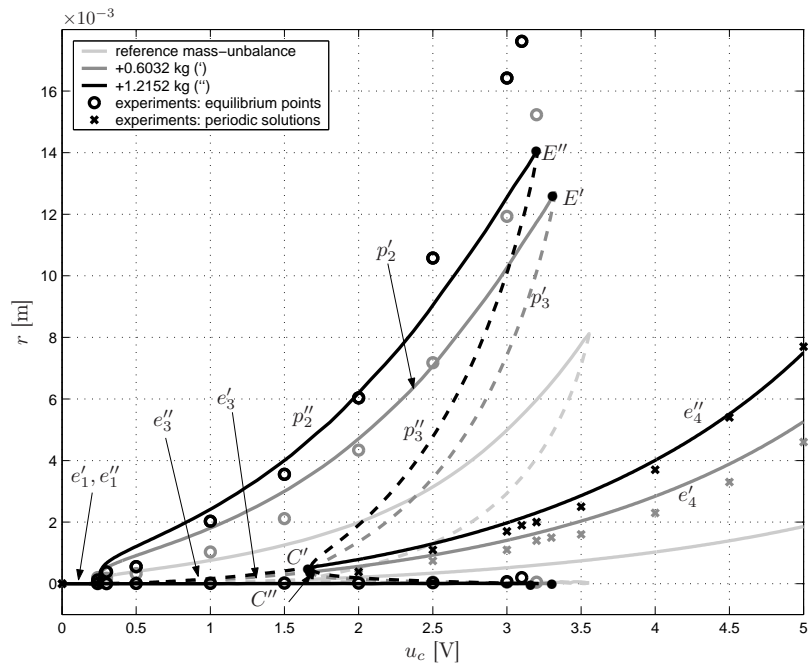
### 5.3.2 Various Levels of Mass-Unbalance

Since the input voltage which can be applied to the DC motor is limited ( $u \in [-5, \text{V}, 5, \text{V}]$ ), we can only observe the influence of various mass-unbalance to the friction-induced torsional vibrations.

In order to do so, additional masses  $\Delta m = 0.6032\text{ kg}$  or  $\Delta m = 1.2152\text{ kg}$  are added to the existing mass-unbalance (see figure 3.4) at a distance of approximately  $d_\Delta = 10\text{ cm}$ . Next, for each added mass, no normal force is applied at the brake, the lower disc is fixed using the  $x$ - and  $y$ -constraints (shown in figures 3.6 and 3.7), the



(a) Angular velocity  $\omega_l$ .



(b) Radial displacement  $r$ .

Figure 5.24: Simulated and experimental bifurcation diagrams for various mass-unbalance applied at the lower disc.

quasi-random signal (shown in figure 3.13(a)) is applied and we estimate the distance  $d_{\Delta}$  in (5.15), assuming that all other parameters of the set-up are known. In such a way we obtain that

$$\begin{aligned} d_{\Delta} &= 10.85 \text{ cm for } \Delta m = 0.6032 \text{ kg, and} \\ d_{\Delta} &= 8.98 \text{ cm for } \Delta m = 1.2152 \text{ kg.} \end{aligned} \tag{5.16}$$

Then, for both mass-unbalances ondina oil 68 is used, 20.5 N normal force is applied and the model (5.1) and (5.15) with parameter estimates shown in table 5.1 and in (5.16) is validated using signals shown in figure 3.13. For those signals, the comparison between the responses of the experimental set-up and estimated model indicates the good quality of the obtained parameters for both mass-unbalances.

Since the predictive quality of the estimated model in steady-state is of great interest, for each added mass-unbalance, we construct numerical and experimental bifurcation diagrams in the same way as it is done in Section 5.3.1 (i.e. when various constant voltages are applied at the input of the DC motor). The obtained diagrams are shown in figure 5.24.

From those bifurcation diagrams, one can conclude that due to an additional mass-unbalance the region, in which friction-induced torsional vibrations occur (see figure 5.24(a)), reduces. Namely, for  $\Delta m = 0.6032 \text{ kg}$  the second fold bifurcation point occurs between  $u_c = 3.2 \text{ V}$  and  $u_c = 3.3 \text{ V}$ , and for  $\Delta m = 1.2152 \text{ kg}$  the fold bifurcation occurs between  $u_c = 3.1 \text{ V}$  and  $u_c = 3.2 \text{ V}$ . The same conclusion is derived in Section 5.2.3, where we discussed the influence of various levels of mass-unbalance to the friction-induced torsional vibrations.

## 5.4 Summary

The aim of this chapter is to provide improved understanding on the interaction between torsional and lateral vibrations in rotor systems with flexibility. For that purpose, we have analyzed an experimental drill-string set-up in which torsional vibrations are induced due to friction at the lower disc and lateral vibrations are induced by the presence of a mass-unbalance at the lower disc. However, the results obtained here are relevant for many other engineering systems with friction, unbalance and flexibility. In this context, one can think of drilling systems which are used for exploration of oil and gas, electrical shavers, various turbines, pumps, fans and many more. According to the presented results the following conclusions can be drawn:

- In this class of systems, two types of torsional vibrations can appear:
  - friction-induced torsional vibrations, and
  - torsional vibrations due to a coupling between torsional and lateral dynamics in the system.

Friction-induced vibrations are induced due to a subtle balance between negative damping at low velocities and viscous friction at higher velocities. When the disc rotates with an angular velocity where negative damping is present in the friction, an instability occurs in the system. Consequently, the lower disc cannot rotate with a constant angular velocity, torsional vibrations occur. Moreover, the amplitude of lateral vibrations increases with respect to the amplitude of the lateral vibrations when no torsional vibrations are present in the system.

Torsional vibrations due to a coupling between torsional and lateral motions occur for input voltages which are higher than a critical voltage related to the critical angular velocity inducing a resonance in lateral direction. In that working region, torsional vibrations can occur even if no negative damping is present in the friction at the lower disc.

- When no torsional vibrations are present in the system, both the upper and lower disc rotate with a constant velocity in steady-state, for a given constant input voltage. Then, due to a mass-unbalance, lateral vibrations are present at the lower disc, i.e. a forward whirling motion occurs at the disc (lateral vibrations). The period time of such motion in the fixed coordinate frame, corresponds to the angular velocity of the disc. Moreover, when the lower disc rotates with the critical angular velocity the amplitude of lateral vibrations reaches its local maximum.

Assume that for a certain input voltage torsional vibrations occur in the system, either due to negative damping in the friction torque at the lower disc or due to a coupling between torsional and lateral dynamics. Then the amplitude of the lateral vibrations increases with respect to the amplitude of the same vibrations which occur when no torsional vibrations are present. Furthermore, the obtained lateral vibrations are not periodic any more in the fixed coordinate frame, since the ratio between period time of torsional vibrations and the period time which corresponds to angular velocity is, in general, an irrational number.

- The influence of various levels of mass-unbalance to the steady-state behaviour of the system is studied on a theoretical, numerical and experimental level. Results on all levels confirm that if the level of mass-unbalance increases, the region, in which friction-induced torsional vibrations occur, decreases. Moreover, numerical results show that if the mass-unbalance is high enough, the torsional vibrations can disappear entirely.
- We cannot study torsional vibrations due to the coupling of torsional and lateral motion, using the experimental drill-string set-up, due to limitations in the DC motor. However, we have analyzed numerically the influence of various levels of mass-unbalance, the stiffness of the low-stiffness string and the damping and stiffness of the construction in lateral direction to the torsional and lateral vibrations which occur due to the coupling between torsional and lateral modes. As a result of this analysis, we conclude that those torsional vibrations appear almost immediately when the input voltage becomes higher than a so-called critical voltage related to a critical angular velocity inducing a resonance in lateral direction. At those input voltages, despite the fact that extra energy is supplied to the system (due to an increase of  $u_c$ ), the potential energy stored in the leaf springs and rods (i.e.  $r$ ) and in the potential energy stored in the low-stiffness spring (i.e.  $-\alpha$ ) both significantly decrease. The extra supplied energy is stored in torsional and lateral vibrations. Moreover, when almost no decrease occurs in the potential energy of the low-stiffness spring (i.e.  $-\alpha_{eq}$  slightly decreases for voltages  $u_c$  which are slightly higher than  $u_{cc}$ ) torsional vibrations disappear and the extra energy supplied to the system transforms mainly to the kinetic energy of the lower disc, since  $\omega_{eq}$  increases.

Finally, we conclude that if the level of mass-unbalance, stiffness of the string

or damping in lateral direction is higher, or if the level of stiffness of the construction in lateral direction is lower, the instability region decreases and consequently the region in which torsional vibrations occur, decreases. However, even if the levels of all those parameters are such that no torsional vibrations are present in the system, the parameters influence the steady-state behaviour of the system in several ways:

- For high levels of mass-unbalance, multiple equilibria occur due to the degree of freedom at the upper part of the set-up (the DC motor, the friction torque and the upper disc). Consequently, for input voltages which are slightly higher than the critical voltage corresponding to the critical angular velocity, the angular velocity at the lower disc suddenly increases in steady-state, while the amplitude of lateral vibrations suddenly decreases.
- If the values of damping in lateral direction are high enough, torsional vibrations disappear and amplitude of lateral vibrations decrease.
- For lower stiffness of the construction in lateral direction, the critical angular velocity occurs for lower input voltages and, even though no torsional vibrations appear, lateral vibrations with high amplitude are present at lower input voltages. On the other hand, if we increase the stiffness, we increase the region where instabilities are present in the system. Nevertheless, such instabilities occur for higher input voltages. Since, in real engineering systems only a limited input voltage can be applied, those instabilities may occur at the input voltages which can never be reached.
- Various levels of string stiffness does not influence the angular velocity and the radial displacement in equilibrium, but only influences the phase lag between the lower and the upper disc. Therefore for high levels of the string stiffness (for which no torsional vibrations occur), only periodic lateral vibrations occur in the system.

## Chapter 6

# Conclusions and Recommendations

Various types of vibrations which appear in a mechanical system often limit the performance and can even endanger the safety of operation of that system. Moreover, more than one type of vibration can appear. In this thesis, we address friction-induced torsional vibrations in flexible mechanical systems, lateral vibrations in rotor systems caused by mass-unbalance and the interaction between those two types of vibrations.

For this purpose, we have designed an experimental drill-string set-up which exhibits both types of vibrations. The set-up consists of a DC-motor, two rotational (upper and lower) discs, a low-stiffness string and an additional brake at the lower disc. The lower disc can rotate around its geometric center and is also free to move in lateral direction. It should be noted that the configuration of the experimental set-up can be recognized in many other mechanical systems, in which friction or unbalance can deteriorate the system performance by induction of vibrations. For example, when the lower disc is fixed in lateral direction, the system represents the configuration of two masses, coupled by a flexibility, of which one is subject to friction and the other is driven by an actuator. In this context, one can think of applications such as printers, pick and place machines, industrial and domestic robots, braking mechanisms and many others. Moreover, when a mass-unbalance is present at the lower disc and the disc can move in lateral direction, this configuration can be recognized in drilling systems which are used for exploration of oil and gas, in electrical shavers, in various turbines, pumps, fans and in many more.

In this chapter we present general conclusions of this thesis and recommendations for further extensions and further research.

### 6.1 Concluding Remarks

The designed set-up is modelled and the parameters of the model are estimated. The comparison between responses of the experimental set-up and estimated model indicates a high quality of the obtained parameter estimates. The steady-state behaviour of the system has been analyzed; first, when only torsional and no lateral vibrations occur and, second, when both torsional and lateral vibrations appear in



the system. As a result of the analysis on a theoretical, numerical and experimental level conclusions, as summarized in the next section, can be drawn.

### 6.1.1 Friction-Induced Torsional Vibrations in Flexible Rotor Systems

- The main cause for friction-induced torsional vibrations is the negative damping in the friction-velocity curve for the friction present at the lower disc. The range in which such vibrations can occur is determined by a subtle balance between negative damping at lower velocities and viscous friction at higher velocities. Moreover, the velocity at which the friction attains its minimum is also important. Namely, when the disc rotates with a (steady-state) velocity at which negative damping is present in the friction, instability is induced in the system. Consequently, the lower disc cannot rotate with a constant velocity any more and torsional vibrations occur (i.e. the constant velocity state is undesirable). However, for higher input voltages, which corresponds to the region where positive damping is present in the friction, both a constant velocity (stable equilibrium point) and torsional vibrations (stable limit cycles) coexist in the system. The size of this region is determined by the negative damping at low velocities in comparison to the level of viscous friction at higher velocities.

The friction characteristics which can induce torsional vibrations cannot be obtained when only a normal force is applied to the brake at the lower disc. However, when a certain lubrication is added between the brake disc and the contact material of the brake, torsional steady-state vibrations appear for constant input voltages. Namely, when lubrication is present in the contact, the friction force is partly due to the contact of the two contact surfaces and partly due to the lubricant and its viscosity. As the sliding velocity increases, the solid-to-solid contact decreases, reducing friction and increasing the acceleration of the moving part. Consequently, negative damping occurs in the friction-velocity curve, which is responsible for the occurrence of torsional vibrations in the set-up.

- In this thesis, we conclude that the level of positive damping in the friction at very small velocities in comparison to the level of negative damping appearing for slightly higher velocities determines which type of torsional vibrations occur in the system: i.e. torsional vibrations with or without stick-slip. Namely, if positive damping at very low velocities does not exist, or if it is small with respect to the negative damping level, then only torsional vibrations with stick-slip can be obtained. Moreover, if the positive damping at very low velocities is high enough with respect to the negative damping level, then torsional vibrations with and without stick-slip can occur.

In real life systems, both torsional vibrations with and without stick-slip can appear. In the set-up, we obtain only torsional vibrations with stick-slip as a result of the contact between bronze brake and a steel brake disc, with ondina oil 68 as a lubricant. On the other hand, when the friction torque is produced as a result of the contact between rubber brake and the brass disc, with water as a lubricant, then both types of torsional vibrations are obtained. For very low angular velocities, the friction is mainly due to the contact between the contacting materials (brake material and lower brake disc). Consequently, the

friction is determined by characteristics of the materials and the appearance of a positive damping for lower velocities in the friction model is related to the types of contact material which produce friction.

- The results on all levels confirm that the sticking phenomenon, which is modelled with a set-valued force law for the friction, plays a crucial role in describing the steady-state phenomena observed in the set-up. Namely, with this friction model, the dynamics of the set-up is described by differential equations with discontinuous right-hand side. With these equations we successfully modelled equilibrium sets, equilibria and stick-slip limit cycling, phenomena which are also observed in the set-up. We also observe a discontinuous fold bifurcation both in simulations and experiments. The performed analysis confirms that the discontinuous bifurcations play a crucial role in the creation and destruction of the observed limit cycling (i.e. torsional vibrations).

### 6.1.2 Interaction Between Torsional and Lateral Vibrations in Flexible Rotor Systems

- If a mass-unbalance is present at the lower disc and the disc can both rotate and move freely in lateral direction, then two types of torsional vibration can appear in the system: friction-induced vibrations and vibrations due to a coupling between torsional and lateral flexibility modes.

The causes for friction-induced vibrations are already summarized in the previous section. Torsional vibrations due to the coupling between torsional and lateral dynamics occur for input voltages which are higher than a so-called critical voltage related to a critical angular velocity inducing a resonance in lateral direction. The critical angular velocity is determined only by the parameters of the system in lateral direction and, at that velocity, the radial displacement of the center of the lower disc reaches a maximum. In that working region, instabilities in the system can occur even if no negative damping is present in the friction at the lower disc. Consequently, torsional vibrations occur at the lower disc.

- Both the numerical and experimental results show that, when there is mass-unbalance at the lower disc, the amplitude of friction-induced torsional vibrations and the region in which these vibrations occur, both decrease. Moreover, we show that if the level of mass-unbalance is high enough then torsional vibrations can even entirely disappear. This fact indicates that a strong coupling between torsional and lateral vibrations exists.
- Due to limitations in the DC motor, we cannot study torsional vibrations due to the coupling experimentally. However, numerical analysis shows that such torsional vibrations can occur at the input voltage which are slightly higher than a so-called critical voltage  $u_{cc}$  related to a critical angular velocity inducing a resonance in lateral direction. At those input voltages, despite the fact that extra energy is supplied to the system (due to an increase of  $u_c$ ), the potential energy stored in the leaf springs and rods (i.e.  $r$ ) and in the potential energy stored in the low-stiffness spring (i.e.  $-\alpha$ ) both significantly decrease. The extra supplied energy is then stored in torsional and lateral vibrations. Furthermore,

when almost no decrease occurs in the potential energy of the low-stiffness spring (i.e. when  $-\alpha_{eq}$  slightly decreases for voltages  $u_c$  which are slightly higher than  $u_{cc}$ ) torsional vibrations disappear and the extra energy supplied to the system transforms mainly to the kinetic energy of the lower disc.

Numerical analyses also shows that a higher level of mass-unbalance, a higher stiffness of the string or a higher damping in lateral direction or a lower level of stiffness of the construction in lateral direction decrease the instability region (i.e. decrease the region in which torsional vibrations occur). Moreover, if the levels of all those parameters are such that no torsional vibrations are present in the system, the parameter changes influence in various ways the steady-state behaviour of the system. Nevertheless, as a result of the preformed analysis, we conclude that only if the damping in lateral direction increases, both torsional and lateral vibrations decrease which is not the case if we change other parameters.

## 6.2 Recommendations

A good understanding of various types of vibrations and the interaction between them is very important in a wide range of mechanical systems, where such vibrations are unwanted. For example, drilling systems, which are used for exploration of oil and gas, undergo various types of vibrations: torsional (rotational) vibrations, lateral (bending) vibrations, axial (longitudinal) vibrations and hydraulic vibrations. The collection of measurement data, in such systems, can be very expensive and the testing of various control strategies on the real drill-string systems can be even hazardous. Therefore, the knowledge obtained here provides an improved understanding of the causes for torsional and lateral vibrations. Moreover based on this knowledge, various control strategies can be designed and tested on the designed set-up to eliminate torsional and lateral vibrations. Furthermore, the results presented here can support the design of various turbines, pumps, fans in preventing the occurrence of or in decreasing the amplitude of friction-induced torsional vibrations and lateral vibrations due to a mass-unbalance.

Therefore, in this section, we provide recommendations for removing vibrations in flexible rotor systems. Furthermore, we list a few open problems which directly arise from this thesis. Further research on these open problems should lead towards an improved understanding of various vibrations in dynamical systems and can support the developments of methods aiming at the avoidance of such vibrations.

- In order to eliminate friction-induced torsional vibrations, the effect of negative damping should be removed from the inertia which is driven by the flexibility (the lower disc in the set-up). In many similar systems, this can be done with appropriate lubrication which should be applied in order to change the form of the friction which is responsible for the vibrations.
- Friction-induced torsional vibrations can be decreased or eliminated by adding an additional mass-unbalance at the disc which is driven by the flexibility if the disc can freely move in lateral direction. However, such a solution increases the amplitude of lateral vibrations and even multiple equilibria can occur for high velocities. Therefore, adding an additional mass-unbalance is advisable only for

systems where the critical angular velocities cannot be reached due to design limitations.

- Torsional vibrations which occur due to the coupling between torsional and lateral motions can be decreased by increasing the damping in the lateral direction. Moreover, with a higher damping level, the amplitude of lateral vibrations also decreases. If we increase the torsional stiffness of the string, torsional vibrations can also disappear. However, the torsional stiffness does not influence the amplitude of lateral vibrations. Finally, if we increase the stiffness in lateral direction, then torsional vibrations and lateral vibrations with high amplitude occur at very high angular velocities (i.e. for very high input voltages). Therefore, since the input voltage is limited in servo motors, such an instability region can occur at velocities outside the working range of the system.
- A lot of research has already been performed on a compensation of friction-induced oscillations in mechanical systems when no flexibility is present in the system, see [Armstrong-Hélouvry et al., 1994a; Hensen, 2002; Hensen et al., 2002; Mallon, 2003; Mallon et al., 2005; Putra, 2004; Putra et al., 2004; Putra and Nijmeijer, 2003, 2004; Van de Wouw et al., 2004]. On the other hand, not a lot of work has been done on compensation of friction-induced vibrations in systems with friction and with flexibility, see [Jansen, 1993; Jansen and Van den Steen, 1995; Olsson, 1996; Olsson and Åström, 1996, 2001]. Based on the constructed nonlinear models, the development of control strategies, which can decrease or even remove vibrations, can be studied and developed. Since the experimental set-up exist in which various vibrations can be induced, it represents an opportunity to experimentally validate such control techniques.

For example, the drilling industry is particularly interested in control strategies which can decrease or eliminate torsional and lateral vibrations and where the control signal is a function of variables which are measured at the motor (torque, angular velocity of the upper disc, motor current). Also, in printing machines, there is a mechanism where a motor drives a printing head via a rubber belt and it is very important to accurately prescribe a velocity of the printing head despite the existence of friction.

- Backward whirl is a phenomenon which sometimes occurs in rotor systems when the shaft (e.g. Bottom-Hole-Assembly in drilling systems) is in contact with the stator (e.g. borehole in drilling systems). Namely, the backward whirl represents a motion in which the center of the shaft moves in the opposite direction with respect to the rotation of the shaft. A lot of theoretical research which considers that phenomenon has already been done. However, a limited number of experimental results are available. With minor improvements of the designed it is possible to decrease the distance between the lower disc of the set-up and the vessel, where the lower disc is placed. Then it would be possible to obtain backward whirl in the set-up and consequently, this phenomenon can be studied both on a theoretical and experimental level.
- We have discussed the global stability properties of equilibrium points and sets of the system in which only torsional vibrations occur (using Lyapunov's direct method). As a result of this analysis, we succeed to relate the local and global stability properties of the equilibria to specific friction characteristics present at

upper and lower disc. Moreover, in terms of the input voltage we have estimated the region in which both isolated equilibria (constant velocity at the lower disc) and limit cycles (torsional vibrations) occur and we even obtain an estimate of the region of attraction of the equilibria.

For the system in which both torsional and lateral vibrations occur, we only discuss global stability properties of the equilibrium sets, which appear when the system is in the sticking region. Consequently, the global stability of the isolated equilibria remains an open issue. Such global stability analysis would provide analytical conditions under which those vibrations disappear.

## Appendix A

# Derivation of Equations of Motion of the Set-Up

In order to derive model of the set-up using the Euler-Lagrange equations, we need to determine the kinetic energy  $\mathcal{T}(\mathbf{q}, \dot{\mathbf{q}})$ , the potential energy  $\mathcal{V}(\mathbf{q})$  and generalized non-conservative forces of the system  $\mathbf{Q}^{nc}$ , where  $\mathbf{q}$  are generalized coordinates defined by

$$\mathbf{q} = [ \theta_u \quad x \quad y \quad \alpha ]^T. \quad (\text{A.1})$$

As already explained in Section 3.2.4, the model is described in a co-rotating coordinate frame  $\{O, \bar{\mathbf{e}}\}$  (see figure 3.12(b)), characterized by the location of its origin  $O$  and the orientation of a frame  $\bar{\mathbf{e}} = [ \bar{\mathbf{e}}_1 \quad \bar{\mathbf{e}}_2 \quad \bar{\mathbf{e}}_3 ]^T$  of three mutually orthogonal unit vectors  $\bar{\mathbf{e}}_1, \bar{\mathbf{e}}_2, \bar{\mathbf{e}}_3$ , where  $\bar{\mathbf{e}}_3 = \bar{\mathbf{e}}_1 \times \bar{\mathbf{e}}_2$ . In this thesis we also use the fixed coordinate frame  $\{O, \bar{\mathbf{e}}^0\}$  (see figure 3.20) with  $\bar{\mathbf{e}}^0 = [ \bar{\mathbf{e}}_1^0 \quad \bar{\mathbf{e}}_2^0 \quad \bar{\mathbf{e}}_3^0 ]^T$ , where  $\bar{\mathbf{e}}_3^0 = \bar{\mathbf{e}}_1^0 \times \bar{\mathbf{e}}_2^0$ . The relationship between  $\bar{\mathbf{e}}$  and  $\bar{\mathbf{e}}^0$  is given by:

$$\bar{\mathbf{e}} = \begin{bmatrix} \cos(\theta_u) & \sin(\theta_u) & 0 \\ -\sin(\theta_u) & \cos(\theta_u) & 0 \\ 0 & 0 & 1 \end{bmatrix} \bar{\mathbf{e}}^0 \text{ and } \bar{\mathbf{e}}^0 = \begin{bmatrix} \cos(\theta_u) & -\sin(\theta_u) & 0 \\ \sin(\theta_u) & \cos(\theta_u) & 0 \\ 0 & 0 & 1 \end{bmatrix} \bar{\mathbf{e}}. \quad (\text{A.2})$$

### Kinetic Energy $\mathcal{T}(\mathbf{q}, \dot{\mathbf{q}})$

The kinetic energy of the system can be described with:

$$\mathcal{T}(\mathbf{q}, \dot{\mathbf{q}}) = \mathcal{T}_u(\mathbf{q}, \dot{\mathbf{q}}) + \mathcal{T}_{m_r}(\mathbf{q}, \dot{\mathbf{q}}) + \mathcal{T}_{m_t}(\mathbf{q}, \dot{\mathbf{q}}). \quad (\text{A.3})$$

In (A.3),  $\mathcal{T}_u$  represents the kinetic energy of the upper disc and it can be computed by:

$$\mathcal{T}_u = \frac{1}{2} J_u \dot{\theta}_u^2. \quad (\text{A.4})$$

Then,  $\mathcal{T}_{m_r}$  is the kinetic energy of the mass  $m_r$  - the mass which rotates around the center of the lower disc (see figure 3.12(b)). It can be computed with

$$\mathcal{T}_{m_r} = \frac{1}{2} m_r (\dot{\vec{r}}_C \cdot \dot{\vec{r}}_C) + \frac{1}{2} J_C (\dot{\theta}_u + \dot{\alpha})^2, \quad (\text{A.5})$$

where all parameters are explained in table 3.2. In (A.5),  $\vec{r}_C$  represents the position of the center of the mass of the mass  $m_r$  and it can be expressed with

$$\vec{r}_C = [ x + e \cos(\alpha) \quad y + e \sin(\alpha) \quad 0 ] \vec{e}.$$

Knowing that

$$\dot{\vec{e}} = \begin{bmatrix} 0 & \dot{\theta}_u & 0 \\ -\dot{\theta}_u & 0 & 0 \\ 0 & 0 & 0 \end{bmatrix} \vec{e}. \quad (\text{A.6})$$

it can be obtained that

$$\begin{aligned} \dot{\vec{r}}_C &= [ r_1 \quad r_2 \quad 0 ] \vec{e}, \text{ with} \\ r_1 &= \dot{x} - e \dot{\alpha} \sin(\alpha) - y \dot{\theta}_u - e \dot{\theta}_u \sin(\alpha), \\ r_2 &= \dot{y} + e \dot{\alpha} \cos(\alpha) + x \dot{\theta}_u + e \dot{\theta}_u \cos(\alpha). \end{aligned} \quad (\text{A.7})$$

If we use (A.7) in (A.5) we obtain that

$$\begin{aligned} \mathcal{T}_{m_r} &= \frac{1}{2} m_r (\dot{x} - e \dot{\alpha} \sin(\alpha) - y \dot{\theta}_u - e \dot{\theta}_u \sin(\alpha))^2 \\ &\quad + \frac{1}{2} m_r (\dot{y} + e \dot{\alpha} \cos(\alpha) + x \dot{\theta}_u + e \dot{\theta}_u \cos(\alpha))^2 + \frac{1}{2} J_C (\dot{\theta}_u + \dot{\alpha})^2. \end{aligned} \quad (\text{A.8})$$

Finally,  $\mathcal{T}_{m_t}$  is the kinetic energy of the mass  $m_t$  - the mass which cannot rotate around the center of the lower disc (see figure 3.12(b)), but only translates with the lower disc (think of the upper bearing housing, the brake, part of the encoder at the lower disc, etc). It can be computed with

$$\mathcal{T}_{m_t} = \frac{1}{2} m_t (\dot{\vec{r}}_A \cdot \dot{\vec{r}}_A), \quad (\text{A.9})$$

where  $\vec{r}_A$  represents the position of the geometric center of the lower disc, which can be expressed with

$$\vec{r}_A = [ x \quad y \quad 0 ] \vec{e}. \quad (\text{A.10})$$

From (A.6) and (A.10) it follows that

$$\dot{\vec{r}}_A = [ \dot{x} - y \dot{\theta}_u \quad \dot{y} + x \dot{\theta}_u \quad 0 ] \vec{e}. \quad (\text{A.11})$$

If we use (A.11) in (A.9) we obtain

$$\mathcal{T}_{m_t} = \frac{1}{2} m_t (\dot{x} - y \dot{\theta}_u)^2 + \frac{1}{2} m_t (\dot{y} + x \dot{\theta}_u)^2. \quad (\text{A.12})$$

Consequently, from (A.3), (A.4), (A.8) and (A.12) we obtain the following expression for the kinetic energy of the system:

$$\begin{aligned} \mathcal{T}(\mathbf{q}, \dot{\mathbf{q}}) &= \frac{1}{2} m_r (\dot{x} - e \dot{\alpha} \sin(\alpha) - y \dot{\theta}_u - e \dot{\theta}_u \sin(\alpha))^2 \\ &\quad + \frac{1}{2} m_r (\dot{y} + e \dot{\alpha} \cos(\alpha) + x \dot{\theta}_u + e \dot{\theta}_u \cos(\alpha))^2 \\ &\quad + \frac{1}{2} m_t (\dot{x} - y \dot{\theta}_u)^2 + \frac{1}{2} m_t (\dot{y} + x \dot{\theta}_u)^2 + \frac{1}{2} J_u \dot{\theta}_u^2 + \frac{1}{2} J_C (\dot{\theta}_u + \dot{\alpha})^2. \end{aligned}$$

## Potential Energy $\mathcal{V}(\mathbf{q})$

The potential energy of the system can be described with:

$$\mathcal{V}(\mathbf{q}) = \mathcal{V}_r(\mathbf{q}) + \mathcal{V}_l(\mathbf{q}). \quad (\text{A.13})$$

In (A.13),  $\mathcal{V}_r$  represents the elastic energy stored in the drill-string and it can be computed with

$$\mathcal{V}_r = \frac{1}{2}k_\theta\alpha^2. \quad (\text{A.14})$$

Moreover,  $\mathcal{V}_l$  represents the elastic energy in lateral direction (deformation of the leaf spring and rods of the constraints), which can be expressed with

$$\mathcal{V}_l = \frac{1}{2}k(\vec{r}_A \cdot \vec{e}_1^0)^2 + \frac{1}{2}k(\vec{r}_A \cdot \vec{e}_2^0)^2. \quad (\text{A.15})$$

If we use (A.2) and (A.10) in (A.15), the following expression for  $\mathcal{V}_l$  is obtained:

$$\mathcal{V}_l = \frac{1}{2}k x^2 + \frac{1}{2}k y^2. \quad (\text{A.16})$$

Consequently, from (A.13), (A.14) and (A.16) the following expression is obtained for the potential energy of the system:

$$\mathcal{V}(\mathbf{q}) = \frac{1}{2}k_\theta\alpha^2 + \frac{1}{2}k x^2 + \frac{1}{2}k y^2.$$

## Non-Conservative Forces $\mathbf{Q}^{nc}(\mathbf{q}, \dot{\mathbf{q}})$

In the set-up, a dissipative torque due to the friction at the upper part of the set-up

$$\vec{T}_u = -(k_m u - T_{fu}(\dot{\theta}_u))\vec{e}_3^0, \quad (\text{A.17})$$

a dissipative torque due to the friction at the lower part of the set-up

$$\vec{T}_l = T_{fl}(\dot{\theta}_l)\vec{e}_3^0, \quad (\text{A.18})$$

and a dissipative force due to the damping forces present in lateral direction

$$\vec{F}_b = -b(\dot{\vec{r}}_A \cdot \vec{e}_1^0)\vec{e}_1^0 - b(\dot{\vec{r}}_A \cdot \vec{e}_2^0)\vec{e}_2^0. \quad (\text{A.19})$$

exist.

The non-conservative forces  $\mathbf{Q}^{nc}(\mathbf{q}, \dot{\mathbf{q}})$  can be determined with:

$$\mathbf{Q}^{nc}(\mathbf{q}, \dot{\mathbf{q}}) = \mathbf{Q}_u^{nc}(\mathbf{q}, \dot{\mathbf{q}}) + \mathbf{Q}_l^{nc}(\mathbf{q}, \dot{\mathbf{q}}) + \mathbf{Q}_b^{nc}(\mathbf{q}, \dot{\mathbf{q}}), \quad (\text{A.20})$$

where  $\mathbf{Q}_u^{nc}$ ,  $\mathbf{Q}_l^{nc}$  and  $\mathbf{Q}_b^{nc}$  are associated with the non-conservative forces and torques in (A.17), (A.18) and (A.19), respectively.

In (A.20),  $\mathbf{Q}_u^{nc}$  is due to the non-conservative forces present at the upper part of the set-up and it can be determined with:

$$\mathbf{Q}_u^{nc} = \left( \frac{\partial \theta_u}{\partial \mathbf{q}} \right)^T (-\vec{e}_3^0) \cdot \vec{T}_u.$$



Since

$$\frac{\partial \theta_u}{\partial \mathbf{q}} = [ 1 \ 0 \ 0 \ 0 ],$$

then

$$\mathbf{Q}_u^{nc} = [ k_m u - T_{fu}(\dot{\theta}_u) \ 0 \ 0 \ 0 ]^T. \quad (\text{A.21})$$

Similarly,  $\mathbf{Q}_l^{nc}$  in (A.20) is due to the non-conservative forces present at the lower part of the set-up in torsional direction and can be determined with:

$$\mathbf{Q}_l^{nc} = \left( \frac{\partial \theta_l}{\partial \mathbf{q}} \right)^T (-\vec{e}_3^0) \cdot \vec{T}_l.$$

Since  $\theta_l = \theta_u + \alpha$ , then

$$\frac{\partial \theta_l}{\partial \mathbf{q}} = [ 1 \ 0 \ 0 \ 1 ].$$

Consequently,

$$\mathbf{Q}_l^{nc} = [ -T_{fl}(\dot{\theta}_u + \dot{\alpha}) \ 0 \ 0 \ -T_{fl}(\dot{\theta}_u + \dot{\alpha}) ]^T. \quad (\text{A.22})$$

Finally,  $\mathbf{Q}_b^{nc}$  in (A.20) is due to the non-conservative forces present at the lower part of the set-up in lateral direction and can be determined with:

$$\mathbf{Q}_b^{nc} = \left( \frac{\partial \vec{r}_A}{\partial \mathbf{q}} \right)^T \cdot \vec{F}_b. \quad (\text{A.23})$$

Vector  $\vec{r}_A$  is given by (A.10) and according (A.2) it can be represented with

$$\vec{r}_A = [ x \cos(\theta_u) - y \sin(\theta_u) \ x \sin(\theta_u) + y \cos(\theta_u) \ 0 ] \vec{e}^0,$$

in the fixed coordinate frame. Then,

$$\left( \frac{\partial \vec{r}_A}{\partial \mathbf{q}} \right)^T = \begin{bmatrix} -x \sin(\theta_u) - y \cos(\theta_u) & x \cos(\theta_u) - y \sin(\theta_u) & 0 \\ \cos(\theta_u) & \sin(\theta_u) & 0 \\ -\sin(\theta_u) & \cos(\theta_u) & 0 \\ 0 & 0 & 0 \end{bmatrix} \vec{e}^0. \quad (\text{A.24})$$

Consequently, if we substitute (A.19) and (A.24) in (A.23) the following expression for  $\mathbf{Q}_b^{nc}$  is obtained

$$\mathbf{Q}_b^{nc} = \begin{bmatrix} -bx(\dot{y} + x\dot{\theta}_u) + by(\dot{x} - y\dot{\theta}_u) \\ -b(\dot{x} - y\dot{\theta}_u) \\ -b(\dot{y} + x\dot{\theta}_u) \\ 0 \end{bmatrix}. \quad (\text{A.25})$$

Finally, according to (A.20), (A.21), (A.22) and (A.25) the following expression for the non-conservative forces  $\mathbf{Q}^{nc}$  is obtained:

$$\mathbf{Q}^{nc}(\mathbf{q}, \dot{\mathbf{q}}) = \begin{bmatrix} k_m u - T_{fu}(\dot{\theta}_u) - T_{fl}(\dot{\theta}_u + \dot{\alpha}) - bx(\dot{y} + x\dot{\theta}_u) + by(\dot{x} - y\dot{\theta}_u) \\ -b(\dot{x} - y\dot{\theta}_u) \\ -b(\dot{y} + x\dot{\theta}_u) \\ -T_{fl}(\dot{\theta}_u + \dot{\alpha}) \end{bmatrix}.$$

## Appendix B

# Local and Global Asymptotic Stability Conditions

### Stability Conditions when $T_{fl}(\omega_l)$ is a Monotonically Increasing Function

When  $T_{fl}(\omega_l)$  is as shown in figure 4.4(a), the incremental sector condition (4.26) holds for every  $\mathbf{x}_{teq}, \mathbf{x}_t \in \mathbb{R}^3$ . From (4.24) and (4.25) it can be concluded that  $\dot{V}_t(\mathbf{x}_t, \mathbf{x}_{teq}) \leq 0$  for every  $\mathbf{x}_{teq}$  and every  $\mathbf{x}_t \in \mathbb{R}^3$ . Therefore, every equilibrium point of the system is stable in the sense of Lyapunov.

It can also be shown that only attractive sliding modes or transversal intersections can occur at the switching surfaces  $\Sigma_1$  and  $\Sigma_2$  with

$$\Sigma_1 = \{\mathbf{x}_t \in \mathbb{R}^3 \mid \omega_u = 0\}, \quad \Sigma_2 = \{\mathbf{x}_t \in \mathbb{R}^3 \mid \omega_u + \dot{\alpha} = 0\}.$$

and that repulsive sliding modes are not present. Uniqueness of solutions is therefore guaranteed [Leine, 2000; Leine and Nijmeijer, 2004] which could also be inferred from the fact that the set-valued friction laws  $T_{fu}(\omega_u)$  and  $T_{fl}(\omega_l)$  take values in minimal closed convex sets for zero relative velocity and are always dissipative.

### Isolated Equilibria

When  $\omega_{eq} > 0$ , it can be concluded that  $\dot{V}_t(\mathbf{x}_t, \mathbf{x}_{teq}) = 0$  for  $\mathbf{x}_t \in \mathcal{L}_p$ , with

$$\mathcal{L}_p = \{\mathbf{x}_t \in \mathbb{R}^3 \mid \omega_u = \omega_{eq}, \dot{\alpha} = 0\}.$$

If  $\mathbf{x}_t \in \mathcal{L}_p$  then  $\omega_u = \omega_{eq} = \text{const}$ ,  $\dot{\alpha} = 0$ . Consequently, for an invariant subset of  $\mathcal{L}_p$  it should hold that  $\dot{\omega}_u = \ddot{\alpha} = 0$  for  $t \rightarrow \infty$ . If we substitute this into the differential equations (4.1) of the system, then the obtained equations can only be satisfied in the equilibrium point. This leads to the conclusion that the equilibrium point  $\mathbf{x}_{teq}$ , defined with (4.23), represents the largest invariant set on  $\mathcal{L}_p$  when  $\omega_{eq} > 0$ . The application of LaSalle's invariance principle [Sastry, 1999; Van de Wouw and Leine, 2004] now proves that the equilibrium point  $\mathbf{x}_{teq}$  is attractive and the whole state space  $\mathbb{R}^3$  represents the region of attraction. Therefore, since we have proven that every

equilibrium point is stable and globally attractive for  $\omega_{eq} > 0$ , we can conclude that all those equilibrium points are globally asymptotically stable, when the friction torque shown in figure 4.4(a) is present in the system. We illustrate this fact graphically in figure 4.4(b). Similarly, it can be also proven that all equilibrium points are globally asymptotically stable for  $\omega_{eq} < 0$ .

### Equilibrium Set

We have proven that every equilibrium point  $\mathbf{x}_{teq} \in \mathcal{E}_t$  is stable in the sense of Lyapunov. Now, we consider the stability of the equilibrium set  $\mathcal{E}_t$  as a whole. In order to prove that the equilibrium set  $\mathcal{E}_t$  is stable in the sense of Lyapunov, the sets  $\mathcal{S}$ ,  $\mathcal{A}_\delta$  and  $\mathcal{A}_\epsilon$  are introduced:

$$\begin{aligned} \mathcal{S} &= \bigcup_{\forall \mathbf{x}_{teq} \in \mathcal{E}_t} \mathcal{S}_{\mathbf{x}_{teq}}, \quad \mathcal{S}_{\mathbf{x}_{teq}} = \{\mathbf{x}_t \in \mathbb{R}^3 \mid V_t(\mathbf{x}_t, \mathbf{x}_{teq}) < r\}, \quad r > 0, \\ \mathcal{A}_a &= \{\mathbf{x}_t \in \mathbb{R}^3 \mid \|\mathbf{x}_t - \text{prox}_{\mathcal{E}_t}(\mathbf{x}_t)\| \leq a\}, \quad a \in \{\delta, \epsilon\}, \\ \text{prox}_{\mathcal{E}_t}(\mathbf{x}_t) &= \underset{\forall \mathbf{x}_t^* \in \mathcal{E}_t}{\text{argmin}} \|\mathbf{x}_t - \mathbf{x}_t^*\|, \end{aligned} \tag{B.1}$$

where  $\text{prox}_{\mathcal{E}_t}(\mathbf{x}_t)$  defines the proximal point in the set  $\mathcal{E}_t$  of the point  $\mathbf{x}_t$ . According to the previous analysis, it can be seen that for all  $\epsilon > 0$ , we can choose  $r > 0$  such that  $\mathcal{S} \subset \mathcal{A}_\epsilon$ . Then, for the chosen  $\mathcal{S}$  (and  $r$ ),  $\delta$  can be chosen such that  $\mathcal{A}_\delta \subset \mathcal{S}$ . Consequently, for every  $t_0 \geq 0$  it follows that

$$\mathbf{x}(t_0) \in \mathcal{A}_\delta \Rightarrow \mathbf{x}(t) \in \mathcal{A}_\epsilon \quad \forall t \geq t_0, \tag{B.2}$$

since  $\mathcal{A}_\delta \subset \mathcal{S}$  and  $\mathcal{S} \subset \mathcal{A}_\epsilon$ . Consequently, the equilibrium set  $\mathcal{E}_t$  (as a whole) is stable in the sense of Lyapunov.

Let us now show that the equilibrium set  $\mathcal{E}_t$  is globally attractive. For that purpose, let  $V_1(\mathbf{x}_t) := V(\mathbf{x}_t, \mathbf{0})$ . Then the previous analysis yields  $\dot{V}_1(\mathbf{x}_t) \leq 0$  for all  $\mathbf{x}_t \in \mathbb{R}^3$ . Next, for the estimated friction torques  $T_{fu}(\omega_u)$  and the suggested  $T_{fl}(\omega_l)$ , from (4.24) it can be concluded that  $\dot{V}_1(\mathbf{x}_t) = 0$  only for  $\mathbf{x}_t \in \mathcal{L}_0$ , with

$$\mathcal{L}_0 = \{\mathbf{x}_t \in \mathbb{R}^3 \mid \omega_u = 0, \dot{\alpha} = 0\}. \tag{B.3}$$

Consequently, for an invariant subset of  $\mathcal{L}_0$  it should hold that  $\dot{\omega}_u = \ddot{\alpha} = 0$ . If we insert this into the differential equations (4.1) of the system, then the obtained equations are only satisfied if  $\mathbf{x}_{teq} \in \mathcal{E}_t$ . This leads us to the conclusion that the equilibrium set  $\mathcal{E}_t$  represents the largest invariant set on  $\mathcal{L}_0$ .

The application of LaSalle's invariance principle [Sastry, 1999; Van de Wouw and Leine, 2004] now proves that equilibrium set  $\mathcal{E}_t$  is globally attractive and the whole state space  $\mathbb{R}^3$  represents the region of attraction. Finally, since we proved that the equilibrium set  $\mathcal{E}_t$  is stable and globally attractive, we can conclude that  $\mathcal{E}_t$  is globally asymptotically stable.

## Stability Conditions when $T_{fl}(\omega_l)$ is Modelled with a Humped Friction Model

### Isolated Equilibria

When  $T_{fl}(\omega_l)$  is represented by a humped friction model as shown in figure 4.5(a), the incremental sector condition (4.26) can be satisfied in the neighborhood of an equilibrium point for  $\omega_{eq} > 0$ , only when

$$u_c \in (u_{\mathcal{E}p}, u_{e1}) \cup (u_{e2}, \infty), \quad (\text{B.4})$$

where  $u_{\mathcal{E}p}$  is defined by (4.7) and

$$u_{e1} = \frac{T_{cu}(\omega_{e1}) + T_{cl}(\omega_{e1})}{k_m}, \quad u_{e2} = \frac{T_{cu}(\omega_{e2}) + T_{cl}(\omega_{e2})}{k_m}, \quad (\text{B.5})$$

where  $\omega_{e1}$  and  $\omega_{e2}$  are defined with (4.32) (see figure B.1). In other words,  $\dot{V}(\mathbf{x}_t, \mathbf{x}_{teq})$  can be shown to be negative semidefinite when  $\mathbf{x}_{teq}$  is such that

$$\left. \frac{dT_{cl}}{d\omega_l} \right|_{\omega_l = \omega_{eq}} > 0.$$

When the input voltage  $u_c$  satisfies condition (4.29), then the related equilibrium point  $\mathbf{x}_{teq}$  is such that condition (4.26) is satisfied, hence  $\dot{V}(\mathbf{x}_t, \mathbf{x}_{teq}) \leq 0$  for every  $\mathbf{x}_t \in \mathbb{R}^3$ . Then, we can prove that such equilibrium point is globally asymptotically stable, in a similar fashion as proven when  $T_{fl}(\omega_l)$  represents a monotonically increasing function [Mihaĵlović et al., 2005a].

On the other hand, using the Lyapunov candidate function (4.22) we can only prove that equilibrium points are locally asymptotically stable, when

$$u_c \in (u_{g1}, u_{e1}) \cup (u_{e2}, u_{g2}), \quad (\text{B.6})$$

( $u_{g1}$  and  $u_{g2}$  are defined with (4.31); see also figure B.1 where the angular velocities  $\omega_{g1}$  and  $\omega_{g2}$ , corresponding to  $u_{g1}$  and  $u_{g2}$ ), respectively. This proof can be derived in a similar way as it is derived for the case when  $T_{fl}(\omega_l)$  is monotonically increasing function (figure 4.4(a)). Namely, when  $T_{fl}(\omega_l)$  is modelled as shown in figure B.1, then for an equilibrium point  $\mathbf{x}_{teq}$  obtained for

$$\hat{u}_2 = \frac{T_{cu}(\hat{\omega}_2) + T_{cl}(\hat{\omega}_2)}{k_m},$$

( $\omega_{eq} = \hat{\omega}_2$ ),  $\dot{V}_t(\mathbf{x}_t, \mathbf{x}_{teq}) \leq 0$  for every  $\mathbf{x} \in \mathcal{B}_2$ , with

$$\mathcal{B}_2 = \{\mathbf{x}_t \in \mathbb{R}^3 \mid |\omega_l| < |\hat{\omega}_2 - \hat{\omega}'_2|\}.$$

Then an estimate of the region of attraction of  $\mathbf{x}_{teq}$  is given by:

$$\mathcal{I}_{\rho_2} = \{\mathbf{x}_t \in \mathbb{R}^3 \mid \dot{V}_t(\mathbf{x}_t, \mathbf{x}_{teq}) < \rho_2\}, \quad \text{with } \rho_2 = \max_{\mathcal{I}_{\rho} \subset \mathcal{B}_2} \rho,$$

with

$$\mathcal{I}_{\rho} = \{\mathbf{x}_t \in \mathbb{R}^3 \mid \dot{V}_t(\mathbf{x}_t, \mathbf{x}_{teq}) < \rho\}. \quad (\text{B.7})$$

Consequently, if  $\hat{u}_2$  is closer to  $u_{e2}$ , defined by (B.5), then the set  $\mathcal{B}_2$  is smaller and therefore the estimate of the basin of attraction  $\mathcal{I}_{\rho_2}$  of the equilibrium point for  $u_c = \hat{u}_2$  is also smaller. Similarly, when  $u_c = \hat{u}_1$  with

$$\hat{u}_1 = \frac{T_{cu}(\hat{\omega}_1) + T_{cl}(\hat{\omega}_1)}{k_m}.$$

(see figure B.1), then  $\dot{V}_t(\mathbf{x}_t, \mathbf{x}_{teq}) \leq 0$  for every  $\mathbf{x} \in \mathcal{B}_1$ , with

$$\mathcal{B}_1 = \{\mathbf{x}_t \in \mathbb{R}^3 \mid |\omega_l| < |\hat{\omega}_1 - \hat{\omega}'_1|\}.$$

The basin of attraction of the related equilibrium point is

$$\mathcal{I}_{\rho_1} = \{\mathbf{x}_t \in \mathbb{R}^3 \mid \dot{V}_t(\mathbf{x}_t, \mathbf{x}_{teq}) < \rho_1\}, \text{ with } \rho_1 = \max_{\mathcal{I}_{\rho} \subset \mathcal{B}_1} \rho,$$

where  $\mathcal{I}_{\rho}$  is defined by (B.7). Therefore, if  $\hat{u}_1$  is closer to  $u_{e1}$ , then the set  $\mathcal{B}_1$  is smaller and the basin of attraction  $\mathcal{I}_{\rho_1}$  of the equilibrium point for  $u_c = \hat{u}_1$  is also smaller.

In Section 2.2.1 we stress that Lyapunov's stability theorem gives only sufficient conditions for stability. Namely, the fact that  $\dot{V}_t(\mathbf{x}_t, \mathbf{x}_{teq})$  is negative semi-definite in a neighborhood of  $\mathbf{x}_{teq}$  when  $u_c$  satisfies condition (B.6), i.e. when friction damping at the lower disc  $d_l$  is positive does not imply instability when  $u_c$  does not satisfy (B.6). Indeed, using Lyapunov's indirect method, we determined that the system is locally asymptotically stable when  $d_l > d_{min}$ , where  $d_{min}$  represents a negative number defined by (4.20). Consequently, the region of input voltages where the set-up has an asymptotically stable equilibrium is defined with

$$u_c \in (u_{\mathcal{E}p}, u_{s1}) \cup (u_{s2}, \infty), \tag{B.8}$$

which is bigger than the region defined by (B.4). Similar conditions can be derived when  $\omega_{eq} < 0$ . The fact that global stability conditions are not satisfied for all input voltages defined by (B.8), means that for those voltages the possibility of multiple steady-state solutions (i.e. limit cycling) can not be excluded.

## Equilibrium Set

When the friction torque  $T_{fl}(\omega_l)$  shown in figure B.2 (see also figure 4.5(c)) is present in the system, then equilibrium points are globally asymptotically stable for  $u_c > u_{g2}$  where  $u_{g2}$  is defined with (4.31). However, in this case the equilibrium set  $\mathcal{E}_t$  (defined by (4.27)) can only be proven to be locally asymptotically stable using the Lyapunov candidate function (4.22) [Mihajlović et al., 2005a, 2004a].

Namely, in order to analyze the stability properties of the equilibrium set we consider the Lyapunov candidate function (4.22). Its time derivative is given by (4.24). Furthermore, since the friction torque at the upper disc  $T_{fu}(\omega_u)$  represents a monotonically increasing function, then condition (4.25) holds for every  $\mathbf{x}_t \in \mathbb{R}^3$  and every  $\mathbf{x}_{teq} \in \mathcal{E}^t$ . Next, knowing that  $T_{cl}(\omega_a) = T_{sl}$  (see figure B.2) it can be seen that for such a friction function  $|T_{cl}(\omega_l)| > T_{sl}$  for  $|\omega_l| < \omega_a$ . Therefore, for every  $\mathbf{x}_{teq} \in \mathcal{E}_t$  and  $\mathbf{x}_t \in \mathcal{B}_0$ , with

$$\mathcal{B}_0 = \{\mathbf{x}_t \in \mathbb{R}^3 \mid |\omega_l| < \omega_a\},$$

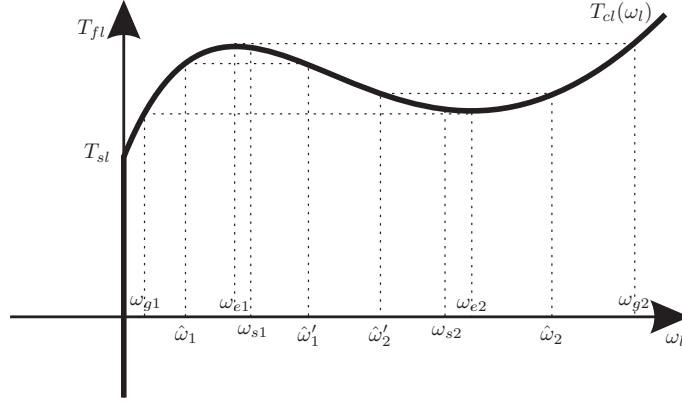


Figure B.1: A humped friction model as shown in figure 4.5(a).

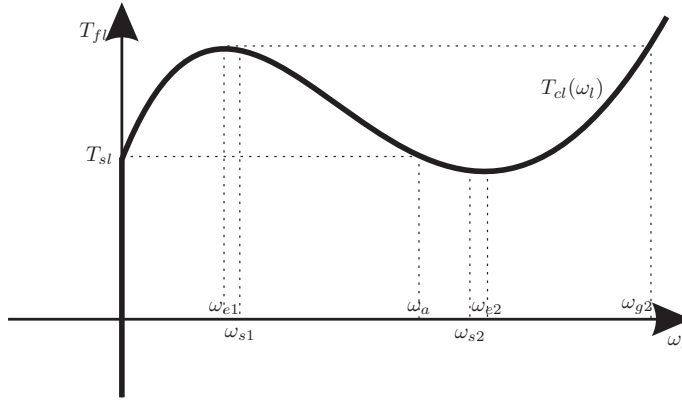


Figure B.2: A humped friction model as shown in figure 4.5(c).

condition (4.26) holds. Consequently,  $\dot{V}_t(\mathbf{x}_t, \mathbf{x}_{teq}) \leq 0$  and each equilibrium point in  $\mathcal{E}_t$  is stable in the sense of Lyapunov. The region of attraction  $\mathcal{I}_{\rho_0}$  of the equilibrium set is defined by:

$$\mathcal{I}_{\rho_0} = \{\mathbf{x}_t \in \mathbb{R}^3 \mid \dot{V}_t(\mathbf{x}_t, \mathbf{x}_{teq}) < \rho_0\}, \text{ with } \rho_0 = \max_{\mathcal{I}_\rho \subset \mathcal{B}_o} \rho,$$

( $\mathcal{I}_\rho$  is defined by (B.7)).

In order to prove that the equilibrium set  $\mathcal{E}_t$  (as a whole) is stable in the sense of Lyapunov, sets  $\mathcal{A}_\delta$ ,  $\mathcal{A}_\epsilon$  and  $\mathcal{S}$  are introduced as defined by (B.1). Then, for all  $\epsilon > 0$ , we can choose  $r$  such that  $r < c$ , with  $c = J_A \omega_a^2 / 2$ , and  $\mathcal{S} \subset \mathcal{A}_\epsilon$ . Furthermore, for the chosen  $\mathcal{S}$  (and  $r$ ),  $\delta$  can be chosen such that  $\mathcal{A}_\delta \subset \mathcal{S}$ . Consequently, for every  $t_0 \geq 0$ , condition (B.2) is satisfied. Namely, for every  $r < c$  it holds that  $\mathcal{A}_\delta \subset \mathcal{S} \subset \mathcal{I}_{\rho_0}$ . Consequently, the equilibrium set  $\mathcal{E}_t$  is stable in the sense of Lyapunov.

Let us now show that the equilibrium set  $\mathcal{E}_t$  is locally attractive. Similarly to the case when  $T_{fl}(\omega_l)$  is as shown in 4.4(a), we introduce first  $V_1(\mathbf{x}_t) = V(\mathbf{x}_t, \mathbf{0})$ . Second, we can prove that  $\dot{V}_1(\mathbf{x}_t) \leq 0$  for all  $\mathbf{x}_t \in \mathcal{C}$  with

$$\mathcal{C}_t = \{\mathbf{x}_t \in \mathbb{R}^3 \mid V_1(\mathbf{x}_t) \leq c\}.$$

Third, we conclude that the equilibrium set  $\mathcal{E}_t$  represents the largest invariant set on  $\mathcal{L}_0 \cap \mathcal{C}_t$ , with  $\mathcal{L}_0$  defined by (B.3). Consequently, the application of LaSalle's invariance principle [Sastry, 1999; Van de Wouw and Leine, 2004] now proves that equilibrium set  $\mathcal{E}_t$  is locally attractive. Moreover, the set  $\mathcal{C}_t$  represents an estimate for the region of attraction. Finally, since we proved that the equilibrium set  $\mathcal{E}_t$  is stable and locally attractive, we can conclude that  $\mathcal{E}_t$  is locally asymptotically stable.

## Appendix C

### Derivation of

$$\dot{V}_i(\mathbf{x}_{i1}, \mathbf{x}_{i2}, \mathbf{x}_{i1eq}, \mathbf{x}_{i1eq})$$

The energy of the considered drill-string system  $V(\mathbf{q}, \dot{\mathbf{q}})$  is defined as

$$V(\mathbf{q}, \dot{\mathbf{q}}) = \mathcal{T}(\mathbf{q}, \dot{\mathbf{q}}) + \mathcal{V}(\mathbf{q}).$$

The kinetic energy  $\mathcal{T}(\mathbf{q}, \dot{\mathbf{q}})$  and the potential energy  $\mathcal{V}(\mathbf{q})$  can be represented by

$$\mathcal{T}(\mathbf{q}, \dot{\mathbf{q}}) = \frac{1}{2} \dot{\mathbf{q}}^T \mathbf{M}(\mathbf{q}) \dot{\mathbf{q}}, \quad \mathcal{V}(\mathbf{q}) = \frac{1}{2} \mathbf{q}^T \mathbf{K} \mathbf{q}, \quad (\text{C.1})$$

where  $\mathbf{q}$  represents the generalized coordinates of the system, defined by (3.12),  $\mathbf{M}(\mathbf{q})$  is given in (3.16) and

$$\mathbf{K} = \begin{bmatrix} 0 & 0 & 0 & 0 \\ 0 & k & 0 & 0 \\ 0 & 0 & k & 0 \\ 0 & 0 & 0 & k_\theta \end{bmatrix}. \quad (\text{C.2})$$

However, when the lower disc rotates with a constant velocity in steady-state (equilibrium point), the energy of the system is not zero in the equilibrium point. Consequently we cannot use the energy as a Lyapunov candidate function. However, if we define  $\bar{V}(\mathbf{q}, \dot{\mathbf{q}}, \mathbf{q}_{eq}, \dot{\mathbf{q}}_{eq})$  in the following way:

$$\begin{aligned} \bar{V}(\mathbf{q}, \dot{\mathbf{q}}, \mathbf{q}_{eq}, \dot{\mathbf{q}}_{eq}) &= \mathcal{T}(\mathbf{q}, \dot{\mathbf{q}} - \dot{\mathbf{q}}_{eq}) + \mathcal{V}(\mathbf{q} - \mathbf{q}_{eq}) \\ &= \frac{1}{2} (\dot{\mathbf{q}} - \dot{\mathbf{q}}_{eq})^T \mathbf{M}(\mathbf{q}) (\dot{\mathbf{q}} - \dot{\mathbf{q}}_{eq}) + \frac{1}{2} (\mathbf{q} - \mathbf{q}_{eq})^T \mathbf{K} (\mathbf{q} - \mathbf{q}_{eq}), \end{aligned}$$

with

$$\dot{\mathbf{q}}_{eq} = [ \omega_{eq} \quad 0 \quad 0 \quad 0 ]^T,$$

then  $\bar{V}(\mathbf{q}_{eq}, \dot{\mathbf{q}}_{eq}, \mathbf{q}_{eq}, \dot{\mathbf{q}}_{eq}) = 0$ . In the sticking phase  $\dot{\mathbf{q}}_{eq} = \mathbf{0}$ , and the following expression holds

$$\bar{V}(\mathbf{q}, \dot{\mathbf{q}}, \mathbf{q}_{eq}, \dot{\mathbf{q}}_{eq}) = \frac{1}{2} \dot{\mathbf{q}}^T \mathbf{M}(\mathbf{q}) \dot{\mathbf{q}} + \frac{1}{2} (\mathbf{q} - \mathbf{q}_{eq})^T \mathbf{K} (\mathbf{q} - \mathbf{q}_{eq}). \quad (\text{C.3})$$



Consequently, the time derivative of  $\bar{V}$  equals

$$\dot{\bar{V}}(\mathbf{q}, \dot{\mathbf{q}}, \mathbf{q}_{eq}, \dot{\mathbf{q}}_{eq}) = \ddot{\mathbf{q}}^T \mathbf{M}(\mathbf{q}) \dot{\mathbf{q}} + \frac{1}{2} \dot{\mathbf{q}}^T \dot{\mathbf{M}}(\mathbf{q}) \dot{\mathbf{q}} + (\mathbf{q} - \mathbf{q}_{eq})^T \mathbf{K} \dot{\mathbf{q}}. \quad (\text{C.4})$$

If we insert (C.1) into the Euler-Lagrange equations (3.11) the following is obtained

$$\ddot{\mathbf{q}}^T \mathbf{M}(\mathbf{q}) + \frac{1}{2} \dot{\mathbf{q}}^T \dot{\mathbf{M}}(\mathbf{q}) + \mathbf{q}^T \mathbf{K} = (\mathbf{Q}^{nc}(\mathbf{q}, \dot{\mathbf{q}}))^T. \quad (\text{C.5})$$

Consequently, in the equilibrium point  $\mathbf{q}_{eq}$  the following holds

$$\mathbf{q}_{eq}^T \mathbf{K} = (\mathbf{Q}^{nc}(\mathbf{q}_{eq}, \mathbf{0}))^T. \quad (\text{C.6})$$

Furthermore, if we subtract expression (C.6) from (C.5), post-multiply the obtained result with  $\dot{\mathbf{q}}$  and substitute the obtained expression in (C.4) the following is obtained:

$$\dot{\bar{V}}(\mathbf{q}, \dot{\mathbf{q}}, \mathbf{q}_{eq}, \dot{\mathbf{q}}_{eq}) = (\mathbf{Q}^{nc}(\mathbf{q}, \dot{\mathbf{q}}) - \mathbf{Q}^{nc}(\mathbf{q}_{eq}, \mathbf{0}))^T \dot{\mathbf{q}}. \quad (\text{C.7})$$

From (3.14), the non-conservative forces  $\mathbf{Q}^{nc}(\mathbf{q}, \dot{\mathbf{q}})$  and  $\mathbf{Q}^{nc}(\mathbf{q}_{eq}, \mathbf{0})$  can be expressed in the following way:

$$\begin{aligned} \mathbf{Q}^{nc}(\mathbf{q}, \dot{\mathbf{q}}) &= \begin{bmatrix} k_m u_c - T_{fu}(\dot{\theta}_u) - T_{fl}(\dot{\theta}_u + \dot{\alpha}) \\ 0 \\ 0 \\ -T_{fl}(\dot{\theta}_u + \dot{\alpha}) \end{bmatrix} \\ &\quad - b \dot{\mathbf{q}}^T \begin{bmatrix} x^2 + y^2 & -y & x & 0 \\ -y & 1 & 0 & 0 \\ x & 0 & 1 & 0 \\ 0 & 0 & 0 & 0 \end{bmatrix}, \\ \mathbf{Q}^{nc}(\mathbf{q}_{eq}, \mathbf{0}) &= \begin{bmatrix} k_m u_c - T_{fu}(0) - T_{fl}(0) \\ 0 \\ 0 \\ -T_{fl}(0) \end{bmatrix}. \end{aligned}$$

If we substitute this into (C.7), and take into account that  $\omega_u = \dot{\theta}_u$  and  $\omega_l = \dot{\theta}_u + \dot{\alpha}$ , the following expression can be obtained

$$\begin{aligned} \dot{\bar{V}}(\mathbf{q}, \dot{\mathbf{q}}, \mathbf{q}_{eq}, \dot{\mathbf{q}}_{eq}) &= -(T_{fu}(\omega_u) - T_{fu}(0))\omega_u - (T_{fl}(\omega_l) - T_{fl}(0))\omega_l \\ &\quad - b \begin{bmatrix} \omega_u & \dot{x} & \dot{y} \end{bmatrix} \begin{bmatrix} x^2 + y^2 & -y & x \\ -y & 1 & 0 \\ x & 0 & 1 \end{bmatrix} \begin{bmatrix} \omega_u \\ \dot{x} \\ \dot{y} \end{bmatrix}. \end{aligned} \quad (\text{C.8})$$

From (5.7), (5.8), on one hand, and (C.2), (C.3), (3.12), (3.16), at the other hand, we see that the Lyapunov candidate function  $V_i(\mathbf{x}_{i1}, \mathbf{x}_{i2}, \mathbf{x}_{i1eq}, \mathbf{x}_{i2eq})$  defined by (5.7) is such that  $V_i(\mathbf{x}_{i1}, \mathbf{x}_{i2}, \mathbf{x}_{i1eq}, \mathbf{x}_{i2eq}) = \bar{V}(\mathbf{q}, \dot{\mathbf{q}}, \mathbf{q}_{eq}, \dot{\mathbf{q}}_{eq})$ . Consequently, the derivative of the Lyapunov candidate function satisfies  $\dot{V}_i(\mathbf{x}_{i1}, \mathbf{x}_{i2}, \mathbf{x}_{i1eq}, \mathbf{x}_{i2eq}) = \dot{\bar{V}}(\mathbf{q}, \dot{\mathbf{q}}, \mathbf{q}_{eq}, \dot{\mathbf{q}}_{eq})$ , i.e. is defined by expression (C.8).

# Bibliography

- Al-Bender, F., Lampaert, V., and Swevers, J. (2004). Modeling of dry sliding friction dynamics: From heuristic models to physically motivated models and back. *Chaos*, **14**(2), 446–460.
- Armstrong-Hélouvry, B. (1991). *Control of Machines with Friction*. Kluwer Academic Publishers, Boston.
- Armstrong-Hélouvry, B., Dupont, P., and Canudas de Wit, C. (1994a). Survey of models, analysis tools and compensation methods for the control of machines with friction. *Automatica*, **30**(7), 1083–1138.
- Aronov, V., D’Souza, A. F., Kalpakjian, S., and Sareef, I. (1983). Experimental investigation of the effect of system rigidity on wear and friction-induced vibrations. *ASME Journal of Lubrication Technology*, **105**, 206–211.
- Ascher, U. M., Mattheij, R. M. M., and Russell, D. R. (1995). *Numerical Solution of Boundary Value Problems for Ordinary Differential Equations*. SIAM, Philadelphia.
- Bailey, J. J. and Finnie, I. (1960). An analytical study of drill-string vibrations. *ASME Journal of Engineering for Industry*, 122–128.
- Batista, A. A. and Carlson, J. M. (1998). Bifurcation from steady sliding to stick slip in boundary lubrication. *Physical review E*, **57**(5), 4986–4996.
- Brett, J. F. (1991). Genesis of bit-induced torsional drill drillstring vibrations. In *Proceeding of the SPE/IADC Drilling Conference*. Amsterdam, The Netherlands, pp. 419–428.
- Brett, J. F. (1992). Genesis of torsional drillstring vibrations. *SPE Drilling Engineering*, **7**(3), 168–174.
- Brockley, C. A., Cameron, R., and Potter, A. F. (1967). Friction-induced vibrations. *ASME Journal of Lubrication Technology*, **89**, 101–108.
- Brockley, C. A. and Ko, P. L. (1970). Quasi-harmonic friction-induced vibrations. *ASME Journal of Lubrication Technology*, **92**, 550–556.
- Brogliato, B. (1999). *Nonsmooth Mechanics*. Springer, London.

- Canudas de Wit, C., Noel, P., Aubin, A., and Brogliato, B. (1991). Adaptive friction compensation in robot manipulators: Low-velocities. *International Journal of Robotics Research*, **10**(3), 189–199.
- Canudas de Wit, C., Olsson, H., Åström, K. J., and Lischinsky, P. (1995). A new model for control of systems with friction. *IEEE Transaction on Automatic Control*, **40**(3), 419–425.
- Coleman, T., Branch, M. A., and Grace, A. (2002). *Optimization Toolbox*. The Mathworks, Natic, Massachusetts.
- Cooperinstruments (2002). <http://www.cooperinstruments.com/pdf/lqb630.pdf>.
- Dankowitz, H. and Nordmark, A. B. (2000). On the origin and bifurcations of stick-slip oscillations. *Physica D*, **136**(3–4), 280–302.
- Deimling, K. and Szilagyi, P. (1994). Periodic solutions of dry friction problems. *Zeitschrift für angewandte Mathematik und Physik ZAMP*, **45**, 53–60.
- Di Bernardo, M., Feigin, M. I., Hogan, S. J., and Homer, M. E. (1999). Local analysis of c-bifurcations in n-dimensional piecewise-smooth dynamical systems. *Chaos, Solutions and Fractals*, **10**(11), 1881–1908.
- Driels, M. (1995). *Linear Control Systems Engineering*. McGraw-Hill, New York.
- Eerles, S. W. E. and Lee, C. K. (1976). Instabilities arising from the frictional interaction of a pin-disk system resulting in noise generation. *ASME Journal of Engineering for Industry*, **98**, 81–86.
- Faasen, R. P. H., Van de Wouw, N., Oosterling, J. A. J., and Nijmeijer, H. (2003). Prediction of regenerative chatter by modelling and analysis of high-speed milling. *International Journal of Machine Tools and Manufacture*, **43**, 1437–1446.
- Feigin, M. I. (1978). On the structure of c-bifurcation boundaries of piecewise continuous systems. *PMM*, **42**, 820–829.
- Feigin, M. I. (1994). *Forced Oscillations in Systems With Discontinuous Nonlinearities*. Nauka, Moscow.
- Fenner, T. R. (1989). *Mechanics of Solids*. Blackwell Scientific Publications, London.
- Fečkan, M. (1998). Bifurcations of periodic and chaotic solutions in discontinuous systems. *Archivum Mathematicum*, **34**, 73–82.
- Filippov, A. F. (1988). *Differential equations with discontinuous right-hand sides*. Kluwer Academic Publishers.
- Finnie, I. and Bailey, J. J. (1960). An experimental study of drill-string vibrations. *ASME Journal of Engineering for Industry*, 129–135.
- Fritz, R. J. (1970a). The effects of an annular fluid on the vibrations of a long rotor, part 1 - theory. *ASME Journal of Basic Engineering*, 923–929.
- Fritz, R. J. (1970b). The effects of an annular fluid on the vibrations of a long rotor, part 2 - test. *ASME Journal of Basic Engineering*, 930–937.

- Galvanetto, U., Bishop, S. R., and Briseghella, L. (1997). Event maps in a stick-slip systems. *Nonlinear Dynamics*, 99–115.
- Gelb, A., Kasper, J. F., Nash, R. A., Price, C. F., and A., S. A. (1978). *Applied Optimal Estimation*. The M.I.T. Press, London.
- Germa, C. (2002). *Self-Excited Oscillations of Drag Bits*. Master thesis, The University of Minnesota, The Faculty of the Graduate School.
- Gunter, E. J., Humphris, R. H., and Springer, H. (1983). Influence of unbalance on the nonlinear dynamical response and stability of flexible rotor-bearing systems. *Rotor Dynamical Instability*, **115**, 37–58.
- Hendriks, M. P. M. (2004). *Analysis of Torsional and Lateral Vibrations in an Experimental Drill-String Set-Up*. Master thesis, Eindhoven University of Technology, Department of Mechanical Engineering.
- Hensen, R. H. A. (2002). *Controlled Mechanical Systems with Friction*. Ph.D. thesis, Eindhoven University of Technology, The Netherlands.
- Hensen, R. H. A., Angelis, G. Z., Van de Molengraft, M. J. G., De Jager, A. G., and Kok, J. J. (2000). Grey-box modeling of friction: An experimental case-study. *European Journal of Control*, **6**(3), 258–267.
- Hensen, R. H. A., Van de Molengraft, M. J. G., and Steinbuch, M. (2002). Friction induced hunting limit cycles: an event mapping approach. In *Proceeding of the 2002 American Control Conference*. Anchorage, AK, pp. 2267–2272.
- Ibrahim, R. A. (1994a). Friction-induced vibration, chatter, squeal, and chaos: Mechanics of contact and friction. *Applied Mechanical Reviews: ASME*, **47**(7), 209–226.
- Ibrahim, R. A. (1994b). Friction-induced vibration, chatter, squeal, and chaos: Dynamics and modeling. *Applied Mechanical Reviews: ASME*, **47**(7), 227–253.
- Jansen, J. D. (1991). Non-linear rotor dynamics as applied to oilwell drillstring vibrations. *Journal of Sound and Vibration*, **147**(1), 115–135.
- Jansen, J. D. (1993). *Nonlinear Dynamics of Oil-well Drill-strings*. Ph.D. thesis, Delft University Press, The Netherlands.
- Jansen, J. D. and Van den Steen, L. (1995). Active damping of self-excited torsional vibrations in oil well drillstrings. *Journal of Sound and Vibration*, **179**(4), 647–668.
- Juloski, A. L., Mihajlović, N., Heemels, W. P. M. H., Van de Wouw, N., and Nijmeijer, N. (2005). Observer design for an experimental drill-string set-up. In *Proceeding of the 44th IEEE Conference on Decision and Control*. Seville, Spain. Submitted.
- Karnopp, D. (1985). Computer simulation of stick-slip in mechanical dynamic systems. *ASME Journal of Dynamic Systems, Measurement, and Control*, **107**(1), 100–103.
- Khalil, H. K. (2000). *Nonlinear Systems*. Prentice Hall, New Jersey.

- Krauter, A. I. (1981). Generation of squeal/chatter in water-lubricated elastomeric bearings. *ASME Journal of Lubrication Technology*, **103**, 406–413.
- Kreuzer, E. and Kust, O. (1996a). Analyse selbsterregter drehschwingungen in torsionsstäben. *ZAMM - Journal of Applied Mathematics and Mechanics / Zeitschrift fuer Angewandte Mathematik und Mechanik*, **76**(10), 547–557.
- Kreuzer, E. and Kust, O. (1996b). Analysis of long torsional strings by proper orthogonal decomposition. *Archive of Applied Mechanics*, **67**, 68–80.
- Kreuzer, E. and Kust, O. (1997). Controlling torsional vibrations through proper orthogonal decomposition. In *Iutam Symposium on Interaction between Dynamics and Control in Advanced Mechanical Systems*. pp. 207–214.
- Kunze, M. and Küpper, T. (1997). Qualitative bifurcation analysis of a non-smooth friction-oscillator model. *Zeitschrift für angewandte Mathematik un Physik ZAMP*, **48**, 87–101.
- Kust, O. (1998). *Selbsterregte Drehschwingungen in schlanken Torsionssträngen: Nichtlineare Dynamik und Regelung*. Ph.D. thesis, Technical University Hamburg.
- Kyallingstad, A. and Halsey, G. W. (1988). A study of slip/stick motion of the bit. *SPE Drilling Engineering*, 369–373.
- Lee, C.-W. (1993). *Vibration analysis of rotors*. Kluwer Academic Publishing, Dordrecht, The Netherlands.
- Leine, R. and Van de Wouw, N. (2001). *Numerical Methods for Computing Periodic Solutions*. Eindhoven University of Technology, The Netherlands.
- Leine, R. I. (2000). *Bifurcations in Discontinuous Mechanical Systems of Filippov-Type*. Ph.D. thesis, Eindhoven University of Technology, The Netherlands.
- Leine, R. I. and Nijmeijer, H. (2004). *Dynamics and Bifurcations of Non-smooth Mechanical Systems*. Springer, Berlin.
- Leine, R. I. and Van Campen, D. H. (2003). Discontinuous fold bifurcations. *Systems Analysis Modelling Simulation*, **43**(3), 321–332.
- Leine, R. I., Van Campen, D. H., De Kraker, A., and Van den Steen, L. (1998). Stick-slip vibrations induced by alternate friction models. *Nonlinear Dynamics*, **16**, 41–54.
- Leine, R. I., Van Campen, D. H., and Glocker, C. (2003). Nonlinear dynamics and modeling of various wooden toys with impact and friction. *Journal of Vibrations and Control*, **5**, 25–78.
- Leine, R. I., Van Campen, D. H., and Keultjes, W. J. G. (2002). Stick-slip whirl interaction in drillstring dynamics. *ASME Journal of Vibrations and Acoustics*, **124**, 209–220.
- Ljung, L. (1999). *System Identification - Theory for the User*. Prentice-Hall, Englewood Cliffs, second edition.

- Mallon, N. (2003). *Reduced-Order Observer Based Friction Compensation for a Controlled One-Link Robot*. Master thesis, Eindhoven University of Technology, Department of Mechanical Engineering.
- Mallon, N. J., Van de Wouw, N., Putra, D., and Nijmeijer, H. (2005). Friction compensation in a controlled one-link robot using a reduced-order observer. *IEEE Transactions on Control Systems Technology*. Submitted.
- Mayers, R. H. (1989). *Classical and Modern Regression with Applications*. Dixbury Press, Boston.
- Mihajlović, N., Van de Wouw, N., Hendriks, M. P. M., and Nijmeijer, H. (2005a). Friction-induced limit cycling in flexible rotor systems: an experimental drill-string set-up. *Nonlinear Dynamics, Special Issue on Experimental Analysis and Control of Nonsmooth Dynamical Systems: Theory and Experiments*. Submitted.
- Mihajlović, N., Van de Wouw, N., Hendriks, M. P. M., and Nijmeijer, H. (2005b). Friction-induced vibrations in an experimental drill-string system for various friction situations. In *ENOC-2005*. Eindhoven, The Netherlands. Accepted.
- Mihajlović, N., Van Veggel, A. A., Van de Wouw, N., and Nijmeijer, H. (2004a). Analysis of friction-induced limit cycling in an experimental drill-string set-up. *ASME Journal of Dynamic Systems, Measurements and Control*, **126**(4), 709–720.
- Mihajlović, N., Van Veggel, A. A., Van de Wouw, N., and Nijmeijer, H. (2004b). Friction-induced torsional vibrations in an experimental drill-string system. In *Proceedings of the 23rd IASTED International conference on Modelling, Identification, and Control*. pp. 228–233.
- Muszynska, A. (1986). Whirl and whip - rotor/bearing stability problems. *Journal of Sound and Vibrations*, **110**(3), 443–462.
- Narendra, K. S. and Parthasarathy, K. (1990). Identification and control of dynamical systems using neural networks. *Journal of Sound and Vibrations*, **1**(1), 4–27.
- Nayfeh, A. H. (1973). *Perturbation Methods*. Wiley, New York.
- Nayfeh, A. H. and Balachandran, B. (1995). *Applied Nonlinear Dynamics: Analytical, Computational and Experimental Method*. John Wiley and Sons, Inc., New York.
- Nayfeh, A. H. and Mook, D. T. (1979). *Nonlinear oscillations*. Wiley, New York.
- Olsson, H. (1996). *Control Systems with Friction*. Ph.D. thesis, Lund Institute of Technology, Sweden.
- Olsson, H. and Åström, K. J. (1996). Friction generated limit cycles. In *Proceeding of the 1996 IEEE Conference on Control Applications*. Dearborn, MI, pp. 798–803.
- Olsson, H. and Åström, K. J. (2001). Friction generated limit cycles. *IEEE Conference on Control Systems Technology*, **9**(4), 629–636.
- Olsson, H., Åström, K. J., Canudas de Wit, C., Gäfvert, M., and Lischinsky, P. (1998). Friction models and friction compensations. *European Journal of Control*, **4**(3), 176–195.

- Parker, T. S. and Chua, L. O. (1989). *Practical Numerical Algorithms for Chaotic Systems*. Springer-Verlag.
- Pfeiffer, F. and Glocker, C. (1996). *Multibody Dynamics with Multilateral Contact*. Wiley series in nonlinear science, John Wiley & Sons, New York.
- Popp, K., Rudolph, M., Kröger, M., and Lindner, M. (2002). Mechanisms to generate and to avoid friction induced vibrations. *VDI-Berichte 1736, VDI-Verlag Düsseldorf 2002*, 1–15.
- Popp, K. and Stelzer, P. (1989). Nonlinear oscillations of structures induced by dry friction. In *Proceeding of the IUTAM Symposium on Nonlinear Dynamics and Engineering Systems*. Springer-Verlag, Berlin, pp. 233–240.
- Popp, K. and Stelzer, P. (1990). Stick-slip vibrations and chaos. *Philosophical Transactions of the Royal Society of London*, **332**, 89–105.
- Putra, D. (2004). *Control of Limit Cycling in Frictional Mechanical Systems*. Ph.D. thesis, Eindhoven University of Technology, The Netherlands.
- Putra, D., Moreau, L., and Nijmeijer, H. (2004). Observer-based compensation of discontinuous friction. In *Proceeding of the 43th IEEE Conference on Decision and Control*. Atlantis, Paradise Island, Bahamas, USA, pp. 4940–4945.
- Putra, D. and Nijmeijer, H. (2003). Limit cycling in observer-based controlled mechanical systems with friction. In *Proceeding of the European Control Conference 2003*. Cambridge, UK.
- Putra, D. and Nijmeijer, H. (2004). Limit cycling in an observer-based controlled system with friction: Numerical analysis and experimental validation. *International Journal of Bifurcation and Chaos*, **14**(9), 3083–3093.
- Richard, T., Gernay, C., and Detournay, E. (2004). Self-excited stick-slip oscillations of drill bits. *C. R. Mecanique*, **332**, 619–626.
- Sastry, S. (1999). *Nonlinear Systems: Analysis, Stability and Control*. Springer, New York.
- Schaevitz (2004). <http://www.msiusa.com/schaevitz/pdf/lvdt/hr-series.pdf>.
- Shell (1997). <http://www.shelldubai.com/industrial/msds/shell-ondina.pdf>.
- Shevitz, D. and Paden, B. (1994). Lyapunov stability theory of nonsmooth systems. *IEEE Transactions on Automatic Control*, **39**(9), 1910–1914.
- Strogatz, S. H. (2000). *Nonlinear Dynamics and Chaos*. Westview Press, Cambridge.
- Tondl, A. (1965). *Some Problems of Rotor Dynamics*. Chapman and Hall Limited, London, UK.
- Tucker, R. W. and Wang, C. (1999). An integrated model for drill-string dynamics. *Journal of Sound and Vibrations*, **224**(1), 123–165.
- Van Campen, D. H. (2000). *Nonlinear Dynamics of Mechanical Systems*. Eindhoven University of Technology, Eindhoven, The Netherlands.



- Van de Vorst, E. L. B. (1996). *Long Term Dynamics and Stabilization of Nonlinear Mechanical Systems*. Ph.D. thesis, Eindhoven University of Technology.
- Van de Vorst, E. L. B., Fey, R. H. B., De Kraker, A., and Van Campen, D. H. (1994). Steady-state behaviour of flexible rotor dynamics systems with oil journal bearings. In *Proceeding of the WAM of the ASME, Symposium on Nonlinear and Stochastic Dynamics*. New York, USA, volume 192, pp. 107–114.
- Van de Vrande, B. L. (2001). *Nonlinear Dynamics of Elementary Rotor Systems with Compliant Plain Journal Bearings*. Ph.D. thesis, Eindhoven University of Technology.
- Van de Vrande, B. L., Van Campen, D. H., and De Kraker, A. (1999). An approximate analysis of dry-friction-induced stick-slip vibrations by a smoothing procedure. *Nonlinear Dynamics*, **19**(2), 157–169.
- Van de Wouw, N. and Leine, R. I. (2004). Attractivity of equilibrium sets of systems with dry friction. *Nonlinear Dynamics*, **35**, 19–39.
- Van de Wouw, N., Mallon, N. J., and Nijmeijer, H. (2004). Friction compensation in a controlled one-link robot using a reduced-order observer. In *Proceedings of 6th IFAC Symposium on Nonlinear Control Systems (NOLCOS)*. pp. 1163–1168.
- Van de Wouw, N., Mihajlović, N., and Nijmeijer, H. (2005a). Friction-induced limit cycling in flexible rotor systems: An experimental drill-string system. In *DETC 2005. ASME Design Engineering Technical Conferences*. Long Beach, California USA. Accepted.
- Van de Wouw, N., Van den Heuvel, M. N., Van Rooij, J. A., and Nijmeijer, H. (2005b). Performance of an automatic ball balancer with dry friction. *International Journal of Bifurcation and Chaos*, **15**(1), 65–82.
- Van den Steen, L. (1997). *Suppressing Stick-Slip-Induced Drill-string Oscillations: a Hyper Stability Approach*. Ph.D. thesis, University of Twente.
- Van der Heijden, G. H. M. (1993). Bifurcation and chaos in drillstring dynamics. *Chaos, Solutions and Fractals*, **3**, 219–247.
- Van der Heijden, G. H. M. (1994). *Nonlinear Drillstring Dynamics*. Ph.D. thesis, University of Utrecht.
- Van Veggel, A. A. (2002). *Experimental Evaluation of Friction-Induced Limit Cycling in the Drill-String Set-Up*. Master thesis, Eindhoven University of Technology, Department of Mechanical Engineering.
- Wiercigroch, M. and Budak, E. (2001). Sources of nonlinearities, chatter generation and suppression in metal cutting. *The Philosophical transactions of the Royal Society of London A*, **359**, 663–693.
- Wiercigroch, M. and Krivtsov, A. M. (2001). Frictional chatter in orthogonal metal cutting. *The Philosophical transactions of the Royal Society of London A*, **359**, 713–738.





# Summary

Self-sustained vibrations which can appear in mechanical systems often limit the performance of such systems or can even cause failure or damage to such systems. Moreover, different types of vibration can appear in dynamical systems. In order to gain an improved understanding and to predict different types of vibrations which appear in mechanical systems, it is important to understand the causes for such vibrations and the interaction between those vibrations.

In this thesis, we address on the one hand friction-induced vibrations in flexible mechanical systems, and on the other hand lateral vibrations caused by mass-unbalance in rotor systems, and the interaction between those two types of vibrations. Although a lot of theoretical research has been done on vibrations in flexible rotor systems, a limited number of papers is available which include experimental results on the friction-induced vibrations and on the interaction between different types of vibrations.

For this purpose, we have designed and constructed an experimental drill-string set-up which exhibits both types of vibration. The set-up consists of a DC-motor, two rotating (upper and lower) discs, a low-stiffness string, which connects the two discs, and an additional brake at the lower disc. The lower disc can rotate around its geometric center and is also free to move in lateral direction. The configuration of the experimental set-up is representative for many other mechanical systems, in which friction or unbalance can deteriorate the system performance by the appearance of vibrations. For example, when the lower disc is fixed in lateral direction (i.e. when the lower disc only rotates), the system forms a configuration of two masses, coupled by a flexibility, of which one is subject to friction and the other is driven by an actuator. In this context, one can think of set-ups such as printers, pick and place machines, industrial and domestic robots, braking mechanisms and many others. Moreover, when mass-unbalance is present at the lower disc and the disc can move in lateral direction, this configuration can be recognized in drilling systems which are used for exploration of oil and gas, in electrical shavers, in various turbines, pumps, fans and so on.

The drill-string set-up is modelled and the parameters of the model are estimated. The comparison between responses of the experimental set-up and estimated model indicates a high accuracy of the obtained parameter estimates. The steady-state behaviour of the drill-string system has been analyzed when various constant input voltages are applied to the DC motor; first, when only torsional and no lateral vibrations occur and, second, when both torsional and lateral vibrations appear in the system.

When analyzing the friction-induced vibrations a discontinuous static friction

model is used. We have chosen such a model and not a more complicated dynamical friction model since it accounts for the friction characteristics which are crucial for the global dynamics of the system but avoids unnecessary complexity. A discontinuous friction model leads to a discontinuous model of the system dynamics which exhibits both friction-induced vibrations and the interaction between friction-induced vibrations and vibrations due to mass-unbalance. As a result of the analysis on a theoretical, numerical and experimental level the following conclusions are drawn.

When analyzing the set-up with only friction-induced torsional vibrations and no lateral vibrations, the main conclusion is that a subtle interplay of negative damping characteristics at low velocities and viscous friction at higher velocities determines the occurrence and nature of friction-induced limit cycling. It also determines the range of parameters for which these limit cycles sustain. Furthermore, the level of positive damping at very low velocities relative to the negative damping level at slightly higher velocities determines whether torsional vibrations with or without stick-slip can occur. Then, both model-based and experimental bifurcation analysis confirm that discontinuous bifurcations play a crucial role in the creation and disappearance of these limit cycles. Also, the way in which such friction characteristics are influenced by physical conditions such as temperature and normal forces on the frictional contact is experimentally studied. An important observation is that the normal force in the frictional contact influences the friction force in a rather complex way and can induce a higher negative damping level (for larger normal forces), which in turn can give rise to limit cycles of a larger amplitude for a larger range of constant input voltages to the DC motor.

The analysis of the set-up, when both torsional and lateral vibrations are present, leads to the main conclusion that two types of torsional vibrations can appear. Firstly, friction-induced torsional vibrations and, secondly, torsional vibrations due to coupling between torsional and lateral dynamics may appear. Furthermore, if mass-unbalance is present at the lower disc, the amplitude of friction-induced vibrations and the region in which these vibrations occur, both decrease compared to the situation without mass-unbalance. Moreover, it is shown that if the mass-unbalance is large enough then torsional vibrations can disappear entirely. Next, on a simulation level it is shown that torsional vibrations due to coupling between torsional and lateral modes appear for input voltages to the DC motor which are higher than the so-called critical voltage, which is related to the critical angular velocity inducing resonance in lateral direction. Due to limitations in the available DC motor, those vibrations are studied only at a simulation level.

Finally, the knowledge obtained in this thesis provides a better understanding of the causes for torsional and lateral vibrations. Moreover, based on this knowledge, various control strategies may be designed and tested on the designed set-up in order to eliminate torsional and lateral vibrations. Furthermore, the results presented here can support the design of various braking mechanisms, pumps and fans in preventing the occurrence of or in decreasing the amplitude of friction-induced torsional vibrations and lateral vibrations due to mass-unbalance.

# Samenvatting

Zelf-exciterende trillingen in dynamische mechanische systemen beperken veelal de prestatie van dergelijke systemen en kunnen zelfs schade of uitval veroorzaken. Bovendien kunnen er verschillende soorten trillingen voorkomen in dynamische systemen. Het is van groot belang de oorzaken van en de interactie tussen deze trillingen te begrijpen om het ontstaan van dergelijke trillingen in mechanische systemen te voorspellen.

In dit proefschrift behandelen we ten eerste trillingen in flexibele mechanische systemen geïnduceerd door wrijving, ten tweede laterale trillingen in dynamische rotor systemen als gevolg van massa-onbalans en ten derde de interactie tussen deze soorten trillingen. Alhoewel veel theoretisch onderzoek is verricht op het gebied van trillingen in dynamische rotor systemen, bestaat er slechts een beperkt aantal publicaties die experimentele resultaten behandelen over trillingen geïnduceerd door wrijving en de interactie tussen de verschillende soorten trillingen.

Hiertoe is een experimentele boorstang-opstelling ontworpen en gebouwd waarin beide soorten trillingen voorkomen. De opstelling bestaat uit een gelijkstroommotor, twee roterende inertia's (boven en beneden), een kabel met lage torsie-stijfheid, welke de twee inertia's verbindt, en een rem op de onderste inertia. De onderste inertia kan roteren rond zijn geometrisch centrum en is bovendien vrij om in laterale richting te bewegen. Deze configuratie komt voor in vele andere mechanische systemen waarin wrijving of massa-onbalans de systeemprestatie kan verslechteren door het optreden van trillingen. Bijvoorbeeld, wanneer de onderste inertia gefixeerd wordt in laterale richting (met andere woorden wanneer de onderste inertia alleen roteert), dan representeert het systeem een configuratie van twee inertia's, gekoppeld door een flexibiliteit, waarvan één inertia wrijving ondervindt en de andere aangedreven wordt. Voorbeelden zijn te vinden in printers, positioneringsmachines, industriële en huishoudelijke robots, rem-mechanismen etcetera. Wanneer de onderste inertia vrij kan bewegen in laterale richting en wanneer massa-onbalans aanwezig is, kan deze configuratie voorkomen in boorsystemen welke gebruikt worden voor de winning van olie en gas, in elektrische scheerapparaten en in verscheidene turbines, pompen en ventilatoren.

De ontworpen opstelling is gemodelleerd en de parameters van dit model zijn geschat. De vergelijking tussen de responsies van de experimentele opstelling en het geïdentificeerde model duiden op een grote nauwkeurigheid van de geschatte parameters. Het limiet-gedrag van dit systeem is geanalyseerd voor verschillende constante ingangsvoltages aan de gelijkstroommotor; ten eerste wanneer enkel torsie-trillingen optreden en, ten tweede, wanneer zowel torsie- en laterale trillingen voorkomen in het systeem.

Bij de analyse van trillingen veroorzaakt door wrijving is een discontinu statisch wrijvingsmodel gebruikt. De keuze voor een dergelijk model, in tegenstelling tot een complexer dynamisch model, is gebaseerd op het feit dat een statisch model de wrijvingskarakteristieken goed beschrijft welke essentieel zijn voor de globale dynamica van het systeem, terwijl onnodige complexiteit vermeden kan worden. Een discontinu wrijvingsmodel leidt evenwel tot een discontinu model van de systeemdynamica.

Gebaseerd op de theoretische, numerieke en experimentele analyses kunnen de volgende conclusies getrokken worden. Ten aanzien van het systeem waarin slechts torsie-trillingen optreden kan geconcludeerd worden dat een balans tussen negatieve demping bij lage snelheden en visceuze wrijving bij hogere snelheden bepalend is voor het ontstaan en de aard van de door wrijving geïnduceerde trillingen. Deze balans bepaalt ook voor welke parameter-waarden trillingen ontstaan. Bovendien bepaalt de balans tussen positieve demping bij zeer lage snelheden en negatieve demping bij enigszins hogere snelheden of trillingen met of zonder stick-slip optreden. Zowel de model-gebaseerde als de experimentele bifurcatie analyse bevestigen dat discontinue bifurcaties een cruciale rol spelen in het ontstaan en verdwijnen van deze limiet cycli. Bovendien is de invloed van fysieke condities, zoals de temperatuur en de normaalkrachten in het wrijvingscontact, op de wrijvingskarakteristieken bestudeerd. Een belangrijke observatie is dat de normaalkracht in het wrijvingscontact de wrijvingskracht op een complexe manier beïnvloedt. Namelijk, grotere normaalkrachten kunnen leiden tot een hogere negatieve demping in de wrijvingskarakteristiek, hetgeen weer kan leiden tot limiet cycli, met een grotere amplitude, die voorkomen in een groter bereik van constante ingangsvoltages aan de gelijkstroommotor.

De analyse van het systeem, waarin zowel torsie-trillingen als laterale trillingen voorkomen, leidt tot de conclusie dat twee soorten torsie-trillingen kunnen ontstaan: ten eerste torsie-trillingen veroorzaakt door wrijving en ten tweede torsie-trillingen als gevolg van de koppeling tussen de dynamica in torsie-richting en laterale richting. Als bovendien massa-onbalans aanwezig is in de onderste inertia, nemen zowel de amplitude en het domein (in termen van ingangsvoltages) van de door wrijving veroorzaakte trillingen af in vergelijking met de situatie zonder onbalans. Wanneer de massa-onbalans groot genoeg is kunnen dergelijke torsie-trillingen zelfs volledig verdwijnen. Op simulatie niveau is het aangetoond dat torsie-trillingen, als gevolg van de koppeling tussen de dynamica in torsie-richting en laterale richting, optreden voor ingangsvoltages groter dan een kritisch voltage. Die kritische ingangsvoltage is gerelateerd aan de kritische hoeksnelheid waarvoor resonantie in laterale richting optreedt. Als gevolg van beperkingen ten aanzien van de beschikbare gelijkstroommotor in de experimentele opstelling is dit soort trillingen alleen onderzocht op simulatie niveau.

Tenslotte leidt de kennis verkregen in dit onderzoek tot een verbeterd begrip ten aanzien van de oorzaken van zowel torsie-trillingen als laterale trillingen in flexibele rotor-dynamische systemen met wrijving. Bovendien kan deze kennis in toekomstig onderzoek gebruikt worden om regelstrategieën, met als doel het onderdrukken van deze trillingen, te ontwerpen en te implementeren op de experimentele opstelling. Verder kunnen de gepresenteerde resultaten het ontwerp van verscheidene rem-mechanismen, pompen en turbines ondersteunen met als doel het vermijden van deze trillingen.

# Резиме

У динамичким системима могу да се појаве различите врсте вибрација, које често деградирају перформансе таквих система а, такође, могу да изазову њихов отказ или оштећење. Зато, да би боље разумели и предвидели појаву различитих врста вибрација, веома је важно разумети разлоге због којих се оне јављају, како и начине на које оне утичу једне на друге.

У овој дисертацији анализирани су: вибрације које се јављају услед трења у механичким системима са флексибилношћу, латералне вибрације у ротационим системима које се јављају због неизбалансираности у ротору, и међусобни утицај ове две врсте вибрација. Иако постоји пуно теоријских истраживања, које анализирају вибрације у ротационим системима са флексибилношћу, мали број радова је доступан који поседују експерименталне резултате и који обухватају анализу међусобног утицаја различитих врста вибрација.

Из тих разлога, пројектован је и конструисан експериментални уређај који репродукује торзионе и латералне вибрације присутне у системима за бушење нафте. Овај уређај састоји се из мотора једносмерне струје, два ротациона диска (горњег и доњег) повезана еластичном жицом и додатне кочнице која је уграђена на доњем диску. Доњи диск може да ротира око свог геометријског центра али може, такође, да се креће и у бочном (латаралном) правцу. Велики број система, у којима трење и неизбалансираност може да погорша перформансе изазивањем вибрација, има сличну конфигурацију као и овај уређај. На пример, када је доњи диск фиксиран у бочном правцу (тј. када доњи диск може да ротира само око своје осе), тада систем представља систем са две масе повезане еластичном опругом, при чему је једна маса подвргнута трењу, док се другом масом управља актуатором. Примери оваквих система налазе се у принтерима, машинама за уградњу чипова на штампаним плочама, индустријским роботима, кочним системима итд. Осим тога, када је неизбалансираност присутна на доњем диску и он може да се помера у латералном правцу, тада овакав уређај подсећа на системе који се користе за бушење и вађење гаса и нафте, електричне бријаче, различите турбине, пумпе, вентилаторе итд.

Пројектован експериментални уређај је моделован и параметри модела су естимирани. На основу поређења одзива уређаја и добијеног модела, закључује се да добијени модел веома добро описује динамичко понашање уређаја. Затим је анализирано понашање уређаја у стационарном стању када су на улаз мотора довођени константни улазни напони: прво, када су само торзионе вибрације присутне (не постоје латералне вибрације) и, друго, када се и торзионе и латералне вибрације појављују у систему.

Приликом анализе торзионих вибрација изазваних трењем, коришћен је дисконтинуални статички модел трења. Такав модел, а не неки компликованији динамички модел трења, изабран је из разлога што статички модел описује неколико, веома битних, карактеристика трења, а и на тај начин избегнута је непотребна сложеност модела. Дисконтинуални модел трења води ка формирању дисконтинуалног модела динамике система, који описује и вибрације проузроковане трењем, као и интеракцију између ових вибрација и вибрација које су последица неизбалансираности доњег диска.

На основу теоријске анализе, као и на основу експерименталних и нумеричких резултата, дошло се до следећих закључака. При анализи експерименталног уређаја у којем су присутне само торзионе вибрације, главни закључак је да однос између негативног нагиба криве трења на малим брзинама и коефицијента вискозног трења на вишим брзинама одређује појаву и природу насталих вибрација. Осим тога, тај однос одређује и скуп параметара при којима вибрације могу да се појаве. Штавише, закључено је да однос између позитивног нагиба криве трења на веома малим брзинама и негативног нагиба на нешто већим брзинама одређује да ли ће торзионе вибрације бити са заустављањем доњег диска или не. Бифуркациона анализа уређаја и његовог модела потврђују да дисконтинуалне бифуркације играју веома значајну улогу у стварању и нестајању ових вибрација. Експериментално је, такође, анализирано како различити физички услови, као, на пример, температура и нормална сила, утичу на силу трења. Као резултат те анализе, утврђено је да нормална сила утиче на силу трења на један веома компликован начин. Наиме, већа нормална сила изазива већи негативни нагиб силе трења, што за последицу има већу амплитуду вибрација и већи опсег улазних константних напона при којима се јављају те вибрације.

При анализи експерименталног уређаја, код кога су торзионе и латералне вибрације присутне, закључено је да могу да се појаве два типа торзионих вибрација: услед трења, и услед интеракције између торзионе и латералне динамике система. Осим тога, услед неизбалансираности доњег диска, показано је да се амплитуда торзионих вибрација смањује, као и опсег улазних константних напона за које се те вибрације јављају. Показано је, штавише, да ако је неизбалансираност довољно велика, торзионе вибрације могу потпуно да нестану. На основу симулационих резултата, утврђено је да се торзионе вибрације услед интеракције између торзионе и латералне динамике јављају за улазне напоне мотора које су веће од тзв. критичног улазног напона. Када се тај напон доведе на улаз мотора, онда доњи диск почиње да се креће тзв. критичном угаоном брзином, која индукује резонанцу у латералном правцу. Због ограничења у мотору, ове вибрације анализирани су само на нивоу симулације.

Материја изложена у овој дисертацији омогућава боље разумевање узрока због којих се јављају торзионе и латералне вибрације. Осим тога, на основу резултата добијених у дисертацији, разне управљачке стратегије могу се пројекти и тестирати на експерименталном уређају у циљу елиминације тих вибрација. Такође, овде презентовани резултати могу да помогну у пројектовању различитих кочионих механизма, пумпи, вентилатора, тако да се онемогући појава вибрација услед трења, латералних вибрација услед неизбалансираности ротора, или да се умањи амплитуда тих вибрација.

# Curriculum vitae

Nenad Mihajlović was born in Zaječar, Serbia and Montenegro on November 7th, 1971. Upon completion of his pre-university education at the Gymnasium "Bora Stanković" in Niš, in 1990 he started his academic education at the Faculty of Electronic Engineering, University of Niš, Serbia and Montenegro. After finishing his graduation project *Linear Fuzzy Knowledge Based Controllers Design* in 1996, he started as a research assistant and a postgraduate student at the Department of Automatic Control, Faculty of Electronic Engineering, University of Niš. The results of his research are presented in his Master thesis *Static Accuracy of the Variable Structure Control Systems*. In 2000 he moved to Eindhoven, the Netherlands, and became a Ph.D. student at the Department of Mechanical Engineering at the Eindhoven University of Technology. The Ph.D. project was entitled *Torsional and Lateral Vibrations in Flexible Rotor Systems with Friction*. Since February 2005, he is employed as a Research Scientist at the Optics and Mechanics Group at the Philips Research Eindhoven.